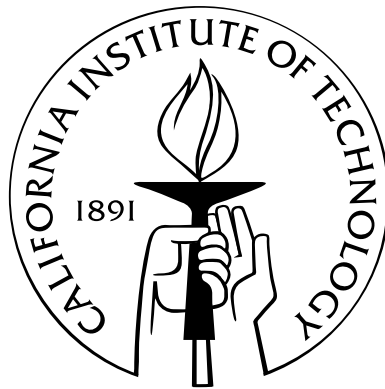


# Structure of the Turbulent Boundary Layer Under Static and Dynamic Impulsive Roughness Perturbation

Thesis by  
Ian Jacobi

In Partial Fulfillment of the Requirements  
for the Degree of  
Doctor of Philosophy



California Institute of Technology  
Pasadena, California

2013  
(Defended June 29, 2012)



# Acknowledgements

This research was supported through the Air Force Office of Scientific Research (# FA9550-08-1-0049 under Program Manager John Schmisser) and by the Presidential Early Career Award for Scientists and Engineers (PECASE # FA9550-09-1-0701). The help and guidance of Beverley McKeon, Michele Guala, Jeff Lehew, and Cody Gonzalez are gratefully acknowledged.

# Abstract

The zero-pressure gradient turbulent boundary layer at Reynolds numbers (based on momentum thickness) ranging from 2700–4100 was perturbed using an impulsively short patch of two-dimensional, spanwise roughness elements. A spatial perturbation was considered in which the roughness patch was held statically on the flat-plate, and the flow downstream of the perturbation was measured by hotwire and particle-image velocimetry. A dynamic perturbation, in which the roughness patch was actuated periodically in time, was also studied, and additional measurements were taken by phase-locking to the dynamic actuation itself.

The static perturbation distorted the boundary layer through the generation of a ‘stress bore’ which modified the mean streamwise velocity gradient. The effect of this stress bore was observed in a modification of statistical and spectral measures of the turbulence, as well as a redistribution of coherent structures in the boundary layer. The characterization of the statically perturbed boundary layer provided a base flow from which to consider the dynamically perturbed flow. The dynamically perturbed flow manifested both effects analogous to the static perturbation, as well as a coherent, periodic, large-scale velocity fluctuation. The extent to which these two features could be treated as linearly independent was studied by a variety of statistical and spectral means. Moreover, the very large scale motion synthesized by the dynamic perturbation was isolated by phase-locked measurement, and its behavior was predicted with reasonable success by employing a resolvent operator approach to a forced version of the Orr-Sommerfeld equation.

The relationship between large-scale motions and an envelope of small-scale motions in the turbulent boundary layer was studied in both the unperturbed and perturbed flows. A variety of correlation techniques were used to interpret the interaction between the different scale motions in the context of a phase-relationship between large and small scales. This phase relationship was shown to provide a physically-grounded perspective on the relationship between the synthetic very large scale motion produced by the dynamic perturbation and the smaller scales in the flow, and was able to provide a foundation for thinking about new approaches to controlling turbulence through large-scale forcing.

# Contents

<b>Acknowledgements</b>	<b>iii</b>
<b>Abstract</b>	<b>iv</b>
<b>List of Figures</b>	<b>viii</b>
<b>List of Tables</b>	<b>xxiii</b>
<b>1 Background</b>	<b>1</b>
1.1 Perturbing the Turbulent Boundary Layer . . . . .	1
1.2 Structure of the Turbulent Boundary Layer . . . . .	2
1.3 Nonequilibrium Boundary Layers . . . . .	4
1.4 Roughness and Roughness Perturbations . . . . .	6
1.5 Spatio-Temporal Perturbations . . . . .	8
1.6 Modeling the Perturbed Boundary Layer and the Resolvent Method . . . . .	9
1.7 The Influence of Synthetic Large-Scale Motions on Boundary Layer Turbulence . . .	13
1.8 The Perturbed Flow and the Generation of Synthetic Large-Scale Motions . . . . .	15
1.9 Experimental Organization . . . . .	15
<b>2 Experimental Setup</b>	<b>18</b>
2.1 Merrill Wind Tunnel Facility . . . . .	18
2.2 Single-Point Velocity Measurements . . . . .	19
2.3 PIV . . . . .	20
2.4 Mean Flow Properties and Resolution Limits . . . . .	23
2.4.1 Spectral Smoothing . . . . .	25
2.5 Roughness . . . . .	26
2.6 Dynamic Actuation and Phase-Locked Measurements . . . . .	28
<b>3 The Impulsive Static-Roughness Perturbation</b>	<b>30</b>
3.1 The Static Impulse Experiment . . . . .	30

3.1.1	Mean Flow Properties . . . . .	30
3.1.2	Internal Layers . . . . .	33
3.1.3	Turbulence Statistics . . . . .	37
3.1.4	Composite Spectra . . . . .	43
3.1.5	Swirling and Vortex Structure . . . . .	48
3.2	Discussion of the Static Impulse Experiment . . . . .	51
<b>4</b>	<b>The Effect of Galilean and Reynolds Decompositions on Vortex Detection</b>	<b>53</b>
4.1	The Trouble with Swirling Strength . . . . .	53
4.2	Vortex Core Identification . . . . .	54
4.3	The Effect of Decomposition Choice . . . . .	59
<b>5</b>	<b>The Impulsive Dynamic-Roughness Perturbation</b>	<b>62</b>
5.1	The Dynamic-Impulse Experiment . . . . .	62
5.2	General Features of the Dynamic Perturbation . . . . .	62
5.2.1	Mean Flow Properties . . . . .	63
5.2.2	Turbulence Statistics . . . . .	65
5.2.3	Internal Layers . . . . .	69
5.2.4	Integral Length Scales . . . . .	70
5.2.5	Composite Spectra . . . . .	71
5.2.6	Decomposition of the Turbulence Intensity by Spectral Contribution . . . . .	73
5.3	The Dynamic Perturbation as an Organized Wave . . . . .	78
5.3.1	Phase-Locked Decomposition . . . . .	79
5.3.2	Experimental Parameters of the Perturbation . . . . .	81
5.3.3	Streamwise Velocity Mode Development . . . . .	84
5.4	Discussion of the Dynamic Impulse Experiment . . . . .	86
<b>6</b>	<b>The Resolvent Method in the Perturbed Boundary Layer</b>	<b>88</b>
6.1	The Forced Orr-Sommerfeld Problem . . . . .	88
6.2	Resolvent Formulation . . . . .	88
6.3	Mode Calculation and Comparison . . . . .	90
6.4	Nonnormality in the Orr-Sommerfeld Operator . . . . .	95
6.5	Discussion of the Resolvent Analysis . . . . .	98
<b>7</b>	<b>Phase Relationships between Large and Small Scales in the Turbulent Boundary Layer</b>	<b>100</b>
7.1	The Scale Interaction Problem . . . . .	100
7.2	Measuring Scale Interactions . . . . .	100

7.3	Modulation Measurements . . . . .	101
7.4	Cross-Correlation Isocontours . . . . .	103
7.4.1	Subfundamental Spatial Cross-Correlation . . . . .	106
7.4.2	Taylor's Hypothesis . . . . .	108
7.4.3	The Effect of Filter Cutoff Size . . . . .	109
7.5	Cospectral Density . . . . .	110
7.6	Demodulation Using a Product Detector . . . . .	116
7.7	Summary . . . . .	121
7.8	Appendix: Synthetic Signals . . . . .	122
7.8.1	Subfundamental Sampling . . . . .	122
7.8.2	Robust Fit of Cospectral Density Ridgeline . . . . .	122
<b>8</b>	<b>Phase Relationships Between Scales in the Perturbed Turbulent Boundary Layer</b>	<b>125</b>
8.1	Interactions with a Synthetic Large Scale . . . . .	125
8.2	Phase-Locked Velocity Maps of the Decomposed Flow . . . . .	125
8.3	The Correlation Coefficient in the Perturbed Flow . . . . .	129
8.4	Cross-Correlation Isocontours . . . . .	129
8.4.1	Cross-Correlation Superposition . . . . .	130
8.4.2	Taylor's Hypothesis . . . . .	137
8.5	Cospectral Density . . . . .	138
8.6	The Physical Manifestation of the Phase Relationship . . . . .	144
8.7	Skewness Decomposition . . . . .	146
8.8	Demodulation . . . . .	150
8.9	Summary . . . . .	150
<b>9</b>	<b>Conclusions</b>	<b>153</b>
9.1	Summary of Results . . . . .	153
9.2	Implications for Flow Control . . . . .	154
9.3	Future Work . . . . .	154
	<b>Bibliography</b>	<b>156</b>

# List of Figures

2.1	(Left) The test section, as shown from the outside, with the direction of flow from left to right. (Right) The plate seated on its supports within the test section, with the direction of flow from bottom of the image to top. The roughness elements and diagnostics traverse are both visible, along with both the acrylic walls and adjustable ceiling of the test section. . . . .	19
2.2	The traverse mechanism attached below the plate, with flow direction from left to right. Also visible is the upper portion of the traverse, on the top side of the plate, with the attached Pitot and hotwire probe holders. In addition, the pressure taps along the plate, and a second port for positioning the traverse, are also visible. . . . .	21
2.3	A line-drawing of the camera stand used to position the high-speed cameras to image the wall-normal-streamwise plane. The stand was itself floated on an optical table to isolate the cameras and laser sheet from any vibrations generated by the operation of the tunnel. . . . .	22
2.4	(Left) The mean velocity profile for the unperturbed smooth wall, measured by hotwire and PIV and plotted in wall units against the profile recorded by DeGraaff and Eaton [2000] at similar $Re_\theta$ . (Right) The streamwise turbulence intensity profile for the unperturbed flow, measured by hotwire and PIV and plotted in wall units. $\times$ hotwire, $Re_\theta = 2940$ ; $+$ PIV, $Re_\theta = 2560$ , with its estimated noise floor shown as the black bar; $-$ DeGraaff and Eaton [2000], $Re_\theta = 2900$ , with their free-stream turbulence intensity marked by $\diamond$ . . . . .	25
2.5	(Left) A schematic of the arrangement roughness elements attached to their base and the corresponding slots in the acrylic insert to the flat plate, through which the roughness elements can pass. (Right) The roughness elements viewed from above the plate, showing the traverse for the hotwire probe holder as well as the armature supporting the roughness patch, visible through the acrylic plate. . . . .	27
2.6	A schematic of the arrangement of the flat plate, the roughness strip, and the diagnostic locations; not to scale. The internal layers are also marked in order to provide an idea of their relative sizes and development rates. . . . .	27

- 2.7 (Left) A line-drawing of the motor assembly, where the crankshaft and piston are shown on the left-hand side, separated by the gear assembly from the motor on the right-hand side. (Right) The motor assembly, *in situ*, in roughly the same orientation, but with the roughness armature attached to the end of the piston . . . . . 28
- 2.8 An average period,  $T$ , of the encoder signal, measured by ensemble averaging the mean displacements from each phase of a phase-locked decomposition. — encoder phase-locked signal; - - undistorted sinusoid . . . . . 29
- 3.1 The development of the unperturbed and perturbed boundary layers, from the hotwire and from the PIV. The Reynolds number based on downstream distance has been corrected to reflect the approximate location of the virtual origin. For the hotwire:  $\diamond$  unperturbed;  $\square$  perturbed; and for the PIV:  $\blacklozenge$  unperturbed;  $\blacksquare$  perturbed; —  $\delta(x)/x = (Re_x)^{-1/5}$  . . . . . 31
- 3.2 The development of the unperturbed and perturbed friction coefficients, from the hotwire. The coefficient derived from the first velocity value measured nearest the wall provides a rather smooth curve, in the unperturbed flow, consistent with the value inferred by Clauser's method, and in the perturbed case, the overshoot in the recovery of  $C_f$  is observed.  $\circ$  unperturbed  $2\nu/U\partial U/\partial y(0)$ ;  $\square$  unperturbed Clauser method;  $\diamond$  perturbed  $2\nu/U\partial U/\partial y(0)$ . The overshoot and recovery trends are consistent with those observed in previous studies. . . . . 32
- 3.3 The mean velocity profile, in outer units, for the perturbed flow, in symbols. Perturbed:  $x/\delta = 0.3 \circ$  ;  $0.6 *$  ;  $1.1 \cdot$  ;  $2.3 \times$  ;  $3.3 \square$  ;  $5.0 \diamond$  ;  $8.4 \triangle$  ;  $12.1 \nabla$  ;  $16.5 \triangleright$  ;  $23.7 \triangleleft$  ; — for profiles of the unperturbed flow at corresponding streamwise positions . . . . . 33
- 3.4 The discrepancy in the mean velocity profiles between the perturbed and unperturbed cases is shown in gray contours; the peaks for each streamwise location at which the velocity discrepancy is greatest are marked ( $\times$ ) and a curve is fitted by least squares ( $-$ ,  $y/\delta = 0.1(x/\delta)^{0.5}$ ). The approximate intercept for the fit is just below the height of the roughness elements:  $0.05y/\delta = 0.83k$ . Also, internal layer best fits, calculated below, are included ( $-$ ,  $\delta_1/\delta = 0.4(x/\delta)^{0.2}$ ;  $\dots$ ,  $\delta_2/\delta = 0.1(x/\delta)^{0.2}$ ) for reference . . . . . 34

- 3.5 The development of the internal layers, calculated by both methods described above. (Left) Plot and fit in outer units. For  $\delta_1$ :  $\square$  via  $y^{1/2}$ -scaling;  $*$  via  $\partial U/\partial x$ ; for  $\delta_2$ :  $\circ$  via  $y^{1/2}$ -scaling;  $\times$  via  $\partial U/\partial x$ ; least squares best fits:  $\cdots \delta_1/\delta = 0.4(x/\delta)^{0.2}$ ;  $-- \delta_2/\delta = 0.1(x/\delta)^{0.2}$ ; (Right) Scaled by the appropriate estimated roughness scales,  $z_{0i}$ . In this case, two distinct slopes are identified for the second internal layer, the first significantly shallower, persists for  $x < 5\delta$  at which point the layer begins to grow more quickly (although the first slope is only a pair of points) and is fit by  $\delta_2/z_{03} = 7.2(x/z_{03})^{0.1}$ ; the latter  $\delta_2/z_{03} = 0.2(x/z_{03})^{0.5}$ ; the first internal layer is fit by  $\delta_1/z_{02} = 570(x/z_{02})^{0.3}$ . 36
- 3.6 The discrepancy in the streamwise turbulence intensity profiles between the perturbed and unperturbed cases is shown in gray contours; the peaks for each streamwise location at which the discrepancy is greatest are marked ( $\times$ ) and a curve is fitted by least squares ( $—$ ,  $y/\delta = 0.2(x/\delta)^{0.4}$ ). Unlike the mean profile map (figure 3.4), the approximate intercept for the fit is above the height of the roughness elements:  $0.10\delta = 1.67k$ . And again, the internal layer boundary best fits, calculated above, are included for comparison. 38
- 3.7 The discrepancy in the streamwise third-order moment profiles between the perturbed and unperturbed cases, in red(+) and blue(-) contours. The least squares fit of the internal layer boundaries are shown:  $\cdots$ ,  $\delta_2/\delta = 0.1(x/\delta)^{0.2}$ ;  $—, \cdots$ ,  $\delta_1/\delta = 0.4(x/\delta)^{0.2}$ . Also shown are the locations of maximum discrepancies in streamwise turbulence intensity ( $\times$ ) from figure 3.6. . . . . . 39
- 3.8 The discrepancy in the streamwise Reynolds stress profiles,  $-\overline{uv}(y)/U_\infty^2$ , between the perturbed and unperturbed cases, from the two PIV measurement locations. The least squares fit of the internal layer boundaries are shown:  $\cdots$ ,  $\delta_2/\delta = 0.1(x/\delta)^{0.2}$ ;  $—, \cdots$ ,  $\delta_1/\delta = 0.4(x/\delta)^{0.2}$ . Note that the deficit in Reynolds stress corresponds closely to the region between the two layer edges. . . . . . 39
- 3.9 Top: The turbulence intensity for the perturbed flow under (Left) standard outer scaling; and (Right) under a velocity scaling based on the mean velocity gradient. Symbols follow figure 3.3. Note the collapse in the near-wall region,  $y/\delta < 0.2$ . Bottom: The results from Andreopoulos and Wood [1982] — the collapse is not as clean because of significant scatter in the  $\sqrt{u^2(y)}$  data and an insufficient number of streamwise locations. . . . . . 41
- 3.10 The discrepancy in the mean velocity gradient scale  $u_s$  between the unperturbed and perturbed flows (equation 3.6) overlaid with the the best fits of the two internal layer boundaries — symbols from figure 3.7. In this case, note that the surplus in shear stress corresponds precisely to the region between the boundaries of the two internal layers. . . . . . 42

- 3.11 The ratio of the maps of integral scales for the perturbed flow to the smooth flow,  $\Lambda_L/\Lambda_{L_0}$  overlaid with the best fits for the two internal layer boundaries as in figure 3.7 and also  $\times$  for extrema (among wall-normal positions) at each streamwise location. 43
- 3.12 The premultiplied spectra of the smooth wall, in terms of streamwise wavenumber and wall-normal location. The current data, at the streamwise location corresponding to  $Re_\theta = 2840$ , —, at the wall-normal locations marked. For comparison, the results of Erm and Joubert [1991] at  $Re_\theta = 2810$ :  $\circ$   $y/\delta = 0.04$ ;  $\diamond$   $y/\delta = 0.10$ ;  $\square$   $y/\delta = 0.35$ . As noted above, the turbulence intensity near the wall tends to be underestimated, and that carries over in this context, where the energy in the small scales also tends to be suppressed slightly. . . . . 44
- 3.13 Composite spectra for the unperturbed case: (Left)  $Re_\theta = 2770$  The white ‘+’ marks the vicinity of the inner peak ( $\lambda_x^+ \approx 1000, y^+ \approx 25$ ), the black  $\circ$  marks the expected location of the VLSM peak at ( $\lambda_x/\delta \approx 6$ ), and  $\cdots$  marks the LSM peak along  $\lambda_x/\delta \approx 3$ ; (Right)  $Re_\theta = 4040$  with markings as in the left plot. Ten contour levels, equally spaced across the color bar, are indicated. . . . . 45
- 3.14 (Left) Composite spectra for the perturbed case: the first streamwise location,  $x = 0.1 \delta = 1.65$  k, is suspected to be within the mean recirculation bubble downstream of the last roughness element; therefore the third streamwise location  $x = 0.6 \delta = 10$  k, which appears to be downstream of the recirculation region, is shown first. (Right) The discrepancy maps for the composite spectra, with a range identical to the spectra themselves, but mirrored for negative values (red are positive, blue negative). The contour line represents a region of spectral content suppressed more than 5% below the unperturbed flow. . . . . 46
- 3.15 (Left) Composite spectra continued from figure 3.14 at additional downstream positions. (Right) Continuation of the discrepancy maps for the composite spectra . . . . 47
- 3.16 The velocity field quivers from the PIV under a Galilean decomposition, where  $0.8 U$  has been subtracted off; the levels correspond to the swirl, calculated by the same decomposition; prograde in blue (solid lines), retrograde in red (dotted lines). . . . . 49
- 3.17 (Left) The profile of swirling strength, averaged in the streamwise direction across the PIV recording window in outer-scaling; (Right) the mean number of distinct vortex cores, per PIV frame, as a function of wall location. — prograde;  $\cdots$  retrograde . . . . 50

4.1 (Top) The velocity vectors, with a constant convective velocity of  $0.8U_\infty$  subtracted are shown, superposed over a map of the signed swirling strength, calculated by means of traditional numerical differentiation, without smoothing. (Bottom) Swirling strength calculated by means of the Savitsky-Golay convolution. Solid contour levels surround prograde patches of swirl; dotted levels surround retrograde patches. . . . . 56

4.2 The velocity vectors, with the local convective velocity subtracted are shown, superposed over a map of the signed swirling strength, calculated by means of the Savitsky-Golay convolution. . . . . 57

4.3 (Left) The swirl profiles, in outer units, for the Galilean decomposition: prograde (circles) and retrograde (diamonds), and from the Reynolds decomposition: prograde (x) and retrograde (asterisk). The mean velocity gradient  $\delta/U_\infty dU/dy$  is shown in the solid black line. (Right) The swirl profiles in inner units . . . . . 58

4.4 The same swirling field as show in (figure 4.2) but this time instead of contour levels of the swirling strength, circles proportional to the area of each vortex core and centered on the vortex core's centroid are shown. . . . . 58

4.5 The mean number of distinct vortex cores, per PIV frame (streamwise extent of  $\approx 2\delta$ ), as a function of wall location. For the Galilean decomposition: prograde (circles) and retrograde (diamonds), and from the Reynolds decomposition: prograde (x) and retrograde (asterisk) . . . . . 59

4.6 The two-point cross correlation between retrograde cores, in the center of each plot, and neighboring prograde cores. On (Left) is the calculation under Galilean decomposition; on (Right) the Reynolds decomposition . . . . . 60

5.1 (Left) The discrepancy in the mean velocity profiles between the dynamically perturbed and unperturbed cases is shown in gray contours; the peaks for each streamwise location at which the velocity discrepancy is greatest are marked (x) and a curve is fitted by least squares ( $—$ ,  $y/\delta = 0.09(x/\delta)^{0.33}$ ). The approximate intercept for the fit is just below the RMS height of the roughness elements:  $y \approx 0.06 \delta = 0.88 k_{rms}$ . Also, internal layer best fits, calculated below, are included ( $- -$ ,  $\delta_1/\delta = 0.39(x/\delta)^{0.19}$ ;  $\dots$ ,  $\delta_2/\delta = 0.14(x/\delta)^{0.05}$ ) for reference. (Right) For comparison, the statically perturbed case is shown, with the least squares fit for the peak discrepancy given by  $y/\delta = 0.08(x/\delta)^{0.48}$  with approximate intercept at  $y \approx 0.05 \delta = 0.86 k$ . . . . . 65

5.2 (Left) The discrepancy in the streamwise turbulence intensity profiles between the perturbed and unperturbed cases is shown in gray contours; the peaks for each streamwise location at which the discrepancy is greatest are marked ( $\times$ ) and a curve is fitted by least squares ( $—$ ,  $y/\delta = 0.12(x/\delta)^{0.54}$ ). The approximate intercept for the fit is the same as for the mean velocity discrepancy:  $y \approx 0.06\delta = 0.88k_{rms}$ . And again, the internal layer boundary best fits, calculated above, are included for reference. (Right) For comparison, the statically perturbed case is shown, with the least squares fit for the peak discrepancy given by  $y/\delta = 0.17(x/\delta)^{0.41}$  with approximate intercept  $0.10\delta = 1.67k$ . 66

5.3 The turbulence intensity for the perturbed flow under (Left) standard outer scaling; and (Right) under a velocity scaling based on the local shear stress,  $u_s$ . Streamwise profiles:  $x/\delta = 0.3 \circ$  ;  $0.6 *$  ;  $1.1 \cdot$  ;  $2.3 \times$  ;  $3.4 \square$  ;  $5.0 \diamond$  ;  $8.4 \triangle$  ;  $12.1 \nabla$  ;  $16.6 \triangleright$  ;  $23.8 \triangleleft$  67

5.4 The ratio of  $u_s$  for the static impulse over  $u_s$  for the dynamic impulse. The rectangle represents the area in figure 5.3 where the  $\sqrt{u'^2(y)}$  profile fails to collapse. . . . . 68

5.5 The discrepancy map for the streamwise velocity triple-product for the (Left) dynamically perturbed case and (Right) the statically perturbed case. . . . . 68

5.6 The development of the internal layers, calculated by both methods described above. Plot and fit in outer units. For  $\delta_1$ :  $\diamond$  via  $y^{1/2}$ -scaling;  $\triangle$  via  $\partial U/\partial x$ ; for  $\delta_2$ :  $\circ$  via  $y^{1/2}$ -scaling;  $\square$  via  $\partial U/\partial x$ ; least-squares best fits: -  $\delta_1/\delta = 0.39(x/\delta)^{0.19}$ ; - -  $\delta_2/\delta = 0.14(x/\delta)^{0.05}$ ; also included for reference, the best fits for the static impulse: --  $\delta_1/\delta = 0.38(x/\delta)^{0.23}$ ; - -  $\delta_2/\delta = 0.12(x/\delta)^{0.24}$  . . . . . 69

5.7 (Left) The discrepancy maps for  $u_s$  and (Right) the map for the third-order moment of the streamwise velocity component. While the third-order moment map tended to highlight the precise inter-layer region for the case of a static perturbation, in the case of the dynamic perturbation, it no longer serves as a useful criterion. . . . . 70

5.8 Top row: Maps of the ratio of integral lengthscales between the dynamically perturbed flow and the unperturbed flow, calculated by (a) the spectral method and (b) integration of the autocorrelation. Bottom row: Maps of the ratio of integral lengthscales: (c) for the statically perturbed flow, calculated by the spectral method and (d) for the dynamically perturbed flow calculated by a modification of the spectral method, whereby the influence of the spectral peak due to the perturbation is accounted for in the limit. . . . . 72

5.9 Composite spectra at  $x/\delta = 0.6$ : (Left) Unperturbed  $Re_\theta = 2770$  The white '+' marks the vicinity of the inner peak ( $\lambda_x^+ \approx 1000, y^+ \approx 25$ ), the black  $\circ$  marks the expected location of the VLSM peak at ( $\lambda_x/\delta \approx 6$ ), and  $\dots$  marks the peak along  $\lambda_x/\delta \approx 3$ ; (Right) Statically perturbed, with markings as in the left plot . . . . . 72

5.10 (Left) Composite spectra for the perturbed case: the first streamwise location,  $x = 0.1\delta = 1.65 k$ , is suspected to be within the mean recirculation bubble downstream of the last roughness element; therefore the third streamwise location  $x = 0.6 \delta = 10 k$ , which appears to be downstream of the recirculation region, is shown first. Levels follow figure 5.9 and are the same as in Jacobi and McKeon [2011a] (Right) The discrepancy maps for the composite spectra, with a range identical to the spectra themselves, but mirrored for negative values (red are positive, blue negative). The contour line represents a region of spectral content suppressed more than 5% below the unperturbed flow. The dark bands, starting at the forcing frequency, represent the input forcing and its associated harmonics. . . . . 74

5.11 (Left) Composite spectra continued from figure 5.10 at additional downstream positions. (Right) Continuation of the discrepancy maps for the composite spectra . . . . 75

5.12 Recreating the turbulence intensity variation (figure 5.2) by integrating the streamwise wavelength spectra over different ranges of wavelengths: on the top, the entire wavelength range is integrated to reproduce the previous result. (Left) is the contour map for the variation of the dynamic impulse from the smooth case; (Right) is for the variation of the static impulse from the smooth.  $\circ$  are the trace of the peaks;  $--$  are the power-law fits for the peaks, expressions of which are given below each panel; all levels are the same as in figure 5.2 . . . . . 77

5.13 A map of  $\tilde{u}(y, t)$  over an average period (abscissa  $t \in [0, \pi]$ ) in outer units (ordinate  $y/\delta$ ) at all of the streamwise locations. The color levels are fixed for all plots, so the amplitude of the mode is physically represented, but the contour lines are scaled per streamwise location and thus represent the shape independent of amplitude. The mean internal layer locations, when interpolatable, are denoted:  $--$  first internal layer, and  $\cdots$  second internal layer . . . . . 80

5.14 The variation in the measurement of values of the streamwise wavenumber for the perturbation,  $k = k_r + ik_i$  when calculated as described above at different wall normal locations. (Left)  $\circ$  The variation in  $k_r$ ;  $—$  mean  $k_r = 0.378$ ;  $—$  Calculated from the peak signal strength,  $k_r = 0.336$ . (Right)  $\circ$  The variation in  $k_i$ .  $—$  mean  $k_i = 0.051$ ;  $—$  Calculated from the peak signal strength,  $k_i = 0.048$ . . . . . 83

5.15 -○- The mean unperturbed convective velocity  $U(y/\delta)$  divided by the real part of the wavespeed  $c_r(y/\delta)$  which was calculated from the gradient of the phase change at each wall-normal position. — The same ratio of speed, but with the real part of the wavespeed  $c_r$  calculated from the gradient of the change in phase at the location of the peak perturbation strength, showing a crossing at  $y_c/\delta = 0.04$ , which indicates the presence of a critical layer. The mean location of the internal layers, identified above in figure 5.6, have been marked for the streamwise component: --- the first internal layer; ... the second internal layer. . . . . 83

5.16 (Left) The amplitude variation in  $\tilde{u}(y, t)/U_\infty$ :  $x/\delta = 0.1 +$ ;  $0.3 \circ$ ;  $0.6 *$ ;  $1.1 \cdot$ ;  $2.3 \times$ ;  $3.4 \square$ ;  $5.0 \diamond$ ;  $8.4 \triangle$ ;  $12.1 \nabla$ ;  $16.6 \triangleright$ ;  $23.8 \triangleleft$  (Right)  $\tilde{v}(y, t)/U_\infty$ : light symbols refer to different PIV runs in order to indicate variability; bold — mean for all PIV . . . . . 85

5.17 (Left) The phase variation of  $\tilde{u}(y, t)$  in degrees:  $x/\delta = 0.1 +$ ;  $0.3 \circ$ ;  $0.6 *$ ;  $1.1 \cdot$ ;  $2.3 \times$ ;  $3.4 \square$ ;  $5.0 \diamond$ ;  $8.4 \triangle$ ;  $12.1 \nabla$ ; — mean for all streamwise locations; bold — mean for all PIV runs. (Right)  $\tilde{v}(y, t)$ : light symbols refer to different PIV runs; bold — mean for all PIV . . . . . 85

5.18 (Left) The variation in the wall-normal location of the peak amplitude of  $\tilde{u}(y, t)$ , with range of  $0.04 < y/\delta < 0.21$ ;  $\circ$ ; — least square best fit  $(y/\delta) = 0.08(x/\delta)^{0.45}$ ;  $\square$  from PIV; (Right) The variation in the wall-normal location of the  $180^\circ$  phase shift in  $\tilde{u}(y, t)$  (approximated by  $\Delta 120^\circ$ ),  $\circ$ ; — least square best fit  $(y/\delta) = 0.58(x/\delta)^{0.29}$ ;  $\square$  from PIV.  $\diamond$  Results from Hussain and Reynolds [1970] for channel flow (under 100 Hz perturbation) . . . . . 86

6.1 Spectrum and pseudospectrum (for  $N = 100$ ) with contour levels (calculated via the  $L_2$  norm of the resolvent) at  $\epsilon = 10^{-5}, 10^{-4}, 10^{-3}$  with decreasing thickness. The eigenvalues are marked as points and the forcing is denoted with an asterisk. The forcing appears near a region of relatively high sensitivity (high-valued norm of the resolvent). The disconnected region is a numerical artifact of the contour routine. (Left) Unperturbed velocity profile. (Right) Perturbed velocity profile . . . . . 91

6.2 (Left) The amplitude variation in  $\tilde{u}(y, t)$ : — from the resolvent analysis using the unperturbed velocity profile; --- from the resolvent analysis using the perturbed velocity profile;  $x/\delta = 0.1 +$ ;  $2.3 \times$  from the experimental hotwire measurements. (Right) The amplitude variation in  $\tilde{v}(y, t)$ : — from the resolvent analysis using the unperturbed velocity profile; — from the experimental PIV measurement with PIV window centered at  $x/\delta \approx 4$ . The location of the internal layers, identified above in figure 5.6, have been marked for the streamwise component: --- the first internal layer; ... the second internal layer. . . . . 94

6.3	(Left) The phase variation of $\tilde{u}(y, t)$ , with markings as indicated in figure 6.2 (Right) The phase variation in $\tilde{v}(y, t)$ with markings as above. The (a) marks a distinctive variation in phase which is a robust feature of all Orr-Sommerfeld type solutions. . . .	95
6.4	Top: (Left) A map of the calculated most-amplified singular mode $\tilde{u}(y, t)$ due to the experimental forcing, over an average period ( $t \in [0, 2\pi]$ ); (Right) The corresponding map for $\tilde{v}(y, t)$ . Bottom: The experimentally measured maps, at $x/\delta \approx 2.3$ assembled via phaselocking, as in figure 5.13 . . . . .	96
7.1	The correlation coefficients for $u_L$ and $u_S$ : (Left) using a Butterworth temporal filter size of $\tau = 3 \delta/U$ . The profile for the hotwire is shown in solid ( $y_c \approx 0.15$ ); that from the PIV in dashes ( $y_c \approx 0.17$ ). Additionally, the coefficient for $u_L$ and $v_S$ measured from the PIV is shown in the dotted line, and shows a zero-crossing much nearer to the wall, $y_c \approx 0.06$ . (Right) using a temporal filter size of $\tau = 0.5 \delta/U$ on the hotwire data and a spatial filter of $\rho = 0.5\delta$ on the PIV data. The profile for the hotwire is shown in solid ( $y_c \approx 0.09$ ); that from the PIV in dashes ( $y_c \approx 0.12$ ). . . . .	103
7.2	The cross-correlation isocontour map for $u_L \star u_S$ , using a temporal cross-correlation (left) from the hotwire measurements ( $y_c \approx 0.12$ ); and (right) from PIV measurements ( $y_c \approx 0.16$ ). The absolute value ridge line is marked with black dots in each. The Butterworth filter size was $\tau = 3 \delta/U$ for both data sets. . . . .	105
7.3	The cross-correlation isocontour map for $u_L \star v_S$ , using a temporal cross-correlation from the PIV measurements ( $y_c \approx 0.08$ ) with filter size $\tau = 3 \delta/U$ . . . . .	105
7.4	The cross-correlation isocontour maps in the spatial domain for (left) $u_L \star u_S$ with $\rho = 0.5 \delta$ and (right) $u_L \star v_S$ with $\rho = 0.5 \delta$ . The streamwise component shows good agreement with temporal results with $y_c \approx 0.14$ , while the wall-normal map shows significant disagreement with $y_c \approx 0.18$ . Note that the wall-normal map indicates significant breakage of the antisymmetry (i.e., a strong negative tail) indicating distortion due to subfundamental sampling. By reducing the filter size for the wall-normal cross-correlation, as explained below, this distortion can be mitigated, as shown in figure 7.5. . . . .	106
7.5	The cross-correlation isocontour maps in the spatial domain for $u_L \star v_S$ with $\rho = 0.25\delta$ . Now the zero-crossing location shows good agreement with the temporal measurements, with $y_c \approx 0.11$ , and the strong antisymmetry breaking is no longer apparent. . . . .	107

7.6 (Left) The peak trace of the spatial (dashed-line) and temporal (solid) cross-correlation functions, both using a filter size  $\tau = 0.5 \delta/U$  and  $\rho = 0.5 \delta$ , and applying Taylor’s hypothesis to the temporal signal. (Right) Converting the phase traces into the correlation coefficient form, for easier comparison. The conversion was also performed with a convective velocity 15% higher than the mean (red dotted line) and 15% lower than the mean (blue dotted line). Therefore, if the blue line is a better fit to the actual spatial measurements, it signifies that the relevant convective velocity is lower than the mean velocity in the flow. . . . . 110

7.7 The zero-crossing locations from the correlation coefficients (squares) and the  $\pi/2$  phase-change locations from the cross-correlations (circles), with a best-fit (blue) assigned to the mean value,  $y/\delta \approx 10^{-0.8}(\tau U/\delta)^{-0.2}$ . Also, the maximum positive value of the correlation coefficient, with a best-fit (red) of  $R_{max} \approx 10^{-0.5}(\tau U/\delta)^{-0.1}$ . Values are recorded for the most downstream measurement, with  $Re_\theta \approx 4100$ . . . . . 111

7.8 The normalized cospectral density,  $Co(f\delta/U_\infty)$ , at  $y/\delta \approx 0.17$ , in black. The red line is the best fit to the extended Gaussian function, defined in equation 7.14. The cospectral density is displayed in a normalized but not premultiplied form in order to identify the frequencies at which the interaction between large- and small-scales is dominant, but not necessarily energetically so, because the energetic strength does not indicate phase interaction strength, as can be observed by analysis of two amplitude-modulating sinusoids. . . . . 113

7.9 (Left) The cospectral density for the cross-correlation of  $u_L$  and  $u_S$  defined by temporal means from the hotwire measurements. The peaks from the amplitude at each wall-normal location are denoted by circles. The filter size of  $\tau = 1 \delta/U$  is marked by a dashed line, which varies as a function of convective velocity. (Right) The same spectral map, constructed from the best-fit extended Gaussian functions, in order to identify the peaks, which are traced by the solid black line. The blue dotted line corresponds to the power law for the VLSM reported by Monty et al. [2009], translated to the frequency domain via Taylor’s hypothesis using the present mean velocity profile. . . . . 113

- 7.10 The premultiplied spectral map of the streamwise turbulent fluctuations from the hotwire measurements, again at the furthest downstream measurement location, corresponding to  $Re_\theta \approx 4100$ , in order to highlight the burgeoning double peak. The peaks from the amplitude at each wall-normal location are denoted by  $\times$  symbols; the ridgeline from the cospectral density is marked in circles with a solid line for the best fit, following the notation in figure 7.9. The dashed line corresponds to the power law for the VLSM reported by Monty et al. [2009], translated to the frequency domain via Taylor’s hypothesis using the present mean velocity profile; the dotted line represents the LSM at  $f\delta/U_\infty \approx 1/3$ . . . . . 115
- 7.11 Illustrations of the relative orientation of the large-scale motions and corresponding envelopes of small-scale fluctuations, in the streamwise direction. The dark and light colors represent positive and negative fluctuations; the dashed lines represent the small-scale envelopes; the solid blocks represent large-scale motions. The top row shows a positive phase difference as measured in the phase of the cospectral density ( $arg[r_c(f\delta/U_\infty)]$ ); the bottom shows a negative phase difference. . . . . 117
- 7.12 (Left) The map of  $arg[r_c(f\delta/U_\infty)]$  with levels colored by the the phase angle, normalized by  $\pi$  to range from  $[-1, 1]$ . The absolute and fitted peaks from the magnitude map are also shown in circles and the solid line, respectively. (Right) The magnitude of the phase following the ridgeline of the peak magnitudes. Note that the crossing location of  $\pi/2$  appears approximately at the zero-crossing location of the correlation coefficient. 118
- 7.13 (Left) The ratio of the peak frequency of the information signal  $m(t)$  denoted  $f_m^*$  to the corresponding frequency of the instantaneous velocity signal spectrum,  $f$ , is shown as a contour map, over the range of the instantaneous velocity signal frequencies and wall-normal locations, normalized in outer units. The dashed black lines mark the spectral limits set by the product detector; the circle and solid line are the ridgeline and fit of the dominant interacting scales from figure 7.9. (Right) Averaging across the boundary layer thickness, the mean value of  $f_m^*$  in outer units for each frequency of the instantaneous velocity spectrum. . . . . 120
- 7.14 The cross-correlation function using two idealized sinusoids to represent the large and small scale motions, with the wavelength of the large scale ten times that of the small scale and the amplitude one hundred times that of the small scale. On the left, the cross-correlation when a full period of the largest scale is captured; on the right, the cross-correlation when only a fraction of the period is sampled. The fraction is selected by assuming a dominant large scale of  $6 \delta$  and using the actual streamwise dimension of the PIV window. . . . . 123

- 8.1 (Top)  $\tilde{u}$  measured by hotwire at  $x/\delta \approx 3.4$  on left and by PIV on right; levels in outer units range from  $[-0.1, 0.1]$ ; (Bottom) is the variation in the envelope of the small-scale motions,  $u'_{rms} - \overline{u'_{rms}}$ , in outer units, with levels  $[-0.01, 0.01]$ , with hotwire measurements on left and PIV on right. The black line represents the profile of the mean amplitude of the fluctuations averaged over a period in order to highlight the wall-normal location of the maximum amplitude with respect to the internal layers, marked with dotted and dashed lines for the hotwire measurements. . . . . 127
- 8.2 (Left) The components of the velocity signal in the wall-normal direction.  $\tilde{v}$  on top,  $v'_{rms} - \overline{v'_{rms}}$  on bottom; both presented in outer units, with levels  $[-0.01, 0.01]$ . (Right) The components of a decomposed Reynolds stress signal.  $\tilde{u}\tilde{v}$  on top,  $(u'v')_{rms} - \overline{(u'v')_{rms}}$  on bottom; again both presented in outer units, with levels  $[-0.0001, 0.0001]$ . Again, the black line represents the profile of the mean amplitude of the fluctuations averaged over a period in order to highlight the wall-normal location of the maximum amplitude. . . . . 128
- 8.3 The correlation coefficient,  $R$ , at  $x/\delta \approx 3.4$  with: red unperturbed; green  $\square$  statically perturbed; blue  $\diamond$  dynamically perturbed. (Left)  $u_L$  and  $u_S$  with filter size  $\tau = 3\delta/U$  from hotwire measurements; and (Right)  $u_L$  and  $v_S$  with filter size  $\tau = 3\delta/U$  . . . . . 129
- 8.4 The isocontour maps of the streamwise cross-correlation function, without normalization, using the hotwire measurements with filter size  $\tau = 3\delta/U$  at streamwise location  $x/\delta \approx 3.4$ . Clockwise from top left: the unperturbed, statically perturbed, and dynamically perturbed flows. Finally, in the bottom left is a cross-correlation map constructed from the mean period of the phase-locked motions, shown above in figure 8.1, where the period has been converted into a temporal measurement by employing the previously ascertained wavelength and convective velocity of the large scales. Contour lines are equispaced between the opposite signed extrema in each graph individually; color levels are identical between different figures. The horizontal line indicates the the wall-normal location of the discontinuity along the ridgeline, representing a phase shift of  $\pi$ . . . . . 131

- 8.5 The isocontour maps of the streamwise cross-correlation function,  $r_{uu}(\Delta t)$ , without normalization, using the hotwire measurements with filter size  $\tau = 3\delta/U$  at streamwise location  $x/\delta \approx 3.4$ . (Left) statically perturbed; (Right) the phaselocked cross-correlation from the dynamically perturbed study. Contour lines are scaled are equispaced between the opposite signed extrema in each graph; color levels are comparable between different figures. The dots trace along the ridgeline of local extrema of the cross-correlation functions. The horizontal line indicates the the wall-normal location of the discontinuity along the ridgeline, representing a phase shift of  $\pi$ . The internal layers are also marked in the phase-locked map, to show that the phase lead as reached  $\pi$  at the location of the second internal layer, past which the phase lead exceeds half a period. . . . . 132
- 8.6 Superposition of the isocontour maps of the streamwise cross-correlation function,  $r_{uu}(\Delta t)$ , following equation 8.5. On the top: (Left)  $r(\Delta t)_{PL} + r(\Delta t)_{st}$ , which can be compared with (Right)  $r(\Delta t)_{dyn}$ ; on bottom: the difference between the linear superposition and the actual cross-correlation in the dynamically perturbed case,  $r(\Delta t)_{cross}$  133
- 8.7 The isocontour maps of the streamwise-to-wall-normal cross-correlation function,  $r_{uv}(\Delta t)$ , without normalization, using the hotwire measurements with filter size  $\tau = 3\delta/U$  at streamwise location  $x/\delta \approx 3.4$ . (Left) statically perturbed; (Right) the phaselocked cross-correlation from the dynamically perturbed study. Contour lines are scaled are equispaced between the opposite signed extrema in each graph; color levels are identical between different figures. The dots trace along the ridgeline of local extrema of the cross-correlation functions. The horizontal line indicates the the wall-normal location of the discontinuity along the ridge-line, representing a phase shift of  $\pi$ . . . . . 134
- 8.8 Superposition of the isocontour maps of the streamwise-to-wall-normal cross-correlation function,  $r_{uv}(\Delta t)$ , following equation 8.5. On the top: (Left)  $r(\Delta t)_{PL} + r(\Delta t)_{st}$ , which can be compared with (Right)  $r(\Delta t)_{dyn}$ ; on bottom: the difference between the linear superposition and the actual cross-correlation in the dynamically perturbed case,  $r(\Delta t)_{cross}$  . . . . . 135
- 8.9 The correlation coefficients of  $u_L \star u_S$ , reconstructed from the cross-correlation ridge-lines, where the temporal phases were converted to spatial phases using Taylor's hypothesis (black solid line). The conversion was also performed with a convective velocity 15% higher than the mean (red dotted line) and 15% lower than the mean (blue dotted line). The actual spatial measurements are shown in the black dashed line. Therefore, if the blue line is a better fit to the actual spatial measurements, it signifies that the relevant convective velocity is lower than the mean velocity in the flow. The measurements both employed a filter size  $\tau = 0.5\delta/U$  and  $\rho = 0.5\delta$ . Clockwise from top left: unperturbed, static, dynamic . . . . . 139

- 8.10 The cospectral density for the cross-correlation of  $u_L$  and  $u_S$  defined by temporal means from the hotwire measurements. The peaks from the amplitude at each wall-normal location are denoted by circles. The filter size of  $\tau = 1\delta/U$  is marked by a dashed line, which varies as a function of convective velocity. Clockwise from top left: the unperturbed flow, statically perturbed, and dynamically perturbed . . . . . 140
- 8.11 (Left) The map of cospectral phase,  $\text{arg}[r_c(f\delta/U_\infty)]$ , for the cross-correlation of  $u_L$  and  $u_S$  defined by temporal means from the hotwire measurements. The peaks from the cospectral density amplitude at each wall-normal location are denoted by circles. The filter size of  $\tau = 1\delta/U$  is marked by a dashed line, which varies as a function of convective velocity. (Right) The magnitude of the phase,  $\text{arg}[r_c(f\delta/U_\infty)]$ , following the ridgeline of the peak magnitudes, in circles. The mean phase, averaged across all large scale frequencies, and weighted by the power in each frequency, is shown in the solid black line. The red and blue lines are the weighted contributions to the mean phase from positive and negative phase components, respectively. Both maps are displayed for the unperturbed flow for reference. . . . . 142
- 8.12 The phase maps and profiles for the perturbed flows, following the labeling in figure 8.11. Top row is the statically perturbed flow; bottom is dynamically perturbed. . . . 143
- 8.13 The magnitude of the phase,  $\text{arg}[r_c(f\delta/U_\infty)]$ , for the dynamic case, as plotted in figure 8.11, however the weighted averaging was performed on a spectrum with a region between normalized frequencies 0.02–0.03 cutout (demarcated by magenta lines), thereby ignoring the dominant contribution from the artificial scale and showing the phase observed when averaged over the remaining non-forced frequencies. The dashed lines are from the statically perturbed flow (with the same cutout). . . . . 145
- 8.14 Illustrations of the relative orientation of the large-scale motions and corresponding envelopes of small-scale fluctuations, in the streamwise direction. (Top, left) Unperturbed, compare Chung and McKeon [2010]. (Top, right) Static perturbation, where the large-scale inclination (in red) is reversed in the region between the two internal layers, which was speculated to be an effect of the roughness perturbation. (Bottom) Dynamic perturbation in isolation (i.e., phase-locked), where the small-scale envelope is that of the large scales from the static perturbation, and the artificial large scale is in red. Note that the cross-over point tends to shift up in the case of the static perturbation and shifts down in a dynamic case where the artificial, highly inclined large structure dominate. Note also that the artificial scale is more inclined than the natural large scale but less than the natural small scales. . . . . 147

8.15	The decomposed skewness, $S_u$ , at $x/\delta \approx 3.4$ with: black $\triangle S_u$ ; red $\square \overline{u_L^3}$ ; purple $\nabla \overline{u_L^2 u_R}$ ; green $\circ \overline{u_L u_R^2}$ ; blue $\times \overline{u_R^3}$ . The first and second internal layers in the perturbed flows are marked with dashed and dotted lines, respectively. The filter size is $\tau = 2.5\delta/U$ , to match that of Mathis et al. [2011]. . . . .	148
8.16	The skewness, $S_u$ , at $x/\delta \approx 3.4$ with: red unperturbed; green $\square$ statically perturbed; blue $\diamond$ dynamically perturbed. The filter size is $\tau = 2.5\delta/U$ , to match that of Mathis et al. [2011]. . . . .	149
8.17	The decomposed skewness, $S_u$ , at $x/\delta \approx 3.4$ with symbols following figure 8.15, for the statically perturbed flow (left) and dynamically perturbed flow (right) . . . . .	150
8.18	The ratio of the peak frequency of the information signal $m(t)$ denoted $f_m^*$ to the corresponding frequency of the instantaneous velocity signal spectrum, $f$ , is shown as a contour map, over the range of the instantaneous velocity signal frequencies and wall-normal locations, normalized in outer units. The dashed black lines mark the spectral limits set by the product detector; the circles are the ridgeline of the dominant interacting scales from figure 8.10. (Left) static (Right) dynamic . . . . .	151

# List of Tables

2.1	Mean flow properties at streamwise extrema of sampling area for hotwire (PIV) . . . .	23
3.1	Mean flow properties at streamwise extrema of sampling area for hotwire (PIV) . . . .	31
3.2	Integrated swirl profiles . . . . .	51
5.1	Mean flow properties at streamwise extrema of sampling area for hotwire (and PIV) .	64
5.2	Parameters for the perturbation . . . . .	84
5.3	Magnitude of perturbation . . . . .	84
7.1	Robust least-squares coefficients for power-law models of dominant modulation in inner and outer scaling . . . . .	124
8.1	Phase-jump locations . . . . .	136



# Chapter 1

## Background

### 1.1 Perturbing the Turbulent Boundary Layer

Fluid flow over a solid surface is a physics problem with a surprisingly long and distinguished pedigree. The first mathematical treatment in the early theory of hydrodynamics led to the counterfactual result that constant relative motion of a solid body with respect to an idealized fluid produced no drag force at all. This mid-eighteenth century paradox persisted as efforts were made to incorporate the viscous properties of real fluids into a satisfactory model for fluid motion. By the first quarter of the nineteenth century, the Navier-Stokes equations were formulated to describe the motion of real fluids, but the key physical insight into the problem of wall-bounded flows did not surface until the twentieth century, with Ludwig Prandtl's proposal of the boundary layer. The boundary layer theory offered the tantalizing simplification that the viscous effects of real fluids in wall-bounded flows were largely confined to a small region of the flow near the solid surface; however, the physical understanding of this small region has remained frustratingly obscure.

As the structure of the boundary layer has been explored in progressively greater detail, a number of fundamental problems have consistently appeared and reappeared, chief among them: the relationship between the statistical picture of wall-bounded turbulence obtained from long-time averaging and the structure or form of the physical dynamics responsible for producing the statistics; the means by which turbulent boundary layers form and sustain themselves; and most practically, the extent to which simple models can provide predictions of the complex behavior observed in the boundary layer. In recent years, these individual questions have started to overlap, with the realization that certain types of coherent fluid motions within the boundary layer — the largest-scale structures — may be responsible for a significant share of the physics. And of course these large-scale motions are more amenable to modeling and simple representations than the enormous range of small-scale motions, while at the same time providing a framework in which to better understand the statistical observations.

The current study seeks to build on the growing consensus on the importance of large-scale

motions in the turbulent boundary layer by introducing an artificially generated large scale in a novel way. The method of generating the artificial large-scale motion is designed to exploit features of surface roughness, boundary layer nonequilibrium, and periodic external forcing, all of which contribute toward a unique perspective on the function of large- and small-scale motions within the boundary layer.

## 1.2 Structure of the Turbulent Boundary Layer

The structure of turbulent boundary layers has been studied for more than a century, and for most of that time, experimenters have recognized that boundary layers can be described in terms of a collection of motions with a broad range of scales of temporal and spatial coherence. Classical treatments of the turbulent boundary layer, like Schlichting [1968] and Townsend [1976], have identified two general regions within the boundary layer which tend to roughly divide these motions into two classes. Near the wall, the dominant constitutive features of the boundary layer tend to be dominated by the effect of the wall and quantitative representations of these features can therefore be scaled by a friction velocity  $u_\tau = \sqrt{\tau/\rho}$  (where  $\tau$  is the shear stress and  $\rho$  is the fluid density) and kinematic viscosity  $\nu = \mu/\rho$  (where  $\mu$  is the dynamic viscosity); far from the wall, in the ‘outer region’ of the flow, viscous shear becomes less significant and the motions in the boundary layer are best described by the lengthscale of the boundary layer itself,  $\delta$  (representing  $\delta_{99}$ , or the wall-normal location at which the mean local velocity is equal to 99% of the free stream). Within the broad division of ‘near wall’ behavior, Tennekes and Lumley [1972] outlines how the boundary layer can be divided into several narrower zones of wall-normal extent, each with different representative physical processes. Nearest to the wall, in a region known as the viscous sublayer, located at wall normal locations below  $y^+ \approx 5$  (where  $(\cdot)^+$  represents inner scaling, in the form of  $(\cdot)u_\tau/\nu$ ), Jiménez and Pinelli [1999] described an autonomous cycle of turbulence production, which serves as an input into the self-sustaining turbulence of the boundary layer as a whole. Schoppa and Hussain [2002] then demonstrated how self-sustaining turbulence generation can produce large scale coherent motions by means of a transient growth analysis. Beyond the viscous sublayer lies a ‘buffer layer’ of high turbulent energy production, where neither the viscous stress nor the Reynolds stress (defined as the first mixed moment of streamwise and wall-normal fluctuations) is negligible. Beyond the buffer layer lies the logarithmic layer, which marks the transition region over which both the inner (viscous) and outer (inertial) scalings are applicable. The use of inner and outer scalings has allowed careful analysis of the statistical quantities associated with turbulent flows, from single and mixed moments of velocity fluctuations, to more fundamental spatial and temporal structure functions (e.g., the extensive work of Fernholz and Finley [1996]). However, the statistical quantities alone are insufficient for a proper apprehension of the boundary layer physics (Robinson [1991]); the coherent motions

within the boundary layer are of fundamental importance, and significant efforts have been directed at both defining and identifying coherent motions, and ultimately relating them to the statistical characterization of turbulence.

Coherent motions present a particularly perplexing challenge to the understanding of the turbulent boundary layer, since they are not easily defined. Marusic et al. [2010b] offer a working definition as: “organized motions that are persistent in time and space and contribute significantly to the transport of heat, mass, and momentum,” but also note that a variety of more-specific definitions, like that of a vortex, are required in order to build a consensus on the mechanisms by which turbulent structures are generated and sustained. Hussain [1986] argued that a foundational part of any definition of coherent structures must be coherent vorticity, although the use of vorticity as an indicator is itself challenging due to the smoothing and thresholding needed for its identification. Despite the challenges in defining precisely what constitutes coherent motion, visual observations of coherent motions are abundant. Falco [1977] conducted pioneering work on characterizing the sizes of coherent structures in the boundary layer, visualizing both small-scale coherent motions (‘typical eddies’) of size approximately  $200\nu/u_\tau$  and large-scale motions on the order of the boundary layer thickness itself. Moreover, Falco [1977] showed that the convection speed of these eddies differed from the local mean velocity, and hypothesized that the difference could be explained by the relationship between the typical eddies and the corresponding large-scale motions in which they reside.

As studies of the large-scale motions progressed, it became clear that they were not limited to merely those scales observed at the intermittent edge of the boundary layer (as observed in Kovasznay et al. [1970]), but rather that large-scale motions really encompassed a family of coherent motions with a broad range of sizes which all scale on outer units. Marusic et al. [2010b] noted two general categories of large-scale motions: large-scale motions (LSMs), in other words, motions with spatial extent on the order of the boundary layer thickness; and very large scale motions (VLSMs) or superstructures, with streamwise coherence on the order of  $10\delta$ . LSMs are observed in both internal and external flows and appear to be the dominant large-scale motion in boundary layers, across all wall-normal locations, as reported in Monty et al. [2009]. VLSMs have been observed in internal wall-bounded flows by Kim and Adrian [1999] as well as in the turbulent boundary layer, by Balakumar and Adrian [2007], but appear to be limited primarily to the inner flow in boundary layers. Monty et al. [2007] observed long meandering patches of coherent local mean velocity in pipe and channel flow, with streamwise extents as long as 25 pipe radii or channel half-heights. The observations of these very large scale coherent motions are important not only because they indicate the possibility of scale interactions across very large spatial distances, but because these large-scale motions, in fact, dominate the overall dynamics in the boundary layer. Guala et al. [2006] demonstrated that the very large-scale motions are both highly energetic (containing more than half of the streamwise

turbulent kinetic energy) and active, in the sense of Townsend [1976], containing more than half of the Reynolds stress. Therefore, understanding just the large-scale motions should provide significant insights into the structure of the boundary layer. However, even within the hierarchy of large-scale motions, there is an additional complication, in that the large-scale motions which are significant in internal flows (like channels and pipes) tend to extend over much longer distances than those observed in external flows (like the boundary layer). Monty et al. [2009] investigated the differences between the energetic signatures of the different large-scale motions, but the relationship between observations in internal and external flows, remains obscure, involving features beyond just the presence of VLSMs.

In order to investigate the dynamics of coherent motions in the turbulent boundary layer, it makes sense to target the most energetic and active motions — the VLSMs — and then explore how they, in turn, interact with smaller-scale motions, which are ultimately associated with the autonomous near-wall cycle responsible for the generation of skin friction. The level of complexity in the boundary layer, in addition to the challenge of defining precisely the different domains which together constitute that complexity, make understanding the boundary layer physics from the ground up a daunting task. However, Clauser [1956] suggested a novel perspective from which to approach turbulence: treat turbulence as a black box. In the same way that the frequency response of a linear mechanical device can be obtained by ‘perturbing’ the device with a hammer and measuring its vibrations, so too the nonlinear boundary layer can be ‘inspected’ by perturbing it and observing its response. By perturbing a boundary layer out of its equilibrium state and observing its response to that perturbation, new insights about the structure and dynamics of the turbulent motions within the boundary layer can be obtained.

### 1.3 Nonequilibrium Boundary Layers

Boundary layer equilibrium was defined by Townsend [1961] to refer to a local condition in regions of high energy production and dissipation, wherein the turbulent motion is dependent only on the local shear stress distribution,  $dU/dy$ , independent of conditions outside those regions. Townsend [1961] then employed this condition of ‘local equilibrium’ to derive the logarithmic velocity scaling of the mean turbulent velocity profile, as well as other features of the boundary layer related directly to the shear stress. However, nonequilibrium boundary layers are of significant interest to a variety of practical flows, as reviewed by Smits and Wood [1985] and more broadly by Morrison [2010]. When the local energy equilibrium balance is interrupted by some sort of perturbation, the nonequilibrium condition tends to spread throughout the boundary layer, after which the boundary layer begins to relax back toward equilibrium. Most experimentation with the nonequilibrium boundary layer has considered static impulse-response or step type perturbations of the surface condition, in the form

of abrupt changes to curvature (e.g., Smits et al. [1979]) or roughness (e.g., Antonia and Luxton [1971a]) or heat flux (e.g., Andreopoulos [1983]). Smits and Wood [1985] identified three degrees of perturbation: weak perturbations, which essentially can be described using local length- and timescales; strong perturbations, where the additional strength requires modeling to include nonlocal length- and timescales or other physical effects; and disruptive perturbations, that substantially change the flow regime to a nonboundary layer form. The former two types are relevant for most of the experimental studies in this area and a variety of practical flow situations; the latter is exemplified by the flow reversal over a backward facing step, and constitutes an entirely independent family of experiments. But even in the less extreme perturbations, where self-preservation is maintained to one degree or another, still the form of the perturbed selfpreserving flow can be significantly different. In an experimental study of the flow over flat plate boundary layers with concave and convex bends, Smits et al. [1979] identified the ‘stress bore’ as a key feature distinguishing the class of modestly perturbed boundary layers from their unperturbed counterparts. The ‘stress bore’ is a region of the boundary layer where newly produced turbulence causes a rise in the statistical moments of the velocity signals above their selfpreserving (unperturbed) values.

One of the few mathematical tools that have been applied to the perturbed, nonequilibrium turbulent boundary layer is rapid distortion theory. Savill [1987] summarized the key results of the theory, which is predicated on the idea that the timescale associated with the distortion process is far smaller than the Lagrangian timescale of the turbulence (the ratio of the integral lengthscale to the root-mean-square (rms) value of the streamwise velocity component). The consequence of such rapid distortions is that linear distortions are expected to produce effects which can be modeled with linear theories, because in a general way, the initial linear perturbation establishes a linear ‘blueprint’ for the evolution of the flow. Rapid distortion theory is built on the use of a transfer function to describe the distortion of a linearized description of the turbulence. Another approach to studying perturbed or forced flows, besides that taken by rapid distortion theory, is the resolvent method, explained below. The resolvent method is designed to explore the inherent receptivity of the turbulent boundary layer to certain types of linear perturbations, and thereby understand the response of the boundary layer to different types of forcing. In fact, the resolvent method can be thought of as a conceptual bridge between the eigenfunction based, traditional hydrodynamic stability theory of Lin [1955] and distortion-matrix- (prespecified operator-) based, rapid-distortion theory; where the resolvent formulation is specially suited to treating the dominant motions in a given flow regime.

Different types of perturbations can be applied to the turbulent boundary layer in order to elicit a nonequilibrium response; however, some perturbations can manifest themselves in both equilibrium and nonequilibrium configurations. In particular, surface roughness can be applied uniformly over a surface, producing an equilibrium fully developed, rough-wall flow field, or roughness can be

employed impulsively, in a step-like configuration, in order produce a nonequilibrium condition. The advantage of employing a roughness type perturbation, then, is that it offers the potential for exploring nonequilibrium while comparing those observations against a control state of equilibrium roughness.

## 1.4 Roughness and Roughness Perturbations

The flow over rough-walled turbulent boundary layers has been studied extensively for the better part of the last century, owing to the significant practical interest in surfaces with some measurable level of roughness. Jiménez [2004] reviewed much of the recent progress in understanding how the rough-wall condition permanently disturbs the classical near-wall cycle that is associated with the smooth-wall boundary layer. The impact of roughness, at its simplest level, is dependent on the roughness height,  $k$ . When the roughness height is less than approximately 5 wall units, the surface has traditionally been considered hydrodynamically smooth. As the roughness height increases, the roughness tends to interfere with the viscous cycle in the buffer layer; as the roughness height extends through the buffer layer into the logarithmic region of the boundary layer, it can significantly impact the energy balance, as shown by Krogstad and Antonia [1994] and Ligrani and Moffat [1986]. In fact, at a certain height, the roughness affects the logarithmic layer to such an extent that the standard dynamics of the turbulent boundary layer are interrupted and the rough wall flow is more accurately described as flow over obstacles.

The roughness layer, the region over which the roughness influences the dynamical processes of the turbulent boundary layer, is a strong function of the roughness geometry, including both the height of the roughness and its distribution on the surface, often defined by a parameter  $\Lambda$  equal to the ratio of the roughness interstitial spacing to the roughness height. (Similar ratios of frontal area to surface area have also been used to characterize rough walls). The geometrical differences tend to divide between two families of roughness, as described in Perry et al. [1969]:  $k$ -type roughness, where the effective roughness,  $k_s$  measured by the changes to the wake function of the turbulent velocity profile (also known as the sand-grain roughness, from Schlichting [1968]), scales on the roughness height,  $k$ ; and  $d$ -type roughness, where the effective roughness appears independent of roughness height and scales on the boundary-layer thickness,  $\delta(d)$ . Within the  $k$ -type roughness family, the ratio of interstitial width-to-height establishes whether the recirculation region downstream of each roughness element reattaches upstream of the succeeding element or not. For ratios of  $\Lambda < 8$ , Leonardi et al. [2003] and Volino et al. [2009b] found that the roughness still behaves as a uniform surface and not as a collection of independent obstacles.

Besides the distribution and height of the roughness elements, the form of the roughness itself is also critically important. For three-dimensional, distributed roughness, Schultz and Flack [2005] and

Flack [2007] showed that outer layer similarity is preserved beyond approximately eight times the roughness height, so long as the the boundary layer thickness is no less than twenty times the roughness height. However, for two-dimensional roughness elements (bars or transverse ribs), Volino et al. [2009a] and Schultz and Flack [2007] showed that the roughness can produce significant modifications to the outer flow turbulence, even at roughness heights for which three-dimensional, distributed roughness would not, although the effect was observed only in boundary layers by Krogstad et al. [2005] and not in turbulent channel flow. In particular, they showed that the ratio of the effective roughness  $k_s$  to the roughness height  $k$  for two-dimensional roughness is nearly an order of magnitude larger than for three-dimensional roughness, meaning that the corresponding roughness layer is an order of magnitude larger.

For clarity, it should be noted that the uniformly rough turbulent boundary layer of any roughness configuration is in equilibrium, where the flow can be described entirely in terms of local turbulent processes, despite the significant modifications to the key turbulent transport processes near the wall. However, when incorporating roughness into a nonequilibrium perturbation to a smooth turbulent boundary layer, obviously two-dimensional roughness elements will produce a greater perturbative ‘impulse’ than distributed three-dimensional elements, while also providing a geometry which can be easily described, something which Jiménez and Pinelli [1999] notes poses a significant problem for distributed roughness.

Flow over a surface which transitions between a rough and smooth boundary condition offers a simple and practically relevant case for nonequilibrium on a flat plate. Antonia and Luxton [1971a] studied the transition from a smooth to rough surface ( $S \rightarrow R$ ) along a flat plate boundary layer. The return to equilibrium (in the mean sense of a return of all statistical measures of turbulence to unperturbed values) downstream of the transition point was monitored by the development of an internal layer corresponding to the adjustment of the flow to the new boundary condition, which started at the roughness transition point and grew quickly (in just a few boundary layer thicknesses) to the edge of the boundary layer itself, thereby re-establishing equilibrium in the flow field. The transition from a rough to smooth wall condition ( $R \rightarrow S$ ) showed significantly slower growth of the corresponding internal layer (as expected due to turbulent diffusion), and the restoration of equilibrium was not observed even  $16\delta$  downstream in a second experimental study by Antonia and Luxton [1972]. Subsequently, the problem of a spatial impulse of roughness on an otherwise smooth boundary was considered by Andreopoulos and Wood [1982], since it provided an opportunity to isolate the influence of the roughness in a patch short enough to avoid establishment of a new smooth or rough equilibrium downstream of single transition point. In this way, the additional lengthscale of the roughness was introduced to the turbulent boundary layer and the response of the boundary layer could be observed downstream independent of the continued presence of the roughness itself. The growth of two internal layers, one from each boundary transition, was observed to be consistent

with their independent growth rates, but other features of the flow indicated a nonlinear response to the impulse, and the overall recovery was dominated by the  $R \rightarrow S$  transition.

Andreopoulos and Wood [1982], borrowing the language of Smits et al. [1979], identified a propagating peak of Reynolds shear and normal stresses, downstream of the impulse, as a ‘stress bore’ — showing that the stress behavior in nonequilibria due to changes in geometry shares key features in common with that of roughness-based nonequilibria. This peak was located between the two internal layers, which mark the mean domain of influence of the perturbation, and just as the second internal layer persisted even far downstream of the perturbation, so too the stress bore left an impression on the flow field even far downstream. Pearson et al. [1997], in a similar experiment, although at significantly lower Reynolds number based on momentum thickness,  $\theta$ , ( $Re_\theta \approx 1400$  compared to  $Re_\theta = 4300 - 7600$  in Andreopoulos and Wood [1982]) explored the structural effect of a similar roughness strip on the near-wall flow, showing that streaks associated with the quasi-streamwise vortices of the near-wall cycle were suppressed by the roughness, and recovered only some distance downstream of the trailing edge of the roughness strip. Wu and Christensen [2006] also considered the effect of a step-change in roughness on the distribution of Reynolds stress across the internal layer.

The essential idea of a short impulse of roughness can be thought of conceptually as the injection of a spatial scale, associated with the roughness, into the flow. The flow then relaxes in a complex way governed by at least two independent timescales, one for the evolution of the stress bore and one for the near-wall cycle interruption and recovery near the perturbation. However, since the dominant contributions to active boundary layer motions are associated with very large scales, the ideal perturbation to utilize in order to explore the ‘black box’ is a targeted, large-scale motion. In order to achieve that, the static impulsive roughness can be reconfigured to manifest a specific temporal scale and thereby a finite wavelength in the flow.

## 1.5 Spatio-Temporal Perturbations

In the static roughness perturbation, the scales of motion introduced to the problem are a function of the geometry of the roughness patch alone; by actuating the roughness patch dynamically in time, an additional and precisely controllable timescale can be introduced into the flow. In this way, a more detailed understanding of the mechanics of the relaxation towards an equilibrium state can be obtained, since the relaxation processes observed in the static impulse problem can be viewed in the context of a collection of input timescales, each of which can be individually isolated. The development of the stress bore and the redistribution of turbulent spectral energy density downstream of the dynamic perturbation, in contrast to the statically perturbed case, can be used to better understand the important timescales in nonequilibrium flow conditions. Moreover,

the extent to which the dynamic wave associated with the periodic oscillation of the roughness and the spatially impulsive roughness effects themselves can be treated separately can also be considered.

Hussain and Reynolds [1970] and Hussain and Reynolds [1972] first considered the problem of a temporal perturbation to the turbulent boundary layer, separate from any surface perturbation at the wall. They utilized a thin oscillating ribbon near the wall of a channel to disturb a turbulent base flow at a fixed frequency and amplitude and observed the evolving properties of the perturbation downstream. This approach paralleled the early transition studies of Schubauer and Skramstad [1943] in the laminar boundary layer, in which the asymptotic solution of the Orr-Sommerfeld equations by Tollmien [1929] was first tested. The use of a vibrating ribbon served to minimize any mean influence on the turbulent flow, while injecting a pure sinusoidal input; the consequence of this minimization, however, was that the strength of the perturbation was small compared to the background turbulent fluctuations in the flow, and in outer scaling was actually equivalent to the strength of the perturbation used in the laminar transition experiments.

Other experiments have considered different methods of injecting periodic oscillations into the turbulent boundary layer, both far from the wall and at the wall itself. Patel [1977] considered oscillations in the free stream and observed a strong correspondence between the response of turbulent and laminar boundary layers; in fact, the distribution of streamwise turbulence intensity was essentially unchanged by the periodic fluctuations in the free stream, and thus they were unable to explore the coupling of the input forcing with the turbulence fluctuations. Brereton et al. [1990] also considered free-stream oscillations and reported a similar robustness of the turbulence fluctuations to the changing free stream. Park et al. [2001] considered forcing at the wall itself, using an oscillating jet embedded in a slot, in order to reduce skin friction at the wall. They observed significant changes to the turbulence structure in the boundary layer, including evidence of a stress bore. Moreover, they showed that a series of spanwise vortical structures was produced by the forcing.

Besides the experimental challenge of characterizing the turbulent boundary layer under dynamic forcing, the prediction of the forced state of the boundary layer is essential to understanding the boundary layer dynamics. Although none of the previous cases of dynamic surface forcing have considered this prediction problem, Reynolds and Hussain [1972] laid the foundation for extending the analysis of perturbed laminar flows to turbulent flows in their ribbon experiments away from the wall.

## 1.6 Modeling the Perturbed Boundary Layer and the Resolvent Method

Predicting the physics of the perturbed boundary layer has long been understood in the context of hydrodynamic stability analysis. The key result of hydrodynamic stability for parallel flows is the

Orr-Sommerfeld equation, which represents a linearization of the Navier-Stokes equation, enforcing continuity with the use of stream functions. Small perturbations of the mean flow are assumed, and an eigenvalue problem is formulated from the linearized equation in order to describe the growth and decay of these small perturbations, as derived in Lin [1955] and Drazin and Reid [2004]. Tollmien [1929] solved the Orr-Sommerfeld equation for a laminar boundary layer by asymptotic matching of independent viscous and inviscid solutions; Schlichting [1933] calculated numerically the approximate asymptotic solutions which were ultimately validated in careful experiments by Schubauer and Skramstad [1943]. Despite these early successes, the solution of the Orr-Sommerfeld equation remained a nettlesome problem in applied mathematics for the better part of a century, for a variety of reasons.

The first difficulty with the Orr-Sommerfeld equation is fundamental to the governing equation itself, irrespective of the particular method of solution, whether by asymptotic methods or numerical routines, and that is the assumption of parallel flow. In internal flows, like the channel, parallel flow requirements are enforced for all time and streamwise locations, as is a finite domain for the solution. In boundary layer flows, both of these assumptions fail: the boundary layer grows as it develops and the domain of solution is semi-infinite. Significant mathematical efforts were applied to the problem of solving the Orr-Sommerfeld equation in infinite and semi-infinite domains, many of which are summarized by Herron [1987]. In the finite domain, the set of eigenvalues is both discrete and infinite; however, in infinite domains two sets of eigenvalues are present: a finite discrete set as well as a continuous set. Grosch and Salwen [1978] and Salwen and Grosch [1981] consider the difficulties which emerge from the continuous portion of the spectrum, chief among them being the unresolved question of whether the eigenfunctions form a complete set altogether. The related problem of the growth of the boundary layer was treated by Gaster [1974], who concluded that the parallel flow assumption is often sufficient for considering sufficiently large Reynolds numbers (a problematic conclusion for laminar stability studies).

Most modern solutions of the Orr-Sommerfeld equation utilize numerical methods, following on the early work of Osborne [1967] and Jordinson [1970] using iterative solutions, and subsequently spectral methods like Orszag [1971]. However, the use of numerical methods quickly led to the identification of a further difficulty in the eigenvalue solution of the Orr-Sommerfeld problem because the Orr-Sommerfeld operator is nonnormal. Reddy et al. [1993] called attention to the significant consequences of this nonnormality which places a limit on the accuracy with which the eigenspectrum can be calculated and proposed the use of pseudospectrum to estimate the true eigenspectrum. The pseudospectrum is essentially the set of eigenvalues and neighboring values which are slight perturbations of those eigenvalues.

Despite these inherent difficulties in the solution of the Orr-Sommerfeld equation governing laminar flows, Reynolds and Hussain [1972] extended the equation to treat the periodically perturbed

turbulent flow in a channel. They considered various turbulence modifications to the Orr-Sommerfeld equation in order to model the experimental observations in Hussain and Reynolds [1972]. In particular they considered what they called a ‘quasi-laminar’ closure scheme, wherein the Reynolds stresses were neglected and the presence of turbulence appeared in the model only via the mean turbulent velocity profile, as well as a number of eddy viscosity approaches. Using these approaches, they estimated the wave-numbers of the perturbations expected in the flow. They concluded that inclusion of the Reynolds stress terms was essential for accurate predictions and that the quasi-laminar approach failed in two respects: 1) it was unable to accurately predict the wavespeeds (eigenvalues) experimentally measured, and 2) the mode shapes of velocity fluctuations (eigenfunctions) predicted were disproportionately more peaked than those observed in the experiments.

However, the modeling efforts of Reynolds and Hussain [1972] deserve reconsideration in light of the recent work of McKeon and Sharma [2010] which employed a ‘resolvent analysis’ to the Orr-Sommerfeld equation associated with turbulent pipe flow. The resolvent analysis shares the same starting point as the traditional eigenvalue analysis of the Orr-Sommerfeld equation, by applying a Reynolds decomposition to the Navier Stokes equation, but instead of linearizing the result, the nonlinear terms are retained and grouped on the right-hand side of the governing equation as an ‘internal forcing’,  $f$ . In this way, the model equation is restructured to appear like the standard Orr-Sommerfeld linear eigenvalue problem on the left-hand side, but with ‘internal forcing’ on the right-hand side representing the natural nonlinearities inherent in the flow. By inverting the linear operator, the problem was shown to be equivalent to the resolvent (or propagator) of the Orr-Sommerfeld operator acting on the ‘internal forcing’,  $f$ . McKeon and Sharma [2010] proposed that the most amplified singular mode of the resolvent, formulated for particular combinations of streamwise and spanwise wavenumbers and frequencies identified from experiments, could be used to represent key features of the overall flow field, in much the way that proper-orthogonal decomposition (POD) methods employ singular modes to identify reduced-order representations of complicated flow fields (Hellström and Smits [2011]). The dominant modes were identified as the turbulent analogues of the well-studied ‘critical’ and ‘wall’ neutral disturbances in linear stability analysis (where the overlap or nonintersection of these critical and wall layers determine the ‘upper’ and ‘lower’ branches of the neutral stability curve). Importantly, the standard closure problem, which challenged Reynolds and Hussain [1972], was circumvented, to the extent that one or more singular modes superposed can represent the flow field, and only the mean turbulent velocity profile is needed for construction of the Orr-Sommerfeld resolvent.

The most obvious difference between the standard eigenmode approach and the resolvent methodology is the type of modal decomposition assumed. Because, as noted above, the Orr-Sommerfeld operator is not normal — a property which Trefethen and Embree [2005] note was not widely appreciated for most of the history of its study — its corresponding eigenfunctions are not orthogonal

and its eigenvalues are highly sensitive to small perturbations. The nonorthogonality of the eigenfunctions make them particularly ill-suited for representation of high-Reynolds-number flows, as noted by Schmid and Henningson [2001]. On the other hand, the resolvent analysis avoids the entire difficulty associated with eigenvalues, by employing a Schmidt decomposition, which produces an orthogonal (complete) set of singular basis functions even for nonnormal operators.

The resolvent method is naturally suited to handling the case of a forced or perturbed flow field, in which the right-hand side of the governing equation includes not only the natural nonlinearities of the unforced problem, labeled ‘internal forcing’, but also the ‘external forcing’ injected into the flow. The resolvent analysis also implicitly treats a superposition of all of the forcing, even strong perturbations which modify the mean flow, since they can be taken into account via the mean velocity profile, and as stated above, the solution requires no explicit closure treatment. The downside of this, however, is that the relative strength of the ‘external forcing’ to the ‘internal forcing’ may be important, in terms of the number of modes necessary to adequately describe the flow. In other words, if the perturbation is relatively weak compared to the ‘internal forcing’ of the natural nonlinearities in the base flow, the perturbed dynamics may not be captured with just a single mode of the resolvent. Of course this problem of the relative strength of the perturbation also afflicts the quasi-laminar approach, and indeed Reynolds and Hussain [1972] considered a superposition of different eigenmodes to adequately capture the dynamics. The method of two-dimensional roughness perturbation described above naturally generates a stronger perturbation to the base flow than was considered in the experiment of Hussain and Reynolds [1970], which was, by comparison, closer to the very low perturbation level used in transition studies of laminar flows, like Schubauer and Skramstad [1947]. This difference in perturbation strength indicates that the contribution of the ‘external forcing’ to the overall forcing of the problem should be significant in the current experiments (and not overwhelmed by natural nonlinearities in the base turbulent flow), which would allow for the possibility that a small number of singular modes could adequately capture the velocity fluctuations of the forced system. Moreover, the relatively stronger perturbation also provides insight into more realistic forcing generated by various mechanical flow control schemes.

However, ultimately, the primary disqualification of the quasi-laminar scheme in Reynolds and Hussain [1972] was its inaccurate prediction of eigenmode shapes compared to measurements of velocity fluctuations. Although the resolvent approach entirely avoids the sensitive choice of eigenvalues and modes, certain deficiencies in the mode predictions by the resolvent are expected to persist due to the sensitivity of the mode shapes to the choice of mean velocity profile, and the associated ambiguity inherent in choosing a representative mean velocity profile in a nonequilibrium flow.

The motions generated by dynamic forcing, whether at the surface or using the ribbon mechanism, tend toward large-scale motions due to experimental constraints, with wavelengths on the

order of the boundary layer thickness itself. On the other hand, the nonequilibrium boundary layers produced by surface roughness tend to manifest significant changes to the small scale turbulent fluctuations, particularly in the region of the stress bore. In order to fully explore the dynamics of the perturbed boundary layer, the relationship between these large- and small-scale effects must be investigated.

## 1.7 The Influence of Synthetic Large-Scale Motions on Boundary Layer Turbulence

The relationship between large- and small-scale motions in wall-bounded turbulence has been well known, since early measurements by Blackwelder and Kovasznay [1972] which suggested a connection between the large-scale features of the boundary layer, including intermittent bulges, and the activity of small-scale motions. And these motions were long understood to be coherent over certain time and length scales of the flow. Theodorsen [1952] had originally proposed a hairpin shape for coherent motions in the boundary layer, and the idea of coherent structures playing an integral part in the mathematical scaling of the turbulent boundary layer was then developed further in the attached eddy hypothesis of Townsend [1976]. With advances in particle-image velocimetry (PIV) measurements of full planes of the boundary layer velocity field, Adrian et al. [2000b] and Tomkins and Adrian [2003] observed evidence for a hierarchy of coherent, small hairpin-shaped structures, organized into larger packets with discernible boundaries and orientation in the flow. Metzger and Klewicki [2001] showed that the large coherent motions are likely responsible for not only the structure of the mean velocity field and gradient, but also the small-scale turbulence processes occurring within the near-wall region, via the mean velocity gradient's effect on turbulent kinetic energy production in the buffer layer. With this observation, the precise relationship between large- and small-scale motions drew significant interest. The idea that the large scales modulated small-scale motions (where 'modulation' should be considered for some general class of interactions) was first studied extensively in Bandyopadhyay and Hussain [1984]. More recent studies by Hutchins and Marusic [2007], Mathis et al. [2009a], Mathis et al. [2009b], Chung and McKeon [2010], and Guala et al. [2011] have all explored the observation that large-scale fluctuations can often be associated with corresponding modification of different measures of small-scale motions.

The significant implications of a large-scale modulation effect are obvious in the model of Marusic et al. [2010a] for predicting near-wall viscous fluctuations based on a 'universal', large-scale signal. The modulation relationship has been understood as an amplitude modulation of small-scale fluctuations by large-scale structures in turbulent, wall-bounded flows, and it has been supposed that the large-scale motions responsible for the modulation are the attached, very large scale motions (VLSM) in the flow. The amplitude modulation can be observed easily by inspection of properly filtered in-

stantaneous velocity signals, as in Mathis et al. [2009a], but variation of the modulation effect with wall-normal location within the boundary layer means more sophisticated ways of characterizing the modulation are required. Recent attention has been directed at the use of a Pearson-type correlation coefficient,  $R$ , in Mathis et al. [2009a] to relate the large- and small-scale motions. Schlatter and Örlü [2010] and Mathis et al. [2011] noted that the similarity of the profile of  $R$  to the streamwise skewness is not merely a coincidence, but reflects a fundamental mathematical connection between the two measures, the physical significance of which is not currently well understood. Indeed, it is because of the underlying significance of the modulation effect to understanding basic boundary layer physics, even aside from its potential as an aid in designing predictive tools, that it requires more careful exploration.

Bandyopadhyay and Hussain [1984] studied the relationship between large-scale motions and an envelope of small-scale fluctuations in a variety of shear flows, using single-point hot-wire measurements. They concluded that fluctuations in the large-scale motions in the turbulent boundary layer tend to lead corresponding fluctuations in the envelope of small-scale motions. Subsequently, Mathis et al. [2009a] labeled this relationship a form of amplitude modulation and characterized the strength of the modulation across the boundary layer by introducing a correlation coefficient. Most of the previous studies have concentrated on the modulation in the streamwise velocity component, although Hutchins and Marusic [2007] reported evidence for amplitude modulation in the wall-normal velocity component of channel flow DNS measurements, observed via time traces, although there was little spectral evidence for modulation in this direction. Hutchins et al. [2011] returned to the question of the relative orientation of the large- and small-scale fluctuations and employed conditional averaging of hotwire velocity measurements against hot-film measurements of the velocity gradient at the wall of a turbulent boundary layer. They observed that fluctuations in the small-scale variance tended to lead corresponding fluctuations in streamwise velocity, when averaged conditionally on low-stress events near the wall. A similar conditional averaging, using LES simulations of a turbulent channel flow, had been performed earlier by Chung and McKeon [2010]. They again observed that fluctuations in the small-scale envelope of fluctuations tended to lead the corresponding large-scale motions. In addition, they considered conditional averaging of the spanwise and wall-normal velocity fluctuating components and showed similar phase relations with the streamwise mean velocity. Additional experimental measurements performed by Guala et al. [2011] in the atmospheric surface layer, following precisely the approach of Bandyopadhyay and Hussain [1984], also reported the small-scale envelope leading the large-scale motions, and due to their unique experimental environment were able to observe this effect down to dissipative scales.

The nonequilibrium boundary layer offers a unique perspective on interactions between large and small scales, by producing modifications to both quantities. In this study, the large-scale motion associated with dynamic forcing and the small-scale changes associated with a roughness impulse,

can be viewed as an magnification of the natural processes at work in the unperturbed boundary layer. Indeed, by combining many of the elements of nonequilibrium boundary layers, a perturbation can be designed which enhances and clarifies the subtle and obscure dynamics inside wall-bounded turbulence of all types.

## 1.8 The Perturbed Flow and the Generation of Synthetic Large-Scale Motions

A perturbation for investigating the black box of turbulence can be constructed in order to exploit the key features of the nonequilibrium boundary layer. By utilizing a short patch of roughness as an impulsive impulse, a conceptual analogy is preserved between the impulsive flow and an equilibrium boundary layer over a fully developed, uniformly rough wall flow, and this analogy can be explored experimentally. Two-dimensional roughness then makes the geometric description of the roughness straightforward, while providing a significant nonequilibrium disruption of the natural turbulent processes in the boundary layer with a minimal spatial footprint. The streamwise shortness of the spatial extent of the roughness provides for a narrow localization of the internal layers and stress bore, which in turn makes characterization of the difference between the unperturbed and perturbed regions of the flow simpler.

Modifying the same static impulse to produce a periodically oscillating rough surface then allows for careful consideration of the separate effects of the large-scale motion associated with the periodic forcing and the roughness patch itself. Moreover, dynamic forcing at the surface was shown (e.g., Park et al. [2001]) to produce a strong structural modification of the boundary layer. The strength of a roughness perturbation, in contrast with a vibrating ribbon, is more likely to elicit a commensurably strong response from the boundary layer which is easier to measure. In light of the resolvent approach to conceptualizing the forced boundary layer, when the forcing is at least as strong as the ‘natural’ non-linearities in the unperturbed flow, the coherence of the input perturbation can be more easily preserved and thereby will elicit a more coherent response from the boundary layer dynamics.

## 1.9 Experimental Organization

The two traditional categories of static and dynamic nonequilibrium perturbation, which have separately provided the basis for the contemporary understanding of perturbed wall-bounded flows, together lay the foundation for an experimental plan to investigate the perturbed flat plate boundary layer in an integrated way.

The initial characterization of the unperturbed turbulent boundary layer leads directly to a

reconsideration of static impulse studies, with the purpose of conceptualizing the statically perturbed flow as a ‘base flow’ from which to think about dynamic perturbation. The static perturbation phase of this study therefore begins to bridge the gap between the statistical picture of Andreopoulos and Wood [1982] and the Pearson et al. [1997] flow visualizations, by (a) closer examination of the nature and behavior of the internal layers and their relation to other statistical properties of the flow, which offer the best intuitive perspective on how impulsive perturbations affect a turbulent flow; (b) an examination of the turbulent spectra associated with the downstream flow, to understand how the previous observations about the near-wall cycle manifest themselves energetically; and (c) an analysis of the distribution of swirling content and discrete vortex cores in the flow field downstream of the perturbation, in order to understand the structural modifications occurring in the flow and how their relaxation relates to the other measures of the return to equilibrium.

The dynamic phase of the study then proceeds along two parallel axes designed: 1) to connect the key features of the statically perturbed boundary layer — the internal layers, stress bore, near-wall energetic changes, and integral scale-size effects — to a dynamic perturbation of similar spatial type; and 2) to utilize that dynamic perturbation to examine the effect of exciting a specific temporal fluctuation on the flow field, by employing a resolvent analysis. The dynamic perturbation was designed to target large-scale motions in the boundary layer, subject to the physical constraints imposed on mechanical actuation. Thus both experimental measurements and predictive analysis, in support of the experiments, come together to present a comprehensive picture of the perturbed flow. In particular, the relationship between the synthetic very large scales generated in the flow by the periodic oscillation and the roughness effects themselves are explored in the context of the evolving consensus on the interaction of large- and small-scale fluctuations in even unperturbed boundary layers.

In the process of rethinking the relationship between large and small scales, the widely observed modulation effect between large and small scales in the turbulent boundary layer is reinterpreted in light of the observation by Chung and McKeon [2010] that the widely-used correlation coefficient is fundamentally a measure of a phase relationship. A variety of correlation based techniques are deployed in pursuit of a detailed characterization of the large-to-small-scale interactions in both streamwise and wall-normal directions. These same techniques, in particular a cospectral analysis of large- and small-scale motions, are then applied to the dynamically perturbed flow, in order to measure the extent to which linear theories can adequately describe the complex dynamics of the forced flow.

Ultimately, the forced turbulent boundary layer is analyzed by linear techniques at a variety of levels, from the composition of the stress bore common to all nonequilibrium flows, to the prediction of the dynamic oscillations of very large scale motions, to the relationship between natural and artificial, large and small scales in the flow. The ability to describe and ultimately predict the key

features of the turbulent boundary layer with simple, linear techniques, is the first step towards both better physical and functional descriptions of turbulence, on the one hand, and smarter tools for controlling and modifying wall-bounded flows, on the other.

## Chapter 2

# Experimental Setup

### 2.1 Merrill Wind Tunnel Facility

The turbulent boundary layer experiments were performed in the Merrill wind tunnel at Caltech. The facility is a closed loop (recirculating) wind tunnel, manufactured by Engineering Laboratory Design (Minnesota) with a  $2' \times 2'$  test section that extends for  $8'$ . The test section is connected to the tunnel between the first and fourth ‘elbows’ of the loop, where the fourth elbow is upstream of the test section. Between the fourth elbow and the upstream end of the test section, the flow is conditioned by a series of flow straighteners preceding a contraction ( $6.25 : 1$ ). The temperature in the tunnel is held constant at approximately ambient  $22^\circ\text{C}$  by adjusting the flow-rate in a cold-water heat exchanger, positioned between the third and fourth elbows of the loop. The desired temperature is maintained by a digital controller which senses the temperature at a thermocouple attached upstream of the contraction.

The test section, shown in figure 2.1, has an adjustable ceiling, deformable at ten equidistant locations along its length, in order to maintain zero pressure gradient along a flat plate installed at the mid-height of the section. The flat plate has a parabolic leading edge situated approximately  $2'$  from the end of the contraction and a trailing edge flap at the end of the test section used to maintain the stagnation point on the top surface (the measurement side) of the leading edge. The plate itself is assembled from seven interlocking pieces of optical-grade acrylic (five of which are interchangeable) suspended in the test section by a series of sections of  $12'$  aluminum channel beam. Five ports with airtight plugs are spaced along the centerline of the plate in the downstream three sections to allow positioning of a traversing mechanism (Velmex BiSlide stepping motor, model # PNX10-0040-01-71) which holds the hotwire and Pitot probes. The traverse has a total traversing length of  $4''$  (measured from the base of the plate) with a resolution of  $2.5 \mu\text{m}$  per turn. The traverse is controlled via a script in LabVIEW in order to step through a full velocity profile, after the initial point is set manually, by calibration against a physical standard with a camera (Nikon D300, using a 170 mm Tamron SP-AF-180 F3.5 Macro 1:1). The error in the near-wall positioning was on the



Figure 2.1: (Left) The test section, as shown from the outside, with the direction of flow from left to right. (Right) The plate seated on its supports within the test section, with the direction of flow from bottom of the image to top. The roughness elements and diagnostics traverse are both visible, along with both the acrylic walls and adjustable ceiling of the test section.

order of 100–200  $\mu\text{m}$ , with a bias towards overestimating the height due to reflections from the flat plate which distorted the image in the camera. Pressure taps are positioned along the length of the plate, just off the centerline, and connect to a pressure scanner (Scanivalve, model DSA3217) for use in adjusting the test section ceiling to maintain zero pressure gradient.

The flow conditions in the tunnel are controlled by modifying the pitch of the fan blades (using a pneumatic, balanced diaphragm actuator) and the frequency of the fan (using an inverter-type, digital frequency controller). The maximum tunnel speed in the test section is approximately 49 m/s. Most of the experiments were performed at approximately 20 m/s, achieved with an inverter frequency of 27 Hz and a pressure associated with the fan blade pitch of 12 psi. The normalized turbulence intensity in the freestream, at this operating condition, was approximately 0.2%. By adjusting the ceiling, the spatial variation in the pressure coefficient was maintained at  $\Delta C_p \ll 0.01$  over the range of streamwise measurement locations along the flat plate. The boundary layer over the flat plate was tripped 19.0 mm downstream of the tip of the parabolic leading edge by a 0.76 mm-diameter cylindrical wire glued to the surface, and the effectiveness of the trip was confirmed by identification of the virtual origin for the turbulent boundary layer, as described in section 2.4. The velocity field above the flat plate was measured by Pitot tube, hot-wire, and particle image velocimetry (PIV); preliminary measurements of the velocity gradient at the wall were performed using oil film interferometry.

## 2.2 Single-Point Velocity Measurements

In order to measure the velocity field by Pitot tube and hot-wire anemometry, wall-measurement-type Pitot and hot-wire probes were affixed to a rig attached to the traverse, shown in figure 2.2,

allowing each probe to be lowered or raised from the surface of the wall, while maintaining negligible inclination with respect to the incoming free stream.

The Pitot tube measures the stagnation pressure in the free stream and the static pressure was measured using the pressure port at the wall, at the same streamwise location as the tube. The tube itself had inner diameter 0.012", and outer diameter 0.02", with a bend angle of 12° in order to maintain an orientation parallel to the free stream, very near to the wall. The bend angle was necessary for both the Pitot tube and the hotwire probe in order to enable measurements very near to the wall without creating a significant blockage effect. The pressure measurements were performed with a Baratron MKS 20 Torr pressure transducer (#220DD) with 20 Torr range, and accuracy 0.15% of the pressure. The transduced voltages were then acquired using a digital data acquisition board (National Instruments NI 6154) and National Instrument's LabVIEW software. The mean pressure was converted to mean velocity,  $U$ , using Bernoulli's equation, including a correction for temperature and humidity effects on the ambient air density.

For the anemometry, the downstream flow was measured using a 5  $\mu\text{m}$ -diameter,  $l = 1.25$  mm active-length, platinum-plated-tungsten, boundary-layer-type probe (Dantec #55P05 boundary-layer type) and an A.A. Labs anemometer (AN-1005). The anemometer employs a Wheatstone bridge, the output of which was amplified to maximize use of the range of the data acquisition board which spanned  $\pm 10$  V. The hot-wire signals were sampled at  $f_s = 60$  kHz, although the frequency response cutoff of the anemometer was ultimately determined to be lower than expected. Following the pulse-response test described in Freymuth [1977], the actual frequency response was estimated at approximately 15 kHz. All data records were of duration  $T = 50$  s, yielding  $3 \times 10^6$  points, recorded in 6 consecutive blocks. The hotwire was calibrated *in situ*, using the Pitot probe to measure the mean freestream velocity,  $U_\infty$ , and employing a fifth-order polynomial fit for the hotwire voltage signal. Velocity time series for the instantaneous streamwise velocity component,  $\hat{u}$ , were then recorded at 27 logarithmically spaced wall normal locations at each streamwise location along the length of the plate, where the wall normal locations were obtained by automating the traverse and data storage operations using LabVIEW.

## 2.3 PIV

To obtain both wall-normal velocity components, as well as information about the spatial structure of the velocity field above the flat plate, PIV measurements were taken at two streamwise locations centered on 980 mm and 1530 mm downstream of the leading edge, which correspond roughly to the streamwise extrema of the hotwire measurements. A laser sheet, produced by a double-pulsed Yag laser (Photonics model DM-20 527) was positioned to illuminate the streamwise-wall normal plane, just off the centerline of the plate (in order to avoid distortions from the traverse

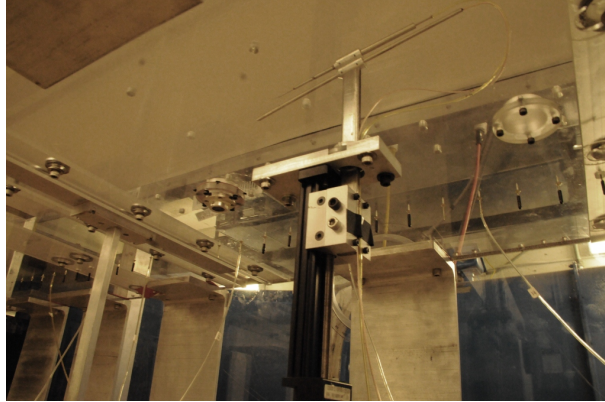


Figure 2.2: The traverse mechanism attached below the plate, with flow direction from left to right. Also visible is the upper portion of the traverse, on the top side of the plate, with the attached Pitot and hotwire probe holders. In addition, the pressure taps along the plate, and a second port for positioning the traverse, are also visible.

ports), roughly mirroring the spanwise location of the pressure taps. The laser sheet was generated from a collimated beam in the spanwise direction, below the test section, which was converted into a sheet with a cylindrical lens and directed by mirrors up through the optically clear walls beneath the test section to produce a sheet perfectly plumb in the wall normal direction. The flow field was seeded with an aerosol of bis(2-ethylhexyl)sebacate (DEHS) ( $0.25 \mu\text{m}$  modal size) using a mechanical atomizer (LaVision Aerosol Generator #1108926). The seeding density had a half-life of approximately 5 minutes and thus the wind-tunnel was periodically re-seeded during operation, by injecting the aerosol stream into the downstream end of the test section by means of a wide hose (1" inner diameter) connected to the atomizer. The illuminated, seeded flow was recorded at a resolution of  $1024 \times 1024$  pixels from a Photron Fastcam APX-RS camera using a macro lens (170 mm Tamron SP-AF-180 F3.5 Macro 1:1) such that the physical size of the PIV images was  $38 \times 38 \text{ mm}^2$ , allowing for full coverage of the boundary layer thickness. To position the camera, a support rig was constructed, illustrated in figure 2.3, to allow easy switching between streamwise measurement locations. Moreover, the camera support and the entire optical arrangement (laser, lens, and mirrors) were affixed to an optical table (Newport ST, series I-2000) in order to isolate the PIV measurements from vibrations associated with the operation of the tunnel.

The laser was operated in double-pulsed mode, meaning the laser generated pairs of laser pulses at 1000 Hz, where the frames within each pair were separated by a time period much smaller than the period between pairs. The high speed camera was synchronized with the laser pulsing, such that pairs of images were recorded at 1000 Hz, with each member of the pair illuminated by a unique pulse. The desired freestream velocity for the experiments was 20 m/s, with a window length in the streamwise direction of 38 mm, comprising 1024 pixels; in order to constrain the motion between correlated frame pairs to less than 5 pixels (optimal for the correlation algorithm), the maximum

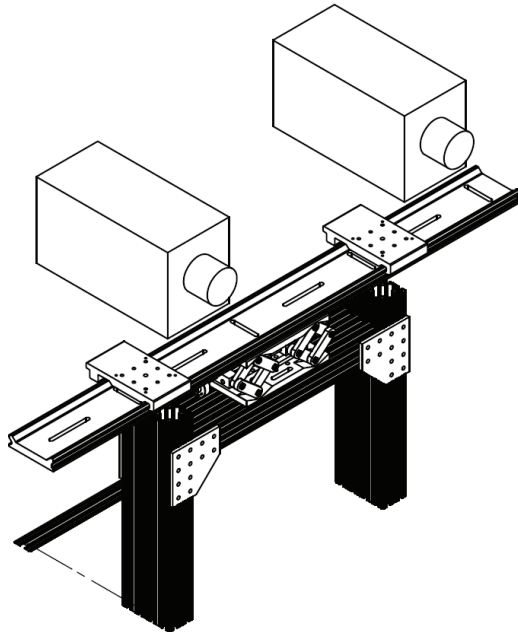


Figure 2.3: A line-drawing of the camera stand used to position the high-speed cameras to image the wall-normal-streamwise plane. The stand was itself floated on an optical table to isolate the cameras and laser sheet from any vibrations generated by the operation of the tunnel.

elapsed time between frames is limited to  $10 \mu\text{s}$ . Therefore, the velocity vectorization was performed pairwise, between frames separated in time by  $10 \mu\text{s}$ , and the resulting velocity field itself was resolved temporally according to the actual sampling frequency of 1000 Hz.

The pairwise velocity calculations require precise identification of the inter-pulse time; however, this time cannot be set *a priori* by the laser controller, since it is a complex function of the laser pulse frequency and power. Therefore, to ascertain the precise inter-pulse time, a photosensor diode with a response time significantly smaller than the desired inter-pulse spacing (Thorlabs FDS02, rise time 47 ps) was employed, and the voltage was amplified and output to a digital oscilloscope (Tektronix, model TDS-2012). The laser controller software (DaVis 7 by LaVision) was modified by the manufacturer, upon request, to allow for a time-offset factor to be input into the controller, and by iterating choices of offsets with measurements of the actual inter-pulse spacing, the pulse separation was fixed to  $10 \mu\text{s}$  within less than 1%. After recording the images of the seeded flow, the image pairs were processed in commercial PIV software (by LaVision) using a double-pass approach with windows of 32 and then 16 pixels square at 50% overlap to produce each velocity vector. The first two vectors nearest the wall were discarded, due to seeding reliability issues and reflection difficulties in that domain of the flow field.

$x$ (cm)	$U_\infty$ (m s <sup>-1</sup> )	$\delta$ (mm)	$\theta$ (mm)	$Re_\theta$ $= U\theta/\nu$	$Re_\tau$ $= u_\tau\delta/\nu$
0.50 (7.4)	20.16 (20.60)	17.0 (17.6)	2.1 (1.9)	2770 (2560)	910 (970)
58.0 (62.4)	20.09 (20.42)	24.1 (25.8)	3.1 (2.9)	4070 (3870)	1200 (1320)

Table 2.1: Mean flow properties at streamwise extrema of sampling area for hotwire (PIV)

## 2.4 Mean Flow Properties and Resolution Limits

In order to consider the resolution limitations of the measurement systems, the bulk flow properties in the wind tunnel for both the hotwire and PIV rounds of experiments are summarized in table 2.1, and some key features of the flow field are described below. The streamwise location,  $x$ , is measured from 0.880 m downstream of the leading edge of the plate, which is the location at which subsequent perturbation of the flow is initiated in the current experiments, as discussed in section 2.5. The boundary layer growth of the unperturbed flow indicates a virtual origin for the turbulent boundary layer, based on comparison with Prandtl’s quasi-empirical formulation, at approximately 0.22 m downstream of the leading edge trip, and thus 0.66 m upstream of the first measurement location. The mean boundary layer thickness,  $\delta$ , represents the wall-normal location at which 99% of the mean freestream velocity is reached. The Reynolds number,  $Re$ , is given in terms of momentum thickness,  $\theta$ . The Reynolds number can also be formulated as the Karman number,  $Re_\tau = \delta u_\tau/\nu$ , using the friction velocity,  $u_\tau$ , where the friction velocity can be expressed as  $\sqrt{\tau/\rho}$ , with  $\tau = \mu\partial U/\partial y$ ;  $\rho$  is the fluid density,  $\mu$  is the dynamic viscosity, and  $\partial U/\partial y$  is the mean velocity gradient in the wall normal direction. The kinematic viscosity is denoted  $\nu = \mu/\rho$ .

The friction velocity was estimated by the Clauser chart method (see Fernholz and Finley [1996]), with confirmation via the Karman momentum integral (Schlichting [1968]), and direct evaluation from the mean velocity gradient measured nearest to the wall. The friction velocity was also measured independently by oil film interferometry in order to confirm the general range of values produced by the Clauser method, although the detailed oil-film results are not reported in the present study since they are part of ongoing efforts to improve the reliability of oil-film measurements.

These flow conditions indirectly place constraints on the practical resolution of the hotwire anemometry. The hotwire had  $l/d = 250$  and  $l^+ = 67$ , where  $(\cdot)^+ = (\cdot)u_\tau/\nu$  is referred to as inner scaling. According to Hutchins et al. [2011], such a large value of  $l^+$  at this relatively low  $Re_\tau = u_\tau\delta/\nu$  can result in measurements that significantly underestimate the turbulence intensity  $\sqrt{u^2(y)}$  near the wall, where  $u$  denotes the fluctuating component of the instantaneous velocity signal, such that  $\hat{u} = U + u$ . Using the correlations provided in Hutchins et al. [2011], an underestimate of the peak in  $\sqrt{u^2(y)}$  by as much as 30% is expected in the present study. The spatial resolution in terms of the Kolmogorov scale,  $\eta$ , estimated by the local equilibrium approximation (following Morrison et al. [2004]) was  $(2\pi/l)\eta \approx 0.15$ . The frequency response of the anemometer also constrains

the temporal resolution available. In frequency space, the smallest energetically relevant scale in the flow can be estimated following the rule of thumb in Hutchins et al. [2011] to be  $u_\tau^2/3\nu \approx 13$  kHz. This is below the frequency response cutoff, at  $f_a \approx 15$  kHz, and thus the chief resolution issues from the hotwire measurements are expected to be spatial, related to the hotwire itself. Detecting long-time trends in timeseries requires sufficiently long time series such that even after applying a windowing procedure, the largest relevant scales in the signal can still be detected. In most of the spectral analysis conducted in this study, the full timeseries of  $3 \times 10^6$  points are divided into approximately 100 windows, which are then processed by fast Fourier transform with 50% overlap using the classical Hanning window. Therefore, the largest resolvable scale is approximately 0.5 s, or, applying Taylor’s hypothesis, approximately  $60 \delta$ .

For the PIV measurements, constraints on the small-scales are twofold: temporal and spatial. The low sampling rate of the PIV severely limits the temporal resolution of the subsequent measurements: the smallest resolvable scale, temporally, is  $2.29 \delta$ , applying Taylor’s hypothesis. However, spatially, each vector represents an area of  $0.017 \times 0.017$  outer units or  $16.3 \times 16.3$  inner units, which means the smallest resolvable scale in a spatial spectral sense is approximately  $0.03 \delta$ . For the large scales, since the PIV time series are 1.024 s in duration, the largest resolvable scale, employing Taylor’s hypothesis, is  $119 \delta$ , while the largest spatial scale is limited by the streamwise extent of the PIV window to  $2.14 \delta$ . There is thus no overlap in the scales resolvable by the spatial and temporal PIV measurements, although the hotwire measurements can be compared to spatial PIV results. It is important to note that the limits on the PIV resolution are essentially implicit filters — a low-pass for the temporal measurements and a high-pass for the spatial measurements. For studies of large-scale features of the velocity signals, the high-pass filter in the spatial PIV poses a peculiar problem, known as subfundamental sampling.

Subfundamental sampling results from attempting to perform spectral analysis (or a calculation that is implicitly spectral, like the cross-correlation) on signals which are shorter than the period of the relevant scale of interest. Strader II [1980] discussed this problem and concluded that the only way to mitigate the distortion in spectra is by appropriate adjustment of filter cutoffs. But, the precise nature of the distortions can actually be investigated by considering a simple model problem, discussed further in section 7.4.1, which then enables inferences to be drawn from the nature of the observed distortions in quantities like the cross-correlation function.

The velocity profiles for the unperturbed flow (and turbulence intensity profiles, below) are compared against those reported by DeGraaff and Eaton [2000] for  $Re_\theta = 2900$  which corresponds to the fifth or sixth downstream recording position,  $Re_\theta = 2850$ – $2940$  in figure 2.4. The mean profiles demonstrate excellent agreement. For the turbulence intensity profile, the degree of the underestimate of the magnitude of the near-wall peak is lower than that predicted by application of the fit in Hutchins et al. [2011] for the value of  $l^+$  — on the order of 20% at the peak — but as mentioned

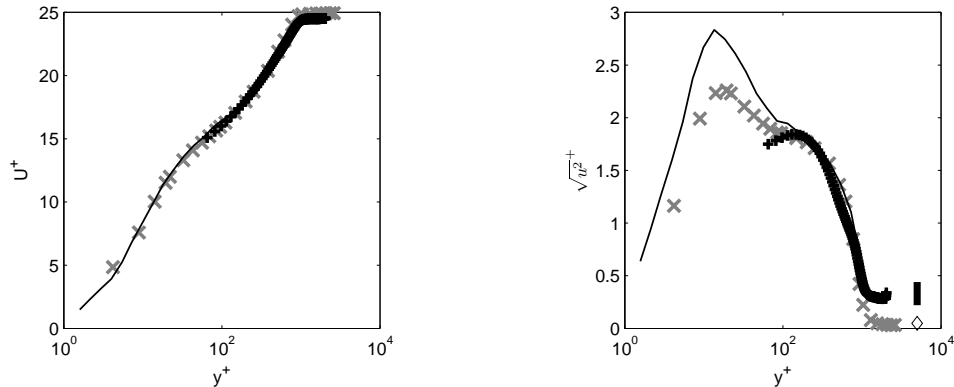


Figure 2.4: (Left) The mean velocity profile for the unperturbed smooth wall, measured by hotwire and PIV and plotted in wall units against the profile recorded by DeGraaff and Eaton [2000] at similar  $Re_\theta$ . (Right) The streamwise turbulence intensity profile for the unperturbed flow, measured by hotwire and PIV and plotted in wall units.  $\times$  hotwire,  $Re_\theta = 2940$ ;  $+$  PIV,  $Re_\theta = 2560$ , with its estimated noise floor shown as the black bar; — DeGraaff and Eaton [2000],  $Re_\theta = 2900$ , with their free-stream turbulence intensity marked by  $\diamond$

above, the discrepancy is not significant to comparisons between perturbed and unperturbed flows, which is the heart of this study. In any case, it would appear that the underestimate can be attributed entirely to the spatial resolution of the probe. The noise floor for the PIV is the error in the peak-location of the cross-correlation algorithms, estimated by Westerweel [1997] at between 0.05–0.1 pixels, which for the current recording translates into a floor of free-stream turbulence intensity of 0.9–1.8%, or in the inner units shown below,  $u_{floor}^+ \approx 0.22$ –0.44, significantly higher than that of the hotwire.

### 2.4.1 Spectral Smoothing

Spectral analysis of the velocity signals from the hotwire measurements is used extensively, both in the form of premultiplied spectral densities of the streamwise fluctuating velocity components and cospectral densities between large- and small-scale motions. Spectral density estimation is beset by a number of challenges in producing a smooth and unbiased representation of the actual spectral energy density. For the spectral estimates of the streamwise velocity component, Welch’s method was applied to the full time record ( $3 \times 10^6$  points) using approximately 150 windows of equal length with 50% overlap between windows. The premultiplied spectra were validated against the results of Erm and Joubert [1991] in section 3.1.4, but precise quantitative comparison was difficult since the precise smoothing and spectral estimation methods utilized in previous studies are not commonly reported. Welch’s method involves incoherent averaging of the spectra of the individual windows and thus obliterates the phase information contained within the Fourier components of the original time series. In order to preserve that phase information for the cospectral energy density estimates,

coherent averaging of the individual windows was employed. However, Lyons [2011] noted that coherent averaging tends to reduce the quality of the smoothing of the spectral estimate. In order to compensate for that loss in smoothness, the bin size of the spectra was reduced in order to linearly smooth the spectra further, such that the spectrum of turbulent fluctuations from the coherent averaging matched the result from Welch’s method (which required averaging across approximately 10 bins, using the same windows as in the Welch’s analysis). However, besides the modification of the bin size, a fitting procedure was also employed in order to accurately capture the location of the peak in the spectrum, without diffusing the peak over multiple frequencies by averaging. The fitting procedure, detailed in section 7.5, involved fitting a modified Gaussian curve to the raw spectrum by an iterative least-squares procedure. Again, precise quantitative comparison with prior studies was unavailable. Ultimately, the variation observed in the current experiments was qualitatively consistent with observed statistical variability in other studies, and there were no indications of significant systematic bias in the spectral analysis.

## 2.5 Roughness

Downstream of the trip, an insert was fitted into the smooth flat plate allowing for a short patch of two-dimensional roughness elements to protrude above the surface of the plate. The insert itself consisted of rows of slots, which were designed to allow corresponding rows of roughness elements to pass through from their base positioned beneath the plate, illustrated in figure 2.5. Thus the roughness elements, while sitting on their base, could be arranged to protrude an arbitrary height above the surface of the plate, ranging from being flush with the surface, to extending as much as 5mm above the surface of the plate. The insert was positioned such that leading edge of the first row of roughness elements (the smooth-to-rough, or  $S \rightarrow R$ , transition) occurred 880 mm downstream of the trip of the flat plate, or at a Reynolds number based on the freestream velocity,  $U_\infty$ , of  $Re_l = 1.15 \times 10^6$  and  $Re_\theta = 2770$ . The roughness patch extended for 25.3 mm or approximately  $1.5 \delta$  of the smooth wall boundary layer. In this sense, the patch of roughness elements can be considered ‘short’ or impulsive in the streamwise direction, fulfilling the criterion of Andreopoulos and Wood [1982] that a spatial perturbation is impulsive if it persists for less than  $10 \delta$ .

The short patch of roughness elements, referred to as the impulse or perturbation, consisted of four bars of two-dimensional, k-type roughness, each 1.57 mm thick and separated (interstitially) by 6.35 mm, illustrated in figure 2.6 along with a sketch of the relative orientation of the roughness patch to the internal layers generated in the boundary layer. During the ‘static roughness’ experiments, the base upon which the roughness patch is supported was fixed in position to produce a roughness height of 1 mm, giving a ratio of rod spacing  $p$  to roughness height  $k$  of  $p/k = 7.14$  which is consistent with the work of Leonardi et al. [2003] and Volino et al. [2009b] in fully developed, two-dimensional

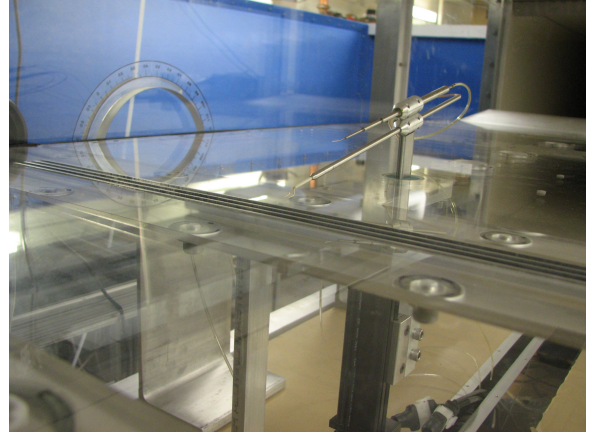
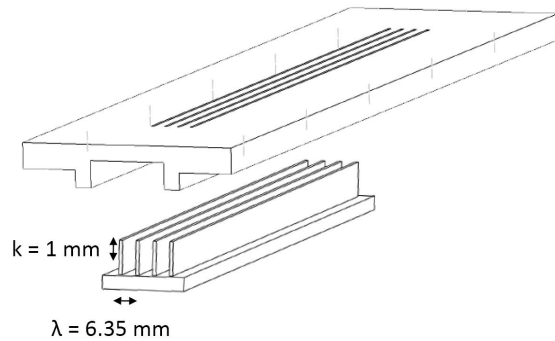


Figure 2.5: (Left) A schematic of the arrangement roughness elements attached to their base and the corresponding slots in the acrylic insert to the flat plate, through which the roughness elements can pass. (Right) The roughness elements viewed from above the plate, showing the traverse for the hotwire probe holder as well as the armature supporting the roughness patch, visible through the acrylic plate.

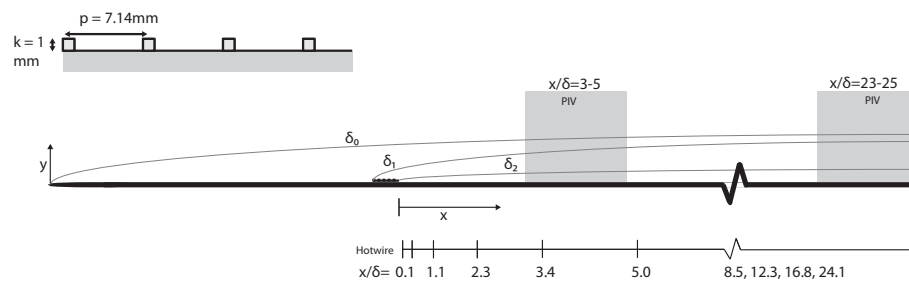


Figure 2.6: A schematic of the arrangement of the flat plate, the roughness strip, and the diagnostic locations; not to scale. The internal layers are also marked in order to provide an idea of their relative sizes and development rates.

roughness and was designed to maximize the roughness-type behavior. For larger ratios of  $p/k$ , the roughness elements would appear as separate and independent obstacles as opposed to members of a patch of roughness, since the flow would have room to reattach downstream of each element, prior to encountering its neighbor. For smaller ratios, the magnitude of the obstacle-effect of the roughness on the flow decreases as the reattachment process is cut progressively shorter.

The roughness elements themselves were machined aluminum, fitted into an aluminum base. The acrylic insert to the flat plate was sanded to allow the roughness elements to pass through the slots in the plate smoothly, while avoiding any cross-flow between the upper and lower sides of the plate. The tightness of the fit was verified by filling the upper side of the plate with dry ice and observing that the distinctively tinted vapor was contained and did not sink through any open areas in the slots.

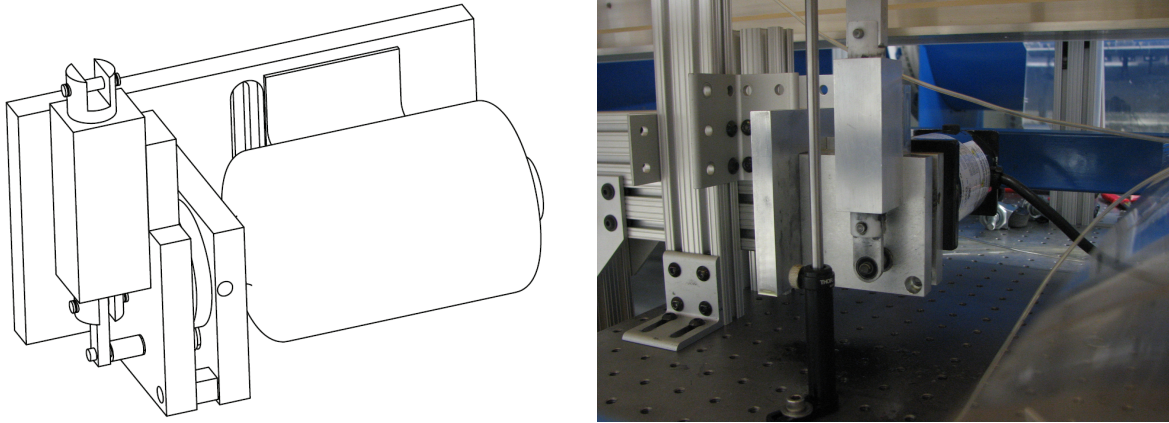


Figure 2.7: (Left) A line-drawing of the motor assembly, where the crankshaft and piston are shown on the left-hand side, separated by the gear assembly from the motor on the right-hand side. (Right) The motor assembly, *in situ*, in roughly the same orientation, but with the roughness armature attached to the end of the piston

## 2.6 Dynamic Actuation and Phase-Locked Measurements

Besides positioning the roughness in a fixed or static orientation, the armature of the roughness patch allowed for actuation of the roughness elements dynamically, between their being flush with the surface of the plate, and an adjustable maximum amplitude. The armature supporting the base of the roughness elements was connected, beneath the test section, to a piston and crankshaft assembly, which in turn was powered by a DC motor (Dayton 4z142, 1/27 hp 1800 rpm), illustrated in figure 2.7. The amplitude of the reciprocating motion of the roughness elements was therefore set by the offset of the connecting rod to the center of the shaft. This offset was fixed nominally at 1 mm, anticipating some small amount of slippage due to wear, such that the actual displacement of the roughness elements (from TDC to BDC) was approximately  $k = 1.64$  mm. The root-mean-square height for a periodic motion with this maximum amplitude was therefore  $k_{rms} = 1.16$  mm, which approximately matched the previously reported case of static roughness elements, which had  $k = 1.0$  mm. This matching was obtained in order that the degree of time-averaged blockage between the case of static roughness elements and dynamically actuated elements was roughly the same. (Alternatively, the maximum amplitude could have been matched to achieve a common instantaneous ‘impulsive’ strength of the perturbation in the wall-normal direction.)

In order to measure the precise location of the roughness armature, a magnetic linear encoder (Renishaw LM10) with  $1 \mu\text{m}$  spatial resolution was affixed to the roughness armature. The quadrature-encoding was then performed using the 250 MHz internal counter in the National Instruments DAQ, by which the precise, directional motional of the armature was resolved in Labview. The encoder signal was then sampled simultaneously with the anemometer signals at 60 kHz in order to allow for phase-locked sampling of the anemometer signals by using the reference encoder

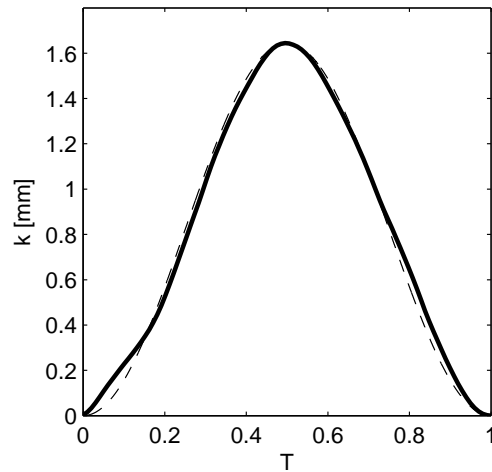


Figure 2.8: An average period,  $T$ , of the encoder signal, measured by ensemble averaging the mean displacements from each phase of a phase-locked decomposition. — encoder phase-locked signal; - - undistorted sinusoid

signal. An average period of the peak height of the roughness elements is shown in figure 2.8, where a height of 0 represents the elements being flush with the remainder of the flat plate, and a positive displacement is the height above the plate. The oscillation was not perfectly sinusoidal due to slippage and frictional nonuniformities in the slots through which the armature reciprocated, although the deviations appear quite small.

The actual phase-locking was performed as a postprocessing step, in order to account for any slight drift in the operating frequency of the motor over the course of a signal measurement. The peaks and troughs of the encoder signal were detected, by peak-finding procedures assisted by least-squares cosine fitting of the measurements. After identifying each period of the encoder signal, the periods were divided into a fixed number of blocks, representing the different composite portions of a single period. Ultimately, the blocks were ensemble-averaged across all of the periods in order to yield phase-locked mean velocity information. This phase-locking could have been carried out independent of the encoder signal (without determining the absolute position of the roughness elements) by ignoring any small deviations in the operating frequency of the dynamic actuation. This latter method was, in fact, applied to the PIV measurements. But, by locking to the encoder signal in the hotwire measurements, the relative phase information between the input perturbation and velocity measurements at different streamwise locations was preserved.

## Chapter 3

# The Impulsive Static-Roughness Perturbation

### 3.1 The Static Impulse Experiment

For the static-roughness study, the two-dimensional roughness array was used to perturb the turbulent boundary layer following the approach of Andreopoulos and Wood [1982], and the downstream response of the flow field was interrogated by hotwire anemometry and particle-image velocimetry. The effect of the perturbation on the mean flow properties (§3.1.1) is considered first, in comparison to the unperturbed boundary layer, with particular emphasis on the development of internal layers (§3.1.2). The static roughness impulse also affects the turbulent statistics of the flow (§3.1.3), which in turn can be viewed through the prism of the spectral distribution of turbulent energy (§3.1.4). Finally, the structural effect of the roughness perturbation on the distribution of coherent velocity structures in the flow is analyzed (§3.1.5) in order to ground the statistical observations in a physical understanding of the flow field. Significant portions of the following experiment were first reported in Jacobi and McKeon [2011a].

#### 3.1.1 Mean Flow Properties

The essential flow properties for both the hotwire and PIV rounds of experiments are summarized in table 3.1, and some key features of the flow field are described below. As noted previously, the boundary layer growth of the unperturbed flow indicates a virtual origin for the turbulent boundary layer 0.66 m upstream of the roughness impulse location (figure 3.1).

The friction velocity  $u_\tau$  for the unperturbed flow was estimated by the Clauser method (3.1) with  $\Delta U = 0$

$$\frac{U}{u_\tau} = \kappa^{-1} \ln \frac{yu_\tau}{\nu} + C - \frac{\Delta U}{u_\tau} = \kappa^{-1} \ln \frac{y}{z_0} \quad (3.1)$$

	$x$ (cm)	$U_\infty$ (m s <sup>-1</sup> )	$\delta$ (mm)	$\theta$ (mm)	$Re_\theta$ $= U\theta/\nu$	$Re_\tau$ $= u_\tau\delta/\nu$
Unperturbed	0.50 (7.4)	20.16 (20.60)	17.0 (17.6)	2.1 (1.9)	2770 (2560)	910 (970)
	58.0 (62.4)	20.09 (20.42)	24.1 (25.8)	3.1 (2.9)	4070 (3870)	1200 (1320)
Perturbed	0.25 (7.4)	20.20 (20.65)	17.2 (18.4)	2.1 (2.2)	2770 (2970)	
	58.0 (62.4)	20.07 (20.50)	24.4 (26.7)	3.3 (3.1)	4330 (4150)	

Table 3.1: Mean flow properties at streamwise extrema of sampling area for hotwire (PIV)

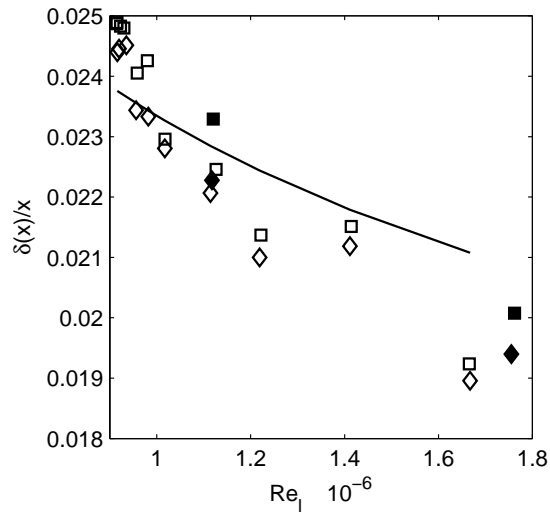


Figure 3.1: The development of the unperturbed and perturbed boundary layers, from the hotwire and from the PIV. The Reynolds number based on downstream distance has been corrected to reflect the approximate location of the virtual origin. For the hotwire:  $\diamond$  unperturbed;  $\square$  perturbed; and for the PIV:  $\blacklozenge$  unperturbed;  $\blacksquare$  perturbed; —  $\delta(x)/x = (Re_x)^{-1/5}$

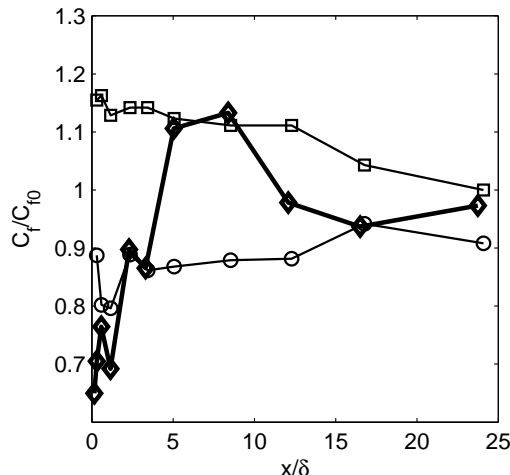


Figure 3.2: The development of the unperturbed and perturbed friction coefficients, from the hotwire. The coefficient derived from the first velocity value measured nearest the wall provides a rather smooth curve, in the unperturbed flow, consistent with the value inferred by Clauser’s method, and in the perturbed case, the overshoot in the recovery of  $C_f$  is observed.  $\circ$  unperturbed  $2\nu/U\partial U/\partial y(0)$ ;  $\square$  unperturbed Clauser method;  $\diamond$  perturbed  $2\nu/U\partial U/\partial y(0)$ . The overshoot and recovery trends are consistent with those observed in previous studies.

and also independently verified by the momentum integral approach; this method was also applied for the perturbed case, employing the roughness function  $\Delta U$ . However, for the perturbed case, neither method strictly applies, due to the non-equilibrium conditions downstream of the perturbation. Therefore, in addition to these inferential techniques, the friction velocity is also reported directly by linear fit using the no-slip condition and the first velocity measurement nearest the wall (which occurs at  $y^+ \approx 3 - 7$ ), although here too the result is suspect since the linear profile is not strictly applicable this far out, in addition to the uncertainty in the wall position which can significantly affect the value of the slope of the velocity profile. Using this technique, the perturbed flow is seen to demonstrate a reduction in  $C_f$  immediately downstream of the roughness strip, and then an overshoot in the recovery, similar to the report by Pearson et al. [1997], and characteristic of a non-linear component of the response to the perturbation (figure 3.2). Since each of these techniques suffers from significant sources of uncertainty, scaling throughout the remaining results is accomplished in terms of outer variables or in terms of the inner scales corresponding to the unperturbed case only.

The mean velocity profiles for the unperturbed and perturbed flow were recorded both by hotwire and PIV, and are shown above in figure 2.4 with validation to previous experiments. Here, the mean velocity profiles are compared between the perturbed and unperturbed flows in figure 3.3. Immediately downstream of the perturbation, there is a significant velocity deficit, particularly for  $y/\delta < 0.3-0.4$ , which corresponds to about 6 times the roughness height  $k$ . This deficit persists until approximately  $15 \delta$  downstream of the trailing edge of the perturbation. There appears to be

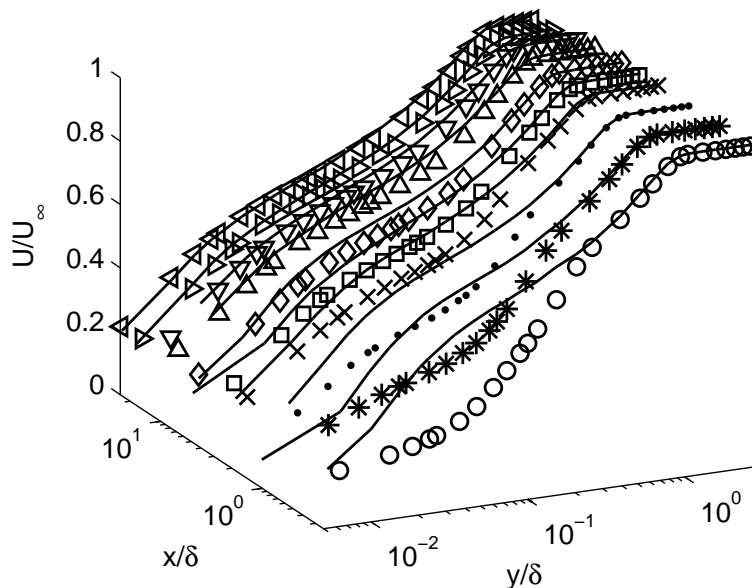


Figure 3.3: The mean velocity profile, in outer units, for the perturbed flow, in symbols. Perturbed:  $x/\delta = 0.3 \circ$ ;  $0.6 *$ ;  $1.1 \cdot$ ;  $2.3 \times$ ;  $3.3 \square$ ;  $5.0 \diamond$ ;  $8.4 \triangle$ ;  $12.1 \nabla$ ;  $16.5 \triangleright$ ;  $23.7 \triangleleft$ ; — for profiles of the unperturbed flow at corresponding streamwise positions

a persistent, albeit small, velocity deficit even farther downstream and across the velocity profile, consistent with the results of Andreopoulos and Wood [1982].

By plotting the discrepancy in the mean velocity profiles between the perturbed and unperturbed cases,

$$\Delta \frac{U}{U_\infty}(x, y) = \frac{U}{U_\infty}(x, y)_{\text{perturbed}} - \frac{U}{U_\infty}(x, y)_{\text{unperturbed}}, \quad (3.2)$$

as a contour map in wall-normal and streamwise directions, the recovery behavior of the mean velocity profile can be seen quite clearly (figure 3.4). The ‘growth rate’ of the peak of the velocity discrepancy can also be plotted as a means of estimating the rate at which the discrepancy moves away from the wall (while simultaneously decreasing in magnitude).

From the mean velocity profiles, the major relaxation of the perturbed flow appears to occur over a distance on the order of  $10 \delta$ , although even then the relaxation is not complete. The noise in the wall shear stress result precludes drawing a conclusion about the rate of its relaxation.

### 3.1.2 Internal Layers

The internal layers, marked  $\delta_1$  and  $\delta_2$  in figure 2.6, represent the mean extent to which different boundary conditions have influenced the flow. Andreopoulos and Wood [1982], following prior theoretical work, sought to identify the boundaries of the internal layers and measure their growth as a function of the strength of the perturbations due to the roughness patch, a quantity measured

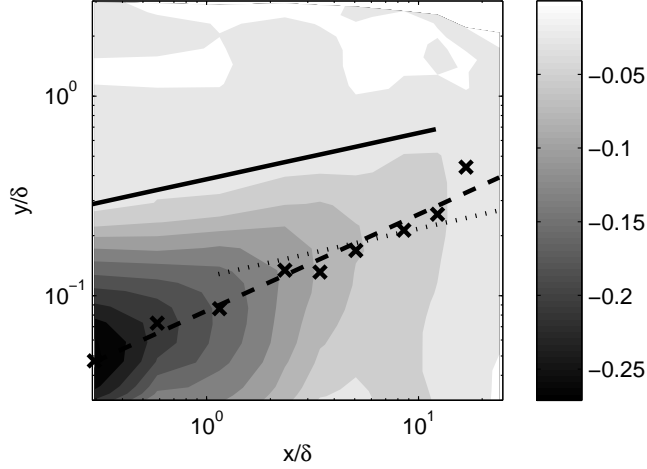


Figure 3.4: The discrepancy in the mean velocity profiles between the perturbed and unperturbed cases is shown in gray contours; the peaks for each streamwise location at which the velocity discrepancy is greatest are marked ( $\times$ ) and a curve is fitted by least squares ( $-$ ,  $y/\delta = 0.1(x/\delta)^{0.5}$ ). The approximate intercept for the fit is just below the height of the roughness elements:  $0.05y/\delta = 0.83k$ . Also, internal layer best fits, calculated below, are included ( $-$ ,  $\delta_1/\delta = 0.4(x/\delta)^{0.2}$ ;  $\cdots$ ,  $\delta_2/\delta = 0.1(x/\delta)^{0.2}$ ) for reference

by the logarithmic difference between the two roughness heights,  $z_{0i}$ , associated with each transition,  $S \rightarrow R$  and  $R \rightarrow S$ .  $z_{01}$  represents the incoming, unperturbed flow,  $z_{03}$  the flow far downstream of the perturbation, and  $z_{02}$  the flow over the impulse itself. In order to measure the roughness height, Clauser's formulation (3.1) can be rewritten assuming that the near wall velocity profile scales on that height, as (3.3).

$$z_0 = \frac{\nu}{u_\tau} \exp[-\kappa(C - \Delta U/u_\tau)] \quad (3.3)$$

It follows that the roughness scale of the incoming flow,  $z_{01}$  is simply  $z_{01} = \frac{\nu}{u_\tau} \exp[-\kappa C] \approx 0.0026$  mm since there is no velocity deficit there. The roughness function  $\Delta U/u_\tau$  can then be measured experimentally by simple subtraction of the experimental profile, in the physical region of the logarithmic layer for the unperturbed flow, from the logarithmic fit, using  $\kappa = 0.41$  and  $C = 4.9$  (following Andreopoulos and Wood [1982] for consistency). Far downstream,  $\Delta U/u_\tau \approx 0.31$  and thus  $z_{03} \approx 0.0028$  mm for the roughness height downstream of the impulse. Although no data were collected over the elements themselves, using the downstream position nearest to the impulse yields  $\Delta U/u_\tau \approx 4.12$  and  $z_{02} \approx 0.014$  mm. Thus the strength of the impulse can be estimated by  $M_{S \rightarrow R} = \ln\left[\frac{z_{01}}{z_{02}}\right] \approx -1.7$  and  $M_{R \rightarrow S} = \ln\left[\frac{z_{02}}{z_{03}}\right] \approx 1.6$ . Antonia and Luxton [1971a] reported  $M_{S \rightarrow R} = -4.6$  and  $M_{R \rightarrow S} = 5.8$ ; Andreopoulos and Wood [1982] reported  $M_{S \rightarrow R} = -3.67$  and  $M_{R \rightarrow S} = 4.34$  (although it is worth noting that there appears to be a sign error in their results which, if corrected, would result in  $M_{R \rightarrow S} = 2.86$ ). The smooth to rough transition is expected to have a stronger roughness step,

since the corresponding velocity deficit should be greater than the velocity deficit once recovery is underway downstream; this expectation is met by both the current results and the corrected results from Andreopoulos and Wood [1982]; Antonia and Luxton [1972] do not formally report their rough-to-smooth step strength, but a value for their study is reported by Andreopoulos and Wood [1982] (but perhaps with the same sign error?) which is not amenable to simple correction.

The calculations of impulse strength are ultimately unreliable, however, both because of the nonequilibrium nature of the flow, which in principle renders much of this analysis unjustified in a general sense and also in this particular experiment, the logarithmic region of the velocity profile is quite small (only 2–4 data points) except very far downstream, so there is a significant challenge in fitting both of the open parameters in the log law simultaneously (and for the above analysis, the value of  $u_\tau$  was fixed to the smooth wall value, exposing further uncertainty). However, similar trouble beset previous results also, so at least for comparative purposes these values are instructive in indicating that the steps are comparable between experiments. Also, the general trend that the  $S \rightarrow R$  transition is more abrupt than the  $R \rightarrow S$  transition indicates that the  $R \rightarrow S$  nonequilibrium condition should persist farther downstream, in terms of the extent of influence of the perturbation on the flow, since the abrupt transition will equilibrate more quickly.

As described above, the internal layers represent precisely this extent of the influence of the new boundary condition on its neighboring flow, in the mean sense. There are two methods for ascertaining the location of the internal layer: Andreopoulos and Wood [1982] employed streamwise differentiation of successive mean velocity profiles to identify regions of the profile which indicate the existence of a finite layer by virtue of their streamwise constancy; Antonia and Luxton [1971b] proposed, by dimensional argument, that the form of the velocity profile which emphasizes the functional dependence of the velocity gradient on the local wall shear stress must scale the mean velocity profile as  $y^{1/2}$ . By plotting successive profiles of the mean velocity profile in that scaling, kinks appear in the profile which naturally correspond to the boundaries of different internal layers, and can be identified by visual inspection. Neither of these methods is wholly adequate, due to numerical noise in the differentiation step in the former, and the somewhat subjective identification procedure for ‘kinks’ in the latter, but both methods tend to converge and thus reinforce a reasonably clear picture of the internal layer development.

The internal layer development can be scaled on the corresponding roughness scales developed above or alternatively can be scaled on the standard outer scaling for the boundary layer as a whole (figure 3.5), where a line is fitted by least-squares regression to a power law model. Previous studies reported using the roughness scaling to identify three distinct regimes for the growth of the internal layers; in the current study it appears that perhaps two distinct regions can be identified, but not with high confidence.

The internal layer growth can also be measured dimensionally (without scaling), and it is found

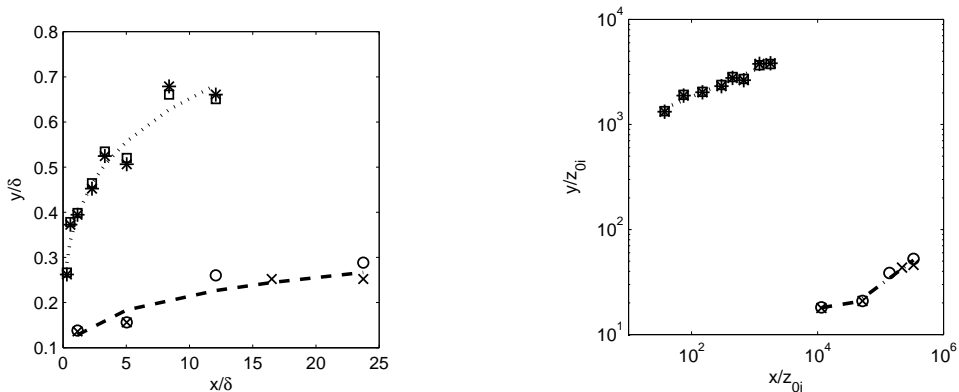


Figure 3.5: The development of the internal layers, calculated by both methods described above. (Left) Plot and fit in outer units. For  $\delta_1$ :  $\square$  via  $y^{1/2}$ -scaling;  $*$  via  $\partial U/\partial x$ ; for  $\delta_2$ :  $\circ$  via  $y^{1/2}$ -scaling;  $\times$  via  $\partial U/\partial x$ ; least squares best fits:  $\cdots$   $\delta_1/\delta = 0.4(x/\delta)^{0.2}$ ;  $- -$   $\delta_2/\delta = 0.1(x/\delta)^{0.2}$ ; (Right) Scaled by the appropriate estimated roughness scales,  $z_{0i}$ . In this case, two distinct slopes are identified for the second internal layer, the first significantly shallower, persists for  $x < 5\delta$  at which point the layer begins to grow more quickly (although the first slope is only a pair of points) and is fit by  $\delta_2/z_{03} = 7.2(x/z_{03})^{0.1}$ ; the latter  $\delta_2/z_{03} = 0.2(x/z_{03})^{0.5}$ ; the first internal layer is fit by  $\delta_1/z_{02} = 570(x/z_{02})^{0.3}$ .

that  $\delta_1 \sim x^{0.3}$  and  $\delta_2 \sim x^{0.1}$ , such that the exponent of the dimensional growth rate for the second internal layer is approximately half that of the first internal layer, consistent with the findings of Antonia and Luxton [1971a] and Antonia and Luxton [1972], who reported growth rates of  $\delta_1 \sim x^{0.7}$  and  $\delta_2 \sim x^{0.4}$ .

It is worth noting that for the outer-scaled internal layer growth, Pearson et al. [1997] also observed roughly the same exponents for the two internal layer boundaries,  $\delta_1/\delta \sim (x/\delta)^{0.15}$  and  $\delta_2/\delta \sim (x/\delta)^{0.17}$ . So, although the scaling on roughness height does not appear to produce the trends previously reported, the outer scaling appears to collapse both internal layers to the same power such that they are distinguished only by a multiplicative constant, suggesting that the traditional outer scaling is not only more reliably measured, but potentially more instructive.

The second internal layer (representing the  $R \rightarrow S$  transition) does not appear to approach the edge of the boundary layer at all; rather it persists at an intermediate height, near the edge of the inner layer, for all of the streamwise recording positions. This behavior is consistent with the observation above that the  $R \rightarrow S$  transition is less abrupt, along with the findings of previous experimenters.

The least squares fit for the evolution of the first internal layer, which represents the abrupt  $S \rightarrow R$  transition, can be plotted to overlay the velocity discrepancy contour map (figure 3.4) where it appears to trace out the far edge of the velocity deficit. This coincidence is expected, since the first internal layer represents the introduction of the velocity deficit into the flow field via the blockage effect of the first two-dimensional roughness elements on the incoming flow. The reduction of the

blockage, at the  $R \rightarrow S$  transition, does not manifest itself in the mean velocity discrepancy map due to its lack of abruptness. A final observation about the growth of the internal layers is that the layer thicknesses grow, on average, faster than the mean boundary layer thickness itself (as seen through the outer-scaled plots), and thus distortions in the velocity field and gradients within the internal layers are anticipated, and will be explored in the following section.

### 3.1.3 Turbulence Statistics

Turbulence statistics were calculated in the streamwise direction from the hotwire, along with some measurements from the PIV for validation (although the wall-normal range of the PIV was insufficient to reach the near-wall peak and was primarily aimed at the region of flow at or above the height of the roughness elements themselves). The hotwire results tend to underestimate the turbulence intensity for  $y^+ < 200$  which is approximately the edge of the inner layer, compared with the results of DeGraaff and Eaton [2000] in figure 2.4, as expected based on the high value of  $l^+$ . The PIV suffered a similar drop in turbulence intensity as it approached the inner layer, likely due to spatial smoothing over the intense gradients in this near-wall region. However, as mentioned above, the remainder of the study is purely comparative between the unperturbed base flow and the perturbed flow field, so the underestimate of the near-wall peak should not be significant.

Successive profiles of the streamwise turbulence intensity (not shown) indicate a large ‘hump’ in the profile, which, in uniformly rough walls, is usually associated with differences in near-wall transport due to the influence of the roughness. The ‘hump’ is centered at  $y = 0.08 \delta = 1.3 k$  immediately downstream of the roughness but evolves throughout the downstream flow field. As with the velocity discrepancy contours, the discrepancy in the streamwise turbulence intensity profiles between the perturbed and unperturbed cases,

$$\Delta \frac{\sqrt{u^2(y)}}{U_\infty}(x, y) = \frac{\sqrt{u^2(y)}}{U_\infty}(x, y)_{perturbed} - \frac{\sqrt{u^2(y)}}{U_\infty}(x, y)_{unperturbed}, \quad (3.4)$$

can be viewed as a contour map in wall-normal and streamwise directions in order to visualize the recovery behavior of the flow field (figure 3.6).

In this case, the peaks correspond to the ‘hump’ visible in the individual profiles; however, the contour plot makes clear that this ‘hump’ moves away from the wall as it decreases in magnitude, and the rate of that progression is faster than the growth rate of either of the two internal layers, meaning that the internal layers represent a quantity which is not simply related to the transport processes due to the roughness surface condition. Indeed, the fact that the maxima of the ‘hump’ reside outside the second internal layer,  $\delta_2$ , was already identified by Andreopoulos and Wood [1982] as signifying that the flow is not merely a linear superposition of individual  $S \rightarrow R$  and  $R \rightarrow S$  transitions, in which case the peaks in second-order statistics would occur at  $y = \delta_2$ .

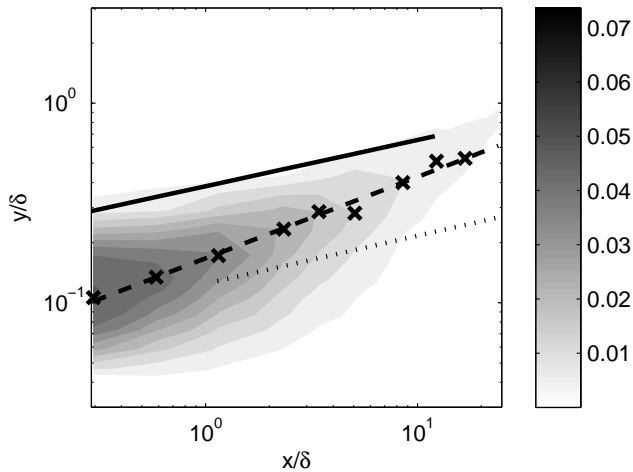


Figure 3.6: The discrepancy in the streamwise turbulence intensity profiles between the perturbed and unperturbed cases is shown in gray contours; the peaks for each streamwise location at which the discrepancy is greatest are marked ( $\times$ ) and a curve is fitted by least squares ( $—$ ,  $y/\delta = 0.2(x/\delta)^{0.4}$ ). Unlike the mean profile map (figure 3.4), the approximate intercept for the fit is above the height of the roughness elements:  $0.10\delta = 1.67k$ . And again, the internal layer boundary best fits, calculated above, are included for comparison.

The successive profiles of the third-order streamwise moment of  $u(y, t)$ , also show a positive bulge at roughly the height of the roughness elements, along with a corresponding negative bulge at  $y = 0.16 \delta = 2.7 k$ . Plotting the discrepancy map again (figure 3.7) shows that the negative bulge roughly coincides with the region between the two internal layers – the region which was directly influenced by contact with the roughness strip. Overlaying the peak of  $\sqrt{u^2(y)}$  from figure 3.6, however, shows that this peak value tracks the sign change in the third-order moment — and is thus outside of the edge of the second internal layer — as implied by the observation of Andreopoulos and Wood [1982] that the advection and  $V$  are both zero in this region. Using the third-order moment discrepancy plot is thus only a rough indicator of the location of the internal layers, but the physical intuition provided is likely still useful. Since the third-order moment can be interpreted as expressing a flux of streamwise kinetic energy (writing  $\overline{u^3} \sim \overline{uu^2}$ ), the negative bulge then represents deceleration between the boundaries of the internal layers, and it captures this region much more precisely than merely the deficit in the mean velocity profile itself. From the PIV measurements, discrepancy maps for the Reynolds stress at two streamwise locations were measured (figure 3.8); consistent with Andreopoulos and Wood [1982], they indicate that the internal layers also manifest themselves clearly in mixed moments. However, as should be clear from the above analysis, these moments are not necessary for characterizing to a significant degree the development of the internal layers, and the spatial resolution limitations of both the PIV and cross-wires present a significant disadvantage when characterizing the near-wall cycle.

Andreopoulos and Wood [1982] observed similar trends, although in a region farther from the

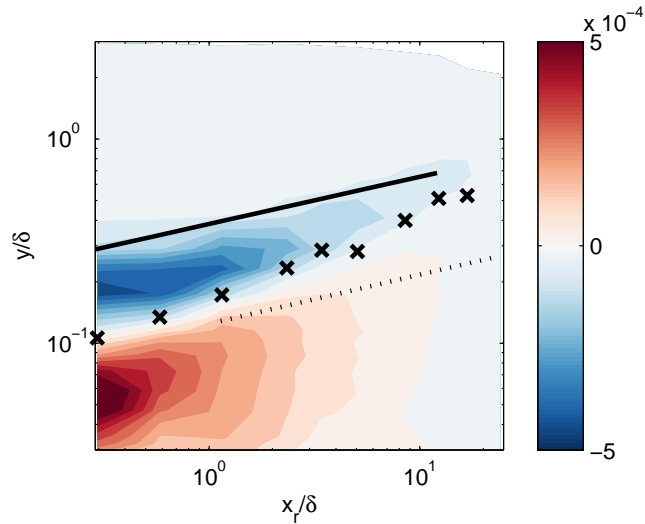


Figure 3.7: The discrepancy in the streamwise third-order moment profiles between the perturbed and unperturbed cases, in red(+) and blue(-) contours. The least squares fit of the internal layer boundaries are shown:  $\cdots$ ,  $\delta_2/\delta = 0.1(x/\delta)^{0.2}$ ;  $—$ ,  $\cdots$ ,  $\delta_1/\delta = 0.4(x/\delta)^{0.2}$ . Also shown are the locations of maximum discrepancies in streamwise turbulence intensity ( $\times$ ) from figure 3.6.

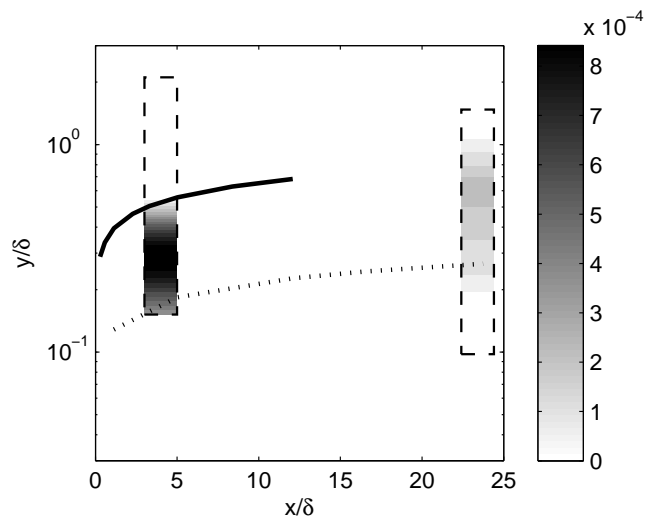


Figure 3.8: The discrepancy in the streamwise Reynolds stress profiles,  $-\overline{uv}(y)/U_\infty^2$ , between the perturbed and unperturbed cases, from the two PIV measurement locations. The least squares fit of the internal layer boundaries are shown:  $\cdots$ ,  $\delta_2/\delta = 0.1(x/\delta)^{0.2}$ ;  $—$ ,  $\cdots$ ,  $\delta_1/\delta = 0.4(x/\delta)^{0.2}$ . Note that the deficit in Reynolds stress corresponds closely to the region between the two layer edges.

wall. They noted that the hump observed in the turbulence intensity plots recalls similar behavior in the experiments of Smits et al. [1979], wherein a flow was perturbed by an impulse of curvature in the form of an abrupt concave or convex bend in an otherwise flat flow field. For the concave bend, the shear stress was observed to increase significantly in the short distance of the curvature impulse, and the peak of this increase shear propagated outward as a ‘stress bore’. Similarly, a bore in the turbulence intensity was observed to propagate outward, and it was noted that this evolution of the bore was a consequence of both turbulent transport and interactions between the mean shear and local processes. Considering the possibility that the bore dynamics are biased towards influence from the mean shear throughout the boundary layer, then the observed ‘hump’ in the turbulence intensity plots, which varies with streamwise position downstream of the perturbation, should be scalable by a quantity related to the mean velocity gradient,  $u_s$  (3.5), which represents the continued influence of the near-wall perturbation even farther from the wall.

$$u_s = \sqrt{\left(U_\infty \delta \frac{\partial U}{\partial y}\right)} \quad (3.5)$$

Under this scaling (figure 3.9) the ‘hump’ of the  $\sqrt{u^2(y)}$  does collapse at all streamwise locations. This collapse indicates that the ‘hump’ observed in the present study can be considered as a manifestation of the ‘stress bore’ in the sense outlined in Smits et al. [1979]. By applying the discrepancy map approach to this mean velocity gradient scaling,  $u_s$ , defined in equation 3.6, the physical region occupied by the stress bore can be identified visually.

$$\Delta \left(U_\infty \delta \frac{\partial U}{\partial y}\right)^{1/2} = \left(U_\infty \delta \frac{\partial U}{\partial y}\right)_{perturbed}^{1/2} - \left(U_\infty \delta \frac{\partial U}{\partial y}\right)_{unperturbed}^{1/2} \quad (3.6)$$

The discrepancy map (figure 3.10) immediately shows that, in a rough sense, the stress bore is identical to the region between the boundaries of the two internal layers. Thus, both the deceleration bulge of the third-order moment  $\sqrt[3]{u^3(y)}$  and the surplus bulge in  $u_s$  provide two physically motivated and robust ways of locating the boundaries of the internal layers, and thereby identifying the region of downstream flow under the influence of an impulsive perturbation. In particular, the fact that the positive bulge in the discrepancy map for  $u_s$  neatly demarcates the region between the edges of the two internal layers shows that the ‘stress bore’ analogy is powerfully descriptive – there is, indeed, an identifiable and persistent ‘bore’ of shear stress implanted in the downstream flow by the impulsive perturbation.

From a different perspective, roughness is understood to affect the local scale sizes in a flow, so another approach to identifying regions of the flow field influenced by the roughness impulse is to look for regions in which scale sizes vary from the corresponding smooth wall flow. The integral time scale, which is a scale characteristic of the largest scales in the flow, can be defined by the autocorrelation of the velocity time signal, and can be transformed via Taylor’s hypothesis into a

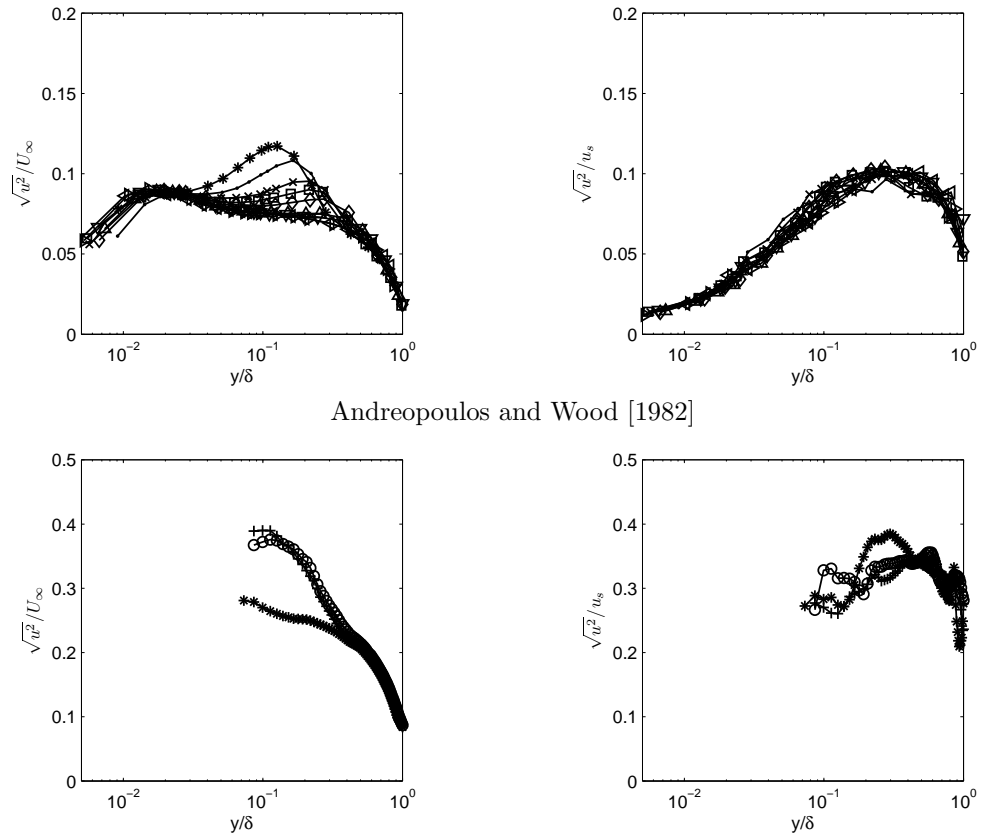


Figure 3.9: Top: The turbulence intensity for the perturbed flow under (Left) standard outer scaling; and (Right) under a velocity scaling based on the mean velocity gradient. Symbols follow figure 3.3. Note the collapse in the near-wall region,  $y/\delta < 0.2$ . Bottom: The results from Andreopoulos and Wood [1982] — the collapse is not as clean because of significant scatter in the  $\sqrt{u^2(y)}$  data and an insufficient number of streamwise locations.

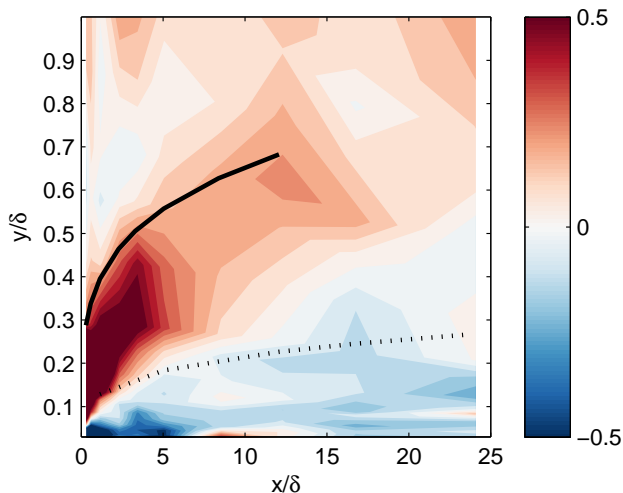


Figure 3.10: The discrepancy in the mean velocity gradient scale  $u_s$  between the unperturbed and perturbed flows (equation 3.6) overlaid with the the best fits of the two internal layer boundaries — symbols from figure 3.7. In this case, note that the surplus in shear stress corresponds precisely to the region between the boundaries of the two internal layers.

length scale; alternatively, it can be calculated from the streamwise energy spectrum (3.7).

$$\Lambda_L(x, y) = U(y) \int_0^\infty R_{11}(x, y, t) dt = \frac{2}{\pi} \lim_{k_x \rightarrow 0} \phi_x(k_x) \quad (3.7)$$

The integral scale at each wall-normal and streamwise location reveals the relative distribution of the largest scales in the flow field, under the unperturbed and perturbed boundary conditions. The wall-normal distribution in the unperturbed flow has a maximum around  $y/\delta \approx 0.1$  with a rapid decay ( $\Lambda_L \rightarrow 0$ ) at the wall and a slow decay ( $\Lambda_L \rightarrow 0.4\delta$ ) towards the edge of the boundary layer. The integral scales increase about 15% on average over the streamwise extent of the plate. The perturbed flow field shows a disruption of this distribution, as the size of the largest scales is depressed near the perturbation. A map of the ratio of these two sets of integral scales (figure 3.11) indicates that the integral scale in the perturbed case is as little as half the size of the unperturbed flow, in the immediate vicinity of the perturbation. However, in the region of flow between the mean boundaries of the two internal layers, there appears to be an increase in the size of the integral scales — this increase is even more prominent when the lengthscale is calculated by the spectral method. Antonia and Luxton [1971a] reported that integral lengthscales were significantly suppressed downstream of the  $S \rightarrow R$  transition, but inflated downstream of the  $R \rightarrow S$  transition, with the change occurring near the boundary of the internal layer in each case. However, their cases dealt with the transition from one equilibrium condition to another; for the impulsive disturbance, the  $R \rightarrow S$  transition should be only partial, since the rough condition was never fully established. Therefore the region of increase in the integral scales between the boundaries of the two internal layers reflects the displacement of

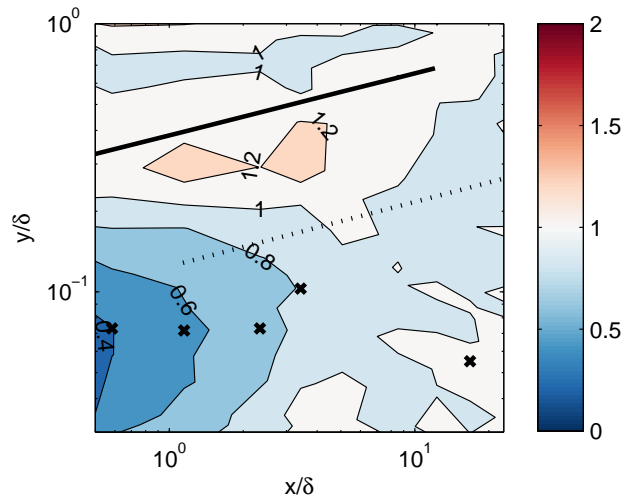


Figure 3.11: The ratio of the maps of integral scales for the perturbed flow to the smooth flow,  $\Lambda_L/\Lambda_{L_0}$  overlaid with the best fits for the two internal layer boundaries as in figure 3.7 and also  $\times$  for extrema (among wall-normal positions) at each streamwise location.

larger scales from near the wall to the outer flow, at the  $S \rightarrow R$  transition; then the smaller scales which began to develop over the roughness persist within the second internal layer, while the integral scales regrow, yielding the significant decrease in length-scales observed downstream near the wall

### 3.1.4 Composite Spectra

The individual temporal spectra from the time-series were transformed by Taylor’s hypothesis into spatial spectra in streamwise wavenumber,  $k_x$ . For the unperturbed case, these spectra were compared at a similar Reynolds number to the results of Erm and Joubert [1991] for validation (figure 3.12). Although there were some discrepancies in the validation, consistent with the underestimate in turbulence intensity near the wall reported above, the overall comparative analysis between perturbed and unperturbed flows remains unaffected. And as noted above, the friction velocity used in all the normalizations corresponds to the incoming unperturbed flow.

Composite premultiplied spectra can be assembled from contours of the individual  $1D$  spectra when arranged in wall-normal sequence. This procedure, explained in detail in Hutchins and Marusic [2007], provides a physical sense of the distribution of spectral energy when the composite spectra are viewed in logarithmic coordinates since equal energetic contributions appear as equal contour areas of the composite spectra at a given wall-normal distance. Considering first the smooth wall composite spectra, at the beginning and end of the test section (to view the maximum spread of  $Re_\theta = 2770\text{--}4070$ ) allows identification of a few key features (figure 3.13), including the inner peak  $\lambda_x^+ \approx 1000, y^+ \approx 25$  and the peak for very large scale motions (VLSM) at  $\lambda_x/\delta \approx 6$  as well as the large-scale motion (LSM) peak, common to all boundary layer flows, at  $\lambda_x/\delta \approx 3$  described in detail

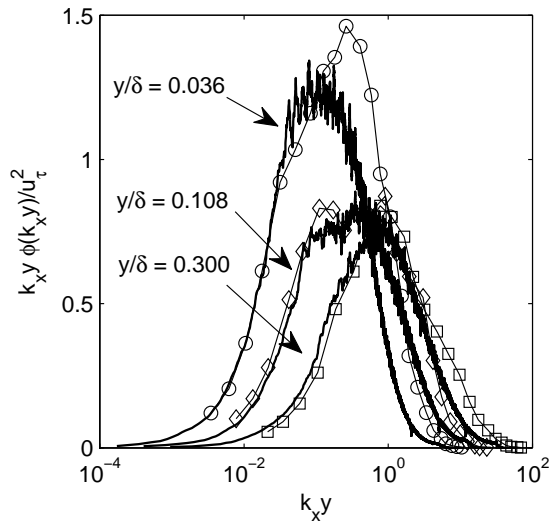


Figure 3.12: The premultiplied spectra of the smooth wall, in terms of streamwise wavenumber and wall-normal location. The current data, at the streamwise location corresponding to  $Re_\theta = 2840$ , —, at the wall-normal locations marked. For comparison, the results of Erm and Joubert [1991] at  $Re_\theta = 2810$ :  $\circ$   $y/\delta = 0.04$ ;  $\diamond$   $y/\delta = 0.10$ ;  $\square$   $y/\delta = 0.35$ . As noted above, the turbulence intensity near the wall tends to be underestimated, and that carries over in this context, where the energy in the small scales also tends to be suppressed slightly.

in Monty et al. [2009]. The LSM peak at  $\lambda_x/\delta \approx 3$  is quite prominent at both flow points, while the larger VLSM peak at  $\lambda_x/\delta \approx 6$  only begins to appear at the furthest downstream position (and even then its presence is subtle). The near-wall peak is quite distinct across a broad range of wavelengths; its location farther from the wall than other investigators found is a consequence of measurement error of the wall-normal location.

The composite spectra are produced for the perturbed flow at all of the downstream measurement locations in figures 3.14 and 3.15 (left column). Although the first few streamwise locations are situated in the immediate vicinity of the recirculation bubble downstream of the last roughness element, and thus the sense of the hotwire signals is not reliable, the abrupt change in the shape of the  $\sqrt{u^2(y)}$  profile which occurs between  $x/\delta = 0.1$  and  $x/\delta = 0.6$  indicates that  $x = 1.1 \delta = 18.3 \text{ k}$  is well outside of the mean recirculation region. Yet at this location there is still an unambiguous suppression of the near-wall peak, particularly at the higher wavelengths. This reduction in the energy of specifically larger scales is consistent with the decrease in the integral scale  $\Lambda_L$ , representing the largest significant scales in the flow, which was found in the immediate vicinity of the impulse. The recovery of the near-wall peak occurs much more quickly than the dissipation of the displaced spectral energy — located in the region of the ‘hump’ in the  $\sqrt{u^2(y)}$  profiles — implying that the timescale for the generation (or regeneration) of the near-wall cycle is significantly smaller than dissipative timescales in the flow. In addition, the dissipation of the displaced spectral energy is not uniform across wavelength space, rather the higher wavelengths dissipate first, leaving a strong

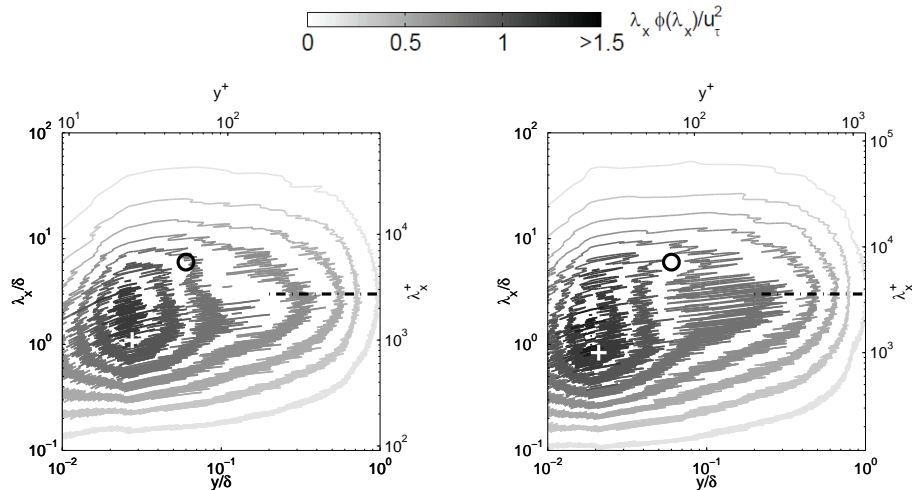


Figure 3.13: Composite spectra for the unperturbed case: (Left)  $Re_\theta = 2770$  The white ‘+’ marks the vicinity of the inner peak ( $\lambda_x^+ \approx 1000, y^+ \approx 25$ ), the black  $\circ$  marks the expected location of the VLSM peak at ( $\lambda_x/\delta \approx 6$ ), and  $\cdots$  marks the LSM peak along  $\lambda_x/\delta \approx 3$ ; (Right)  $Re_\theta = 4040$  with markings as in the left plot. Ten contour levels, equally spaced across the color bar, are indicated.

residual concentration of spectral energy around  $\lambda_x/\delta \approx 1-2$ , which then eventually dissipates far downstream, leaving only the natural LSM peak at  $\lambda_x/\delta \approx 3$ . This residual displaced energy can therefore be considered as an artificial enhancement to the natural LSM for boundary layers. On the right column of figures 3.14 and 3.15, discrepancy plots of the composite spectra were formed, as was done for the statistical quantities above, but with the additional subtlety that the wavelength spectra between the perturbed and unperturbed flows varied as a consequence of the use of Taylor’s hypothesis, and thus for comparison the unperturbed composite spectrum was regridded (by cubic interpolation) to the range of the perturbed spectrum, prior to the subtraction. The unperturbed composite spectra were reasonably robust in the streamwise direction thus making this sort of subtraction justifiable, at least for qualitative observations. These composite spectra discrepancy maps show clearly the suppression of the near-wall cycle and the displacement of that energy away from the wall.

The interruption of the near-wall cycle, with its quasi-streamwise vortices, was observed directly by Pearson et al. [1997] who were able to visualize the flow over the roughness strip itself. They reported a recovery of the ‘mushroom-like structures’ characteristic of the quasi-streamwise vortices about  $x \approx 0.15 \delta \approx 5 k$  downstream of the trailing edge of the roughness strip, which is somewhere downstream of any recirculation behind sandpaper-type roughness. Similarly, from the spectral maps above, it appears that the near-wall cycle does not begin to recover until well past the reattachment point for the two-dimensional roughness, indicating a minimum regeneration time for the cycle.

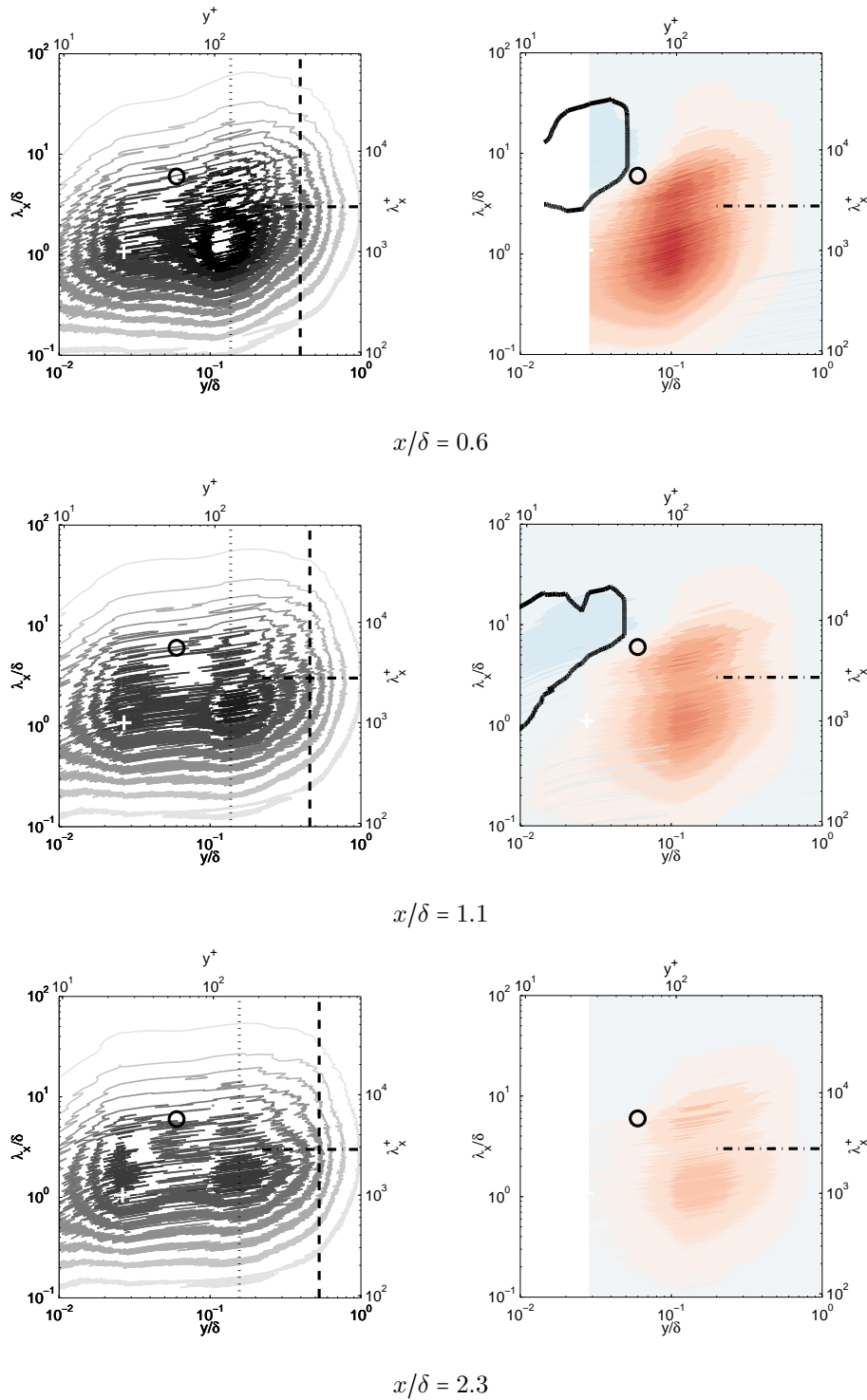


Figure 3.14: (Left) Composite spectra for the perturbed case: the first streamwise location,  $x = 0.1 \delta = 1.65 \text{ k}$ , is suspected to be within the mean recirculation bubble downstream of the last roughness element; therefore the third streamwise location  $x = 0.6 \delta = 10 \text{ k}$ , which appears to be downstream of the recirculation region, is shown first. (Right) The discrepancy maps for the composite spectra, with a range identical to the spectra themselves, but mirrored for negative values (red are positive, blue negative). The contour line represents a region of spectral content suppressed more than 5% below the unperturbed flow.

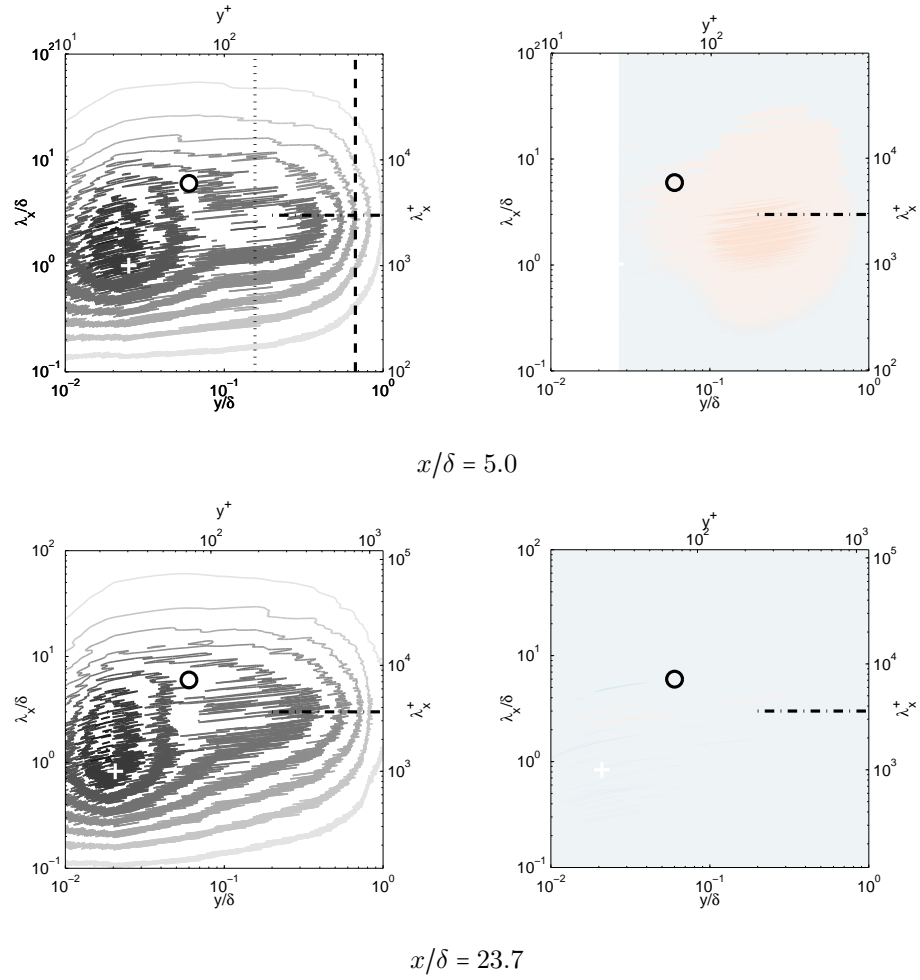


Figure 3.15: (Left) Composite spectra continued from figure 3.14 at additional downstream positions. (Right) Continuation of the discrepancy maps for the composite spectra

### 3.1.5 Swirling and Vortex Structure

Employing both velocity components in the wall-normal-streamwise plane, from the PIV measurements, allows identification of coherent swirling motions in the velocity field. A variety of measures of coherent swirling motion have been proposed over the years, from thresholding the magnitude of the vorticity field to a variety of functions of the velocity gradient tensor, reviewed by Jeong and Hussain [1995], but the ‘swirling strength’ has been widely adopted for its perceived robustness in identifying swirling motions without bias from shear in the flow. Swirling strength is defined using the magnitude of the imaginary eigenvalue from the local velocity gradient tensor,  $|\lambda_{ci}|$ , following Zhou et al. [1999], where the velocity gradient tensor is composed of the instantaneous velocity measurements, shown in equation 3.8. The naturally unsigned swirling strength can be assigned a directional sense by means of the local sign of the spanwise vorticity field. Negative swirl is referred to as prograde since it is consistent with the rotational sense of the mean shear; positive swirl is referred to as retrograde, following Wu and Christensen [2007]. The use of instantaneous velocity signals in the definition of swirling strength actually has significant implications for the interpretation of the relationship between coherent swirling motions and the mean velocity gradient, which will be explored briefly in chapter 4.

$$\lambda_{ci} = \frac{1}{2} \mathcal{J} \left( \sqrt{\left( \frac{\partial \hat{u}}{\partial x} + \frac{\partial \hat{v}}{\partial y} \right)^2 - 4 \left( \frac{\partial \hat{u}}{\partial x} \frac{\partial \hat{v}}{\partial y} - \frac{\partial \hat{u}}{\partial y} \frac{\partial \hat{v}}{\partial x} \right)} \right) \quad (3.8)$$

Two representative frames taken from the PIV results illuminate some of the differences in instantaneous swirl distribution (figure 3.16). In particular, an increase in the population of prograde vortex cores farther from the wall, in the vicinity of  $y/\delta = 0.2-0.3$  is readily apparent, as is a decrease in prograde cores very near the wall, although the bias of prograde against retrograde is a topic of ongoing investigation.

The swirling strength field can be averaged over time to produce a profile of the total swirling strength as a function of wall-normal distance (figure 3.17, left column). The perturbation appears to contribute to an increase in overall swirling at around  $y/\delta = 0.2-0.3$  at  $x/\delta \approx 4$ , with a bias towards the increase in prograde swirl. The integrals of the prograde and retrograde swirling profiles are calculated across the boundary layer and then normalized by the prograde integral for the upstream unperturbed flow (table 3.2, leftmost columns). The relatively constant values of the integrated swirl profiles suggest that total swirling is roughly conserved; any generation over the roughness elements, if it occurs, is presumably balanced by the disruption of the near-wall cycle, and the incoming swirling content is merely displaced and reorganized by the roughness impulse.

By using a thresholding criterion based on the mean swirl and the minimum resolvable vortex size, individual vortex cores were identified and counted in order to construct a parallel series of plots, where instead of total swirling strength, the average number of vortex cores per frame of the

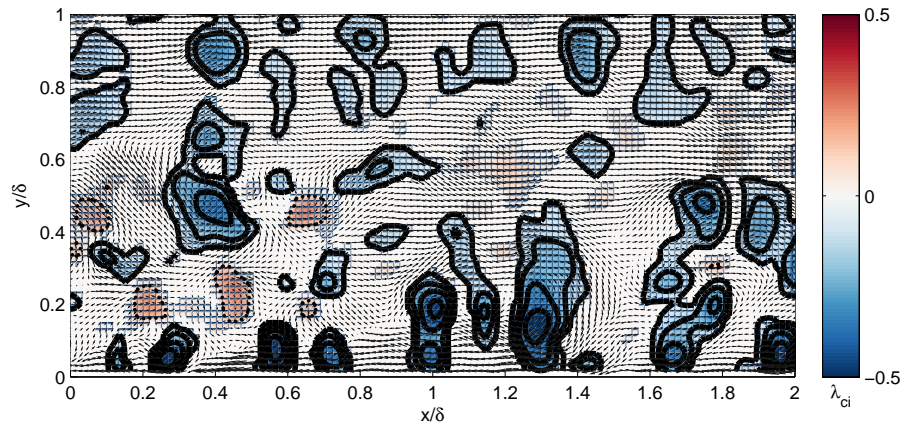
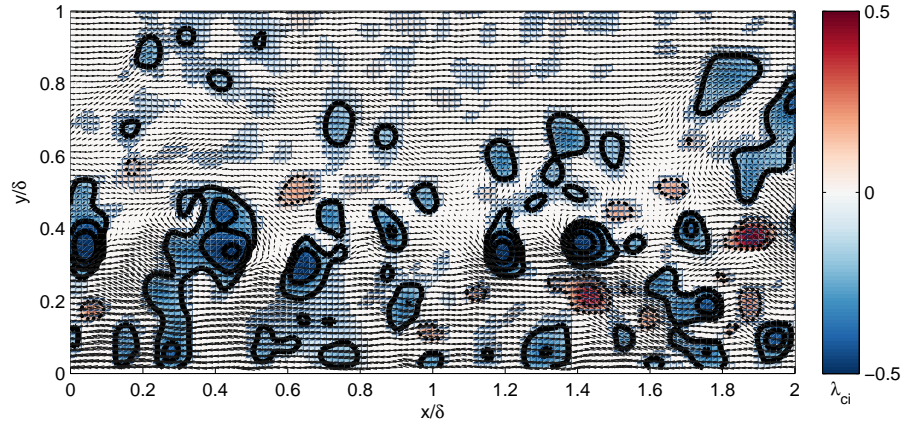
Unperturbed,  $x/\delta = 4.2$ Perturbed,  $x/\delta = 4.0$ 

Figure 3.16: The velocity field quivers from the PIV under a Galilean decomposition, where  $0.8 U$  has been subtracted off; the levels correspond to the swirl, calculated by the same decomposition; prograde in blue (solid lines), retrograde in red (dotted lines).

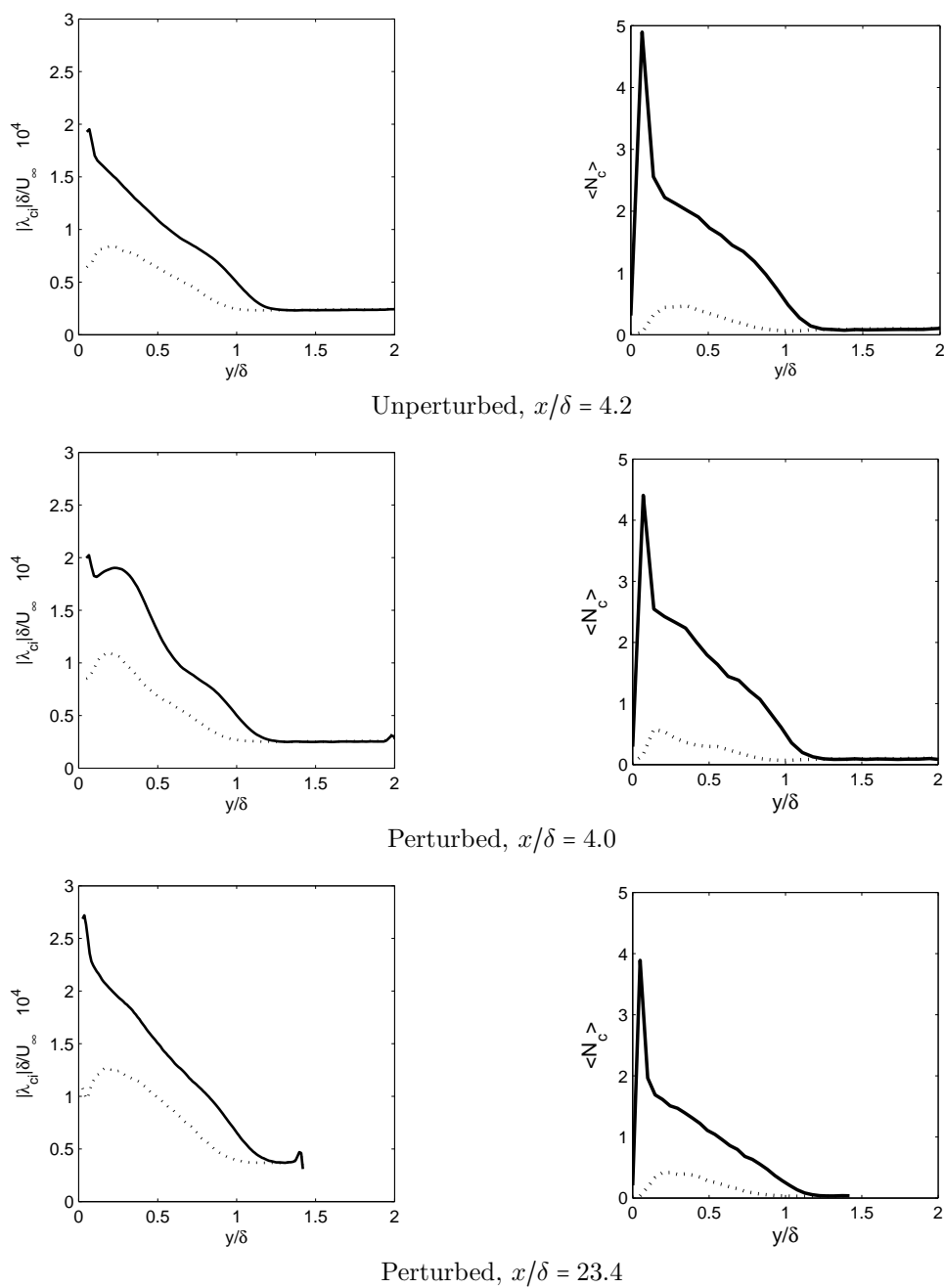


Figure 3.17: (Left) The profile of swirling strength, averaged in the streamwise direction across the PIV recording window in outer-scaling; (Right) the mean number of distinct vortex cores, per PIV frame, as a function of wall location. — prograde; ... retrograde

	Prograde Swirl	Retrograde Swirl	Prograde Cores	Retrograde Cores
Unperturbed, $x/\delta = 4.2$	<b>1.00</b>	0.61	<b>1.00</b>	0.18
Perturbed, $x/\delta = 4.0$	1.00	0.60	1.03	0.19
Perturbed, $x/\delta = 23.4$	1.02	0.63	0.91	0.17

Table 3.2: Integrated swirl profiles

PIV viewing field,  $\langle N_c \rangle$ , as a function of wall-normal distance are measured (figure 3.17, right column). The distribution of discrete cores shows a similar rise in core counts farther from the wall.

As with the aggregate swirl, the integrals of the prograde and retrograde mean core count profiles are calculated across the boundary layer and then normalized by the prograde integral for the upstream unperturbed flow (table 3.2, rightmost columns). The number of cores, like the aggregate swirl, remains roughly constant, again indicating the redistributive influence of the impulse. Both the aggregate and discrete distributions tend to relax back to the shape of the unperturbed distribution (although not the integral) by the far downstream PIV measurement station.

## 3.2 Discussion of the Static Impulse Experiment

The impulsive roughness perturbation influenced the entire downstream flow field, as far as could be measured, and the extent of the influence was seen to correspond to the growth of two internal layers, as identified in previous work. These internal layers, which previously had been identified from the mean velocity profile, were shown to correspond to both a deceleration of the streamwise velocity, measured via the streamwise third-order moment, and to a change in the mean velocity gradient – both quantities which are easily obtainable from just a single velocity component, and importantly, can be obtained by simple subtraction, without the noisy streamwise differentiation employed in previous investigations. These methods provide a means of measuring the extent of the influence of the impulse, which was shown to generate a stress bore in the flow. The manifestation of this stress bore in the streamwise turbulence intensity was shown to be scaled by a velocity scale based on the mean velocity gradient, indicating that the stress bore itself is, in some sense, disconnected from the boundary condition, and dependent on purely local flow conditions. The immediate consequence of this is the long streamwise persistence of the bore that has been observed by a number of previous experimenters.

The structural observations of Pearson et al. [1997] about the suppression of the near-wall cycle were illustrated through the significant alteration to the spectral energy distribution downstream of the perturbation. This energetic redistribution, which involved (a) a displacement of spectral energy away from the location of the near-wall peak, (b) a subsequent suppression of the near-wall peak itself, and then (c) a gradual dissipation of the displaced energy and (d) a regrowth of the near-wall

cycle downstream, was biased towards lower wavelengths, indicating that the impulsive perturbation did not affect the flow bluntly, in all areas of the spectrum, but rather the disruption and recovery of the flow are presumably a strong function of the nature of the perturbation itself — raising the possibility that a perturbation could be ‘designed’ to achieve particular redistributive goals in the spectral energy organization of the flow. This spectral result was supported by the depression of integral scales in the immediate vicinity of the impulse, and the corresponding nonequilibrium that the impulse engendered in the downstream flow field. The recovery of the near-wall cycle and the dissipation of displaced near-wall structural content were observed to operate on different timescales, consistent with the claim that the stress bore is largely or entirely a local phenomenon.

Finally, the impulse was shown to have a direct impact on discrete structures in the flow field, affecting the location of prograde and retrograde vortex cores and the distribution of aggregate swirl. All of these features of the impulsive perturbation by a roughness strip provide the basic framework for developing methods to alter and control turbulent boundary layers by exploiting the ability of small perturbations to affect vast regions of flow. Of course, a direct measure of wall shear stress would be required in order to make any concrete conclusions about the effect of these perturbations on skin friction. It is also worth noting that the current experiment considered a reasonably large impulse height, despite the small impulse magnitude as measured by the roughness function, and therefore the results perhaps have application to a broader class of problems beyond roughness including perturbation by obstacles.

Ultimately, the static impulse provides a spatial modification of the turbulent boundary layer, by injecting a new set of lengthscales associated with the roughness impulse into the flow. However, if instead of a purely static impulse, the impulse were dynamic, with an associated timescale, then in addition to the spatial scale of the roughness, the timescale would also be injected into the flow field. In this way, a more detailed understanding of the mechanics of the relaxation can be obtained, since the relaxation processes observed in the static impulse can be viewed in the context of a particular input timescale. Then, the development of the stress bore and the redistribution of turbulent spectral energy density downstream of the dynamic perturbation can be used to better understand the important timescales in nonequilibrium flow conditions. Moreover, by actuating the very same roughness impulse in time, the extent to which the dynamic wave associated with the periodic oscillation of the roughness strip can be separated from the spatially impulsive roughness effects themselves, can also be considered.

## Chapter 4

# The Effect of Galilean and Reynolds Decompositions on Vortex Detection

### 4.1 The Trouble with Swirling Strength

The distribution of swirling strength was employed as a measure of the structural effect of the static perturbation in section 3.1.5. However, this proxy means of representing swirling coherent structures in the boundary layer is not without its own difficulties. Indeed, the different approaches to identifying regions of swirling motion in turbulent velocity fields continue to be a source of intense discussion. Adrian et al. [2000a] elaborated on the way in which the choice of velocity field decomposition for use in swirling analysis can significantly affect the identification of swirling regions and individual vortex cores. The two primary decomposition methods are the Galilean decomposition, where a constant convective velocity is subtracted from the instantaneous velocity to field, to reveal vortical structures moving at that velocity (the ‘accepted’ method used in section 3.1.5); and the Reynolds decomposition, the standard bearer for most turbulence analysis, which involves subtracting the local mean convective velocity from the instantaneous field. The Galilean approach involves iteratively selecting different constant convective velocities (often expressed as percentages of the free stream velocity), and subtracting them from the instantaneous velocity field in order to reveal swirling motions. These swirling motions then represent coherent ‘vortices’ in the sense of Robinson [1991], where a vortex is said to exist when “instantaneous streamlines mapped onto a plane normal to the [supposed] vortex core exhibit a roughly circular or spiral pattern when viewed from a reference frame moving with the center of the [supposed] vortex core”. In support of his conclusion that an iterative approach using Galilean decompositions is ideal for vortex core identification in most circumstances, Adrian et al. [2000a] noted that such a decomposition preserves the “relative shears between adjacent structures in the flow”.

For wall-bounded flows, in the streamwise-wall-normal plane, the identification of vortices from the Reynolds decomposition of the velocity field will differ from the identification by means of a Galilean decomposition. The difference is due to the fact that the Reynolds decomposition implicitly compensates for the presence of a mean velocity gradient. Assuming for the moment that vortices convect at the local mean velocity of the flow, then the Galilean choice of velocity at the vortex center itself will correspond to the Reynolds decomposition velocity. However, moving away from the vortex center in the wall-normal direction, the two velocity field decompositions will diverge, because the Reynolds decomposed field takes into account the mean velocity gradient. Therefore, the instantaneous streamlines used in the definition of Robinson [1991] will appear different. If the vortex core does not, in fact, convect at the local mean velocity, as was shown by Lehew et al. [2011], then there is an additional source of divergence between the streamlines of the two flow field decompositions.

The fundamental question raised by these two possible flow decompositions is which useful for conceptualizing real coherent structures? In the view of Robinson [1991], using a Galilean frame, the vortex is identified by assuming that it is composed of a contribution from the mean shear. In the Reynolds decomposed view, the vortex is identified independent of the mean shear. In other words, if we take a vortex defined by either decomposition and view it in a Galilean frame, the vortex defined by the Galilean decomposition will, by definition, appear as a circle, whereas the vortex defined by the Reynolds decomposition will appear as an ellipse, with eccentricity dependent on the mean shear. Then the question can be rephrased: which object is more practical for identifying coherent structures, the circle or the ellipse? If we consider the hairpin model of Theodorsen [1952], the head of the hairpin will appear as a circle in only a single plane (the symmetry plane of the hairpin itself); in all other streamwise-wall-normal planes, the hairpin head will appear elliptical. Therefore the consequence of this choice of velocity decomposition is of significant practical and fundamental interest. This brief chapter will examine the choice of velocity field decomposition as it relates to the increasingly common procedure of calculating swirling strength for the identification of vortical structures.

## 4.2 Vortex Core Identification

In two-dimensions, the unsigned swirling strength can be calculated from the magnitude of the imaginary part of the complex eigenvalue of the velocity gradient tensor, defined by Jeong and Hussain [1995] and Zhou et al. [1999], given as

$$\lambda_{ci} = \frac{1}{2} \Im \left( \sqrt{\left( \frac{\partial \tilde{u}}{\partial x} + \frac{\partial \tilde{v}}{\partial y} \right)^2 - 4 \left( \frac{\partial \tilde{u}}{\partial x} \frac{\partial \tilde{v}}{\partial y} - \frac{\partial \tilde{u}}{\partial y} \frac{\partial \tilde{v}}{\partial x} \right)} \right) \quad (4.1)$$

where the local velocities  $\tilde{u}$  and  $\tilde{v}$  are placeholders which represent the remainder after either Galilean or Reynolds decomposition. In the Galilean decomposition,  $\tilde{u}$ , the local velocity, is equal to the instantaneous velocity  $\hat{u}$  subtracting some constant convective velocity  $U_c$ , as  $\tilde{u} = \hat{u} - U_c$ . In the Reynolds decomposition, the local velocity  $\tilde{u}$  is the instantaneous velocity subtracting the local mean,  $\hat{u} - U$ , or, in other words, the local fluctuating velocity,  $u$ . The appropriate sign can be applied to the swirling strength by means of the vorticity,  $\omega$ , in order to distinguish between prograde swirl (where the direction of rotation is negative, in the mathematical sense, and thus is consistent with the rotation generated by the mean shear) and retrograde swirl (where the direction of rotation is positive).

A 2D Savitsky-Golay algorithm (see Meer and Weiss [1992] and Pan et al. [2007]) was applied to the streamwise and wall-normal velocity fields measured by PIV, in order to produce the spatial derivatives needed for swirling strength and vorticity calculations. The Savitsky-Golay method essentially assigns local polynomial fits to otherwise noisy data in order to allow smooth derivatives to be taken while preserving key features, like local extrema. It is thus ideally suited for identifying regions of vorticity and swirl. An appropriate Savitsky-Golay convolution kernel was produced for the first derivatives in the streamwise direction,  $u_x, v_x$ , and the calculation was accomplished by two-dimensional convolution of the kernel with the velocity fields. The transpose of the kernel was then employed for the  $y$ -derivatives  $u_y, v_y$ . In all convolutions, ‘reflective’ boundary conditions were enforced on the edges of the velocity fields, instead of the more customary zero-padding the matrices, in order to avoid producing artifacts in the gradients. The kernel had a symmetric window size of 7 velocity vectors, and first-order polynomials were employed. By accomplishing the differentiation via the convolution, the effect of noise in the velocity field on the subsequent swirling strength and vorticity calculations was significantly reduced.

Considering first the velocity field with a constant convective velocity subtracted (Galilean decomposition), in order to identify rotational features, the traditional method for calculating rotation by means of numerical differentiation can be compared with the Savitsky-Golay convolution method, (figure 4.1). It is immediately apparent that the Savitsky-Golay approach reduces significantly the influence of noise on the final swirling strength field, and thus allows for more accurate identification of specific regions of swirl. It is also clear that the prograde swirl dominates the flow field under this analysis.

Now, if the Reynolds decomposition of the instantaneous velocity field is used, the result (figure 4.2) shows a significant change in the distribution of swirl between prograde and retrograde orientations.

In order to better quantify this distinction between the two methods of calculating the swirl, the swirl can be averaged across the streamwise direction, over  $10^4$  instantaneous velocity fields, to produce a profile of the swirl, under each calculation technique, in figure 4.3. Under the Reynolds

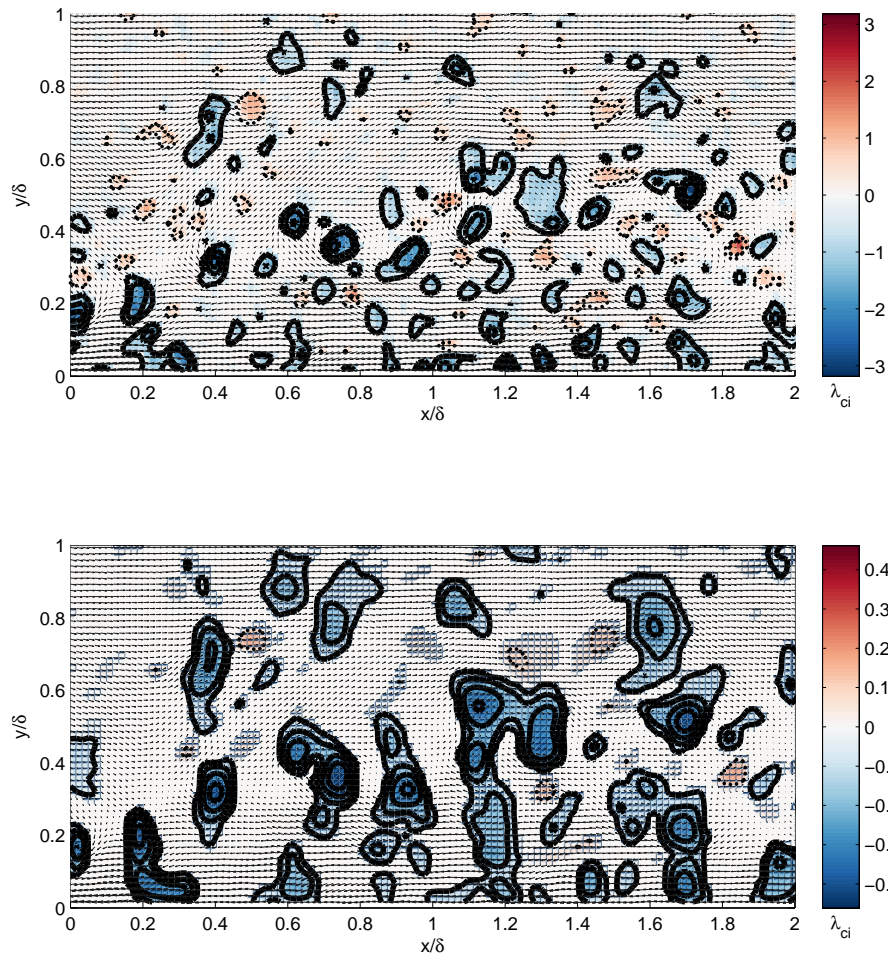


Figure 4.1: (Top) The velocity vectors, with a constant convective velocity of  $0.8U_\infty$  subtracted are shown, superposed over a map of the signed swirling strength, calculated by means of traditional numerical differentiation, without smoothing. (Bottom) Swirling strength calculated by means of the Savitsky-Golay convolution. Solid contour levels surround prograde patches of swirl; dotted levels surround retrograde patches.

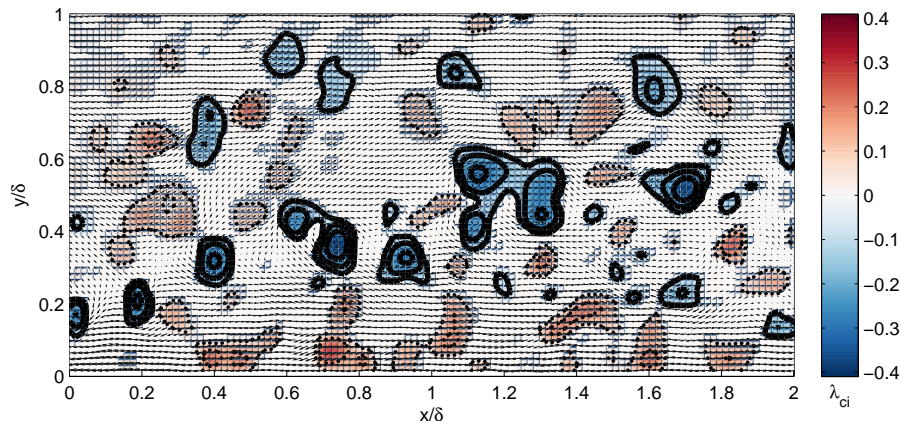


Figure 4.2: The velocity vectors, with the local convective velocity subtracted are shown, superposed over a map of the signed swirling strength, calculated by means of the Savitsky-Golay convolution.

decomposition, the swirl profiles for prograde and retrograde swirl have similar magnitude across the boundary layer, with slightly more prograde swirl. Using the traditional Galilean decomposition, however, there appears to be roughly twice as much prograde swirl as retrograde across most of the boundary layer.

Aside from the aggregate swirl, individual vortex cores can be identified by application of size and intensity thresholding to the regions of swirl in each instantaneous velocity field, and the distribution of such cores can also be compared. The threshold levels for the identification of vortex cores are problem-specific and were optimized using the mean swirl field to capture all easily observable patches of swirl (figure 4.4). The vortex core identification routine was then used to catalog all of the vortex cores and their corresponding centroids, in order to generate a profile of the expected number of vortex cores at a given wall-normal location, in figure 4.5. As in the aggregate swirl, the Reynolds decomposition appeared to yield equal quantities of prograde and retrograde vortex cores across the boundary layer, whereas the Galilean decomposition produced significantly more prograde than retrograde cores, close to a ratio of 5 : 1. The discrepancy in ratio compared to the aggregate swirl is a result of vortex selection criteria, which have some inherent bias against the smaller retrograde vortex cores. But the overall under-representation of retrograde vortices under Galilean decomposition is consistent between both analyses.

Following the work of Natrajan et al. [2007], a two-point correlation function can be constructed between prograde and retrograde vortex cores. As with Natrajan et al. [2007], there is a clear angular inclination, in the downstream direction, between pairs of prograde and retrograde cores, but there also appears to be a weaker association inclined toward the upstream. However, when the swirl is calculated using the Reynolds decomposition, only the magnitude of this ‘X’-preferred orientation is

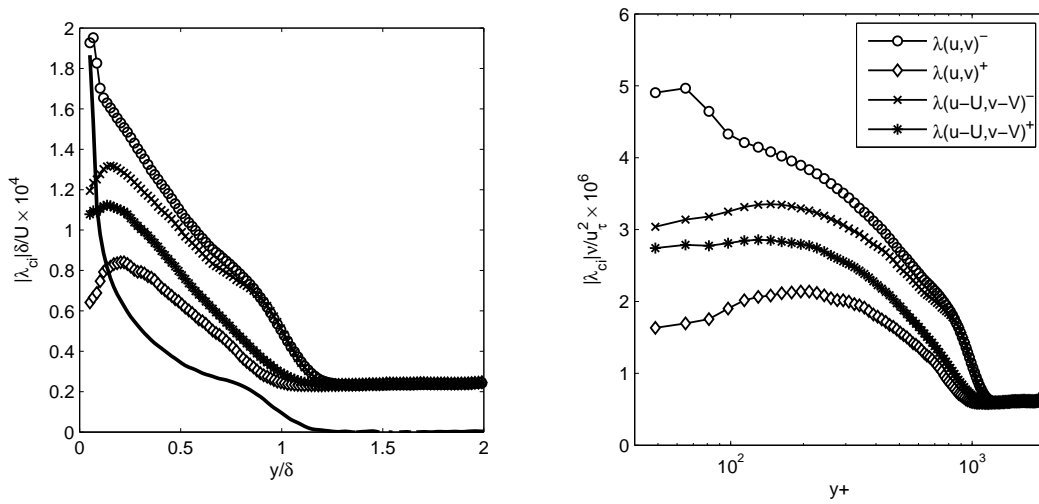


Figure 4.3: (Left) The swirl profiles, in outer units, for the Galilean decomposition: prograde (circles) and retrograde (diamonds), and from the Reynolds decomposition: prograde (x) and retrograde (asterisk). The mean velocity gradient  $\delta/U_\infty dU/dy$  is shown in the solid black line. (Right) The swirl profiles in inner units

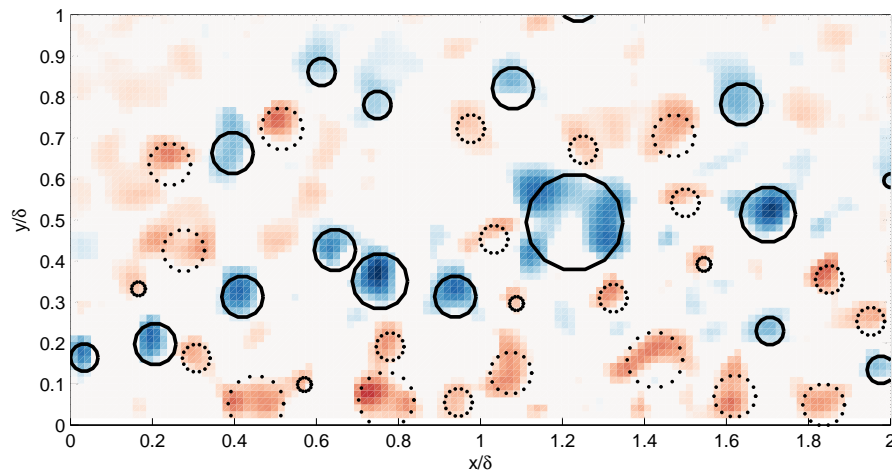


Figure 4.4: The same swirling field as show in (figure 4.2) but this time instead of contour levels of the swirling strength, circles proportional to the area of each vortex core and centered on the vortex core's centroid are shown.

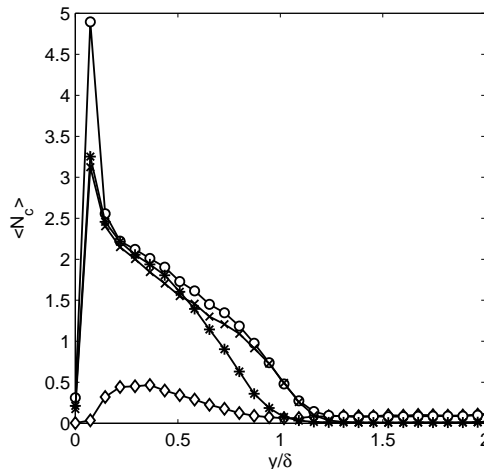


Figure 4.5: The mean number of distinct vortex cores, per PIV frame (streamwise extent of  $\approx 2\delta$ ), as a function of wall location. For the Galilean decomposition: prograde (circles) and retrograde (diamonds), and from the Reynolds decomposition: prograde (x) and retrograde (asterisk)

magnified significantly, suggesting that the perceived orientation of vortices is robust to the choice of flow decomposition, even where the actual number of vortices differs significantly.

### 4.3 The Effect of Decomposition Choice

Under the Galilean decomposition, the definition of the swirling strength, in equation 4.1 above has the identical mathematical form whether the instantaneous ( $\hat{u}$ ) or local ( $\check{u} = \hat{u} - U_c$ ) velocity is used, since the constant convective velocities ( $U_c$ ) do not contribute to the velocity gradient tensor. Therefore, we can rewrite the swirling strength for the Galilean decomposition in terms of the instantaneous velocity. Then, we can substitute the Reynolds decomposition for the instantaneous velocity and make zero-pressure gradient boundary layer assumptions, shown in equation 4.2.

$$\begin{aligned}
 \lambda_{ci} &= \frac{1}{2} \mathfrak{J} \left( \sqrt{\left( \frac{\partial \hat{u}}{\partial x} + \frac{\partial \hat{v}}{\partial y} \right)^2 - 4 \left( \frac{\partial \hat{u}}{\partial x} \frac{\partial \hat{v}}{\partial y} - \frac{\partial \hat{u}}{\partial y} \frac{\partial \hat{v}}{\partial x} \right)} \right) \\
 &= \frac{1}{2} \mathfrak{J} \left( \sqrt{\left( \frac{\partial (U+u)}{\partial x} + \frac{\partial (V+v)}{\partial y} \right)^2 - 4 \left( \frac{\partial (U+u)}{\partial x} \frac{\partial (V+v)}{\partial y} - \frac{\partial (U+u)}{\partial y} \frac{\partial (V+v)}{\partial x} \right)} \right) \quad (4.2) \\
 &\approx \frac{1}{2} \mathfrak{J} \left( \sqrt{\left( \frac{\partial (u)}{\partial x} + \frac{\partial (v)}{\partial y} \right)^2 - 4 \left( \frac{\partial (u)}{\partial x} \frac{\partial (v)}{\partial y} - \frac{\partial (U+u)}{\partial y} \frac{\partial (v)}{\partial x} \right)} \right)
 \end{aligned}$$

For the Reynolds decomposed flow, we can replace the local velocity  $\check{u}$  with the fluctuating velocity from the Reynolds decomposition,  $u$ , and apply the same simplifying boundary layer assumptions,

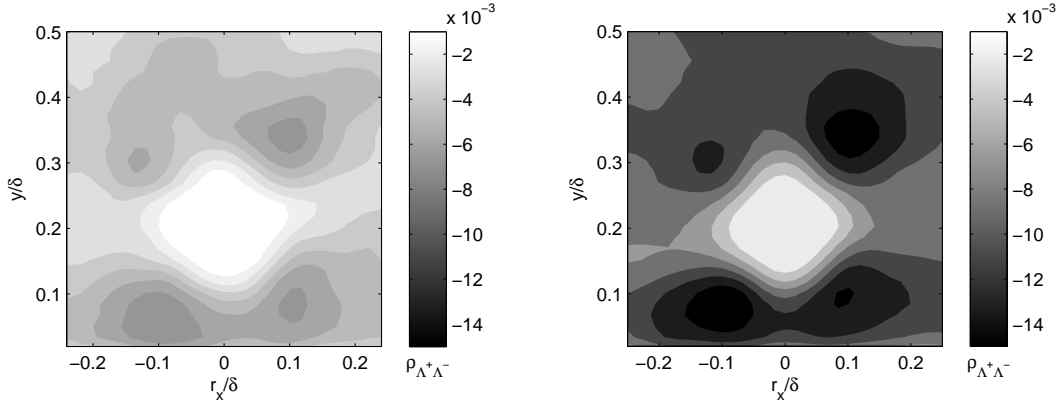


Figure 4.6: The two-point cross correlation between retrograde cores, in the center of each plot, and neighboring prograde cores. On (Left) is the calculation under Galilean decomposition; on (Right) the Reynolds decomposition

shown in equation 4.3.

$$\lambda_{ci} \approx \frac{1}{2} \mathcal{J} \left( \sqrt{\left( \frac{\partial(u)}{\partial x} + \frac{\partial(v)}{\partial y} \right)^2 - 4 \left( \frac{\partial(u)}{\partial x} \frac{\partial(v)}{\partial y} - \frac{\partial(u)}{\partial y} \frac{\partial(v)}{\partial x} \right)} \right) \quad (4.3)$$

The difference between the two decompositions when used in the swirling strength is the presence of the factor  $\left( \frac{\partial U}{\partial y} \frac{\partial v}{\partial x} \right)$  in the Galilean form and its absence in the Reynolds decomposed form. This is consistent with the understanding of the different decompositions, above, where the Galilean decomposition essentially includes a contribution from the mean shear. This term can potentially alter the magnitude of the discriminant. If  $\left( \frac{\partial v}{\partial x} \right) > 0$ , then the presence of the mean shear will minimize the overall magnitude of the swirl; if  $\left( \frac{\partial v}{\partial x} \right) < 0$  then the magnitude of the swirl will increase. Therefore, for vortex detection schemes dependent on a threshold of the swirling strength, the case of  $\left( \frac{\partial v}{\partial x} \right) < 0$  will produce additional vortex identifications. And, as noted above, the sign of the swirl is determined by the vorticity,  $\omega = \frac{\partial v}{\partial x} - \frac{\partial(u+U)}{\partial y}$ . Therefore, the additional vortex identifications due to the mean shear are likely to be prograde (negative vorticity). The effect of the mean shear expresses itself through the magnitude of the swirling strength, and holding the threshold constant, the swirling strength applied to a Galilean decomposed velocity field is expected to yield more prograde vortices than would the case of a Reynolds decomposed velocity field.

The effect of the mean shear under Galilean decomposition can be observed when the mean streamwise velocity gradient,  $\frac{\partial U}{\partial y}$  is normalized in outer units and plotted against the swirling profiles, as in figure 4.3. It is quite clear that there is a strong correspondence between the mean shear

and the swirl profiles, when calculated via Galilean decomposition. In particular, very near the wall, where the velocity gradient is highest, is precisely where the distinction between the prograde and retrograde swirl content becomes most acute — the prograde swirl has a sharp local peak in this region, whereas the retrograde swirl profile becomes locally concave. And beyond the near-wall region, but still within the edge of the boundary layer, where the velocity gradient is still significant, the shape and magnitude of the prograde and retrograde swirl profiles remain quite distinct. Integrating the profiles shows that the total prograde content is roughly twice the retrograde content, consistent with the findings of Wu and Christensen [2006]. In contrast, the swirl profiles calculated from a Reynolds decomposition of the instantaneous velocity field show a consistent convex peak in the near-wall region, for both prograde and retrograde swirl, as well as a similar shape and magnitude through the remainder of the boundary layer. These same patterns were consistent with the results from the core-counting routine as well.

Returning to the original question of which method of decomposition appears most useful when considering wall-bounded turbulence, it appears that at least part of the answer may depend on the ultimate application. The vortices identified by Reynolds decomposition, which are roughly equally distributed between prograde and retrograde, may represent a more abstract conceptualization of the flow field, in which zero-mean coherent oscillating modes (or traveling waves) are the basic building blocks. Such a conceptualization is supported by the work of McKeon and Sharma [2010] and may be particularly amenable to modeling efforts, where the challenge is to describe small-scale motions using only general knowledge of the flow (e.g., the mean velocity gradient) without detailed knowledge of the small-scale fluctuations.

## Chapter 5

# The Impulsive Dynamic-Roughness Perturbation

### 5.1 The Dynamic-Impulse Experiment

The dynamic impulse study was designed to connect the key features observed in the statically perturbed boundary layer — the internal layers, stress bore, near-wall energetic changes, and integral scale-size effects — to a dynamic perturbation of similar spatial type. Section 5.2 provides the statistical and spectral view of the perturbed flow, with emphasis on how the dynamic perturbation contrasts with the static perturbation considered previously, and the extent to which the roughness and wave-like features of the perturbation can be separated. The wave-like features are studied more carefully in section 5.3 by employing a phase-locked decomposition of the velocity signal to identify the shapes of the velocity fluctuations in the flow field, which will ultimately lead to a resolvent analysis of the fluctuating velocity field. Significant portions of the following experiment were first reported in Jacobi and McKeon [2011b].

### 5.2 General Features of the Dynamic Perturbation

The measured velocity signal  $u(y, t)$  in the dynamic analysis can be expressed by the standard Reynolds decomposition as equation 5.1

$$\hat{u}(y, t) = U(y) + u(y, t) \tag{5.1}$$

where the mean profile is  $U(y)$  and the turbulent fluctuation about the mean is  $u'(y, t)$ , with free stream velocity  $U_\infty$ , as above. However, the fluctuation, in principle, can be further decomposed, following Hussain and Reynolds [1970], into a periodic component  $\tilde{u}(y, t)$  contributed by the periodic input perturbation, and then a turbulent fluctuation about the periodic component,  $u'_t(y, t)$ , such

that the overall decomposition obeys equation 5.2.

$$\hat{u}(y, t) = U(y) + \tilde{u}(y, t) + u'_t(y, t) \quad (5.2)$$

The details of this phase-locked composition are provided in section 5.3.1, and for now, the overall fluctuation  $u'(y, t)$  will be treated.  $\sqrt{u'^2}$  is the root mean square value of  $u'(y, t)$ ;  $\sqrt[3]{u'^3(y)}$  is the cube-root of the third moment of  $u'(y, t)$ . The streamwise position  $x$  is measured from the trailing edge of the roughness patch.

In this section, the mean flow properties for the unperturbed smooth flow and the flow perturbed by the dynamic impulse are presented, with comparison to a few key results from the static perturbation study. The behavior of the dynamic impulse is also compared to previous impulsively perturbed flows and the internal layers resulting from the perturbation are identified and interpreted. The effect of the perturbation on the turbulence statistics, the spectral energy density distribution, and the spatial distribution of integral lengthscales in the downstream flow are all presented and interpreted in light of the time-varying nature of the perturbation. Finally, spectral methods are presented which motivate the division of the effect of the dynamic perturbation into two separate regimes: an impulsive roughness perturbation and an organized wave.

### 5.2.1 Mean Flow Properties

The essential flow properties for both the hotwire and PIV experiments are summarized in Table 5.1, and some key features of the flow field are described below. The dynamically perturbed case refers to a perturbation by the roughness patch when the patch was actuated by the motor; the statically perturbed case refers to the results of chapter 3 with the identical roughness elements fixed in position at a roughly equivalent amplitude. The streamwise growth rate of the boundary layer thickness was approximately the same for both the static and dynamically perturbed flows, and both perturbed boundary layers grew more quickly than the unperturbed boundary layer.  $\delta$  refers to the value of  $\delta_{99}$  at a given streamwise position under each flow regime;  $\delta_0$  is the incoming boundary layer thickness.

The friction velocity  $u_\tau = \sqrt{\frac{\tau_w}{\rho}}$  was estimated by the Clauser method and also independently verified by the momentum integral approach and by inference from the velocity gradient very near the wall. As discussed in the previous work on the static perturbation, neither the Clauser method nor the momentum integral approach strictly applies, due to the nonequilibrium conditions downstream of the perturbation. Calculating the velocity gradient by using the first mean velocity measurement nearest the wall, and a no-slip condition, is also problematic, due to both the uncertainty in the wall position and the location of the first point at the outer edge of the linear regime. Despite these caveats, using this linear-fit technique, the dynamically perturbed flow shows a drop in  $C_f$

Wall	$x$ (mm)	$U_\infty$ (m s <sup>-1</sup> )	$\delta$ (mm)	$\theta$ (mm)	$\delta^*$ (mm)	$Re_\theta$ $= U\theta/\nu$	$Re_\tau$ $= u_\tau\delta_{99}/\nu$
Unperturbed	5 (7.4)	20.16 (20.60)	17.0 (17.6)	2.1 (1.9)	2.9 (2.9)	2770 (2560)	910 (970)
	58 (62.4)	20.09 (20.42)	24.1 (25.8)	3.1 (2.9)	4.3 (4.3)	4070 (3870)	1200 (1320)
Static	2.5 (7.4)	20.20 (20.65)	17.2 (18.4)	2.1 (2.2)	3.6 (3.5)	2770 (2970)	
	58 (62.4)	20.07 (20.50)	24.4 (26.7)	3.3 (3.1)	4.6 (4.6)	4330 (4150)	
Dynamic	2.5 (7.4)	20.13 (20.78)	17.0 (18.3)	2.1 (2.2)	3.3 (3.3)	2770 (2990)	
	58 (62.4)	20.11 (20.54)	24.3 (26.5)	3.2 (3.1)	4.5 (4.5)	4330 (4160)	

Table 5.1: Mean flow properties at streamwise extrema of sampling area for hotwire (and PIV)

immediately downstream of the roughness strip (similar to the static impulse), and then an oscillating recovery (in contrast to the nonoscillatory recovery previously reported for the statically perturbed case). The average spatial period of this oscillation is approximately  $6\delta$ , compared to the wavelength of the dynamic perturbation of about  $20\delta$  measured below, suggesting tentatively that the relaxation is decoupled or only weakly dependent on the dynamic impulse and is thus a function of the smaller wavelength structures associated with the roughness. The general trend in the recovery of  $C_f$ , including the overshoot and oscillation, is consistent with previous work for a static roughness impulse by Andreopoulos and Wood [1982] and Pearson et al. [1997]. However, since all of the  $C_f$  measurement techniques suffer from significant sources of uncertainty, scaling throughout the remaining results is accomplished in terms of outer variables or, when noted, in terms of the inner scales corresponding to the unperturbed case only. An independent measure of  $\tau_w$  would enable more robust analysis; in particular, the measurement of skin-friction in a non-equilibrium boundary layer being forced dynamically in time poses additional measurement challenges and is a topic of current investigation.

The strength of the dynamic perturbation can be quantified in terms of its effect on the roughness function  $\Delta U/u_\tau$  from the traditional law of the wall, as described in Antonia and Luxton [1971a], where  $M$  is the logarithmic ratio of the roughness heights at each surface condition determined via the roughness function. Section 3.1.2 discussed a number of challenges to employing this metric for nonequilibrium perturbations, but despite the caveats outlined there, the technique shows the expected result that the strength of the dynamic impulse is weaker than the corresponding impulse in the static case: the  $M_{S \rightarrow R}$  transition was approximately  $-1.0$  (versus  $-1.7$  in the statically perturbed flow) and the  $M_{R \rightarrow S}$  transition was approximately  $1.0$  (versus  $1.6$ ). Indeed, the ratio of the static to dynamic impulse strengths is  $\approx \sqrt{2}$  as would be expected considering the impulse strength would scale on the instantaneous maximal amplitude, whereas the time-averaged blockage was selected to be held constant.

The mean velocity profiles were compared between the dynamically perturbed and unperturbed flows. Immediately downstream of the perturbation, there is a significant velocity deficit, particularly for  $y/\delta < 0.3$ – $0.4$ , which corresponds to about 6 times the roughness height. This deficit persists

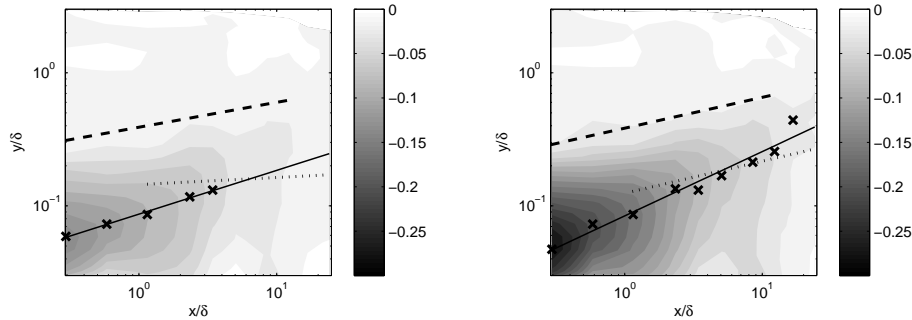


Figure 5.1: (Left) The discrepancy in the mean velocity profiles between the dynamically perturbed and unperturbed cases is shown in gray contours; the peaks for each streamwise location at which the velocity discrepancy is greatest are marked ( $\times$ ) and a curve is fitted by least squares ( $—$ ,  $y/\delta = 0.09(x/\delta)^{0.33}$ ). The approximate intercept for the fit is just below the RMS height of the roughness elements:  $y \approx 0.06 \delta = 0.88 k_{rms}$ . Also, internal layer best fits, calculated below, are included ( $- -$ ,  $\delta_1/\delta = 0.39(x/\delta)^{0.19}$ ;  $\dots$ ,  $\delta_2/\delta = 0.14(x/\delta)^{0.05}$ ) for reference. (Right) For comparison, the statically perturbed case is shown, with the least squares fit for the peak discrepancy given by  $y/\delta = 0.08(x/\delta)^{0.48}$  with approximate intercept at  $y \approx 0.05 \delta = 0.86 k$ .

until approximately  $15\delta$  downstream of the trailing edge of the perturbation. There appears to be a persistent, albeit small, velocity deficit even further downstream and across the velocity profile, consistent with the results of Andreopoulos and Wood [1982] for static roughness. By plotting the discrepancy in the mean velocity profiles between the perturbed and unperturbed cases (equation 5.3) as a contour map in wall-normal and streamwise directions (following the procedure described in section 3.1.1) the recovery behavior of the mean velocity profile can be seen quite clearly in figure 5.1. Least squares curve fits for the wall-normal location of the peak velocity deficit at each streamwise measurement location are provided for comparison. The discrepancy map for the static perturbation is also provided for comparison.

$$\frac{\Delta u}{U}(x, y) = \frac{u}{U}(x, y)_{perturbed} - \frac{u}{U}(x, y)_{smooth} \quad (5.3)$$

The velocity deficit is smaller in both wall-normal and streamwise extent than that of the statically perturbed case, as expected, and thus the recovery appears to occur more quickly, although still on the order of  $10 \delta$ .

### 5.2.2 Turbulence Statistics

Turbulence statistics were calculated in the streamwise direction from the hotwire signals. Plotting successive profiles of the streamwise turbulence intensity  $\sqrt{u'^2(y)}$  shows a large ‘hump’ in the profile, similar to that seen in the statically perturbed case but broader in wall-normal extent and higher in amplitude. This hump had previously been interpreted as a key manifestation of the stress bore generated in the flow by the perturbation. For a dynamic perturbation, this bore is expected to

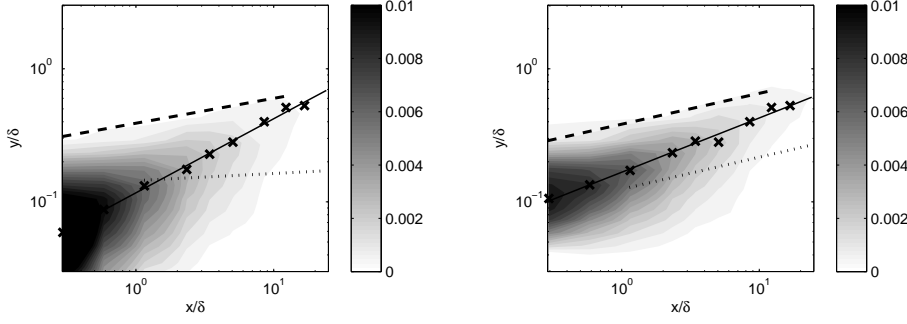


Figure 5.2: (Left) The discrepancy in the streamwise turbulence intensity profiles between the perturbed and unperturbed cases is shown in gray contours; the peaks for each streamwise location at which the discrepancy is greatest are marked ( $\times$ ) and a curve is fitted by least squares ( $—$ ,  $y/\delta = 0.12(x/\delta)^{0.54}$ ). The approximate intercept for the fit is the same as for the mean velocity discrepancy:  $y \approx 0.06\delta = 0.88k_{rms}$ . And again, the internal layer boundary best fits, calculated above, are included for reference. (Right) For comparison, the statically perturbed case is shown, with the least squares fit for the peak discrepancy given by  $y/\delta = 0.17(x/\delta)^{0.41}$  with approximate intercept  $0.10\delta = 1.67k$ .

span a broader range of wall-normal locations, since the roughness operates at a range of locations from  $y = 0 \rightarrow k$ , and indeed the hump is seen to extend from near the wall out to the location of the edge of where the hump in the statically perturbed case resides, with its peak centered at  $y = 0.08\delta = 1.3k$  immediately downstream of the roughness.

As with the velocity discrepancy contours, the discrepancy in the streamwise turbulence intensity profiles between the perturbed and unperturbed cases (equation 5.4) can be viewed as a contour map in wall-normal and streamwise directions in order to visualize the recovery behavior of the flow field (figure 5.2). In this case, the magnitude and streamwise extent of the discrepancy appears comparable between the dynamically perturbed flow and the static perturbation, except in the immediate vicinity of the perturbation itself.

$$\frac{\Delta\sqrt{u'^2}}{U}(x, y) = \frac{\sqrt{u'^2}}{U}(x, y)_{perturbed} - \frac{\sqrt{u'^2}}{U}(x, y)_{smooth} \quad (5.4)$$

As reported for the static impulse, the hump in the turbulence intensity plots, which varies with streamwise position downstream of the dynamic impulse, is a manifestation of the underlying stress bore, and thus can be scaled by a velocity scale based on the mean velocity gradient,  $u_s$  (equation 5.5) which represents the continued influence of the near-wall perturbation even farther from the wall and downstream, governed by local effects.

$$u_s = \sqrt{\left(U_\infty\delta\frac{\partial U}{\partial y}\right)} \quad (5.5)$$

Under this scaling (figure 5.3) the hump collapses for streamwise locations  $x > 2\delta$ , consistent with the

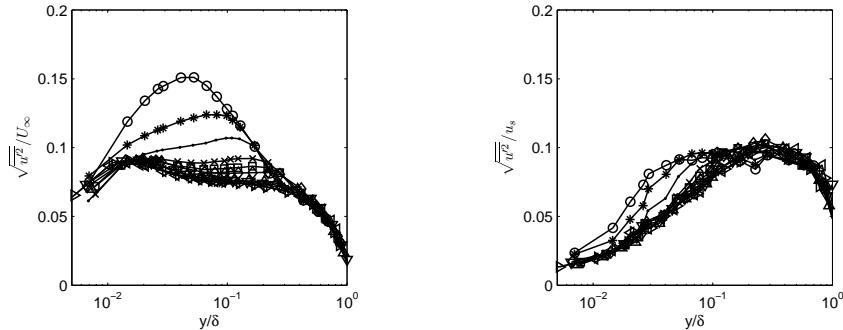


Figure 5.3: The turbulence intensity for the perturbed flow under (Left) standard outer scaling; and (Right) under a velocity scaling based on the local shear stress,  $u_s$ . Streamwise profiles:  $x/\delta = 0.3$   $\circ$  ;  $0.6$   $*$  ;  $1.1$   $\cdot$  ;  $2.3$   $\times$  ;  $3.4$   $\square$  ;  $5.0$   $\diamond$  ;  $8.4$   $\triangle$  ;  $12.1$   $\nabla$  ;  $16.6$   $\triangleright$  ;  $23.8$   $\triangleleft$

idea that the inter-layer region under dynamic perturbation also behaves as a stress bore reflecting the boundary condition enforced for that region. However, for  $x \lesssim 2 \delta$ , the scaling does not appear to collapse the profiles in the region  $y < 0.06 \delta < 0.88 k_{rms}$  — in precisely the region nearest the wall that also shows the deviation in the  $\sqrt{u'^2(y)}$  contours between the static and dynamic cases — which indicates that this failure of the  $u_s$ -scaling might reflect a fundamental difference between the two types of perturbation. By plotting the contours of the ratio between  $u_s$  under the two regimes, in figure 5.4, two distinct regions become clear. Between the mean edges of the two internal layers, the value of  $u_s$  is about 30% larger in the static than dynamic cases, consistent with the expected result from a roughness effect corrected for the RMS roughness height. In the region in the immediate vicinity of the roughness elements, however, the ratio is reversed. The velocity gradient of the dynamically perturbed case dominates here, perhaps due to the oscillating roughness elements — which generate a much higher shear locally about the trailing edge of the last element. In this region, it is the dynamic (or long wavelength) feature of the oscillation which dominates, as opposed to the more permanent feature of the spatial impulse seen farther from the wall. Thus we expect the reverse trend, that the mean velocity gradient should underestimate the dynamic extrema of the gradient and thus the scaling  $u_s$  should be lower than necessary in this region; this is indeed the case, where the magnitude of underestimate is approximately given by the ratio of the RMS to mean values of the gradient.

The successive profiles of the triple product  $\sqrt[3]{u'^3(y)}$  show a negative region at  $y = 0.09 \delta = 1.3 k_{rms}$ , but not the positive region at the the roughness height that was observed in the statically perturbed case. The discrepancy maps (figure 5.5) highlight the difference between the dynamic and statically perturbed cases.

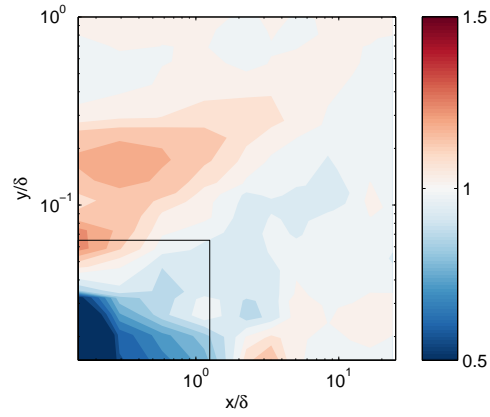


Figure 5.4: The ratio of  $u_s$  for the static impulse over  $u_s$  for the dynamic impulse. The rectangle represents the area in figure 5.3 where the  $\sqrt{u'^2(y)}$  profile fails to collapse.

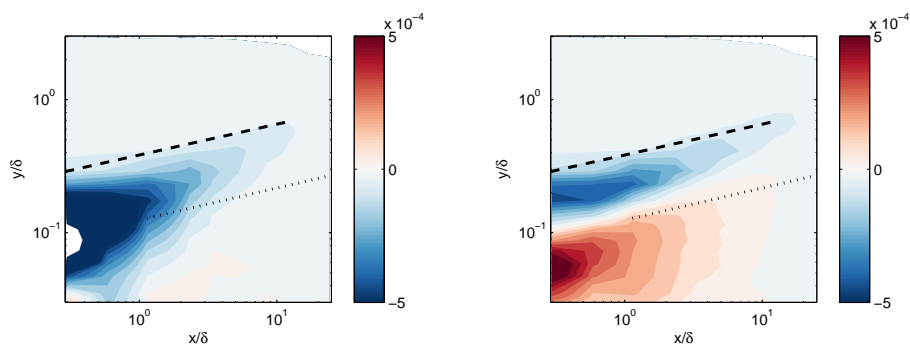


Figure 5.5: The discrepancy map for the streamwise velocity triple-product for the (Left) dynamically perturbed case and (Right) the statically perturbed case.

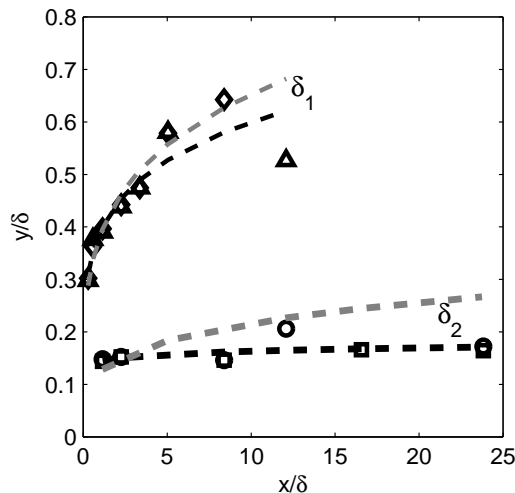


Figure 5.6: The development of the internal layers, calculated by both methods described above. Plot and fit in outer units. For  $\delta_1$ :  $\diamond$  via  $y^{1/2}$ -scaling;  $\triangle$  via  $\partial U/\partial x$ ; for  $\delta_2$ :  $\circ$  via  $y^{1/2}$ -scaling;  $\square$  via  $\partial U/\partial x$ ; least-squares best fits:  $-\delta_1/\delta = 0.39(x/\delta)^{0.19}$ ;  $-\delta_2/\delta = 0.14(x/\delta)^{0.05}$ ; also included for reference, the best fits for the static impulse:  $-\delta_1/\delta = 0.38(x/\delta)^{0.23}$ ;  $-\delta_2/\delta = 0.12(x/\delta)^{0.24}$

### 5.2.3 Internal Layers

The internal layers, sketched in figure 2.6, represent the extent to which different boundary conditions have influenced the flow. Since the strength of the impulse  $M$ , noted above, is less for the dynamic case, it would be expected that the internal layers should grow more slowly, and indeed, both internal layers grow more slowly under the dynamic perturbation than under static perturbation.

In chapter 3, two physically motivated methods were developed for locating the internal layers, both involving constructing discrepancy maps between the perturbed flow field and the unperturbed field. In one case, a map is constructed from the velocity scale related to the mean velocity gradient,  $u_s$  (equation 5.5) and this is shown for the present study in figure 5.7; in the other, a map is constructed from the third-order moment of the streamwise velocity signal. Both maps tend to identify the edge of the first internal layer quite easily for both dynamic and static perturbations. The second internal layer edge arguably appears in the  $u_s$  map for the dynamic perturbation in the negative layer near the wall. But the third-moment map shows no trace of the second internal layer, and thus fails to provide a method of identifying the internal layers.

The third-moment map identified the stress bore successfully under the static perturbation in figure 3.7 as a region of increased third-moment values of the streamwise velocity signal over the unperturbed values. In section 8.7, this increase in the third-moment statistics is shown to be associated with increased large-scale motions. Within the second internal layer, the third-order moment decreased under static perturbation, indicating increased small-scale motions associated with a newly-born and growing boundary layer, downstream of the roughness strip. For the dynamic

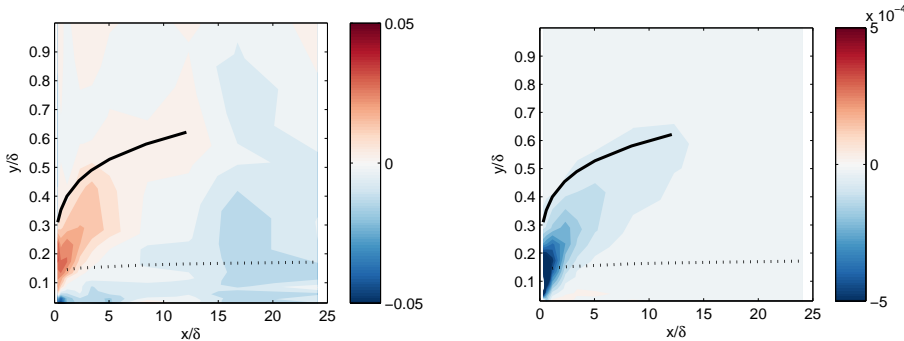


Figure 5.7: (Left) The discrepancy maps for  $u_s$  and (Right) the map for the third-order moment of the streamwise velocity component. While the third-order moment map tended to highlight the precise inter-layer region for the case of a static perturbation, in the case of the dynamic perturbation, it no longer serves as a useful criterion.

perturbation, the decrease in third-order moment values was dominant, even near the wall, consistent with the dominance of an artificial large scale motion, characterized in section 5.3.

#### 5.2.4 Integral Length Scales

Roughness is understood to affect the local scale sizes in a flow, so another approach to identifying regions of the flow field influenced by the roughness impulse is to look for regions in which scale sizes vary from the corresponding unperturbed flow, by considering changes in the integral lengthscale  $\Lambda_L$  (equation 5.6), as elaborated in section 3.1.3, where  $R_{11}$  is the auto-correlation of the streamwise velocity signal.

$$\Lambda_L(x, y) = U(y) \int_0^\infty R_{11}(x, y, t) dt \quad (5.6)$$

There is a second method for identifying the internal lengthscale, by using the streamwise spectrum (equation 5.7) and considering the limit as wavenumber approaches 0. This method is attractive in general because it avoids a number of the difficulties associated with integrating the streamwise autocorrelation, as described in Bultjes [1975], but in particular, the contrast between the spectral and autocorrelation methods is insightful in the case of dynamic forcing.

$$\Lambda_L(x, y) = \frac{2}{\pi} \lim_{k_x \rightarrow 0} \phi_x(k_x) \quad (5.7)$$

The integral scale at each wall-normal and streamwise location reveals the relative distribution of the largest scales in the flow field, under the smooth and perturbed boundary conditions. A map of the ratio of these two sets of integral scales, perturbed normalized by unperturbed, determined by each calculation method for the dynamic perturbation is provided in figure 5.8ab. The spectral method shown in 5.8a identifies two distinct regions: one of increased integral scales, between the

edges of the two internal layers and one of decreased scales nearer to the wall. This same effect was seen also in the map of the statically perturbed flow, shown in figure 5.8c. The variation of the integral lengthscales between both internal layers indicates that neither is in a state of equilibrium. When the calculation is conducted by means of the autocorrelation, the resulting map, shown in figure 5.8b shows a large region of increased scales and no significant suppressed scales. In order to resolve the discrepancy, the map was recalculated using the spectral approach, but this time, instead of extrapolating the flat portion of the spectrum from the very lowest measured wavenumber to produce the limit  $k_x \rightarrow 0$ , the limit was taken by extrapolating an average of the low wavenumber spectral magnitudes which included the peak of the (low wavenumber) input perturbation. The result, shown in figure 5.8d, reproduces very closely the result from the autocorrelation.

The difference between the two spectral calculations is the inclusion or exclusion of the spectral peak associated with the input perturbation. When it is excluded by the limiting process, then the distribution of scales looks the same as the statically perturbed flow. But when it is included, by altering the limit such that the spectral peak is averaged into the region of the flat spectra at low wavenumbers, then the distribution of scales is significantly biased by the input of large scales — seen also in the autocorrelation method in figure 5.8b, which includes this contribution. In other words, we see that the two contributions of the dynamic perturbation are separable in terms of the effect they have on the scales of the flow.

### 5.2.5 Composite Spectra

In order to further investigate the impact of the dynamic perturbation on the structural composition of the flow field, the temporal spectra for each wall-normal and streamwise position were transformed by Taylor’s hypothesis into spatial spectra in streamwise wavelength  $\lambda_x$ . Following the procedure outlined in Hutchins and Marusic [2007], composite premultiplied spectra (in  $\lambda_x$  and wall-normal position  $y$ ) are reproduced for the unperturbed and statically perturbed flows of section 3.1.4 for reference in figure 5.9 (original figures 3.13 and 3.14). This procedure was then performed at all of the streamwise measurement locations downstream of the dynamic perturbation (figures 5.10 and 5.11). Key features of the turbulent boundary layer spectra, elaborated in Monty et al. [2009], were superimposed over the composite spectra in order to put the features of the perturbed flow in the spatial context of the accepted characteristics of the unperturbed spectra, namely: the inner peak at  $\lambda_x^+ \approx 1000, y^+ \approx 20$ ; the peak for superstructures at  $\lambda_x/\delta \approx 6$ ; and the large-scale motion (LSM) peak at  $\lambda_x/\delta \approx 3$ . Note, however, that the relatively low Reynolds number means that the latter two signatures are weak in the spectra shown here. The region of the mean recirculation bubble was estimated to extend to  $x/\delta \lesssim 0.3$ , based on the location of a significant change in the profile of  $\sqrt{u'^2(y)}$ .

The spectral composite maps for the dynamic perturbation share a few key trends in common

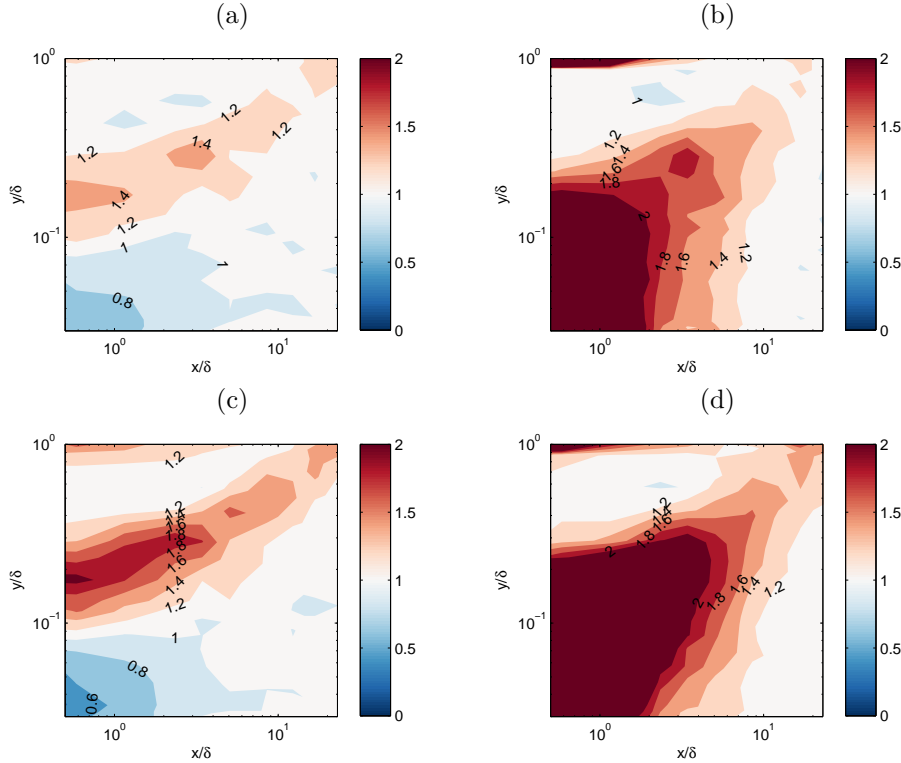


Figure 5.8: Top row: Maps of the ratio of integral lengthscales between the dynamically perturbed flow and the unperturbed flow, calculated by (a) the spectral method and (b) integration of the autocorrelation. Bottom row: Maps of the ratio of integral lengthscales: (c) for the statically perturbed flow, calculated by the spectral method and (d) for the dynamically perturbed flow calculated by a modification of the spectral method, whereby the influence of the spectral peak due to the perturbation is accounted for in the limit.

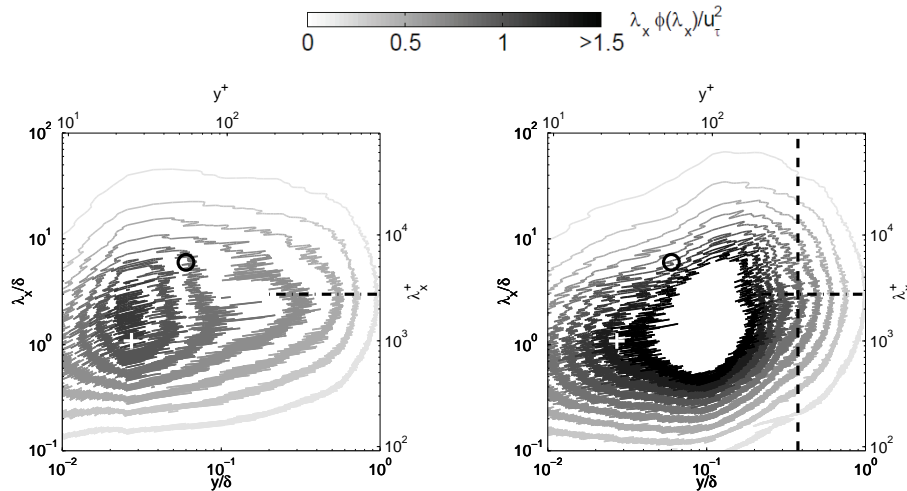


Figure 5.9: Composite spectra at  $x/\delta = 0.6$ : (Left) Unperturbed  $Re_\theta = 2770$  The white '+' marks the vicinity of the inner peak ( $\lambda_x^+ \approx 1000, y^+ \approx 25$ ), the black  $\circ$  marks the expected location of the VLSM peak at ( $\lambda_x/\delta \approx 6$ ), and  $\dots$  marks the peak along  $\lambda_x/\delta \approx 3$ ; (Right) Statically perturbed, with markings as in the left plot

with the static perturbation: in both, beyond the streamwise point at which the mean flow is unambiguously reattached downstream of the roughness, there is a clear suppression of the near wall peak, particularly at long wavelengths. In addition, for both perturbations, a large region of increased turbulent spectral intensity appears displaced from the wall. And as with the static perturbation, the dissipation of this region of displaced intensity appears to occur more slowly than the corresponding recovery of the near-wall peak. However, in addition to these common features, the dynamic perturbation is distinguished by a spectral signature of the initial perturbation which persists throughout the entire boundary layer and throughout all of the streamwise measurement locations, as shown in figure 5.10 and 5.11. The presence of this spectral signature of the dynamic perturbation, even at the last measurement location, more than  $20 \delta_0$  downstream, indicates that the flow field remains distinctively perturbed even after other statistical measures of the flow's relaxation show an approximate return to equilibrium. The periodic signature's vast extent also demonstrates the ability of even a localized impulsive perturbation to affect the entire downstream flow field, even far from the wall, which shows significant promise for flow control applications. Moreover, the choice of forcing frequency was selected in order to force precisely the range where the superstructure peak is expected at high Reynolds number (which is not clearly defined in the unperturbed flow at least until far downstream, where  $Re_\theta = 4040$ ).

The right columns of figures 5.10 and 5.11 show discrepancy plots of the composite spectra, similar to those formed for the statistical quantities above. As mentioned in section 3.1.4, there is an additional subtlety that the wavelength spectra between the perturbed and unperturbed flows vary as a consequence of the use of Taylor's hypothesis. In order to subtract equivalent ranges, the unperturbed composite spectrum was regridded (by cubic interpolation) to the range of the perturbed spectrum, prior to the subtraction. The unperturbed composite spectra were reasonably robust in the streamwise direction thus making this sort of subtraction justifiable, at least for qualitative observations. The discrepancy maps highlight both the imprint of the organized wave, as well as the partial suppression and recovery of the signature of the near-wall cycle discussed above.

## 5.2.6 Decomposition of the Turbulence Intensity by Spectral Contribution

The integral scale map in figure 5.8a showed suppressed scales near the wall, and by comparison with the statically perturbed flow it was shown that this suppression is a consequence of the spatial impulse aspect of the perturbation. On the other hand, the integral scale map in figure 5.8b (along with the composite spectra in figure 5.10) demonstrated that the organized wave aspect of the perturbation contributed long structures, which actually supplemented the loss of these same-sized structures due to the displacement effect. This same two-part effect was seen also in the  $\sqrt{u'^2(y)}$  statistics. The

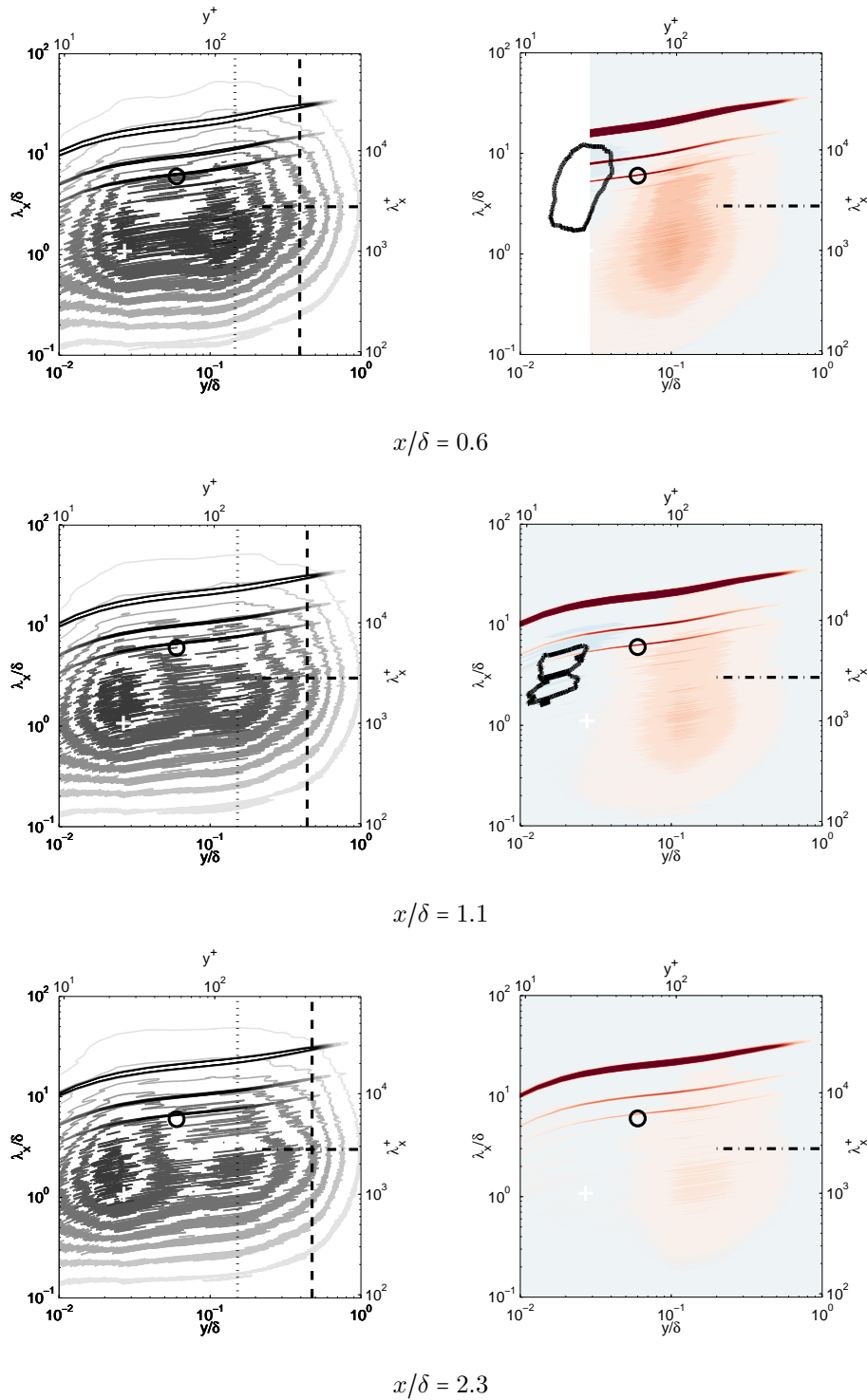


Figure 5.10: (Left) Composite spectra for the perturbed case: the first streamwise location,  $x = 0.1\delta = 1.65$  k, is suspected to be within the mean recirculation bubble downstream of the last roughness element; therefore the third streamwise location  $x = 0.6\delta = 10$  k, which appears to be downstream of the recirculation region, is shown first. Levels follow figure 5.9 and are the same as in Jacobi and McKeon [2011a] (Right) The discrepancy maps for the composite spectra, with a range identical to the spectra themselves, but mirrored for negative values (red are positive, blue negative). The contour line represents a region of spectral content suppressed more than 5% below the unperturbed flow. The dark bands, starting at the forcing frequency, represent the input forcing and its associated harmonics.

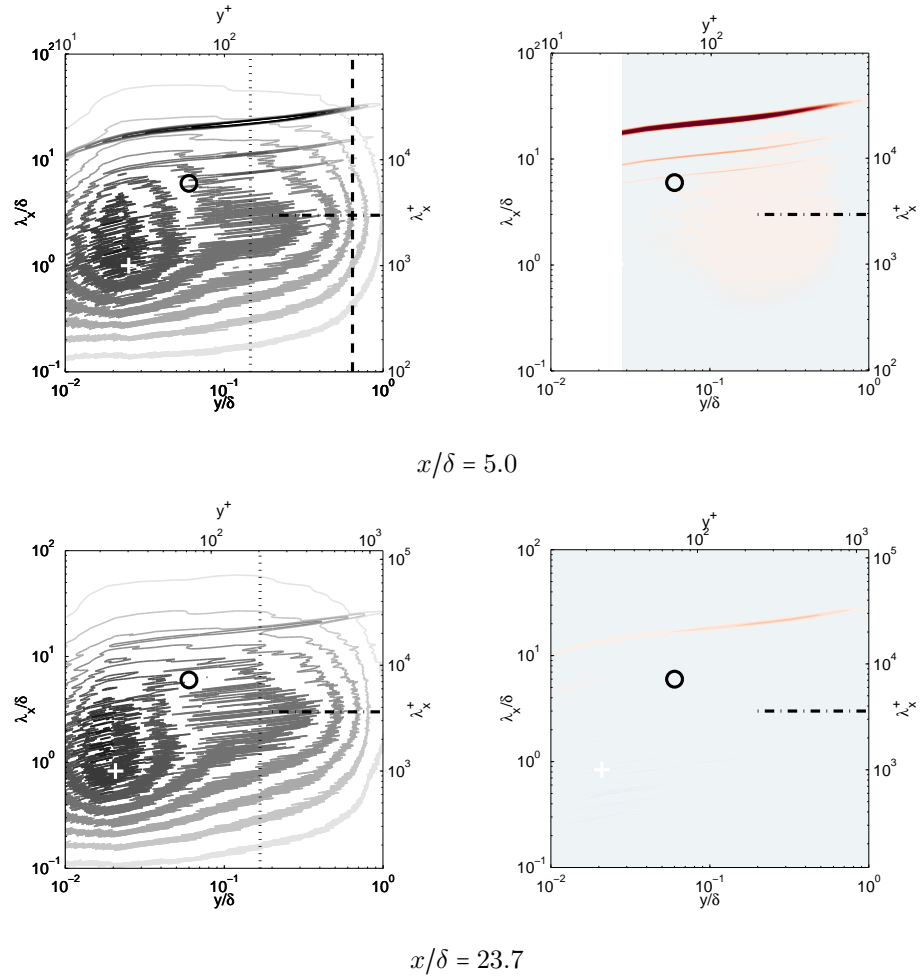


Figure 5.11: (Left) Composite spectra continued from figure 5.10 at additional downstream positions. (Right) Continuation of the discrepancy maps for the composite spectra

profile for the dynamic perturbation showed a broader hump which encompassed the wall-normal locations of the static perturbation and extended far closer to the wall. That hump appears in the composite spectra as the broad energetic region, farther from the wall than the near-wall peak, but in approximately the same region of wavelength space. Since the two different features of the dynamic perturbation – the organized wave and the impulsive roughness – manifest themselves distinctly from a spectral perspective, it seems reasonable to consider exploiting this spectral distinction in order to disentangle the statistical picture. Since the spectra at each wall normal location are normalized by the corresponding values of  $\sqrt{u'^2(y)}$  (equation 5.8), a decomposition of the  $\sqrt{u'^2(y)}$  profiles by spectral contribution is possible, in order to isolate the particular influence of the dynamic perturbation above and beyond the static perturbation.

$$\overline{u'^2}(x, y) = \int_{\lambda_x=\lambda_a}^{\lambda_x=\lambda_b} \Phi(\lambda'_x, x, y) d\lambda'_x \quad (5.8)$$

Now, if structures associated with the impulsive static roughness are presumed significantly smaller than those associated with the dynamic perturbation, which can be inferred from the dynamic composite spectra (figure 5.10), then the wavelength-space of the composite spectra can be partitioned into large and small wavelengths, corresponding to the distinctive contributions from the static and dynamic parts of the perturbation. The composite spectra are integrated over bands of wavelengths ( $\lambda_a \rightarrow \lambda_b$ ) in order to reproduce the previous discrepancy contour plots of figure 5.2, but this time including contributions to  $\overline{u'^2}(x, y)$  from only distinct wavelength bands (figure 5.12). The division between large and small wavelengths was set at  $7\delta$  in order to include the superstructure peak ( $\approx 6\delta$ ) on the ‘small wavelength’ side of the division, which allows for separating the artificially injected, longer wavelengths more easily.

A line has been fitted by least-squares regression to the peaks of the deviation,  $\Delta\overline{u'^2}(x, y)$ , of the perturbed  $\overline{u'^2}(x, y)$  from that of the unperturbed flow. This line shows that a power-law relation describes the shift of the hump associated with the perturbations, as the hump shifts away from the wall and as it decreases in magnitude moving downstream. However, the rate at which this shift occurs is observed to be quite different between the static and dynamic perturbation, as seen in the difference in the inclination of the propagation of the hump between left and right columns. The consequence of this difference is that the hump associated with the static perturbation is expected, ignoring mixing and other effects downstream, to clear the boundary layer  $75\delta$  downstream of the impulse (extrapolating the power law to  $y/\delta = 1$ ), whereas the hump associated with the dynamic perturbation would clear the boundary layer in  $50\delta$ .

However, if the contour plot of the deviation is recalculated according to the above procedure for only small wavelength contributions to  $\overline{u'^2}(x, y)$ , then the static and dynamic cases appear identical. And since, for the static case, this particular range is assumed to relate to near-wall turbulent

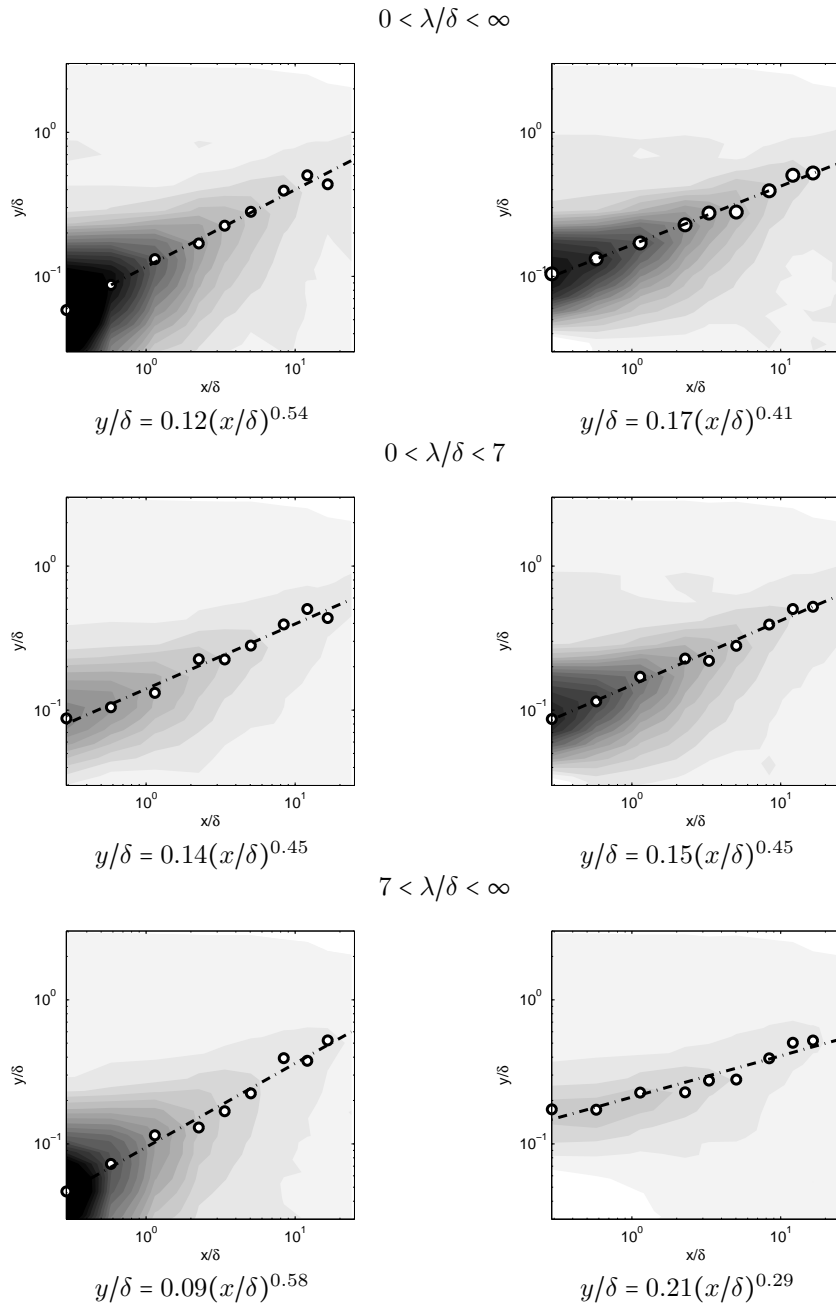


Figure 5.12: Recreating the turbulence intensity variation (figure 5.2) by integrating the streamwise wavelength spectra over different ranges of wavelengths: on the top, the entire wavelength range is integrated to reproduce the previous result. (Left) is the contour map for the variation of the dynamic impulse from the smooth case; (Right) is for the variation of the static impulse from the smooth.  $\circ$  are the trace of the peaks;  $---$  are the power-law fits for the peaks, expressions of which are given below each panel; all levels are the same as in figure 5.2

motions which were displaced over the two-dimensional roughness, as well as any shedding from the elements, it could be inferred that this range also describes similar behavior in the dynamic case. It is observed further that the structures associated with this range move away from the wall at an identical rate between the static and dynamic cases. Whereas, when the contours are recalculated based on contributions from large wavelengths — the kind associated with the dynamic perturbation — the shift of the associated hump away from the wall occurs at detectably different rates between the two cases, in addition to the difference in amplitudes.

In some sense, the hump from the dynamic perturbation has been decomposed into a contribution which behaves like the hump seen in the statically perturbed case, as well as additional energetic content from the dynamic aspect, and these two distinct contributions behave differently both in spatial extent in the flow field and in the rate at which they evolve downstream. The common features include the effect on the spectral signature of the near-wall cycle, the stress bore, and the internal layers. However, the particular contribution from the dynamic case, in the form of the structured (organized) addition of energy to the flow, manifests itself in the redistribution of scales in the flow. The caveat to this proposed decomposition is that, as indicated by the harmonics visible in the spectra of figures 5.10 and 5.11, nonlinear dynamics are certainly present. In order to bolster the claim of separability then, a phase-locked decomposition of the velocity signals is considered in the following sections in order to demonstrate that, at least for practical engineering of the flow field, the linear interactions are the most significant.

### 5.3 The Dynamic Perturbation as an Organized Wave

Having established that the effect of the dynamic perturbation appears to manifest itself in two different ways: as an impulsive roughness effect and as a coherent and persistent organized wave, a phase-locked decomposition following Hussain and Reynolds [1970] is now developed, employing equation 5.2, and key flow properties are examined within that context. In particular, distinct fluctuating velocity modes are identified, and it is shown that they present the classic features of critical-layer organized waves. The properties of the wave are measured here in order to employ a modified Orr-Sommerfeld operator in chapter 6 to predict the observed mode-shapes. The Orr-Sommerfeld analysis involves a linearization of the NSE; this will be justified in the present case following McKeon and Sharma [2010], since the amplification of the input disturbance (forcing) is significant enough to be considered dominant in the following resolvent-analysis of the Orr-Sommerfeld equation.

### 5.3.1 Phase-Locked Decomposition

Considering the standard form of the phase-locked decomposition, used by Hussain and Reynolds [1970], and reported in equation 5.2, the fluctuation from the Reynolds decomposition  $u'(y, t)$  is further divided into a contribution from the periodic perturbation,  $\tilde{u}(y, t)$ , and a fluctuation about that periodic contribution  $u'_t(y, t)$ .  $\tilde{u}(y, t)$  is calculated from the phase average of the velocity signal,  $\langle u(y, t) \rangle$ . The phase average is obtained by first dividing the period of the disturbance into  $n$  segments, then sampling the velocity signal at each segment and finally averaging across segments so that the angle-brackets represent an ensemble average over phases.  $\tilde{u}(y, t)$  is then the difference between the mean value,  $U(y)$ , and the phase-averaged value,  $\langle u(y, t) \rangle$ , and itself has, by definition, zero mean.

By combining the measurements of  $\tilde{u}(y, t)$  at all of the wall-normal locations, maps of the wall-normal variation of  $\tilde{u}(y, t)$  over a mean period (written as  $[0, 2\pi]$ , as determined from the experimental frequency) can be generated for each streamwise measurement location, as shown in figure 5.13. In all of the following phase-locked maps, the contour lines (with levels at intervals of 20% of the maximum) indicate contours scaled on the streamwise-local amplitudes, whereas the color levels are scaled to be consistent across all streamwise positions to allow comparison of relative amplitudes. The persistence of the distinctive shapes of the variation in the decomposed velocity signals, visible via the contour lines even at the most downstream measurement location, testifies to the strong coherence of the stress wave and to the fact that it is a local phenomenon, independent of the fact that the adjacent wall condition is smooth. Also, the periods are plotted to reflect the physical phase shift moving downstream, from which the wavenumber of the perturbation is inferred below.

The contours of the variations in  $\tilde{u}(y, t)$  highlight both the inclination of each mode to the wall and its concentration relatively close to the wall (most prominently for  $y/\delta < 0.2$ ). The colors (indicating the sign and magnitude of each variation) show a phase shift of  $180^\circ$  in the wall-normal direction, although this phase shift is most obvious only for the first five streamwise locations. Importantly, the location of the maximum amplitude tends to drift away from the wall moving downstream, and since the plots are shown in outer units, the rate of this drift is faster than the boundary layer growth. The modes appear to have a shallow downstream inclination for small wall-normal distances, but then lean upstream further from the wall.

In order to obtain the maps for the wall-normal velocity component, a similar phase-locking analysis was conducted on the PIV data. The nature of the velocity decomposition for the case of the PIV is somewhat different due to the additional streamwise variation within the PIV field. The PIV fields were first averaged in the streamwise direction, over  $x$  and then the decomposition described above was applied (equation 5.9) such that there are in fact two turbulent contributions:  $v'_1(y, t)$  is the fluctuation about the streamwise-averaged, phase-averaged field, and  $v'_2(x, y, t)$  is the

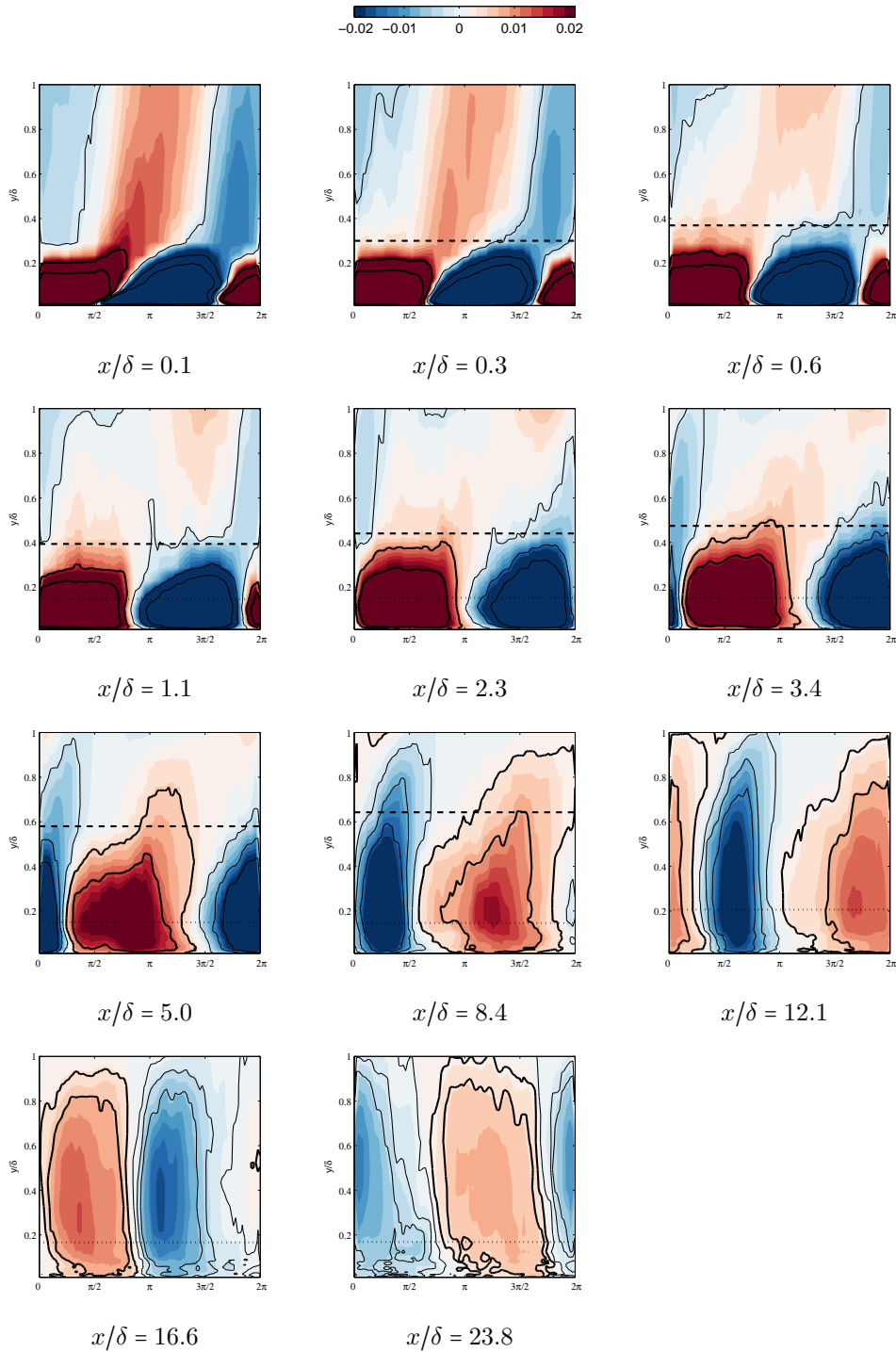


Figure 5.13: A map of  $\tilde{u}(y, t)$  over an average period (abscissa  $t \in [0, \pi]$ ) in outer units (ordinate  $y/\delta$ ) at all of the streamwise locations. The color levels are fixed for all plots, so the amplitude of the mode is physically represented, but the contour lines are scaled per streamwise location and thus represent the shape independent of amplitude. The mean internal layer locations, when interpolatable, are denoted:  $--$  first internal layer, and  $\cdots$  second internal layer

fluctuation about phase-averaged field due to the variation in the  $x$ -domain.

$$v(x, y, t) = V(y) + \bar{v}(y, t) + v'_1(y, t) + v'_2(x, y, t) \approx V(y) + \bar{v}(y, t) + v'_t(y, t) \quad (5.9)$$

For computational simplicity, these two separate turbulent contributions were treated together, such that the  $v'_t(y, t)$  from an extension of equation 5.1 to the wall-normal component is equivalent to  $v'_1(y, t) + v'_2(y, t)$  under the present analysis. The PIV phase-locking was also accomplished somewhat informally, without an external reference, by comparison with the velocity signal nearest to the wall, where the signal was well preserved and strong enough to allow for a reliable phase-lock as shown by validation against the formally phase-locked hotwire analysis. The wall-normal phase-locked maps are reproduced in Section 6.3 (figure 6.4). The wall-normal contours show more elongated shapes, not attached closely to the wall like the streamwise modes, and they also contrast with the streamwise modes for their lack of prominent inclination and  $180^\circ$  phase-shift. The mean amplitude of the streamwise modes was  $\approx 2$  times the magnitude of the wall-normal modes, whereas the peak of the streamwise mode was roughly an order of magnitude larger than the wall-normal mode peak ( $\approx 5.7$ ).

The significance of the fluctuating quantities  $u'_t(y, t)$  and  $v'_t(y, t)$  and their relationship to the periodically changing quantities will be presented in chapters 7 and 8.

### 5.3.2 Experimental Parameters of the Perturbation

Having observed the output of the dynamic perturbation in the form of distinct modal shapes in both velocity components, the question of the precise nature of the input remains. While the input frequency can be set externally and the roughness is essentially two-dimensional, the flow effectively sets the streamwise wavelength through the lengthscale associated with flow separation and reattachment either side of the roughness perturbation. However, the use of multiple, phase-locked, streamwise measurements provides a straightforward means of inferring the wavenumber of the dynamic perturbation from the streamwise development of the amplitude and phase of the modes. The detailed calculations are described extensively in Hussain and Reynolds [1970] and Hussain and Reynolds [1972] and a brief overview is provided below.

The real part of the wavenumber  $k_r$  is inferred from the rate of change of the phase of the perturbation (denoted by the angle symbol,  $\angle$ ) with streamwise distance,  $k_r = \partial(\angle \tilde{u})/\partial(x/\delta)$ . This relationship is linear for most of the downstream extent of the perturbation (and therefore the slope is obtained by least-squares fitting to a line, equation 5.10).

$$\angle \tilde{u} = 0.336(x/\delta) + 1.040 \quad (5.10)$$

However, in the immediate vicinity of the roughness perturbation, for  $x/\delta \lesssim 1$ , the rate of change is faster, and is described with a logarithmic fit (equation 5.11).

$$\angle \tilde{u} = 63.5 \log_{10}(x/\delta) + 61.0 \quad (5.11)$$

The faster growth rate is a consequence of the velocity deficit (or region of reversed flow) immediately downstream of the roughness. As this deficit quickly recovers, the rapid change in the mean velocity profile results in a nonlinear phase change over a very short distance. Previous studies by Hussain and Reynolds [1972] considered only locations sufficiently far from the input for the linear growth rate to be obtained. By considering closer points also, the phase-shift can be used as a second confirmation that the measurements beyond  $x/\delta \approx 1$  are well clear of any significant flow reversal; however this estimate is quite conservative, since it also includes significantly decelerated, but not reversed flow, and thus is consistent with the previous estimate of the recirculation bubble itself for  $x/\delta < 0.3$ . The important consequence of this is that the wavespeed inferred by the linear fit applies only to the region where the linear fit is itself valid.

The streamwise variation was measured at the wall-normal locations where the wave amplitude was largest. However, the same process could be carried out at all of the wall-normal measurement locations, conducting a series of streamwise comparisons for each wall-normal location (in outer units). Using this method results in a significant amount of variation, as shown in figure 5.14. Following a similar method, the imaginary component of the wavenumber can also be inferred and is shown; this quantity will be discussed below. It is clear, however, from figure 5.14 that the error is not random, but rather is strongly biased by the wall-normal location of the measurements, with higher magnitudes of both wavenumbers in the inner region of the boundary layer outside the buffer layer, and decreasing magnitude moving towards the wall or towards the intermittent edge of the boundary layer. To understand this discrepancy between the two methods of calculating the wavenumbers, the ratio of the real component of the wavespeed to the mean convective velocity is plotted in figure 5.15, where the complex wavespeed is defined as  $c = \omega/k = c_r + ic_i$ ,  $\omega$  being the input frequency. The fact that the wavespeed measured as a function of wall-normal location  $c_r(y)$  is smaller than the wavespeed at the location of maximum wave amplitude  $c_r$  across most of the boundary layer (except in the intermittent region) is a consequence of the observation that the location of the maximum wave amplitude drifts away from the wall faster than the rate of boundary layer growth, as reported above. In other words, over a fixed streamwise distance, the peak perturbation has traveled further away from the wall and thereby advanced further in phase than it would have if it remained at a fixed height in outer units.

Calculating the wavenumber at the location of maximum amplitude yields a wavespeed of  $c = 0.464 - 0.066i$  in outer units, which means that the disturbance is not strictly ‘neutral’, but rather

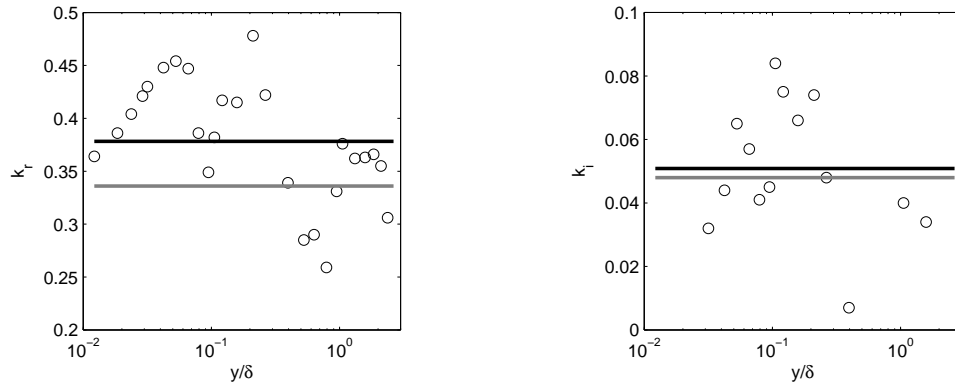


Figure 5.14: The variation in the measurement of values of the streamwise wavenumber for the perturbation,  $k = k_r + ik_i$  when calculated as described above at different wall normal locations. (Left)  $\circ$  The variation in  $k_r$ ; — mean  $k_r = 0.378$ ; — Calculated from the peak signal strength,  $k_r = 0.336$ . (Right)  $\circ$  The variation in  $k_i$ . — mean  $k_i = 0.051$ ; — Calculated from the peak signal strength,  $k_i = 0.048$ .

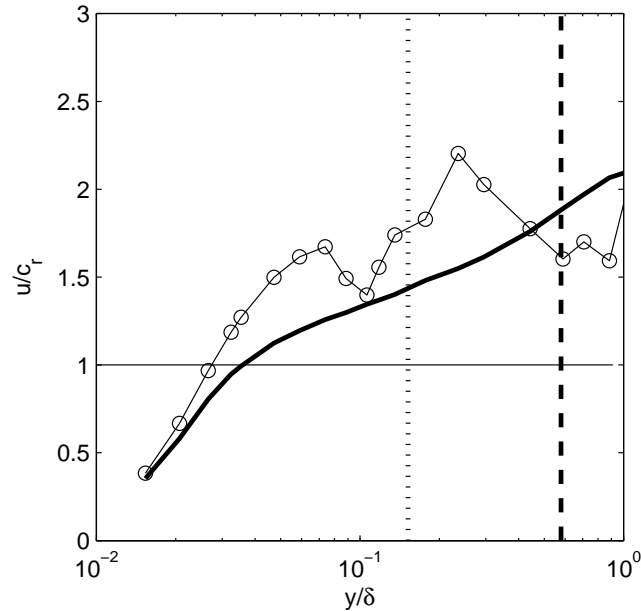


Figure 5.15:  $\circ$ — The mean unperturbed convective velocity  $U(y/\delta)$  divided by the real part of the wavespeed  $c_r(y/\delta)$  which was calculated from the gradient of the phase change at each wall-normal position. — The same ratio of speed, but with the real part of the wavespeed  $c_r$  calculated from the gradient of the change in phase at the location of the peak perturbation strength, showing a crossing at  $y_c/\delta = 0.04$ , which indicates the presence of a critical layer. The mean location of the internal layers, identified above in figure 5.6, have been marked for the streamwise component: --- the first internal layer;  $\cdots$  the second internal layer.

	$k_r$	$k_i$	$Re$ $= U\delta/\nu$	$f$ (Hz)	$\omega_r$ $= 2\pi f\delta/U$	$\lambda$ $= 2\pi/k_r$	$y_c$
Experiment	0.336	0.048	$2.24 \times 10^4$	30	0.159	18.70	0.04*
Schlichting [1950]	0.466	0	$2.62 \times 10^3$		0.163	13.48	0.209
Schubauer and Skramstad [1943]	0.528		$2.64 \times 10^3$	103	0.161	11.90	0.2
Hussain and Reynolds [1970]	0.981	0.073	$1.38 \times 10^4$	25	0.746	6.40	—

\* value at  $x/\delta = 0.1$ ; see discussion below

Table 5.2: Parameters for the perturbation

	$ \tilde{u} /U$	$ \tilde{u} /\sqrt{u'^2}$
Experiment	$2.5 \times 10^{-2}$	0.325
Schubauer and Skramstad [1943]	$1.7 \times 10^{-2}$	
Hussain and Reynolds [1970]	$5.8 \times 10^{-3}$	0.059

Table 5.3: Magnitude of perturbation

decays, consistent with the results of Hussain and Reynolds [1972]. The wavelength for the dynamic perturbation appears to be quite long — constituting approximately 17% of the total length of the plate or a little more than a third of the section downstream of the perturbation. The key parameters for the perturbation are provided in Table 5.2 (along with additional comparisons, relevant to the subsequent analysis), where all terms are nondimensionalized in outer units, except the frequency of the perturbation,  $f$ , which is left dimensional for comparison. Note that the equivalence of the wavespeed with the local mean velocity,  $u/c_r = 1$ , which occurs in the vicinity of  $y/\delta = 0.04$  is a characteristic of a ‘critical’ disturbance, as will be discussed further below.

The amplitude of the perturbation is also of significant interest. In particular, the ability of a single mode or small number of modes of the resolvent analysis, in chapter 6, to accurately represent the observed dynamics is expected to depend on the relative strength of the ‘external forcing’ in relation to the ‘internal forcing’. As noted in section 5.1, the forcing considered by Hussain and Reynolds [1970] was actually weaker, in one sense, than that achieved by the ribbon in early transition studies of laminar flow, shown in table 5.3, presumably making the signature of the perturbation difficult to discriminate from other influences in the flow. The current experiment, by virtue of the roughness perturbation, generates a stronger perturbation, thereby increasing the likelihood that a small number of modes of the resolvent should adequately describe the flow.

### 5.3.3 Streamwise Velocity Mode Development

The qualitative observations regarding the shape of the modes, shown in figure 5.13, can be made more precise by calculation of the wall-normal profiles of the amplitude (figure 5.16) and phase (figure 5.17) of each mode, as they vary throughout the boundary layer, where the modes were picked out by means of a Fourier transform of the instantaneous velocity signal. This procedure was

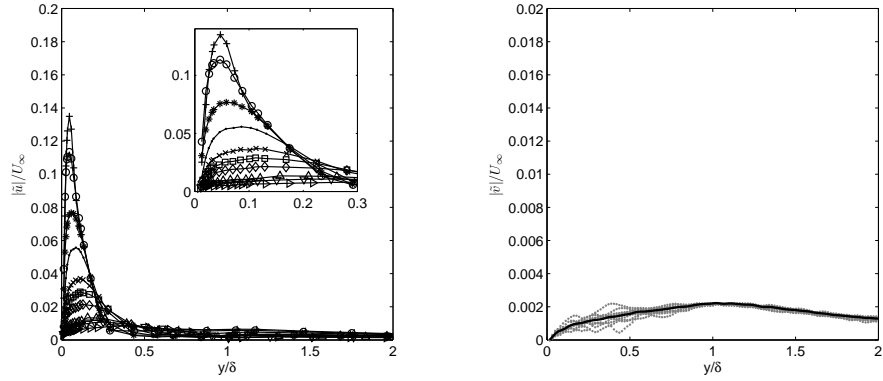


Figure 5.16: (Left) The amplitude variation in  $\tilde{u}(y, t)/U_\infty$ :  $x/\delta = 0.1 +$ ;  $0.3 \circ$ ;  $0.6 *$ ;  $1.1 \cdot$ ;  $2.3 \times$ ;  $3.4 \square$ ;  $5.0 \diamond$ ;  $8.4 \triangle$ ;  $12.1 \nabla$ ;  $16.6 \triangleright$ ;  $23.8 \triangleleft$  (Right)  $\tilde{v}(y, t)/U_\infty$ : light symbols refer to different PIV runs in order to indicate variability; bold — mean for all PIV

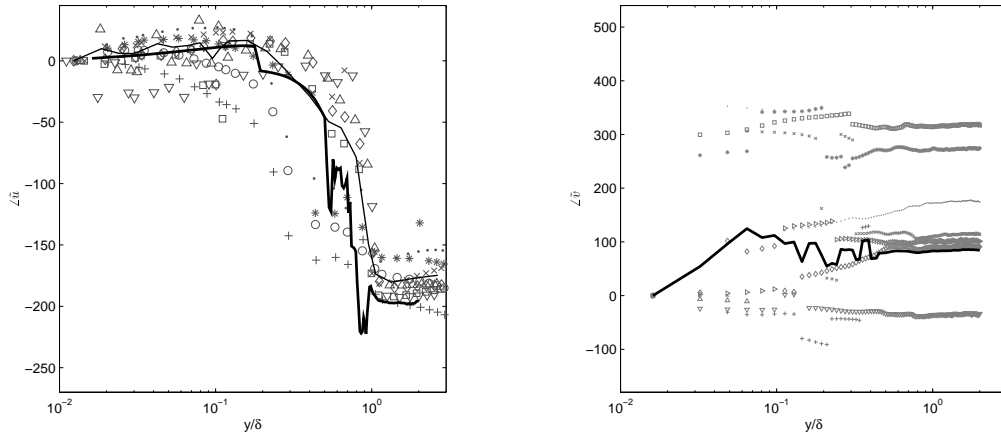


Figure 5.17: (Left) The phase variation of  $\tilde{u}(y, t)$  in degrees:  $x/\delta = 0.1 +$ ;  $0.3 \circ$ ;  $0.6 *$ ;  $1.1 \cdot$ ;  $2.3 \times$ ;  $3.4 \square$ ;  $5.0 \diamond$ ;  $8.4 \triangle$ ;  $12.1 \nabla$ ; — mean for all streamwise locations; bold — mean for all PIV runs. (Right)  $\tilde{v}(y, t)$ : light symbols refer to different PIV runs; bold — mean for all PIV

carried out for all of the PIV measurements taken at a single streamwise location, as well as the full range of streamwise locations interrogated with the hotwire.

The variation of the amplitude of the streamwise mode shows a reasonably sharp peak near the wall, followed by a decay. The peak for the mean of the PIV runs is located at  $y/\delta = 0.13$ ; the mean for the hotwire profiles is in roughly the same location, although there is significant variation in peak location with streamwise location. But in general, the variation in amplitude and phase for both velocity components substantiate the qualitative description offered above for a closely attached streamwise mode with a sharp phase change and a larger unattached wall-normal mode with minimal phase variation.

The streamwise variation was also identified for the location of the  $180^\circ$  phase shift in  $\tilde{u}(y, t)$ ,

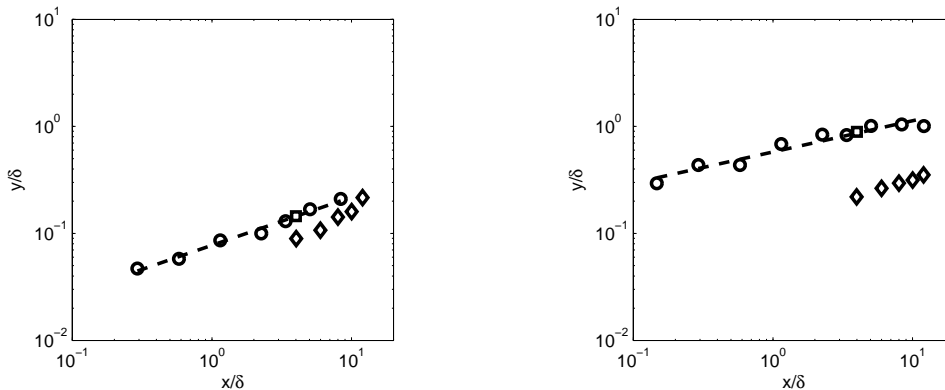


Figure 5.18: (Left) The variation in the wall-normal location of the peak amplitude of  $\tilde{u}(y, t)$ , with range of  $0.04 < y/\delta < 0.21$ ;  $\circ$ ; — least square best fit  $(y/\delta) = 0.08(x/\delta)^{0.45}$ ;  $\square$  from PIV; (Right) The variation in the wall-normal location of the  $180^\circ$  phase shift in  $\tilde{u}(y, t)$  (approximated by  $\Delta 120^\circ$ ),  $\circ$ ; — least square best fit  $(y/\delta) = 0.58(x/\delta)^{0.29}$ ;  $\square$  from PIV.  $\diamond$  Results from Hussain and Reynolds [1970] for channel flow (under 100 Hz perturbation)

normalizing the initial value of the streamwise mode's phase, at the wall, to 0 for all streamwise locations. Both streamwise trends (figure 5.18) indicate that the mode associated with  $\tilde{u}(y, t)$  is growing downstream of the perturbation, slowly detaching from the wall and enlarging the domain of the in-phase signal.

## 5.4 Discussion of the Dynamic Impulse Experiment

A dynamic impulse of roughness was used to explore the connection between the fundamental features of impulsive perturbations to turbulent boundary layers, as identified in previous work, and the distinctive effects of introducing an organized wave into the flow field. Experiments provided comprehensive measurements of the flow field, which could be decomposed via phase-locking to illuminate the periodic component. In a mean sense, the dynamic impulse manifested a number of the features of the static impulse, from similar internal layers, to deformations of the streamwise statistics, and a partial suppression of the near-wall cycle as observed by spectral composite maps; nevertheless, significant differences warrant special attention. The wave-behavior appeared embedded in the broad shape of the hump in the streamwise turbulence intensity, which was shown to be decomposable into a small-wavelength contribution associated with the roughness impulse and a large-wavelength contribution associated with the organized wave itself. And this distinction between the two contributions of the dynamic impulse was also apparent in the contrast between the integral scale diminution and the spectral composite maps, where turbulence scales were reduced by the roughness impulse, but compensated for by the injection of large scales in the form of the organized wave. These individual observations together suggest that the dynamic impulse provides

a much more nuanced and sophisticated method of modifying the turbulent boundary layer, targeting particular structural sizes and specific spectral features of the near-wall cycle. But the most remarkable feature of the dynamic perturbation is the persistence of the wave organization, as shown through the phase-locked decompositions. Not only the mean flow, but higher-order statistics, and the shear stress embodied the key features of the organized wave, as far downstream as was measurable (more than  $20 \delta$ ). From a short impulse, a dynamic stress wave was introduced to the turbulent boundary layer and continued to alter the flow field locally, completely independent of the restored unperturbed boundary condition. This locality of the disturbance provides a powerful insight into the receptivity of the turbulent boundary layer to small modifications.

Having carefully described the precise behavior of the modes which are exhibited under the dynamic perturbation, the challenge remains to predict them. McKeon and Sharma [2010] proposed that turbulent wall-bounded flow can be modeled as a superposition of propagating modes of velocity fluctuations. Under such a framework, the mode observed as a result of the dynamic perturbation, above, is just a particular component of the overall superposition which constitutes the flow which is being energized by the dynamic impulse. It follows then that the experimental mode should be amenable to the same critical layer analogy employed by McKeon and Sharma [2010].

## Chapter 6

# The Resolvent Method in the Perturbed Boundary Layer

### 6.1 The Forced Orr-Sommerfeld Problem

The resolvent method of McKeon and Sharma [2010] was used to predict the fluctuating velocity modes observed in the turbulent boundary layer under periodic perturbation, by treating the forced boundary layer as a modified form of the classical Orr-Sommerfeld problem. The Orr-Sommerfeld problem treats the linear stability of parallel flows under small perturbations by first considering a linearization of the Navier-Stokes equations and then formulating an eigenvalue problem to describe the growth or decay of those perturbations. Previously, Reynolds and Hussain [1972] considered how the Orr-Sommerfeld equation could be adapted to the problem of a turbulent shear flow, where (unlike the laminar flows in transition studies) the nonlinear terms should be significant, but a new approach based on the resolvent operator is considered here. In the following analysis (section 6.2), the significant features of the traditional Orr-Sommerfeld problem are presented, the case of a forced Orr-Sommerfeld problem is introduced, and the differences between these two problems are considered. The dominant modes of the forced problem are then calculated (section 6.3) using the wave parameters identified previously, and the predicted mode shapes are compared to those recorded by the phase-locked measurements. Discrepancies between predictions and measurements are interpreted in the context of the nonequilibrium boundary layer, and finally, some of the technical challenges involved in solving the resolvent problem in a boundary layer (section 6.4) are discussed.

### 6.2 Resolvent Formulation

The governing Orr-Sommerfeld equation is found from substituting a perturbed velocity field, equation 6.1

$$u(y, t) = U(y) + \tilde{u}(y, t), \quad v(y, t) = \tilde{v}(y, t) \quad (6.1)$$

into the Navier Stokes momentum equation, linearizing the results, and then allowing the perturbation to assume the form of an exponential stream-function, equation 6.2, where the amplitude of the disturbance is purely a function of the wall-normal location.

$$\psi(x, y, t) = \phi(y)e^{i(kx - \omega t)} \quad (6.2)$$

Variables  $y$ ,  $U$ , and  $k$  are all nondimensionalized in outer units by  $\delta$  and  $U_\infty$ . As defined above, the complex wave velocity is  $c = \omega/k = c_r + ic_i$ . After substituting the perturbation, a fourth-order equation for the amplitude of the propagating disturbance  $\phi(y)$  is obtained, equation 6.3

$$(U(y) - c)(D^2\phi(y) - k^2\phi(y)) - D^2U(y)\phi(y) = \frac{1}{ikRe} (D^4\phi(y) - 2k^2D^2\phi(y) + k^4\phi(y)) \quad (6.3)$$

where  $D = \partial/\partial y$ , with physical boundary conditions for the perturbations of no-slip at the wall and decay in the free stream, equation 6.4

$$\tilde{u}(y, t) = \tilde{v}(y, t) = 0, \quad y \rightarrow 0, \infty \quad (6.4)$$

along with parallel flow at the edge of the boundary layer itself.

Importantly, in the limit of high Reynolds number (the inviscid limit) the governing equation presents a singularity at the point  $U(y_c) = c$  where  $y_c$  is known as the critical point. At the point of the singularity, the amplitude of the disturbance would become infinite in a purely inviscid regime, and thus viscosity must be considered not only near the wall but also in a small domain about the critical point itself, known as the critical layer. It is precisely the critical-layer solution to the Orr-Sommerfeld equation which is of interest in the subsequent analysis, since this critical point occurs under the present forcing, as shown in figure 5.15. In the following, references to the features of the critical layer indicate those features of the classical, linear, inviscid analysis with a viscous critical layer, as noted in Maslowe [1986], although the method of analysis in the current study does not formally exclude nonlinear behavior in the way the classical linearization does, due to its use of the resolvent as noted above.

The Orr-Sommerfeld operator  $\mathcal{S}$  can be written as a general eigenvalue problem in two parts, following the notation of Reddy et al. [1993], with  $\mathcal{S} = \mathcal{B}^{-1}\mathcal{A}$  where  $\mathcal{A} = (ikRe)^{-1}(D^2 - k^2)^2 - U(D^2 - k^2) + D^2U$  and  $\mathcal{B} = -(D^2 - k^2)$ , with the complex eigenvalue  $c$ , the wavespeed of the disturbance

$$\mathcal{A}\phi(y) = c\mathcal{B}\phi(y) \quad (6.5)$$

McKeon and Sharma [2010] approached the Orr-Sommerfeld operator described above in a similar way (with the use of a three-dimensional divergenceless basis in place of the two-dimensional stream

function approach) but retained the nonlinear terms from the Reynolds decomposition of the velocity field and grouped them into an ‘internal’ forcing term  $f$ , as described in §5.1. The forced problem then appears as

$$(cI - \mathcal{S})\phi(y) = f \quad (6.6)$$

When  $f = 0$ , the linearized (traditional) Orr-Sommerfeld problem is recovered.  $f$  can also be generalized to include not only the nonlinear ‘internal’ forcing, but also external forcing applied to the system. The operator which acts on  $f$  is defined as the resolvent (or propagator)  $\mathcal{R}$ , where

$$\mathcal{R} = (\sigma I - \mathcal{S})^{-1} \quad (6.7)$$

In this notation, the resolvent set of wavespeeds,  $\sigma$ , is complementary to the set of eigenvalues  $c$  of  $\mathcal{S}$ , following Kato [1966], since singular values of the resolvent are identically the eigenvalues of the Orr-Sommerfeld operator. When considering the ‘internal’ forcing by nonlinearities, McKeon and Sharma [2010] expanded the resolvent operator using a Schmidt decomposition (the continuous form of the singular value decomposition), and wrote the resolvent as

$$\mathcal{R} = \sum_{n=1}^{\infty} \psi_n(y) \rho_n \zeta_n(y)^* \quad (6.8)$$

where  $\rho_n$  are the singular values, and  $\psi$  and  $\zeta$  are the left and right Schmidt bases. McKeon and Sharma [2010] showed how consideration of the dominant singular mode of the decomposed resolvent can predict key features of wall-turbulence, without explicit treatment of the closure problem. Turning to the problem of a perturbed turbulent wall-bounded flow, the ‘black-box’ (or unstructured) forcing in the resolvent treatment now represents both the ‘internal forcing’ of the nonlinearities in the base turbulent flow, along with the ‘external forcing’ injected into the flow by the perturbation, and it should be expected that the resolvent method should again identify the singular modes which similarly represent the dynamics of the system.

### 6.3 Mode Calculation and Comparison

The Orr-Sommerfeld problem was discretized with a spectral approach utilizing the formulation of the Chebyshev differentiation operators outlined in Weideman and Reddy [2000]. The details of the calculation are provided in the section 6.4. The eigenvalue spectrum and pseudospectrum of the resolvent were calculated (figure 6.1) and indicate that the forcing in the present setup is not only stronger than that used by Reynolds and Hussain [1972] but also that the forcing is in a region of the eigenspectrum displaying significant sensitivity. Importantly, the region of increased sensitivity due to the nonnormality is quite broad, particularly at higher forcing frequencies, which may allow

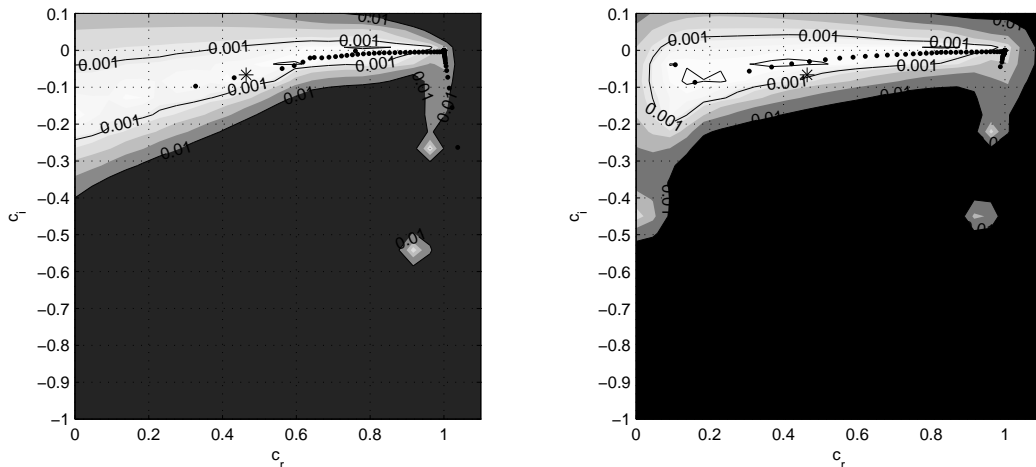


Figure 6.1: Spectrum and pseudospectrum (for  $N = 100$ ) with contour levels (calculated via the  $L_2$  norm of the resolvent) at  $\epsilon = 10^{-5}, 10^{-4}, 10^{-3}$  with decreasing thickness. The eigenvalues are marked as points and the forcing is denoted with an asterisk. The forcing appears near a region of relatively high sensitivity (high-valued norm of the resolvent). The disconnected region is a numerical artifact of the contour routine. (Left) Unperturbed velocity profile. (Right) Perturbed velocity profile

for a significant range of nonresonant forcing that can still be described adequately by the linear eigenfunctions.

A significant subtlety must also be considered in the analysis of the modified Orr-Sommerfeld operator: the choice of the turbulent velocity profile. The flow under consideration here is neither parallel nor under equilibrium conditions: the importance of these two violations of the fundamental assumptions underlying the analysis will be investigated in what follows. Using the incoming, unperturbed turbulent velocity profile (as done in figure 5.15) means that the governing operator remains ignorant of the particular nonequilibrium perturbation used in forcing the flow. In contrast, using a perturbed profile allows the operator to take into account the spatially varying effect of the perturbation on the flow field. Both of these calculations were performed in the remaining analysis.

The mode shapes for the most amplified mode were identified by singular value decomposition of the resolvent  $\mathcal{R}$  with the experimental forcing, using the eigenvalues in table 5.2, and amplitude and phase results are shown in figures 6.2 and 6.3. In addition, the mode shapes for the closest eigenvalue were calculated for comparison between the approaches. Somewhat surprisingly, these two mode shapes appeared to coincide to a significant degree (and were thus excluded from the plots for readability). This appears to be a consequence of the turbulent velocity profile on the Orr-Sommerfeld operator, wherein the distribution of eigenvalues appears to shift closer to the real axis than in the laminar case, thereby lessening the extent of ‘non-self-adjointness’ of the operator. In the limit of a selfadjoint operator, the singular modes and eigenmodes would overlap, so the fact that the discrete portion of the eigenspectrum of  $\mathcal{S}$  tends closer to being real indicates a larger region

over which singular and eigenmodes are expected to appear similar.

In order to assess the quality of the predictions by the resolvent method, certain key features of the experimental measures are considered: (1) the peak of the streamwise mode amplitude, which represents the location of the critical layer; (2) the wall-normal location of the  $180^\circ$  phase shift in the streamwise mode phase; (3) the relative amplitudes of both mode shapes across the boundary layer; (4) the sense of the phase change across the boundary layer.

(1) The calculated streamwise amplitude variation is shown in figure 6.2 for resolvent operators employing both the perturbed and unperturbed velocity profiles. The amplitude for the unperturbed profile shows an absolute peak coincident with the experiment at  $x/\delta \approx 2.3$ , while the overall shape better matches the experiment at the very first streamwise position  $x/\delta \approx 0.1$ , indicating a critical layer location similar to that predicted in figure 5.15. This discrepancy is a consequence of the violation of the nonparallel flow assumption, as the boundary layer grows downstream, as well as the nonequilibrium distortion of the mean velocity profile. By employing the perturbed velocity profile in the resolvent operator, this discrepancy can be ameliorated at least partly, in which case the calculated mode shape appears better matched to the experimental shape at  $x/\delta \approx 2.3$ . However, the difficulty in properly extending the experimental velocity profile to the wall in the perturbed case (as noted in the section 6.4) renders the results significantly noisier and, overall, less easily interpreted. Using either profile, the magnitude of the peak is significantly overestimated. The sharpness of the predicted peak at the critical layer was a key problem identified by Reynolds and Hussain [1972] as a failure of the quasi-laminar approach and a justification for explicit treatment of Reynolds stresses. However, even with explicit treatment of the Reynolds stresses, an overestimate of the sharpness of the critical layer peak might be expected on dissipative grounds, due to the local shear within the critical layer. Since viscous dissipation in the turbulent kinetic energy budget scales with shear (including  $\frac{\partial u'}{\partial y}$ , which would not be included in the Reynolds stress term counted in the energy budget of the mean flow), the larger the amplitude of a streamwise disturbance, the higher the shear between the peak of the disturbance and the neighboring disturbed flow, and the greater the dissipation rate within the disturbance itself. In other words, the region of peak amplitude disturbances is expected to decay faster than regions of lower amplitude, even when Reynolds stresses are accounted for, and in fact Reynolds and Hussain [1972] found that even including an eddy model closure scheme for the Reynolds stress, the peaks flattened but still failed to match measurements. With this preface in mind, it is clear that the mode shape identified by the resolvent analysis significantly overestimates the sharpness of the critical layer peak, even though the overall shape was captured adequately.

(2) The location of the  $180^\circ$  phase shift, shown in figure 6.3, is captured well in its expected location in the outer region of the boundary layer, as noted in the Appendix. However, it is immediately apparent that the sense of the phase shift is reversed in the experiment from that expected

in traditional Orr-Sommerfeld modes. Indeed, there appears to be a close alignment of the phase for wall-normal locations below the location of the second internal layer. In the region between the two internal layers, the phase agreement begins to deteriorate, and beyond the mean edge of the first internal layer the phase trends appears to diverge and take on a mirror appearance to one another. That this divergence occurs beyond the second internal layer and that it does not appear to affect the wall normal location of the phase-shift are both suggestive of the idea that the discrepancy in phase can be explained by the effect of the stress bore, since the location of the  $180^\circ$  phase shift is a consequence of the crossing of the two inviscid solutions in the asymptotic analysis of the Orr-Sommerfeld problem (noted in the Appendix), and thus is a feature of the outer region of the boundary layer.

(3) The wall-normal amplitude shows reasonable agreement in the region below the first internal layer, and as with the streamwise mode phase, that agreement deteriorates in the region between the two internal layers and shows significant disagreement farther away, where the experimental amplitude is higher. This deviation is expected, since the streamwise turbulent fluctuations of the base flow are significantly stronger than the wall-normal fluctuations, generating greater mixing, and hence the experimental wall-normal amplitude will be suppressed less than the streamwise amplitude. Fitting the predictions to the streamwise amplitude will then necessarily result in a seeming underestimate of the wall-normal amplitude.

(4) As noted above, beyond the first internal layer, the sense of the phase appears to be reversed between the experiments and calculations. However, within the second internal layer, the downstream orientation of the modes is captured quite well. In addition, a distinct feature of the calculated modes, noted by an ‘(a)’ in figure 6.3, is a slight reversal in phase just beyond the location of the critical layer. This reversed phase is also seen, although grossly distorted, in the experimental measurements. In the outer region of the boundary layer, where the experimental signals are weaker and the influence of the intermittent edge is more pronounced, the experimental mode shapes indicate an upstream inclination, whereas the predictions show a downstream inclination. Considering all three regions of the boundary layer together, the experimental observations suggest crescent shaped modes, but the predictions indicate sigmoidal shapes. The precise explanation for the phase discrepancy in the streamwise mode outside of the second internal layer is a topic of ongoing investigation. In the wall-normal direction, the phase predictions appear satisfactory, including the inclination at very low wall-normal locations, excusing some experimental noise.

The resolvent approach does not appear to adequately avoid the incorrect peak amplitude prediction which also afflicted the quasi-laminar eigenmode analysis, although the qualitative prediction of the shape and amplitude was quite accurate and may be sufficient for a variety of potential control applications, which can leverage the simplicity of the resolvent calculation. Where the resolvent calculations performed best was within the second internal layer, where the appropriate sense of

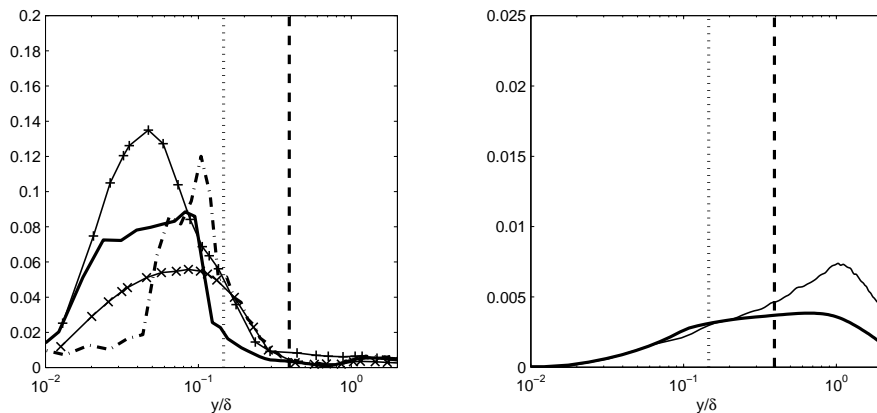


Figure 6.2: (Left) The amplitude variation in  $\tilde{u}(y, t)$ : — from the resolvent analysis using the unperturbed velocity profile; --- from the resolvent analysis using the perturbed velocity profile;  $x/\delta = 0.1 + ; 2.3 \times$  from the experimental hotwire measurements. (Right) The amplitude variation in  $\tilde{v}(y, t)$ : — from the resolvent analysis using the unperturbed velocity profile; — from the experimental PIV measurement with PIV window centered at  $x/\delta \approx 4$ . The location of the internal layers, identified above in figure 5.6, have been marked for the streamwise component: --- the first internal layer; ... the second internal layer.

phase, and thereby orientation of structures, was predicted. The region between the two internal layers represents flow affected by both the roughness effects and the periodic forcing. Within the second internal layer, however, the roughness effect is largely excluded, but the dynamic forcing persists quite strongly, as shown in figure 5.12. Therefore, in some sense, the region within the second internal layer represents a region of flow perturbed only temporally, and the resolvent analysis performs reasonably well. This perspective also contributes to the explanation why using the unperturbed profile achieves better results (besides the difficulty of extrapolating an accurate profile at the wall) — the region in which the results are best is, in fact, largely unperturbed, since it is situated beneath the mean region of the stress bore.

The analysis is significantly complicated by the interplay between the nonequilibrium conditions and the effect of the perturbation itself, aside from the standard challenges of the turbulent boundary layer. However, it is also worth reiterating that the added experimental complication of employing a finite patch of roughness as the forcing mechanism (instead of a thin ribbon) achieves two positive ends: it provides better insight into how a practical forcing mechanism would ultimately behave, and it allows contrast with some of the previous work using wire ribbons, where the weaker forcing in the velocity field was not intimately connected to the mechanism by which it was generated.

The observed spreading of the fluctuating velocity modes and their movement away from the wall — all in violation of the parallel flow assumption — seem to correspond to the observed movement of the stress bore for general nonequilibrium flows, even in the statically perturbed case. These parallels are worthy of future investigation, as they may shed light on the difference between the

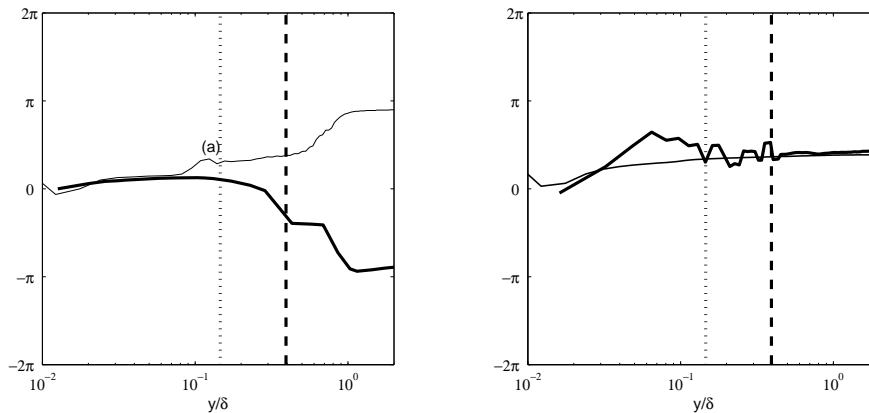


Figure 6.3: (Left) The phase variation of  $\tilde{u}(y, t)$ , with markings as indicated in figure 6.2 (Right) The phase variation in  $\tilde{v}(y, t)$  with markings as above. The (a) marks a distinctive variation in phase which is a robust feature of all Orr-Sommerfeld type solutions.

effects of the re-equilibration process and the changes generated by the dynamic perturbation itself.

Lastly, note that the first singular value output by the resolvent analysis has a magnitude  $\rho_1 = 2-5 \times 10^3$  (where the exact value depends on the assumed mean profile). Since the resolvent formulation of equations 6.6 and 6.7 can be thought of as essentially an input-output relationship and the output (the observed velocity mode) has finite amplitude, this suggests that only a tiny component (in the most amplified direction) of the relatively large forcing due to the dynamic roughness input is responsible for the coherent response of the flow. Therefore it could be expected that a smaller wall forcing with optimized coupling to the flow could achieve the same effect, a topic of current investigation.

## 6.4 Nonnormality in the Orr-Sommerfeld Operator

The nonnormality of the Orr-Sommerfeld operator, described in the introduction, is manifest in the sensitivity of its eigenvalues to small perturbations, and the degree of that sensitivity provides a means of measuring the level of nonnormality. Reddy et al. [1993] outlined the most intuitive method for measuring this degree of nonnormality through the calculation of a ‘pseudospectrum’ defined by the level curves of the norm of the resolvent. The pseudospectrum indicates the extent of the region of high sensitivity about each eigenvalue and makes clear that simply calculating the eigenvalues in the traditional way may not be meaningful without also calculating the accompanying pseudospectrum.

To solve the eigenvalue problem, a spectral approach using Chebyshev collocation matrices was employed. The calculation was first performed on the Blasius solution of the laminar boundary layer

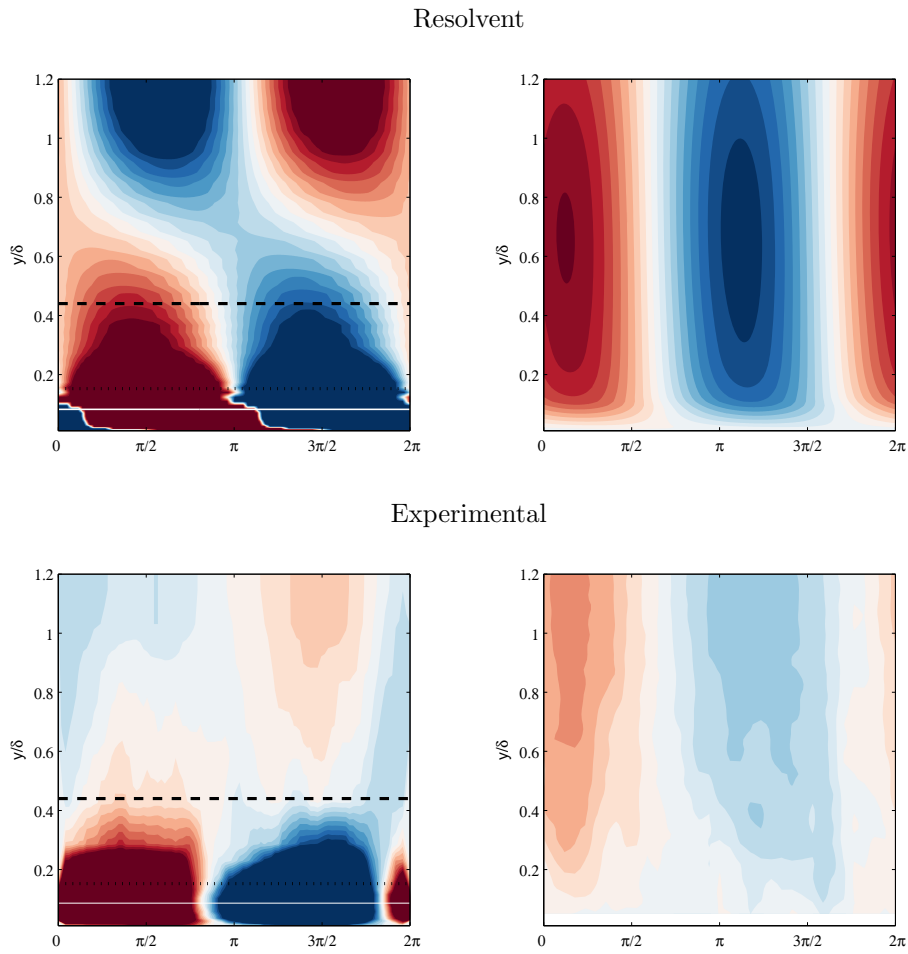


Figure 6.4: Top: (Left) A map of the calculated most-amplified singular mode  $\tilde{u}(y, t)$  due to the experimental forcing, over an average period ( $t \in [0, 2\pi]$ ); (Right) The corresponding map for  $\tilde{v}(y, t)$ . Bottom: The experimentally measured maps, at  $x/\delta \approx 2.3$  assembled via phaselocking, as in figure 5.13

and the least-damped eigenvalues at a variety of Reynolds numbers were calculated and compared to those found by Jordinson [1970] and Danabasoglu and Biringen [1989]. The collocation matrix dimension is  $N$ . The eigenvalues were matched to five decimal places with  $N \geq 40$ . Besides this least-damped eigenvalue, the resolution of other eigenvalues is more difficult. In particular, the presence of nonphysical (spurious) eigenvalues under Chebyshev methods is a well-known consequence of the discretization and has been discussed in Boyd [2000]. To eliminate the spurious values, the approach of Stewart et al. [2009] was adopted, in which the adjoint problem is simultaneously solved and the corresponding complex conjugate eigenvalues are compared to those of the original problem; then nonoverlapping values are eliminated as spurious.

Extending this approach from the Blasius laminar boundary layer to the experimental turbulent boundary layer presents another challenge regarding handling the velocity field closer to the wall than could be resolved by the hotwire measurement. The approach of Spalding [1961] was employed to extend the experimental turbulent boundary layer profile to the wall. However, Spalding's method relies on the measurement of the friction velocity  $u_\tau$ , which is difficult to ascertain for the impulsively perturbed case. It was shown above that the friction velocity tends to decrease immediately downstream of the perturbation and then recover slowly, but the magnitude of that decrease was not measurable with confidence. Therefore, the choice of  $u_\tau$  for the Spalding extension was iterated until the velocity profile appeared continuous ( $u_\tau = 2/3u_{\tau,0}$  with  $\kappa = 0.41$  and  $C = 4.9$  following the usage in chapter 3).

With the experimental turbulent boundary layer in the standard Orr-Sommerfeld operator, the eigenvalues, eigenmodes, and pseudospectrum were calculated. The complexity of the turbulent boundary layer, due both to the matching with the Spalding fit near the wall and also experimental noise, meant that significantly larger collocation matrices were needed to produce smooth eigenmodes and converged eigenvalues. It was found that  $N \gtrsim 100$  assured convergence for the least-damped eigenvalues and produced smooth eigenmode shapes. The danger of overly dense collocation matrices distorting the results near the boundaries was investigated, but trends seemed to smoothly approach convergence in the laminar test case for  $N \approx 100$  which has been used successfully in a variety of other studies (e.g., Schmid and Henningson [2001]). Therefore,  $N$  was fixed with an upper bound of 120 in the current study to avoid distortion, despite an observed dependence of the shape of the critical layer peak on  $N$ . In general, resolving the spectrum for a turbulent wall-bounded flows is quite difficult, as noted by McKeon and Sharma [2010].

In the pseudospectra (figure 6.1), the small vertically oriented collection of eigenvalues near  $c_i = 1$  is just a segment of the poorly resolved continuous portion of the spectrum, which Grosch and Salwen [1978] showed should span the line  $c_i = 1$  for boundary-layer problems. The distribution of other eigenvalues near the real axis is a consistent feature of the calculations – increasing resolution tends to increase the distance to the real axis slightly, but the overall trend is preserved largely

independent of  $N$ , a feature which may help explain the general similarity between singular and eigenmodes identified above.

Finally, a key concept regarding critical layers is worth reiterating. There are two defining characteristics of the streamwise critical layer eigenfunction: an amplitude peak near the location of the critical point,  $y_c$ , and a phase shift of  $180^\circ$  somewhere in the outer region of the boundary layer. A number of classic sources could be easily misinterpreted to suggest that the phase shift should also occur at the critical point itself (Hinze [1975]; Schlichting [1968]), but this is not correct. Schlichting’s asymptotic analysis reveals that the phase shift is a purely inviscid phenomenon, and it occurs where the two inviscid solutions (of the four total solutions) to the Rayleigh equation meet, far from the inner region of the boundary layer. Therefore, these two locations,  $y_c$  near the critical point and  $y_p$  at the phase shift, are expected to be distinct and physically significant. The former represents the center of the critical layer itself, while the latter represents the end of the inviscid solutions, which are not valid too far from the critical point, about which they can be expanded in series.

## 6.5 Discussion of the Resolvent Analysis

The organized wave which was forced externally in the turbulent boundary layer was observed to excite a critical-layer type velocity mode in the downstream flow field, despite the fact that the forcing was not in resonance with an eigenmode of the traditional Orr-Sommerfeld equation. This was possible due to the nonnormality of the Orr-Sommerfeld operator, which was then subsequently exploited to attempt to predict the mode shapes of the fluctuating velocity components. In contrast to previous studies, which utilized a traditional eigenmode analysis of the quasi-laminar Orr-Sommerfeld operator, the present study utilized a resolvent analysis for the first time in a turbulent boundary layer to describe the velocity fluctuations in terms of the singular modes of the resolvent. Additionally, the input forcing, which in previous work was not significantly stronger than the ‘internal forcing’ of the nonlinearities of turbulence, was now strong enough such that the most amplified singular mode of the resolvent of the Orr-Sommerfeld operator accurately captured significant features of the downstream velocity fluctuations, allowing for some discrepancy due to nonparallel flow effects. The final mode calculations provided reasonably accurate qualitative and quantitative predictions of the velocity fluctuations observed in the perturbed flow, although the over-prediction of the peak sharpness of the critical layer which plagued the quasi-laminar studies remained a problem even under the resolvent analysis. In addition, disagreement was noted regarding the inclination of the mode shapes in the outer region of the boundary layer.

A number of difficulties confront analytical analysis of the boundary layer perturbation. The nonparallel condition of the flow and the developing nature of the mean turbulent velocity profile

both introduce streamwise variation into the analysis which complicates matters significantly. In addition, the nonequilibrium nature of the flow is often difficult to distinguish from what might be considered local but permanent changes to the flow structure. All of these difficulties likely contribute to those areas, described in detail above, where the predictions from the Orr-Sommerfeld resolvent analysis disagree with the observations. However, it is important to reiterate that the analysis offered should be viewed as being in the service of interpreting the experimental results, by highlighting those physical features observed which are not easily predicted, and thereby motivating particular areas for further exploration. And thus despite the analytical challenges, the experimental results reported here provide a fresh basis for investigating these questions in more detail. Study of additional frequencies of actuation would likely provide additional insight into the physics of the flow, although the frequency selected for the present study had the advantage of being largely separable from both the effects of blockage due to an equivalent static roughness and activity associated with the unperturbed boundary layer.

Ultimately, the significant coherence of the roughness perturbation allowed a phase-locked analysis of the downstream velocity fluctuations, which were then predicted to reasonable accuracy by employing a resolvent approach which, despite suffering some of the same deficiencies of earlier quasi-laminar methods, is widely understood to be better suited to high Reynolds number turbulent flows.

## Chapter 7

# Phase Relationships between Large and Small Scales in the Turbulent Boundary Layer

### 7.1 The Scale Interaction Problem

After establishing how large-scale motions can be synthesized artificially in the turbulent boundary layer, the problem remains how those large scales, in turn, interact with smaller scales in the flow. In order to approach this problem, the interaction of unperturbed, ‘natural’ large and small scales is considered first, using a variety of correlation based techniques. The process by which the large- and small-scale motions are separated from instantaneous velocity measurements is described, followed by the use of the correlation coefficient, the cross-correlation function, and the cospectral density function to investigate the scale interactions. Special emphasis is placed on the relative phase lag observed between the large and small scale motions. Finally, tentative steps are taken in the use of demodulation techniques for studying the scale interaction problem.

### 7.2 Measuring Scale Interactions

Describing the relation between large and small scales depends on a method to separate the large scales,  $u_L$  from an instantaneous velocity signal,  $u$ , and then to generate an envelope of the small-scales,  $u_S$ , from the remainder,  $u_R = u - u_L$ . This has been accomplished in past studies in three ways: 1) a low-pass (third-order Butterworth, zero-phase) filter followed by an absolute value rectification to generate the envelope, using the approach of Bandyopadhyay and Hussain [1984]; 2) a Fourier filter, followed by a Hilbert-transform technique to generate the envelope, using the approach of Mathis et al. [2009a]; or 3) a moving-average filter followed by a rectified rms envelope, using the approach of Chung and McKeon [2010]. In all cases, the filter size or cutoff will typically be on

the order of an eddy-turnover time, as established by Mathis et al. [2009a]. The choice of filtering approach can have a significant impact on the ease of interpreting the results, and depends on the nature of the available measurements, although general trends remain robust.

The temporal and spatial resolution limits on the PIV measurements were detailed in section 2.4, where it was shown that the temporal PIV can resolve wavelengths from  $[2.29 \delta, 1170 \delta]$  (employing Taylor’s hypothesis), while the spatial PIV can fully resolve wavelengths from  $[0.03 \delta, 2.14 \delta]$ . These two complementary pairs of limits serve as implicit bandpass filters on the flow measurements, and present two fundamental difficulties to the analysis of large- and small-scale interactions: 1) the temporal resolution means that the filter cutoff to separate between large and small scales must be quite large, with  $\tau > 2.29 \delta/U$ , in order to effectively separate measurable fluctuations; and 2) the largest scale resolvable from the spatial measurements is less than the expected size of the dominant large-scales in the turbulent boundary layer  $\lambda_x \sim 10 \delta$ , meaning that any comparisons between small scales and that dominant large-scale will suffer from subfundamental sampling, a known problem studied by Strader II [1980] and discussed in further detail below.

There is an additional difficulty with the temporal filtering of the PIV signals, if a moving-average filter (method 3, above) is utilized: discretization of the filter dimension. Selecting a filter size  $\tau = n\delta/U$  means that the filter should vary with mean convective velocity. But since the temporal discretization of the velocity signal is on the order of the eddy turnover time, this means that setting  $n \approx 1$  for the filter size will actually result in an effective filter that varies from 1-3 ( $\delta/U$ ), due to the discretization. This does not occur in the hotwire measurements where the sampling rate is significantly higher than the desired filter sizes.

Finally, there is a more general difficulty with the use of moving-average filters: they suffer from notoriously slow roll-off, which makes them ideal for smoothing but ill-suited for low-pass discrimination in frequency space. In other words, the moving-average filter will perforce include a mixture of large and small scales together at the same filter cutoff at which a Butterworth filter will accurately discriminate between the scales. Based on all of the above, it appears that a Butterworth or Fourier style filter is better suited to most of the measurements under consideration, in particular given the limited spectral range of the PIV measurements. The Butterworth filter with an absolute value envelope and rectification, as employed in Bandyopadhyay and Hussain [1984], is used to identify the large- and small-scale velocity signals.

### 7.3 Modulation Measurements

After having separated the large-scale fluctuations from an envelope of the small-scale motions, the ‘amplitude modulation coefficient’,  $R$ , following Mathis et al. [2009a], can then be defined as

$$R = \frac{\langle (u_L - U(y))(u_S - \langle u_S \rangle) \rangle}{\langle (u_L - U(y))^2 \rangle^{1/2} \langle (u_S - \langle u_S \rangle)^2 \rangle^{1/2}} \quad (7.1)$$

where  $\langle \cdot \rangle$  represent the ensemble average (making the correlation coefficient a zero-centered type). Chung and McKeon [2010] observed that the natural interpretation of a correlation-coefficient is that of an inner product (see Rodgers and Nicewander [1988] for details), which means that the correlation coefficient represents the phase angle,  $\phi$ , between the two constituents of the velocity signal,  $R = \cos(\phi)$ . In other words, the large-scale signal and the envelope of small-scale motions can be thought of as two sinusoids,  $\exp i(\omega t + \phi_L)$  and  $\exp i(\omega t + \phi_S)$  where the phase difference between them is  $\phi = -(\phi_L - \phi_S)$  (bearing in mind that the phase difference from subtracting Fourier phases has the opposite sign of that measured by the cross-correlation procedure, due to the complex conjugation in the Fourier transform;  $\phi > 0$  means small scales lead in physical space). Therefore, the interpretation of the profile of  $R$  across the boundary layer is an unsigned phase diagram, where positive values of  $R$  indicate a small phase-difference between the large-scale fluctuations and the envelope of small-scale fluctuations; negative values of  $R$  indicate an out-of-phase relationship (with a phase difference approaching  $\pm\pi$ ); and the zero-crossing corresponds to a phase difference of  $\pm\pi/2$ . The zero-crossing location,  $y_c$ , in particular, was observed by Mathis et al. [2009a] to occur at the wall-normal location corresponding to the outer streamwise turbulence energetic peak, and thus conveys information about the dominant large scales in the flow. Figure 7.1 shows the profiles of the correlation coefficients for both streamwise and wall-normal small-scale components, with temporal measurements from hotwire and both temporal and spatial measurements from the PIV. Again, the coefficient for  $u_L$  and  $v_S$  measured from the PIV is shown in the dotted line, and shows a zero-crossing much nearer to the wall,  $y_c \approx 0.08$ . The zero-crossing locations are noted by arrows with the same line-pattern as the corresponding correlation coefficient profile. Both techniques are able to reproduce the well-known profile indicating the usual phase relation between large streamwise scale and the envelope of small streamwise scales. There is some evidence for the same phase relationship between the large-scale streamwise fluctuations and the envelope of small-scale wall-normal fluctuations,  $u_L$  and  $v_S$ , using PIV measurements (where the PIV measurement, made reliably nearest to the wall, occurs at  $y/\delta \approx 0.05$  and  $y^+ \approx 40$ ); the correlation is negative far from the wall and tends toward zero or slightly positive values near the wall. This result is consistent with the report by Hutchins and Marusic [2007] that these two signals are in-phase near the wall when observed in a low Reynolds number DNS, at  $y^+ = 15$ , although there too the effect was quite weak. This weak trend is expected as a result of the relative weakness of the wall-normal fluctuations and thus makes identification of the zero-crossing location more difficult. However, the negative correlation in the outer region is well defined and parallels precisely the behavior of the streamwise coefficient.

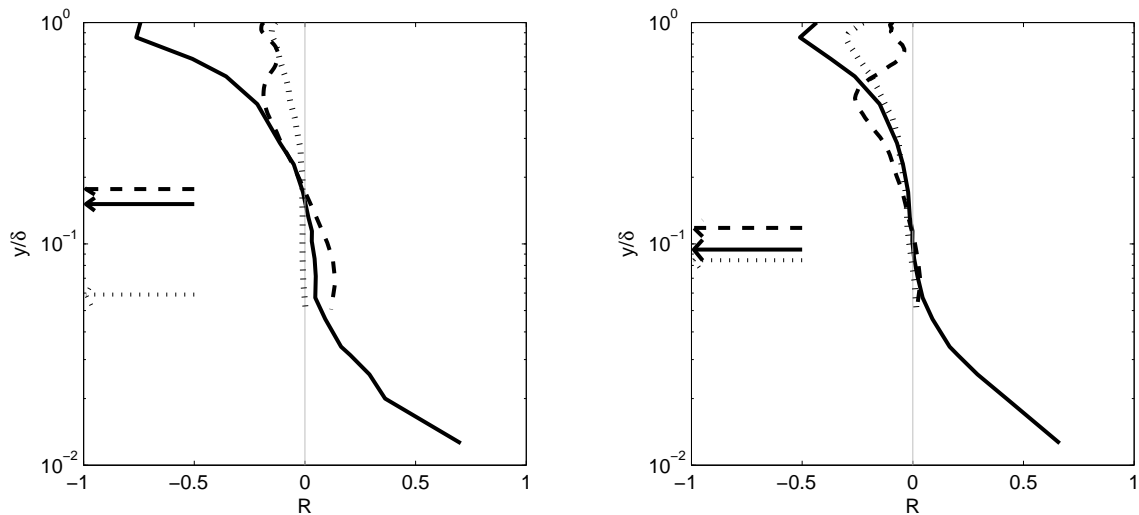


Figure 7.1: The correlation coefficients for  $u_L$  and  $u_S$ : (Left) using a Butterworth temporal filter size of  $\tau = 3 \delta/U$ . The profile for the hotwire is shown in solid ( $y_c \approx 0.15$ ); that from the PIV in dashes ( $y_c \approx 0.17$ ). Additionally, the coefficient for  $u_L$  and  $v_S$  measured from the PIV is shown in the dotted line, and shows a zero-crossing much nearer to the wall,  $y_c \approx 0.06$ . (Right) using a temporal filter size of  $\tau = 0.5 \delta/U$  on the hotwire data and a spatial filter of  $\rho = 0.5\delta$  on the PIV data. The profile for the hotwire is shown in solid ( $y_c \approx 0.09$ ); that from the PIV in dashes ( $y_c \approx 0.12$ ).

The filter cutoffs are  $\tau = 3 \delta/U$  for the temporal filtering and  $\rho = 0.5 \delta$  for spatial filtering, to allow for comparison between temporal hotwire and both temporal and spatial PIV measurements; the detailed dependence of the conclusions on the filter cutoff is discussed in section 7.4.3. In the following analysis, the temporal PIV measurements in the streamwise direction are validated against the measurements from the hotwire, for each analysis technique; this validation then provides confidence in the temporal PIV measurements for the wall-normal component. The spatial PIV measurements suffer from a significant resolution problem, by virtue of the limited window size in comparison to the expected size of relevant large scale motions; the consequences of this spatial resolution problem become most apparent in the cross-correlation analysis in section 7.4 and will be discussed in more detail in section 7.4.1.

## 7.4 Cross-Correlation Isocontours

Despite establishing a positive correlation between the large scale streamwise fluctuations and the envelope of small scale streamwise and wall-normal motions, the precise nature of the phase-relationship remains ambiguous when examined with a correlation coefficient, which obscures the sign of the phase inside the inner product. In order to infer the correct sign of the phase, and thereby the actual physical direction of the modulation effect, the cross-correlation function itself must be employed. Fol-

lowing the definition of Bandyopadhyay and Hussain [1984], the temporal cross-correlation function,  $r(\Delta t)$ , can be defined as

$$\begin{aligned}
 r(\Delta t) &= \frac{\langle (u_L(t + \Delta t) - \langle u_L(t + \Delta t) \rangle)(u_S(t) - \langle u_S(t) \rangle) \rangle}{u_L^{rms} u_S^{rms}} \\
 &= \mathcal{F}^{-1}(\mathcal{F}(u_L - \langle u_L \rangle) \mathcal{F}(u_S - \langle u_S \rangle)^*) \\
 &= u_L \star u_S
 \end{aligned} \tag{7.2}$$

and the spatial cross-correlation  $r(\Delta x)$  follows directly, as with the correlation coefficient. For the envelope of streamwise small scales, these will be denoted  $r_{uu}(\Delta t)$  and  $r_{uu}(\Delta x)$ ; for the envelope of wall-normal small scales,  $r_{uv}(\Delta t)$  and  $r_{uv}(\Delta x)$ . The  $\star$  operator will also be used to represent the cross-correlation operation; the asterisk denotes the complex conjugate. Plotting an isocontour map of the cross-correlation functions at each wall normal location, as shown in figure 7.2, allows for identification of the sign information obscured in the correlation coefficient. (The coefficient,  $R$ , can be recovered from the cross-correlation by simply retrieving the value of the cross-correlation at ‘zero lag’ for each wall-normal location, although note the very slight definitional difference between the two, in terms of the zero-centering, which explains the slight disagreement in cross-over points,  $y_c$ .) By following the ridgeline of peak magnitudes in the cross-correlation, the relative phase-lag between the two signals can be inferred. Across the boundary layer, the phase lag is positive, indicating that the large-scale fluctuations lead the small-scale envelope in a temporal sense, and thus the small-scale envelope leads in a spatial (i.e., physical) sense. This result is consistent with the results of conditional averaging in Chung and McKeon [2010] and Hutchins et al. [2011] and correlation analysis in Guala et al. [2011], but is opposite the result found by Bandyopadhyay and Hussain [1984]. At the location of the zero-crossing in the correlation coefficient, there is a switch in the cross-correlation from peak to trough, which indicates a phase-difference of  $\pi/2$  (where, again, some disagreement with  $R$  results from the linear-interpolation of the location of the  $\pi/2$  phase change).

The isocontour map of the cross correlation can also be calculated for  $u_L \star v_S$  as shown in figure 7.3 from the temporal PIV measurements. The ridgeline shows the same phase-lag trend, with the small-scale wall-normal envelope leading the large-scale streamwise fluctuations spatially, across the boundary layer, albeit with a zero-crossing point occurring nearer to the wall than in the streamwise case.

In order to validate the negative phase lag in the spatial domain by direct measurement, the isocontour maps for both flow directions are calculated from the spatial PIV measurements, figure 7.4. However, there appears to be significant disagreement between the crossover locations in the spatial cross-correlation of the wall-normal component and temporal correlation shown in figure 7.3,

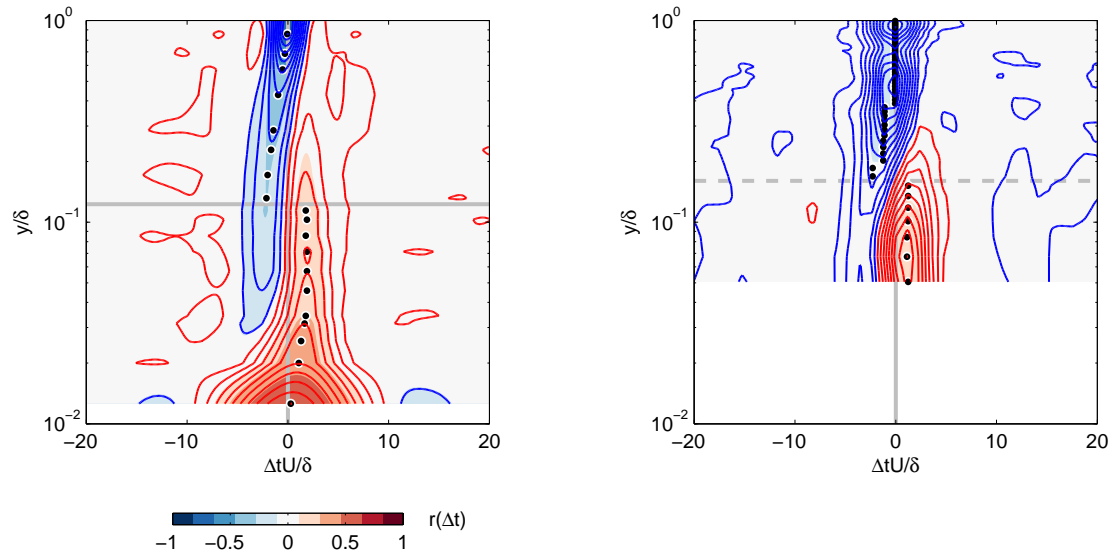


Figure 7.2: The cross-correlation isocontour map for  $u_L \star u_S$ , using a temporal cross-correlation (left) from the hotwire measurements ( $y_c \approx 0.12$ ); and (right) from PIV measurements ( $y_c \approx 0.16$ ). The absolute value ridge line is marked with black dots in each. The Butterworth filter size was  $\tau = 3 \delta/U$  for both data sets.

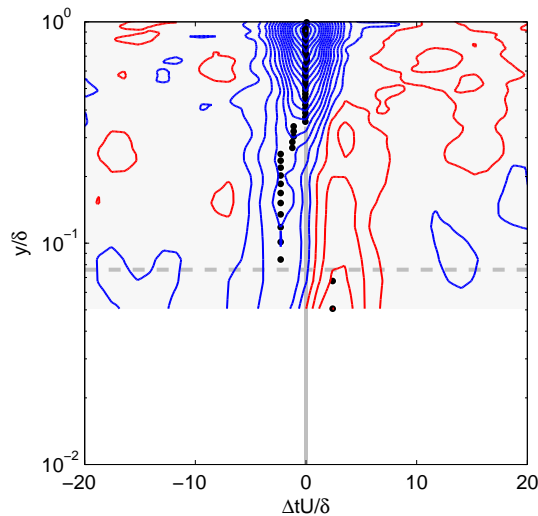


Figure 7.3: The cross-correlation isocontour map for  $u_L \star v_S$ , using a temporal cross-correlation from the PIV measurements ( $y_c \approx 0.08$ ) with filter size  $\tau = 3 \delta/U$ .

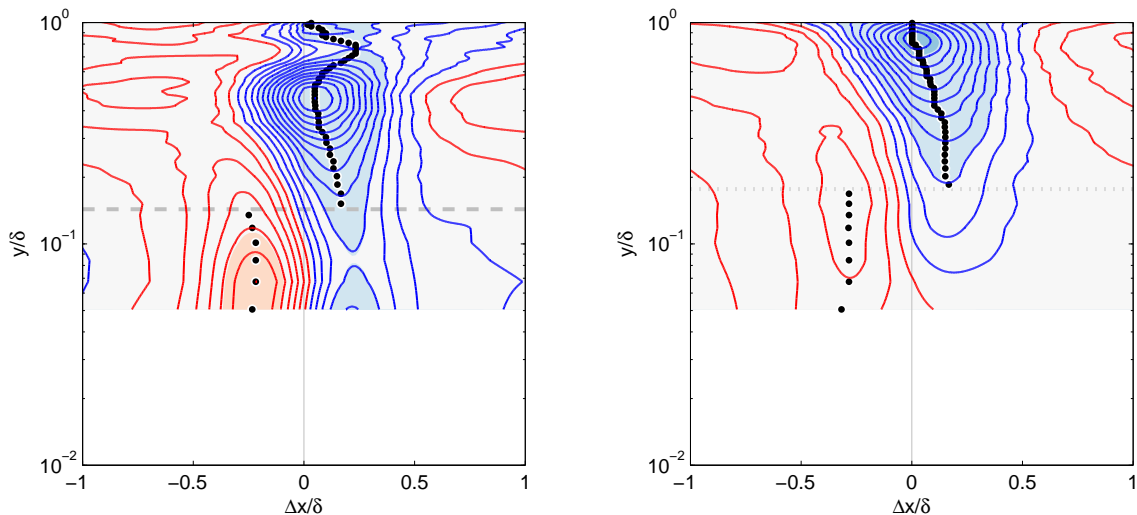


Figure 7.4: The cross-correlation isocontour maps in the spatial domain for (left)  $u_L \star u_S$  with  $\rho = 0.5 \delta$  and (right)  $u_L \star v_S$  with  $\rho = 0.5 \delta$ . The streamwise component shows good agreement with temporal results with  $y_c \approx 0.14$ , while the wall-normal map shows significant disagreement with  $y_c \approx 0.18$ . Note that the wall-normal map indicates significant breakage of the antisymmetry (i.e., a strong negative tail) indicating distortion due to subfundamental sampling. By reducing the filter size for the wall-normal cross-correlation, as explained below, this distortion can be mitigated, as shown in figure 7.5.

a consequence of the spatial resolution limits on the PIV itself, although the streamwise crossing locations appear to be roughly consistent, as will be discussed below in section 7.4.1.

### 7.4.1 Subfundamental Spatial Cross-Correlation

In the spatial cross-correlation, the disagreement between the location of the zero-crossing of the correlation coefficient,  $R$ , (equivalently the zero-crossing of the ‘zero-lag’ value of the cross-correlation function,  $r$ , itself,  $y_c \approx 0.08$ ) and the peak-to-trough jump in the cross-correlation function ( $y_c \approx 0.18$ ) requires explanation, since, by definition, there should not be any significant disagreement between these two measures that are related trigonometrically by the inner product. In the temporal case, this disagreement is much less significant. The discrepancy in the spatial calculation is a result of the subfundamental sampling phenomenon. By employing a simplified two-scale model of scale interaction, described in appendix 7.8.1, the effect of the sub-fundamental sampling can be explored. The overall effect in real boundary layer signals is to cause the peak-to-trough jump to appear artificially further from the wall and distinctly higher than the zero-crossing of the correlation coefficient. In addition, the subfundamental sampling tends to suppress the magnitude of the cross-correlation function at zero lag (i.e., the correlation coefficient). The subfundamental sampling bias is also affected by the size of the filter and the amplitude of the small-scale fluctuations. Because the small-scale

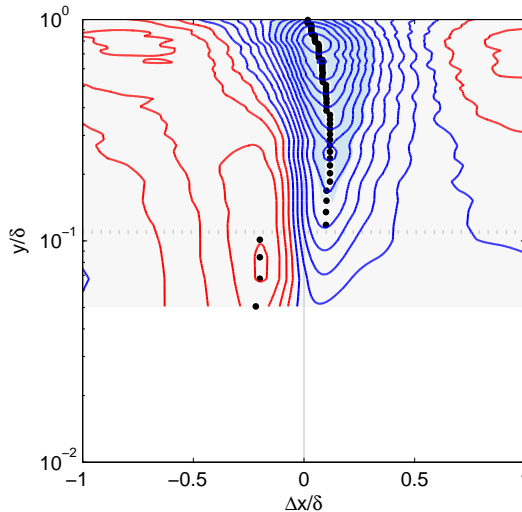


Figure 7.5: The cross-correlation isocontour maps in the spatial domain for  $u_L \star v_S$  with  $\rho = 0.25\delta$ . Now the zero-crossing location shows good agreement with the temporal measurements, with  $y_c \approx 0.11$ , and the strong antisymmetry breaking is no longer apparent.

fluctuations in the wall-normal component have lower amplitude than the streamwise fluctuations, as seen in Hutchins and Marusic [2007], the sub-fundamental sampling effect is made significantly worse. In order to mitigate this distortion, the filter size must be reduced for the wall-normal studies, as shown in figure 7.4 and figure 7.5 with the reduced filter size.

Reducing the filter size in the wall-normal case to reflect the smaller amplitude of fluctuations reduces the distortion of the cross-over location. Although filter size adjustments are a classic means of avoiding the subfundamental sampling problem, nevertheless a physical interpretation for the solution is also possible. With larger filter cutoffs, more of the larger scales tend to be included (and overwhelm smaller scales) in the envelope of so-called small scales. Thus, the phase relationship will necessarily reflect the phase relationship between large-scale streamwise and large-scale (i.e., long wavelength) wall-normal motions. In their study of a forced boundary layer, Jacobi and McKeon [2011b] reported that the artificial large-scale motions in the wall-normal component tend to show little downstream inclination. If the unperturbed, large-scale wall-normal motions behaved similarly, then this would explain why the cross-over point appears further from the wall when large scale motions are included in the small-scale envelope. It would also follow that a truly representative envelope of small scale wall-normal fluctuations should be inclined downstream more than the large scales, which would result in a cross-over point appearing nearer to the wall. The validity of this hypothesis is currently under examination.

Ultimately, the subfundamental sampling effect prevents confident measurement of the location of  $y_c$  from spatial cross-correlation and indeed from the correlation coefficient as well, since essentially

the zero-crossing of the correlation coefficient does not accurately indicate a phase lag of  $\pm\pi/2$ . Despite this note of caution regarding a direct spatial cross-correlation, the isocontour map can still verify at least the correct sense of sign for the phase-relationship, since the ridgeline is distorted only in location but not sign, by the subfundamental sampling effect, when viewed far away from the zero-crossing location. Therefore, from figure 7.4 we can still see that the sense of sign is reversed in the spatial correlation case from that of the temporal correlation, and that fluctuations in the small-scale envelope in both flow directions tend to lead corresponding large-scale streamwise motions.

### 7.4.2 Taylor's Hypothesis

The convective velocity of different size structures within the boundary is often conveniently assumed to correspond to the mean local velocity of the flow, by applying Taylor's 'frozen flow' hypothesis. However, more recent research has indicated that this assumption is not strictly true in a variety of circumstances. Krogstad et al. [1998] showed that there is significant variation in convective velocity with structure size, and that most scales tend to travel faster than the local mean convection velocity near the wall. Although Dennis and Nickels [2008] demonstrated that far from the wall, Taylor's hypothesis can be considered adequate for very large scales, Lehew et al. [2011] employed three-dimensional streamwise velocity power spectra measured in a turbulent boundary layer to show that near the wall and very far from the wall, the deviations from Taylor's hypothesis become more significant. Chung and McKeon [2010] and Lehew et al. [2011] both show that large streamwise scales convect slower than the local mean far from the wall. The extent of these deviations from Taylor's hypothesis can also be inferred from the correlation coefficient approach to measuring the modulation between scales.

The spatial and temporal modulation relationships can be compared by calculating the correlation coefficient from each technique, holding the filter size constant. However, in order to include explicitly the effect of Taylor's hypothesis, the correlation coefficient cannot be used directly, but rather must be reconstructed from the peak trace of the cross-correlation map, where the cosine of the spatial phase difference is equal to the correlation coefficient, and the temporal phase difference can be converted to a spatial phase lag by Taylor's hypothesis. Then, in order to convert between phase (in space) and a phase angle, the spatial phase lag is normalized such that the phase-jump produces an angular lag of  $\pi/2$ . The error introduced by this assumption appears quite minimal, since there is a broad region of relatively constant spatial lag at roughly the same magnitude as that of the phase-jump location; for instance, see figure 7.4. However, the subfundamental sampling problem does tend to distort this phase measure somewhat, thus introducing some uncertainty as to whether the spatial phase lag at the jump is truly representative of an angular lag of  $\pi/2$ . The ridgelines of the cross-correlation maps as well as the reconstructed correlation coefficient are shown in figure 7.6. It appears that using a convective velocity higher than the local mean tends to improve

the agreement between the spatial and temporal correlation coefficients, indicating that the relevant scales captured by the cross-correlation procedure tend to convect faster than the local mean across most of the boundary layer, consistent with the observations of Lehew et al. [2011] near the wall; the reason for faster convection farther from the wall is not readily apparent. However, an alternative explanation for the discrepancy across the entire boundary layer is possible. Using the local mean velocity as the convective velocity, the spatial correlation coefficient magnitude would still tend to underestimate the temporal measurement, since subfundamental sampling tends to suppress the value of the correlation coefficient; therefore, the constant offset discrepancy could be a result of the fact that the PIV window size is smaller than the dominant large-scale. Returning to the simple two-scale pure-sinusoid model employed above and in appendix 7.8.1, an offset of 5% in the normalized correlation coefficient can be generated by a choice of window size that captures only approximately one third of the dominant large-scale (which in the present case means a relevant large scale approximately  $6 \delta$  in length), and similarly larger suppression is due to excluding even larger-scale motions. Therefore, either using a larger convective velocity on the temporal phase measurements or scaling the spatial phase to compensate for the subfundamental sampling effect, will tend to explain the discrepancy between spatial and temporal measurements, and most likely some combination of the two effects. In the end, no specific conclusions about the validity of Taylor’s hypothesis can be drawn, short of reiterating that the spatial and temporal measurements are not in precise agreement, while still preserving common overall trends.

### 7.4.3 The Effect of Filter Cutoff Size

Having suggested that the filter cutoff size with respect to the relevant interacting scales in the flow can be important, especially in the case of the spatial measurements, the significance of the choice of cutoff in designing the envelope also deserves reexamination. Mathis et al. [2009a] investigated the effect of the cutoff wavelength for their correlation coefficient for spectral cutoffs between  $\lambda_x/\delta = 0.2$  to  $\lambda_x/\delta = 4$ . They found that the correlation tended to increase with decreasing cutoff, until  $\lambda_x/\delta = 0.2$ , but for even smaller cutoffs, the correlation tends to decrease again. Moreover, they found that the zero-crossing location was only ‘minutely affected’ by the cutoff choice. Chung and McKeon [2010] observed the opposite trend in correlation value as a function of cutoff, for wall-normal locations near to the wall (although the LES employed in their study may be responsible for the difference), but produced a similar robustness of the zero-crossing location. The significance of the trend is not entirely clear; smaller cutoffs tend to exclude extraneous large scales from overwhelming the small-scale signal, thereby increasing the magnitude of the correlation at all wall-normal locations, as in Mathis et al. [2009a]. Alternatively, this trend might be supposed to apply only near the wall, where the large-scale motions are attached; but in the outer region of the boundary layer, larger cutoffs might be expected to produce higher correlations, since a variety of detached motions may

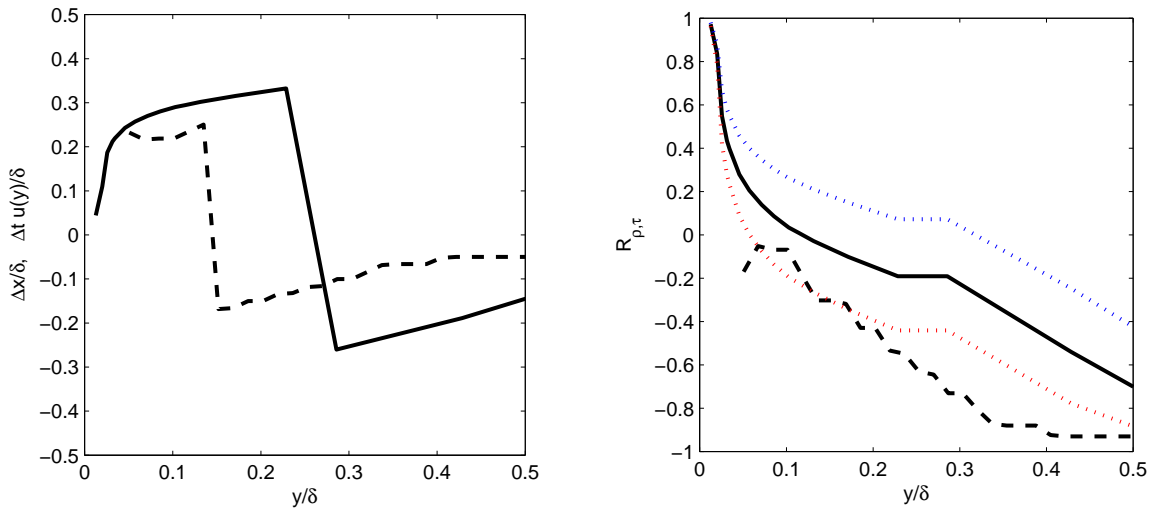


Figure 7.6: (Left) The peak trace of the spatial (dashed-line) and temporal (solid) cross-correlation functions, both using a filter size  $\tau = 0.5 \delta/U$  and  $\rho = 0.5 \delta$ , and applying Taylor’s hypothesis to the temporal signal. (Right) Converting the phase traces into the correlation coefficient form, for easier comparison. The conversion was also performed with a convective velocity 15% higher than the mean (red dotted line) and 15% lower than the mean (blue dotted line). Therefore, if the blue line is a better fit to the actual spatial measurements, it signifies that the relevant convective velocity is lower than the mean velocity in the flow.

also participate in a modulating effect, when included in  $u_S$ . This latter interpretation fits the trend in the current study, wherein the cutoff size produces different effects near and far from the wall, as shown in figure 7.7. The general robustness of the zero-crossing is also shown for filter cutoff  $\tau U/\delta > 0.25$ . Although the zero-crossing, in a gross sense, appears robust to filter effects, the subtle trends remain a topic of current investigation.

## 7.5 Cospectral Density

The correlation coefficient and cross-correlation functions provide tools to analyze the aggregate relationship between the large- and small-scale signals in both temporal and physical space. However, much of what is known about the large-scale motions in the wall-bounded flows can be better described in spectral space, where the size of the motions, in some statistical sense, can be characterized by their energetic contributions at particular frequencies or wavelengths. Normally, this spectral analysis is performed on the instantaneous velocity signals themselves; however, by performing a spectral analysis on the filtered signals, a new perspective on the modulation effect can be gained, and in particular the influence of the enveloping procedure since it is the envelope procedure which ultimately attributes low frequency content to the  $u_R$  signal to produce  $u_S$ .

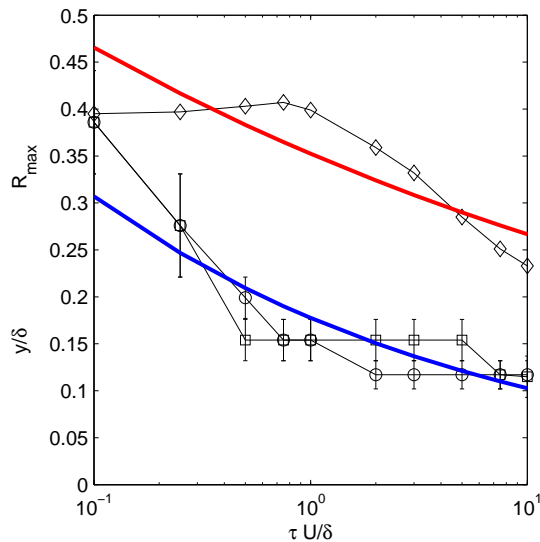


Figure 7.7: The zero-crossing locations from the correlation coefficients (squares) and the  $\pi/2$  phase-change locations from the cross-correlations (circles), with a best-fit (blue) assigned to the mean value,  $y/\delta \approx 10^{-0.8}(\tau U/\delta)^{-0.2}$ . Also, the maximum positive value of the correlation coefficient, with a best-fit (red) of  $R_{max} \approx 10^{-0.5}(\tau U/\delta)^{-0.1}$ . Values are recorded for the most downstream measurement, with  $Re_\theta \approx 4100$ .

By transforming the cross-correlation,  $r(\Delta t)$ , from the temporal domain into the frequency domain by Fourier transform, the cospectral density,  $r_c(u_L, u_S)$  between the large-scale fluctuations and the envelope of the small-scales is produced. The expression representing this quantity is simply equation 7.2 without the final inverse Fourier transform,  $\mathcal{F}^{-1}$ , shown as equation 7.3.

$$r_c(u_L, u_S) = \mathcal{F}(u_L - \langle u_L \rangle) \mathcal{F}(u_S - \langle u_S \rangle)^* \quad (7.3)$$

The transform process, as above, involves windowing the time series and averaging across the windows. However, an additional subtlety arises in the frequency domain about the form of the averaging. In order to smooth the power spectral density estimate, the PSD of each window is averaged ‘incoherently’ in the frequency domain, following Welch’s method; alternatively, the windows can be averaged ‘coherently’ in the time domain, which under certain conditions (of stationarity and ergodicity) can preserve phase information. Assuming the long time series fulfill, at least roughly, these conditions, the coherent approach was employed in the hope of preserving the relevant phase information between different frequencies. Therefore, the argument of the cospectrum,  $\arg[r_c(u_L, u_S)]$  represents the phase difference between each discrete Fourier component of the large scales with the envelope of small-scale motions. The normalized cospectral power can be defined such that the integral of the power in the cospectral density is equal to the covariance of the large- and small-scale signals, as in equation 7.4

$$Co(u_L, u_S) = \frac{r_c(u_L, u_S)r_c(u_L, u_S)^*}{cov(u_L, u_S)} \quad (7.4)$$

Calculating the cospectral density at a single wall-normal location, shown in figure 7.8, provides insight into the general shape of the function. In order to represent the key features of the smoothed spectrum, a fitting technique was employed, whereby a modified Gaussian function is fitted to the underlying spectral data, as described in appendix 7.8.2. Then, by calculating the cospectral density (and its fitted analogue) at each wall-normal location, a map of the cospectral density can be produced, shown in figure 7.9, where a dashed line is used to indicate local-velocity-dependent size of the filter cutoff used to separate the large- and small-scale motions.

The cospectral density map in figure 7.9 shows a peak across most of the wall-normal locations at  $f\delta/U_\infty \approx 0.1$ , which indicates the dominant large-scale motion among all of the large scales participating in the phase relationship with the small-scale envelope. Moreover, the fitted version of the map (figure 7.9b, where the modified Gaussian fit was used to provide a smoothed version of the cospectrum) highlights two distinct regions of dominant large scales: one within the buffer layer, and one in the outer region of the boundary layer.

Guala et al. [2011] also observed two regions in which large-scale motions showed a discernible effect on small scales, by applying conditional averaging to the velocity signals based on the sign of large-scale motions, and then examining the difference between the standard premultiplied power spectral densities of the conditionally averaged signals (positive large-scale spectra minus negative) in the atmospheric surface layer. They noted two peaks in power difference, one near the wall in the buffer layer, situated at higher frequencies, and one further from the wall, at lower frequencies, showing that greater small-scale intensity is associated with positive large-scale excursions near the wall. Importantly, it is also apparent from their results that a variety of large scales, both near the wall and farther away, are involved in this interaction.

In the cospectral density map, it appears that the lower frequency peak is actually situated nearer to the wall, although only slightly so, meaning that near the wall, the increased small-scale activity is associated with the larger wavelength range of large-scale motions, and farther from the wall, the increased small-scale activity is associated with relatively ‘smaller’ large scales. Like the results of Guala et al. [2011], this indicates that different regions of the boundary layer have different phase relationships between large- and small-scale motions, although here the evidence is more specific that near the wall there is a broader range of larger scales that appear to have a footprint on the small-scale envelope.

The trace of the peak in the cospectral density across wall-normal locations appears to yield a distinctive shape over the range of Reynolds number available on the flat plate. The location of this ridgeline represents what will be referred to as the ‘dominant interacting scale’,  $\lambda_x$ , involved in the

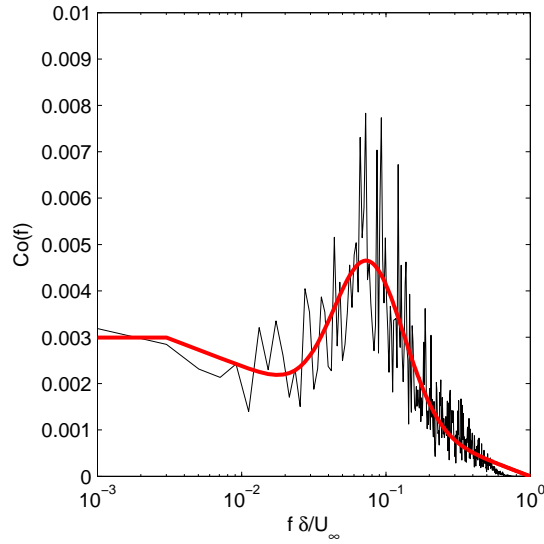


Figure 7.8: The normalized cospectral density,  $Co(f\delta/U_\infty)$ , at  $y/\delta \approx 0.17$ , in black. The red line is the best fit to the extended Gaussian function, defined in equation 7.14. The cospectral density is displayed in a normalized but not premultiplied form in order to identify the frequencies at which the interaction between large- and small-scales is dominant, but not necessarily energetically so, because the energetic strength does not indicate phase interaction strength, as can be observed by analysis of two amplitude-modulating sinusoids.

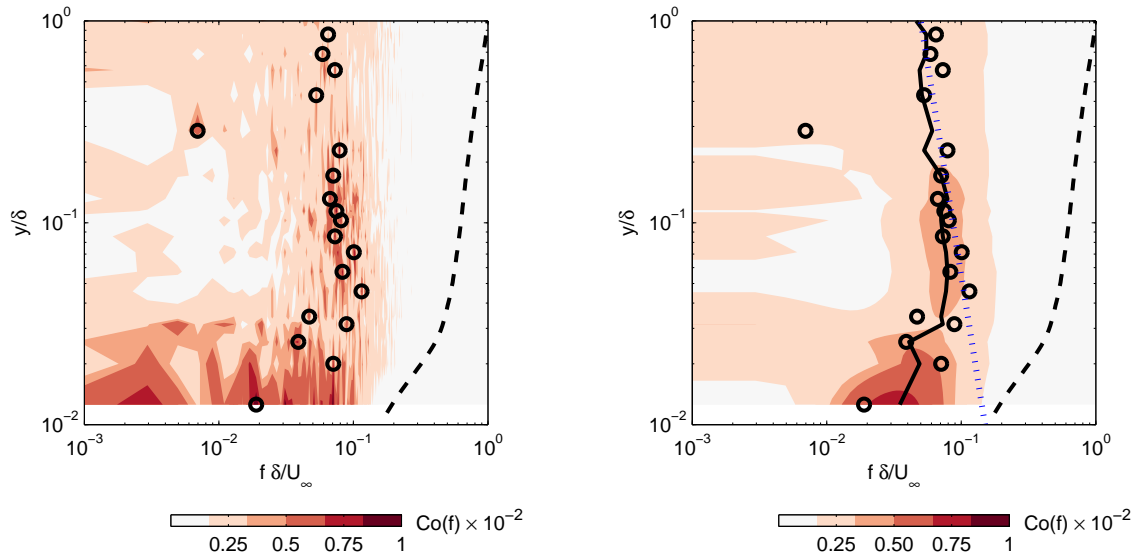


Figure 7.9: (Left) The cospectral density for the cross-correlation of  $u_L$  and  $u_S$  defined by temporal means from the hotwire measurements. The peaks from the amplitude at each wall-normal location are denoted by circles. The filter size of  $\tau = 1 \delta/U$  is marked by a dashed line, which varies as a function of convective velocity. (Right) The same spectral map, constructed from the best-fit extended Gaussian functions, in order to identify the peaks, which are traced by the solid black line. The blue dotted line corresponds to the power law for the VLSM reported by Monty et al. [2009], translated to the frequency domain via Taylor's hypothesis using the present mean velocity profile.

phase relationship with the small-scale envelope. The dominant interacting scale can be expressed as a simple power law function of Reynolds number and wall-normal location, as in equation 7.5, where both frequency and wavelength are employed for subsequent convenience. The robust fitting process used to obtain the power law relations is described in detail in appendix 7.8.2. The dominant interacting scale is that scale, among all of the large scales in the flow, which is most strongly correlated with the envelope of small-scale motions.

$$\begin{aligned} f\delta/U_\infty &= 10^{-0.38}(Re_\theta)^{-0.26}(y/\delta)^{-0.15} & \lambda_x/\delta &= 10^{0.32}(Re_\theta)^{0.28}(y/\delta)^{0.34} & \approx 20(y/\delta)^{0.34} \\ f\delta/U_\infty &= 10^{-0.23}(Re_\tau)^{-0.36}(y/\delta)^{-0.15} & \lambda_x/\delta &= 10^{0.15}(Re_\tau)^{0.38}(y/\delta)^{0.34} & \approx 20(y/\delta)^{0.34} \end{aligned} \quad (7.5)$$

The scaling of the dominant interacting scale involved in the phase relationship can be interpreted in the context of the other key structural features of wall-bounded flows. Monty et al. [2009] reviewed a number of these key features, as observed through the composite spectral maps, including: the highly energetic peak near the wall at  $y^+ \approx 15$ ,  $\lambda_x^+ \approx 1000$ , a dominant (LSM) peak for  $y/\delta > 0.3$ ,  $\lambda_x/\delta \approx 2-3$ , and also a secondary (VLSM) peak at  $y/\delta \approx 0.06$ ,  $\lambda_x/\delta \approx 6$ . The secondary peak tends to persist beyond  $y/\delta > 0.3$  along with the LSM peak for internal flows, but tends to shift to lower wavelengths for the boundary layer such that only the LSM peak is observed in the outer region. The size of the LSM peak, with  $\lambda_x/\delta \approx 2-3$ , is consistent with the typical size of the intermittent bulges in the edge of the boundary layer, as identified by Kovaszny et al. [1970] and Falco [1977]. The implication is that the intermittency at the edge of external flows tends to enforce its dominant scale on the outer region of flow, to the exclusion of a clear VLSM signature. However, the scale of the dominant interacting scale from the cospectral density appears to be quite similar to the size of the VLSM in internal flows. To make a more careful comparison between the two structures, an expansion of the dependence of the dominant interacting scale on wall-normal location can be compared with that of the VLSM. Monty et al. [2009] report that VLSM scaling in the internal flows tends to follow a power law of the form  $\lambda_x^E/\delta \approx 23(y/\delta)^{0.43}$ , similar to the scaling inferred from the boundary layer data of Kim and Adrian [1999] which fits (exactly, with only two points provided)  $\lambda_x^E/\delta \approx 20(y/\delta)^{0.38}$ . Both of these fits for the VLSM scaling agree strongly with the fit for the dominant interacting scale identified above, both in exponent and intercept, showing not only a similar physical size but also gradient across the boundary layer.

By overlaying the peaks from the cospectral density on the premultiplied spectrum of the stream-wise turbulence, from Jacobi and McKeon [2011a], this similarity can be observed quite clearly. Figure 7.10 shows this overlay for a raw spectral map. In some sense, the dominant interacting scale appears precisely where the VLSM would have, if not for the dominance of the boundary layer intermittency. Therefore, the presence of the modulating scale, as inferred from the cospectral density, indicates that VLSM play an important part even in external flows, even if their spectral signature

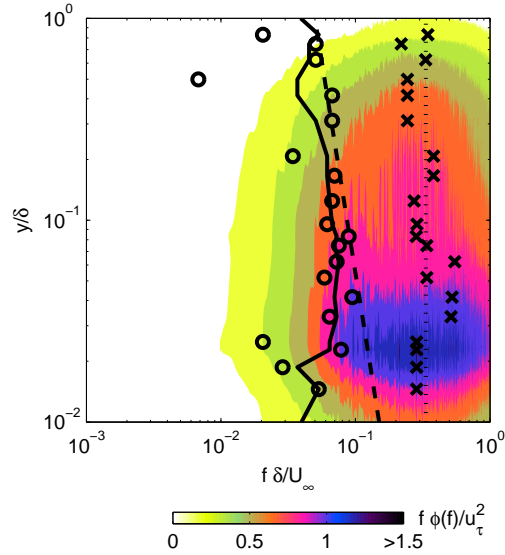


Figure 7.10: The premultiplied spectral map of the streamwise turbulent fluctuations from the hotwire measurements, again at the furthest downstream measurement location, corresponding to  $Re_\theta \approx 4100$ , in order to highlight the burgeoning double peak. The peaks from the amplitude at each wall-normal location are denoted by  $\times$  symbols; the ridgeline from the cospectral density is marked in circles with a solid line for the best fit, following the notation in figure 7.9. The dashed line corresponds to the power law for the VLSM reported by Monty et al. [2009], translated to the frequency domain via Taylor’s hypothesis using the present mean velocity profile; the dotted line represents the LSM at  $f\delta/U_\infty \approx 1/3$ .

not apparent by standard means of analysis.

In addition to identifying the location of the dominant large-scale contribution to the phase relationship with the small-scale envelope, the cospectral density can also identify the precise phase difference between that dominant contribution and the envelope. This phase information for the cumulative effect of all scales was inferred earlier from the cross-correlation maps, in section 7.4. With the cospectrum, we are able to isolate the effect of a single mode of the large-scale motions, and therefore it is convenient to reiterate physically how this phase information can manifest itself in the physical boundary layer. Figure 7.11 shows two sample phase profiles on the left, where the phase profile is recorded from the phase at a particular frequency component of the cospectrum across the boundary layer and represents the phase difference between that particular frequency of the large scale and the envelope of small scales, as described above. On the right side of figure 7.11 are sketches of the corresponding shapes of the large-scale mode (with a fixed downstream inclination angle) and the small-scale envelope (with an inclination set by the relative phase with the large-scale mode). The case of the small-scale envelope leading the large-scale mode, corresponding to a positive phase difference, is shown on top. The negative case is shown on bottom. It should be emphasized that the negative case allows for two possible interpretations: a net lag, or a phase lead by more than half a period. The choice between these two interpretations is made by the context of the rest of the

phase profile, to maintain continuity of phase, as will be discussed in the perturbed flow, in section 8.5.

Returning to the measured cospectrum, figure 7.12 shows both a map of the phase differences over the full range of frequency components, as well as the phase difference following along the ridgeline of the dominant frequencies. Despite the caveats about the use of coherent averaging of the spectral windows, the resulting phase map shows a reasonable representation of the phase shift across the boundary layer, entirely consistent with the cross-correlation approach for the aggregation of the large scales, shown in figure 7.2. In particular, both techniques show that the phase appears to hover about  $\pi/2$  for a broad range of wall-normal locations about the zero-crossing location of the correlation coefficient in the region of logarithmic layer.

By employing the cospectral density maps, it was possible to identify a dominant interacting scale on the order of the size of VLSM and to show that this dominant scale also tends to scale, across the boundary layer, following a power law similar to that governing VLSM scaling in internal flows, which strongly indicates the dynamical significance of the VLSM even far from the wall in an external flow. Moreover, the coherently averaged cospectral density revealed that this dominant interacting scale expressed precisely the phase relationship observed in the cross-correlation analysis of the aggregate large-scale signal.

## 7.6 Demodulation Using a Product Detector

Understanding the phase relationship between large-scale motions and the envelope of small-scale fluctuations as a classical amplitude modulation process means that demodulation, using a product detector technique, should be able to isolate the modulating signal from the instantaneous velocity measurements without the use of scale-separating filters or envelopes. Consider a standard amplitude modulation relationship, where a single-frequency carrier signal  $c(t)$  (at high frequency,  $f_c$  with amplitude  $C(f_c)$ ) is modulated by a low-frequency information signal,  $m(t)$  (at lower frequencies than  $f_c$ ) to produce a signal  $u(t)$ , defined in equation 7.6.

$$u(t) = [C(f_c) + m(t)]c(t; f_c) \quad (7.6)$$

In the case of the large-scale modulation in wall-turbulence, the carrier  $c(t)$  represents the small-scale motions; the information signal  $m(t)$  represents the large-scale motion modulating that those small scales, and the resulting modulated signal  $u(t)$  represents the observed instantaneous velocity. In order to identify the information signal, a product detector can be employed, whereby the instantaneous velocity signal  $u(t)$  is transformed into the frequency domain; then for each potential carrier frequency  $f_c$ , a copy of the original velocity signal is multiplied by a ‘local carrier’ sinusoid at that frequency. Writing the discrete Fourier transform of  $u(t)$  as equation 7.7,

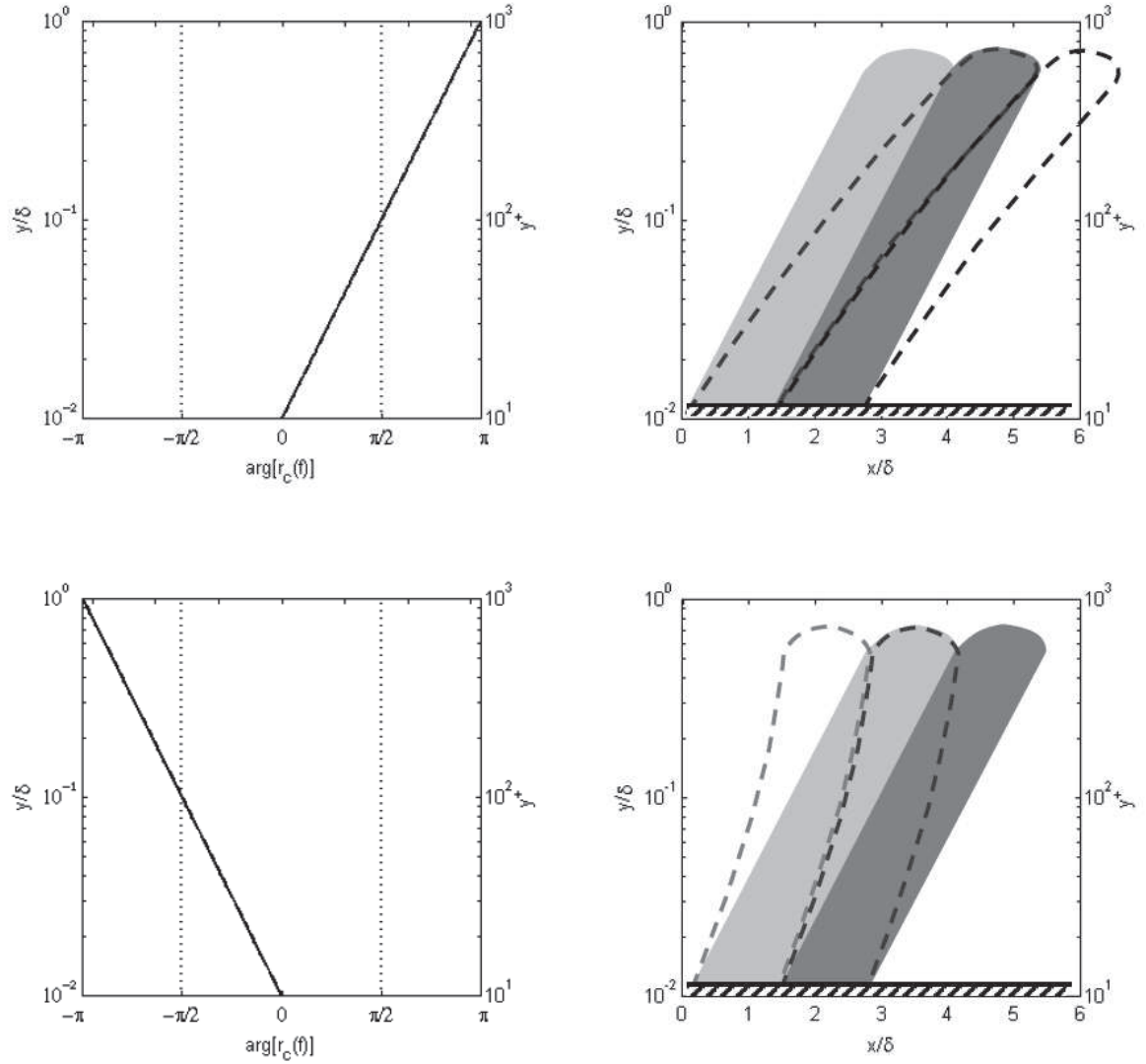


Figure 7.11: Illustrations of the relative orientation of the large-scale motions and corresponding envelopes of small-scale fluctuations, in the streamwise direction. The dark and light colors represent positive and negative fluctuations; the dashed lines represent the small-scale envelopes; the solid blocks represent large-scale motions. The top row shows a positive phase difference as measured in the phase of the cospectral density ( $\arg[r_c(f\delta/U_\infty)]$ ); the bottom shows a negative phase difference.

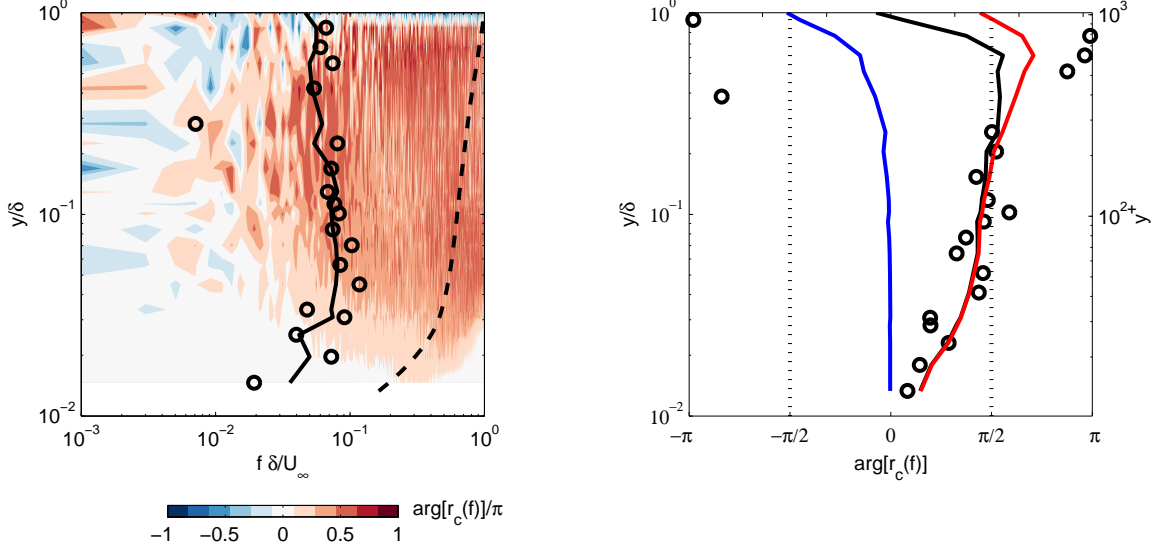


Figure 7.12: (Left) The map of  $\arg[r_c(f\delta/U_\infty)]$  with levels colored by the the phase angle, normalized by  $\pi$  to range from  $[-1, 1]$ . The absolute and fitted peaks from the magnitude map are also shown in circles and the solid line, respectively. (Right) The magnitude of the phase following the ridgeline of the peak magnitudes. Note that the crossing location of  $\pi/2$  appears approximately at the zero-crossing location of the correlation coefficient.

$$u(t) = A_0 + \sum_{j=1}^{\infty} A_j \cos(2\pi f_j t + \theta_j) \quad (7.7)$$

where the phase of each Fourier component,  $\theta_j$  is written explicitly, separate from the magnitude of the Fourier coefficients,  $A_j$ .

Then the product of  $u(t)$  with  $c(t, f_c)$ , written as  $c(t; f_c) = \cos(2\pi f_c t + \theta_c)$ , yields equation 7.8

$$\begin{aligned} u(t)c(t; f_c) &= \left[ A_0 + \sum_{j=1}^{\infty} A_j \cos(2\pi f_j t + \theta_j) \right] \cos(2\pi f_c t + \theta_c) \\ &= \frac{1}{2} [m(t; f_c) + C(f_c)] + \frac{1}{2} [m(t; f_c) + C(f_c)] \cos(4\pi f_c t + 2\theta_c) \end{aligned} \quad (7.8)$$

Finally, the frequencies higher than twice the chosen carrier frequency are filtered away to yield equation 7.9

$$m(t; f_c) + C(f_c) = \left[ A_0 + \sum_{j=1}^c A_j \cos(2\pi f_j t + \theta_j) \right] \cos(2\pi f_c t + \theta_c) \quad (7.9)$$

where the constant  $C(f_c)$  is given by the  $A_c$ . The choice of local carrier frequency  $f_c$  is constrained by a cutoff of the demodulation,  $(f_s/2)/2$ , which limits the new peak in signal  $m(t; f_c)$  to be within the Nyquist criterion,  $f_s/2$ ; failing to observe this constraint results in spurious peaks in  $m(t; f_c)$  at

frequencies lower than  $f_c$ , instead of  $2f_c$ , which can result in misidentifying the peak in  $m(t)$ . The demodulation can also be performed more efficiently in the time domain, by employing a low-pass filter at  $f_c$  on the product of the local carrier and original signal. The result of this demodulation procedure is a signal  $m(t; f_c)$  for each choice of local carrier frequency. However, the problem with this naive approach is the assumption that a single large-scale modulating signal,  $m(t)$  interacts with only a single frequency of the small scales. Of course, it is possible that multiple large scales have multiple modulation relationships with multiple small-scale frequencies. The problem can therefore be written more generally than equation 7.8 as equation 7.10.

$$\begin{aligned}
u(t) &= C_0 + \sum_{k=1}^{\infty} [C_k + M_k(t)] \cos(2\pi f_k t + \theta_k) \\
&= C_0 + \sum_{k=1}^{\infty} \left[ C_k + \left( \sum_{l=1}^{\infty} M_{kl} \cos(2\pi f_l t + \theta_l) \right) \right] \cos(2\pi f_k t + \theta_k) \\
&= C_0 + \sum_{k=1}^{\infty} [C_k + M_k(t)] \cos(2\pi f_k t + \theta_k) + \sum_{k=2}^{\infty} \sum_{l=1}^{k-1} M_{kl} \cos(2\pi f_l t + \theta_l) \cos(2\pi f_k t + \theta_k)
\end{aligned} \tag{7.10}$$

In the case of multiple modulation relationships, the demodulation problem (i.e., the identification of the components  $M_{kl}$  and  $C_k$ ) is ill-posed, as noted by Loughlin and Tracer [1996]. Even with simplifying assumptions, that the frequencies of the carrier  $f_k$  are always higher than those of the modulation,  $f_l$ , still the problem remains intractable. Turner and Sahani [2011] reviews some recent efforts at attacking this problem and propose their own probabilistic technique to isolating the most likely modulation pairs, but a trial of their technique applied to a turbulent velocity signal did not provide usable modulation information. In lieu of a rigorous treatment of the generalized demodulation problem, the naive approach outlined above, in which a broadband large scale is assumed to modulate a single small-scale carrier frequency, can be applied. The resulting spectrum of the broadband modulating signal,  $m(t)$ , is then analyzed, and the ratio of the peak frequency from the spectrum of  $m(t)$ , denoted  $f_m^*$ , to the local carrier frequency,  $f_c$  is examined.

In order to consider the ratio of the peak frequency from the spectrum of  $m(t)$  to the local carrier frequency, the demodulation procedure was performed for a linearly spaced subset of frequencies within the resolvable range of  $u(t)$ , and then repeated at each wall normal location, to construct a contour plot of the ratio of  $f_m^*$ , versus each frequency of the instantaneous velocity signal,  $f$ , as shown in figure 7.13. This naive version of the demodulation procedure indicates that the instantaneous velocity signal shows a broad region of the frequency domain where the ratio of the frequencies is not unity. This range of frequencies could represent a modulation relation between neighboring scale sizes centered roughly on the frequencies identified by the cospectral density as dominant interacting scales (although the variation with wall-normal location across the boundary layer appears to have the opposite concavity). The product detector therefore indicates that it is actually the dominant

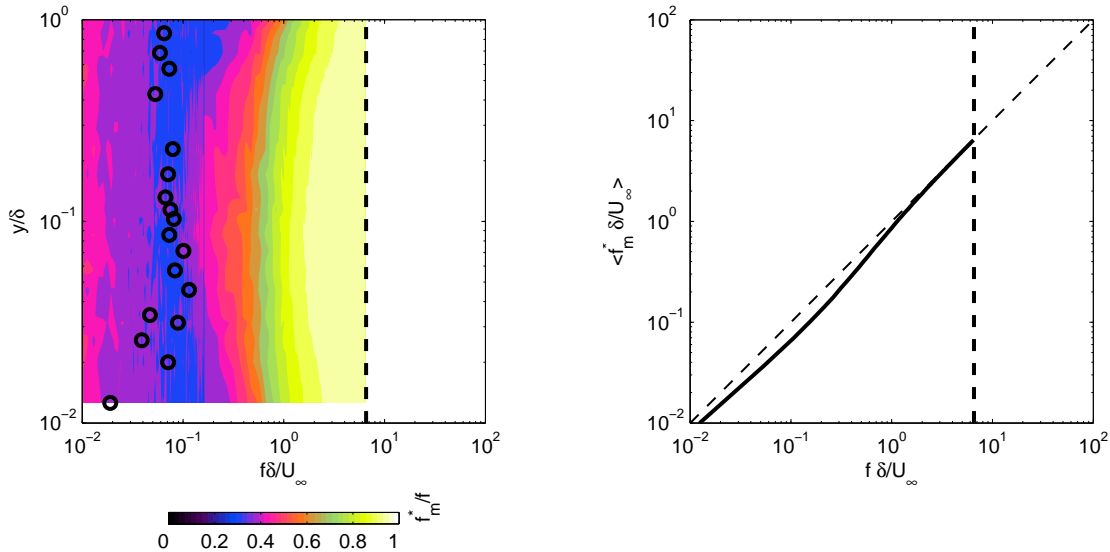


Figure 7.13: (Left) The ratio of the peak frequency of the information signal  $m(t)$  denoted  $f_m^*$  to the corresponding frequency of the instantaneous velocity signal spectrum,  $f$ , is shown as a contour map, over the range of the instantaneous velocity signal frequencies and wall-normal locations, normalized in outer units. The dashed black lines mark the spectral limits set by the product detector; the circle and solid line are the ridgeline and fit of the dominant interacting scales from figure 7.9. (Right) Averaging across the boundary layer thickness, the mean value of  $f_m^*$  in outer units for each frequency of the instantaneous velocity spectrum.

interacting scales, found previously, which are themselves being ‘modulated’ by scales which are, on average, approximately 1.5 times larger, whereas smaller scales, with  $f > 1U_\infty/\delta$  show essentially no modulation. The reason for this appearance of modulation at only lower frequencies is that for lower carrier frequencies, there are fewer possible modulating frequencies available, and hence more room for influence between neighboring frequencies. Therefore, the absence of evidence for the presence of classical modulation at high frequencies should not be interpreted to indicate that such modulation is not, in fact, present.

From the naive demodulation procedure, it appears that amplitude modulation in the classical sense is not detectable for scales smaller than the VLSM, although it may occur at the scale of the VLSM itself. That a range of very large scale motions may be closely aligned to each other in a modulating sense, and in addition that these same very large scales are in turn connected via a phase relationship with smaller scale motions, as observed in the cospectral density, indicate that the analogy of phase-locking between scales in the flow to phase-locked oscillators, as recently described by Bandyopadhyay [2011], deserves additional investigation. Although the naive demodulation procedure is not able to establish unequivocally the presence of classical amplitude modulation, it does show small indications of the presence of a phase relationship among the different very large scales in the boundary layer. Additional study of formal demodulation procedures remains to be performed.

## 7.7 Summary

The relationship between large-scale and small-scale motions in the turbulent boundary layer was explored using both traditional and new techniques. The instantaneous velocity field of a flat plate turbulent boundary layer was measured by both streamwise hotwire and streamwise/wall-normal planar PIV. After separating the large-scale signal of the instantaneous velocity field and constructing an envelope of the fluctuating small scales in both velocity directions, the two quantities were explored using both correlation coefficients and cross-correlations. The cross-correlation approach was employed to establish that fluctuations in the small-scale envelope tend to lead large-scale fluctuations in the spatial domain, in confirmation of a number of more recent investigators but in contrast with the original work of Bandyopadhyay and Hussain [1984]. Moreover, this phase analysis technique was applied for the first time to the wall-normal small-scale motions and a similarly oriented phase relationship was established. Spatial cross-correlations from the PIV were used to confirm the phase-lead of the small-scale envelope in both velocity components. The use of domain-limited PIV windows for spatial measurements presented a particular problem for correlation-based analysis when the dominant large scales are larger than the window size itself; this subfundamental sampling problem was analyzed, including its implications for understanding deviations from Taylor's hypothesis in the context of the spatial and temporal correlations.

The cross-correlation approach was then extended into the frequency domain, by exploring the cospectral density function describing the relationship between large-scale and the small-scale envelope. The cospectral density allowed for identification of a dominant interacting scale, among the large-scale motions in the flow, and this dominant scale was shown to match in both size and growth rate the VLSM observed in internal flows. Therefore, despite the absence of an energetic signature of VLSM in the outer region of external flows, VLSM appear to remain important and their influence on smaller scales in the flow could be observed through the cospectral analysis.

By employing a naive form of a product-detector-style demodulation technique, the scale interaction problem was then reconsidered without the use of an envelope on the small-scale motions. The boundary layer velocity signals were analyzed by comparing the ratio of the peak frequency of the inferred modulating signal to the small-scale carrier, which suggested some form of modulation behavior between neighboring very large scale motions, although there was no evidence of the involvement of a small-scale carrier signal, the presence of which awaits more robust and realistic demodulation techniques.

## 7.8 Appendix: Synthetic Signals

### 7.8.1 Subfundamental Sampling

When the cross-correlation of two pure sinusoids is calculated, the result is a symmetric function if the sinusoids are perfectly in phase, and an antisymmetric function if the two sinusoids are out of phase by  $\pi/2$ . But this rule holds only when the signals are adequately resolved; when less than a full period of the signals is available, the symmetry/antisymmetry rules are broken significantly. In particular, for the case of a phase difference between velocity signals of  $\pi/2$ , the breaking of the antisymmetry of the cross-correlation functions means that the wall-normal location at which this phase difference is measured will no longer correspond to the zero-crossing of the correlation coefficient. The precise form of the discrepancy can be shown by considering two idealized signals separated by precisely that phase difference,  $\cos(x)$  and  $\cos(x + \pi/2)$ , and calculating explicitly the cross-correlation as a function of the sample domain,  $[0, X]$ . For  $X = n\pi, n \geq 2$ , the cross-correlation function is antisymmetric and identifies the phase lag accurately. However, for real (not necessarily integral) values of  $n$  less than 2, the cross-correlation function loses its antisymmetry: the (negative) trough moves closer to zero, thus causing the value of the correlation coefficient to be negative (and not zero) at the location of the  $\pi/2$  phase lag between the signals, as shown in figure 7.14. As described above, the overall effect of this subfundamental sampling in real boundary layer signals is to cause the peak-to-trough switch to appear artificially further from the wall and distinctly higher than the zero-crossing of the correlation coefficient. The subfundamental sampling bias is also affected by the size of the filter and the amplitude of the small-scale fluctuations. The above, idealized model can then be elaborated to represent a velocity signal as a large scale superposed with a single small scale being modulated by the large scale, and thus the filtering effect in addition to the sampling period can be considered numerically. Such an analysis reveals that because the small-scale fluctuations in the wall-normal component have lower amplitude than the streamwise fluctuations, as seen in Hutchins and Marusic [2007], the subfundamental sampling effect is made significantly worse, and thus requires more extreme corrections with the filtering cutoff, as described above.

### 7.8.2 Robust Fit of Cospectral Density Ridgeline

In order to fit the ridgeline of the cospectral density map, which represents the dominant interacting scale between the large scales and the envelope of small-scale fluctuations, a simple power law relationship was assumed, in equation 7.11. By reversing Taylor's hypothesis via the mean velocity profile, equation 7.12, the peak frequency in the cospectral density map can also be written as a power law, in equation 7.13. The power law mean velocity profile fit follows from the standard 1/7 power law form for turbulent boundary layers, with Reynolds number naively included for compatibility

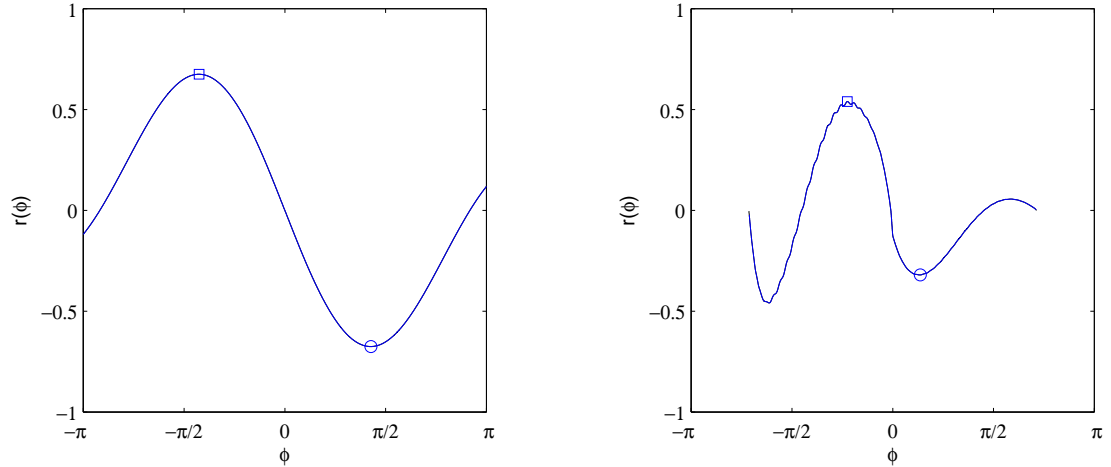


Figure 7.14: The cross-correlation function using two idealized sinusoids to represent the large and small scale motions, with the wavelength of the large scale ten times that of the small scale and the amplitude one hundred times that of the small scale. On the left, the cross-correlation when a full period of the largest scale is captured; on the right, the cross-correlation when only a fraction of the period is sampled. The fraction is selected by assuming a dominant large scale of  $6 \delta$  and using the actual streamwise dimension of the PIV window.

with the overall scaling in equation 7.11.

$$\lambda_x/\delta = 10^a (Re)^b (y/\delta)^c \quad (7.11)$$

$$U/U_\infty = 10^m (Re)^n (y/\delta)^p \quad (7.12)$$

$$\begin{aligned} f\delta/U_\infty &= 10^{-a} (Re)^{-b} (y/\delta)^{-c} (U/U_\infty) \\ f\delta/U_\infty &= 10^{-a+m} (Re)^{-b+n} (y/\delta)^{-c+p} \end{aligned} \quad (7.13)$$

Conducting the power law fit using a robust least-squares approach, the parameters for the fit can be optimized for both Reynolds number based on momentum thickness,  $Re_\theta$  and based on friction velocity,  $Re_\tau$ , shown in table 7.1. From the standard errors, there appears to be no advantage to either inner or outer scaling, although the functional form of the Reynolds number is admittedly simple and the range of Reynolds numbers quite limited. The resulting fits, including a simplified evaluation using the mean Reynolds number, are shown in equation 7.5.

A robust fit approach to fitting a power law to data involves iterating a standard, weighted least squared, and modifying the weights with each iteration using a bisquare function of the residuals.

	$\lambda_x/\delta = 10^a (Re_\theta)^b (y/\delta)^c$			$U/U_\infty = 10^m (Re_\theta)^n (y/\delta)^p$		
	$a$	$b$	$c$	$m$	$n$	$p$
Least Squares ( $y/\delta > 0.5$ )	0.32	0.28	0.34	-0.06	0.02	0.19
Standard Error of Coefficients	0.27	0.08	0.01	0.03	0.01	0.00
	$\lambda_x/\delta = 10^a (Re_\tau)^b (y/\delta)^c$			$U/U_\infty = 10^m (Re_\tau)^n (y/\delta)^p$		
	$a$	$b$	$c$	$m$	$n$	$p$
Least Squares ( $y^+ > 50$ )	0.15	0.38	0.34	-0.08	0.02	0.19
Standard Error of Coefficients	0.31	0.11	0.01	0.04	0.01	0.00

Table 7.1: Robust least-squares coefficients for power-law models of dominant modulation in inner and outer scaling

Even though most outliers in the ridgeline of the cospectral density maps were eliminated by using the extended Gaussian fits, this process tends to produce a fit that is still more robust against the affects of any remaining outliers.

$$Co(f\delta/U_\infty; \alpha, \mu, \sigma, \phi) = \alpha \exp\left(-\frac{(f\delta/U_\infty - \mu)^2}{2\sigma^2}\right) \cos(\phi) + (f\delta/U_\infty) \sin(\phi) \quad (7.14)$$

The resulting fitted power-laws are shown above in equation 7.5.

The cospectral density maps to which the above fitting was applied were calculated by coherent averaging, as noted above. While the coherent averaging technique appeared to succeed in preserving the phase information, in principle, incoherent averaging should provide a smoother power spectral estimate, at the cost of the preserved phase, as noted in Lyons [2011]. Recalculating the cospectral maps using incoherent averaging (not shown) indicates precisely the expected loss of phase information, but, surprisingly, the power appears noisier, although the peak for the dominant large-scale modulation appears roughly consistent. Recalling that the coherent averaging is equivalent to time-domain averaging, the coherently averaged time series is essentially the output of a low-pass filter. In particular, this low-pass filtering would tend to smooth the envelope of the small-scale signal beyond what the envelope rectification accomplished, and thereby eliminate the smallest scales in the envelope. By eliminating the smallest-scale fluctuations, the amplitude modulation effect appears to be clarified — a result which was explored again via the demodulation procedure in section 7.6.

## Chapter 8

# Phase Relationships Between Scales in the Perturbed Turbulent Boundary Layer

### 8.1 Interactions with a Synthetic Large Scale

The introduction of a synthetic large scale into the turbulent boundary layer provides a new angle from which to observe the phase relationship between large- and small-scale motions in general, as well as more particular insights on how artificial large scale might be used to influence or control small-scale motions. As in the previous chapter, correlation techniques are exploited to provide details on the nature of the scale interactions, but, in this case employing the static and dynamic perturbations that have been analyzed in chapters 3 and 5. By using phase-locked measurements of the dynamic perturbation, the dynamic and roughness effects can be isolated within the context of their individual effects on the phase between large- and small-scale motions. Ultimately, careful inferences from the observations of the phase relationship between large and small scales in the perturbed boundary layer provide a visual portrait of the effect of large-scale perturbations on the structure of the turbulent boundary layer.

### 8.2 Phase-Locked Velocity Maps of the Decomposed Flow

The phase-locked decomposition of the instantaneous velocity field, performed in section 5.2 following Hussain and Reynolds [1970], yielded three components: a time average,  $U$ , the phase-locked oscillatory component, representing the synthetic large scale,  $\tilde{u}$ , and the turbulent fluctuations about the synthetic large scale,  $u'$ , related by equation 8.1.

$$\hat{u}(y, t) = U(y) + \tilde{u}(y, t) + u'_t(y, t) \quad (8.1)$$

In the scale interaction analysis above, however, the instantaneous velocity signal  $u$  can be decomposed by filtering into a large-scale signal,  $u_L$ , and a small-scale remainder,  $u_R = u - u_L$  where the envelope of this remainder signal,  $u_S$ , can be defined by rectifying the absolute value of  $u_R$  with the filter used to obtain  $u_L$ , following the approach of Bandyopadhyay and Hussain [1984]. Therefore, when constructing maps of the mean periods of the phase-locked velocity components, the artificial mode  $\tilde{u}$  represents the largest scales in the flow,  $u_L$ , while the variation in the fluctuations about the artificial mode,  $u'_{rms} - \overline{u'_{rms}}$ , represents the envelope of small-scale fluctuations,  $u_S$ , although it should be emphasized that the small scales represented in  $u'_{rms} - \overline{u'_{rms}}$  are small relative to the very large scale motion of  $\tilde{u}$ , but they may not be strictly small in an objective (wavelength-limited) sense. The importance of this distinction may have explanatory power in a number of observations in subsequent sections.

Figure 8.1 shows the streamwise velocity components from both the hotwire and PIV studies. As in section 5.3.3, there is strong agreement between the streamwise hotwire and PIV measurements of the artificial mode,  $\tilde{u}$ ; here we see also close agreement between the two measurements for the envelope of fluctuations,  $u'_{rms} - \overline{u'_{rms}}$ . The close agreement provides confidence in reliability of the wall-normal measurements which were available only from PIV. Figure 8.2 shows the wall-normal components, as well as the Reynolds stress and fluctuations about the phase-locked Reynolds stress. As reported earlier in figure 5.18, the location of the critical layer at the streamwise location of the PIV was  $y/\delta \approx 0.13$ . The peak amplitudes of wall-normal and Reynolds-stress large-scale motions, as well as all of the small-scale envelopes, are consistently above the location of this critical layer, although they remain situated roughly between the locations of the two internal layers.

Visual inspection of the phase-locked velocity maps indicates that the envelopes of the small-scale motions have well defined shapes, like their large-scale counterparts. Moreover, the large- and small-scale components in the streamwise direction (from the hotwire measurements) appear out of phase in the outer region of the boundary layer, and roughly in phase near the wall, consistent with the conclusions from the correlation techniques in the unperturbed flow, reported in section 7.3, that there is a phase shift between the large-scale motions and small-scale envelope, increasing from 0 to  $\pi$  across the boundary layer. These trends appear to hold for the wall-normal motions as well, although the Reynolds stress fluctuations indicate a more complicated phase relationship, which is not analyzed in the present study. The mode shapes associated with the envelopes of the streamwise and wall-normal small-scale motions tend to be more concentrated in the area between the two internal layers than the corresponding large-scale motions, indicating that the small scales associated with the roughness are themselves organized to a significant extent by the dynamic perturbation; to what extent the roughness and dynamic effects can be thought of separately will be examined more quantitatively using the cross-correlation maps in section 8.4.

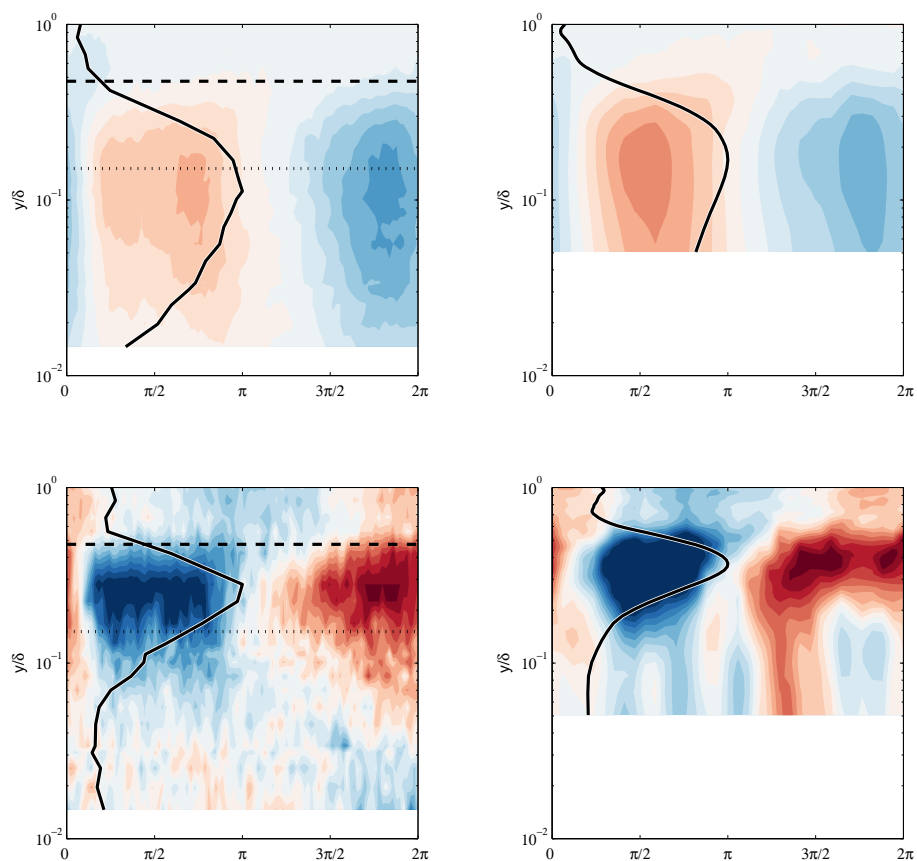


Figure 8.1: (Top)  $\tilde{u}$  measured by hotwire at  $x/\delta \approx 3.4$  on left and by PIV on right; levels in outer units range from  $[-0.1, 0.1]$ ; (Bottom) is the variation in the envelope of the small-scale motions,  $u'_{rms} - \overline{u'_{rms}}$ , in outer units, with levels  $[-0.01, 0.01]$ , with hotwire measurements on left and PIV on right. The black line represents the profile of the mean amplitude of the fluctuations averaged over a period in order to highlight the wall-normal location of the maximum amplitude with respect to the internal layers, marked with dotted and dashed lines for the hotwire measurements.

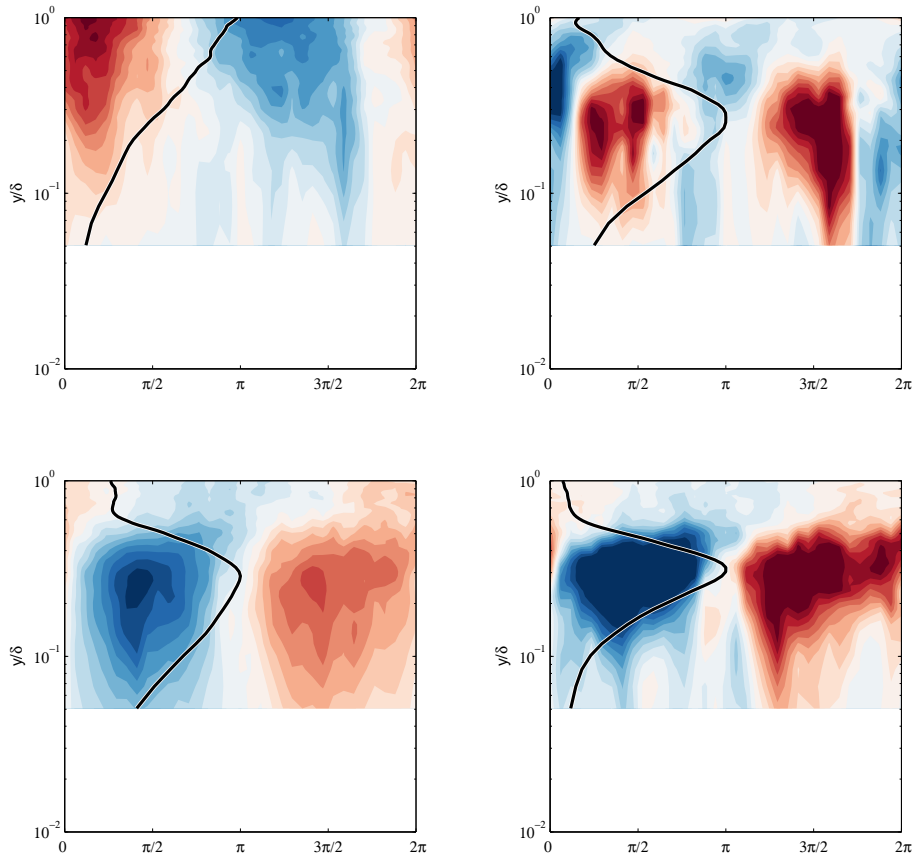


Figure 8.2: (Left) The components of the velocity signal in the wall-normal direction.  $\tilde{v}$  on top,  $v'_{rms} - \overline{v'_{rms}}$  on bottom; both presented in outer units, with levels  $[-0.01, 0.01]$ . (Right) The components of a decomposed Reynolds stress signal.  $\tilde{u}\tilde{v}$  on top,  $(u'v')_{rms} - \overline{(u'v')_{rms}}$  on bottom; again both presented in outer units, with levels  $[-0.0001, 0.0001]$ . Again, the black line represents the profile of the mean amplitude of the fluctuations averaged over a period in order to highlight the wall-normal location of the maximum amplitude.

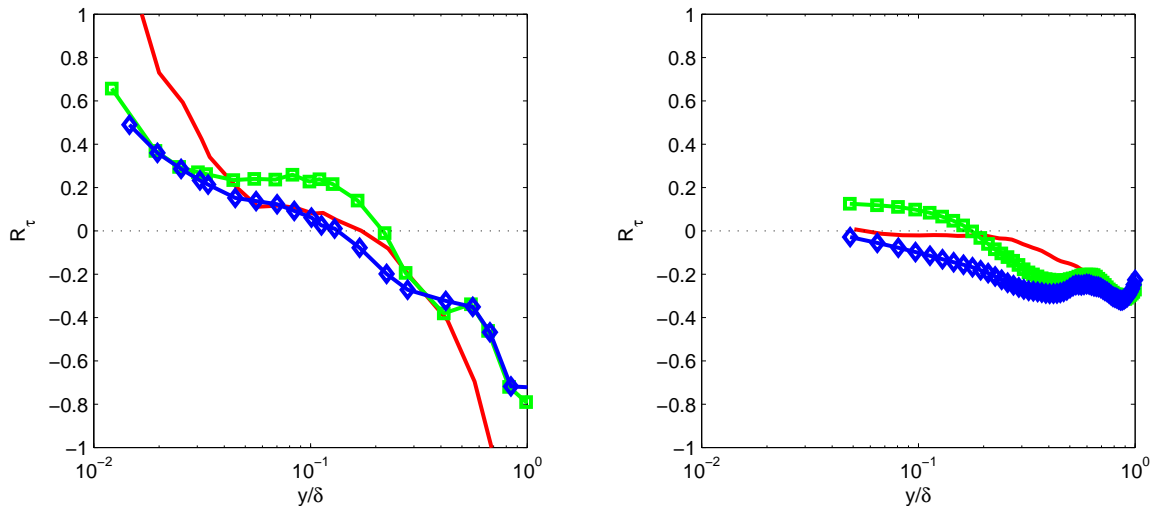


Figure 8.3: The correlation coefficient,  $R$ , at  $x/\delta \approx 3.4$  with: red unperturbed; green  $\square$  statically perturbed; blue  $\diamond$  dynamically perturbed. (Left)  $u_L$  and  $u_S$  with filter size  $\tau = 3\delta/U$  from hotwire measurements; and (Right)  $u_L$  and  $v_S$  with filter size  $\tau = 3\delta/U$

### 8.3 The Correlation Coefficient in the Perturbed Flow

In order to investigate the phase relationship between large and small scales in the perturbed flows more quantitatively, the correlation techniques used previously are applied. The correlation coefficient in the streamwise direction between the large-scale signal,  $u_L$  and the envelope of small-scale fluctuations,  $u_S$ , is calculated for the three flow regimes, shown in figure 8.3a. The correlation coefficient can also be defined meaningfully for the mixed correlation between large-scale motions in the streamwise direction and small-scale fluctuations in the wall normal direction, shown in figure 8.3b. The unperturbed correlation coefficients are repeated from figure 7.1 for comparison.

The correlation coefficients indicate that the zero-crossing tends to shift nearer to the wall in the dynamically perturbed flow and farther from the wall in the statically perturbed flow, for both the streamwise and wall-normal correlations, although the wall-normal correlation does not resolve enough of the near-wall region to provide conclusive evidence of this shift. The magnitude of the coefficient also changes across the entire boundary layer, in both perturbed regimes.

### 8.4 Cross-Correlation Isocontours

The correlation coefficient profiles conceal a wealth of information about the structure of the boundary layer. However, the previous chapter established that in order to obtain signed phase information about the scale interaction, the full cross-correlation function must be employed, following Bandyopadhyay and Hussain [1984]. The standard cross-correlation function,  $r(\Delta t)$ , as used previously,

was normalized by the standard deviations of the two input signals; however, in order to consider superposition effects in the perturbed flows, the cross-correlation functions are left nonnormalized through the remaining analysis. Plotting the isocontour maps of the cross-correlation functions for the two perturbed flows, the phase-locked measurements of the dynamic case, and for comparison the unperturbed flow (already shown in figure 7.2) indicates significant differences between the flow regimes, shown in figure 8.4.

Examination of the isocontour maps confirms the trend in the zero-crossing location for the correlation coefficient: the static perturbation case has a phase-jump (equivalent to a zero-crossing of the correlation coefficient) farther from the wall than the unperturbed case; the dynamic perturbation nearer to the wall. The phase-locked map gives some indication why the dynamic case shows a phase-jump nearer to the wall, since the artificial large scale in isolation appears to have a phase-jump with respect to the envelope of relatively smaller scales significantly nearer to the wall — so much so that farther away from the wall the phase of the small-scale envelope tends to lead the large scales by more than  $\pi$  beyond roughly the location of the second internal layer. In other words, the standard phase profile observed in the unperturbed flow, showing a variation from 0 to  $\pi$ , appears to be compressed into just the second internal layer when considering the phase-locked decomposition of the dynamically perturbed flow. This indication that the phase-locked map can explain at least some features of the overall cross-correlation map of the dynamically perturbed case motivates considering the superposition of the cross-correlation functions.

### 8.4.1 Cross-Correlation Superposition

If we consider the dynamic perturbation as a superposition of a long-wavelength periodic disturbance (superscript  $\tilde{u}$ ) on top of a static (or unperturbed) base flow (superscript  $st$ ), such that the dynamically perturbed large-scale velocity signal is  $u_L^{\tilde{u}} + u_L^{st}$  and the small-scale envelope is  $u_S^{u'} + u_S^{st}$ , then the cross-correlation (denoted  $\star$  as in equation 7.2) between them is given by

$$r(\Delta t)_{dyn} = (u_L^{\tilde{u}} + u_L^{st}) \star (u_S^{u'} + u_S^{st}) = \mathcal{F}^{-1} \left[ ((\mathcal{U}_L^{\tilde{u}} + \mathcal{U}_L^{st}))^* (\mathcal{U}_S^{u'} + \mathcal{U}_S^{st}) \right] \quad (8.2)$$

where the asterisk represents the complex conjugate, as above. The subtraction of the two cross-correlations yields

$$r(\Delta t)_{dyn} = \mathcal{F}^{-1} \left[ \mathcal{U}_L^{*\tilde{u}} \mathcal{U}_S^{u'} + \mathcal{U}_L^{*\tilde{u}} \mathcal{U}_S^{st} + \mathcal{U}_L^{*st} \mathcal{U}_S^{u'} \right] + r(\Delta t)_{st} = r(\Delta t)_{PL} + r(\Delta t)_{cross} + r(\Delta t)_{st} \quad (8.3)$$

where subscript  $PL$  refers to the phase-locked cross-correlation, subscript  $cross$  refers to the cross-terms between the statically perturbed flow and the phase-locked motions of the dynamically per-

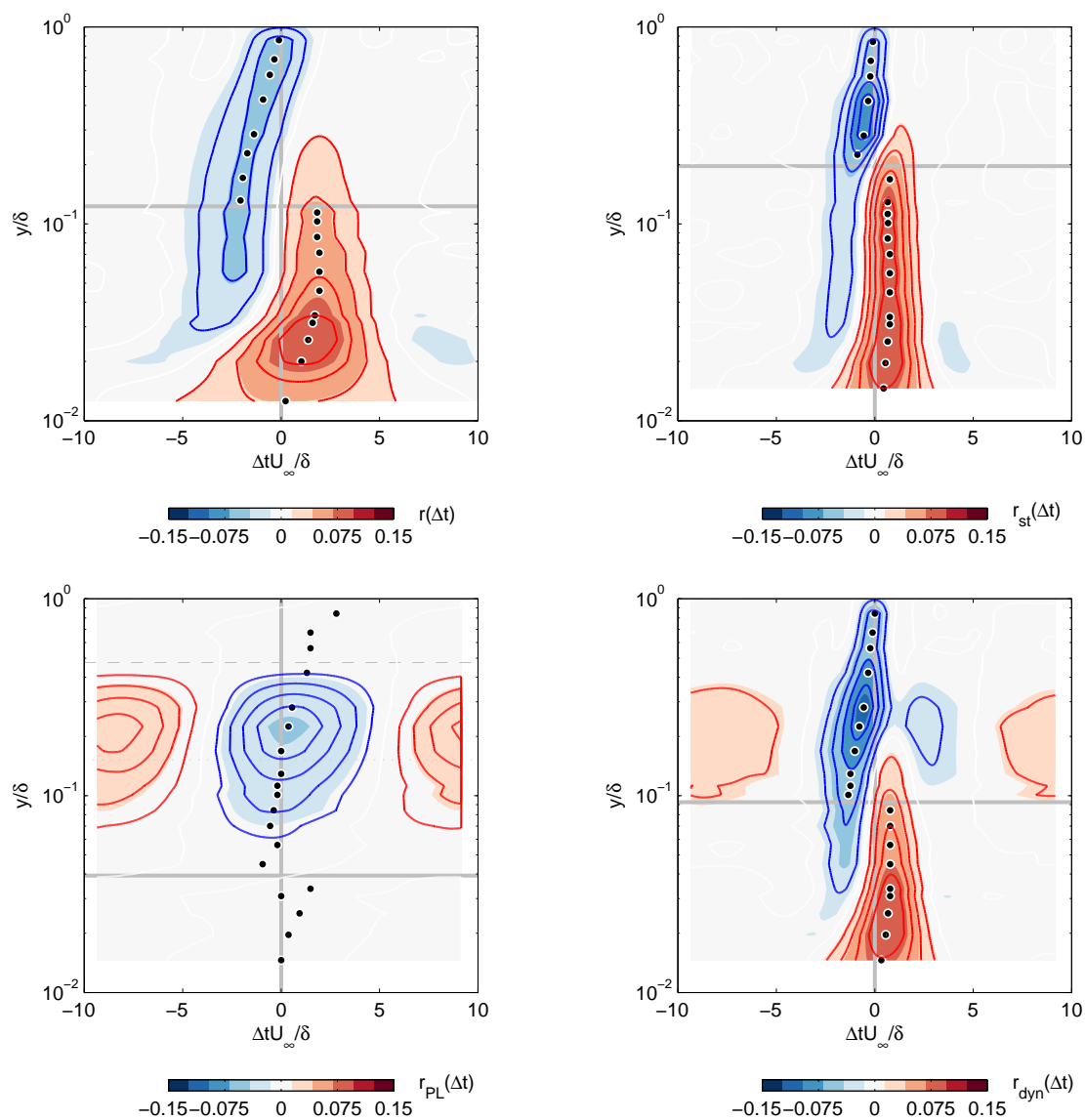


Figure 8.4: The isocontour maps of the streamwise cross-correlation function, without normalization, using the hotwire measurements with filter size  $\tau = 3\delta/U$  at streamwise location  $x/\delta \approx 3.4$ . Clockwise from top left: the unperturbed, statically perturbed, and dynamically perturbed flows. Finally, in the bottom left is a cross-correlation map constructed from the mean period of the phase-locked motions, shown above in figure 8.1, where the period has been converted into a temporal measurement by employing the previously ascertained wavelength and convective velocity of the large scales. Contour lines are equispaced between the opposite signed extrema in each graph individually; color levels are identical between different figures. The horizontal line indicates the the wall-normal location of the discontinuity along the ridgeline, representing a phase shift of  $\pi$ .

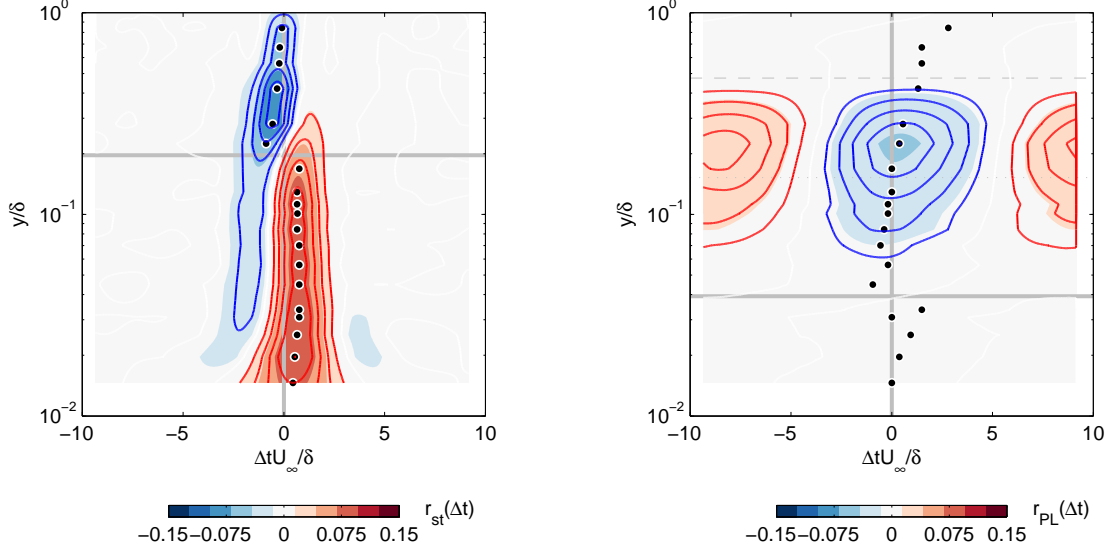


Figure 8.5: The isocontour maps of the streamwise cross-correlation function,  $r_{uu}(\Delta t)$ , without normalization, using the hotwire measurements with filter size  $\tau = 3\delta/U$  at streamwise location  $x/\delta \approx 3.4$ . (Left) statically perturbed; (Right) the phaselocked cross-correlation from the dynamically perturbed study. Contour lines are scaled and equispaced between the opposite signed extrema in each graph; color levels are comparable between different figures. The dots trace along the ridgeline of local extrema of the cross-correlation functions. The horizontal line indicates the the wall-normal location of the discontinuity along the ridgeline, representing a phase shift of  $\pi$ . The internal layers are also marked in the phase-locked map, to show that the phase lead as reached  $\pi$  at the location of the second internal layer, past which the phase lead exceeds half a period.

turbed flow, and

$$r(\Delta t)_{cross} = \mathcal{F}^{-1} \left[ \mathcal{U}_L^{*u} \mathcal{U}_S^{st} + \mathcal{U}_L^{*st} \mathcal{U}_S^u \right] \quad (8.4)$$

or, rewriting the summation:

$$r(\Delta t)_{PL} + r(\Delta t)_{cross} + r(\Delta t)_{st} = r(\Delta t)_{dyn} \quad (8.5)$$

As expected, the cross-correlation representing the phase-relationship between scales in the dynamic perturbation can be expressed as a contribution from the static case, from the phase-locked components representing the artificial large scale, and from the nonlinear interaction of those two individual contributions. The different components of this decomposition, in the streamwise direction, are shown in figures 8.5 and 8.6.

The discrepancy between the values of  $r(\Delta t)_{dyn}$  and  $r(\Delta t)_{PL} + r(\Delta t)_{st}$  is the result of the interaction between the dynamic and static effects, and is shown in the bottom of figure 8.6. The results are consistent between the hotwire and PIV and both indicate that cross- (or interaction-) terms are small compared to the contributions from the phase-locked and static maps, with a mean

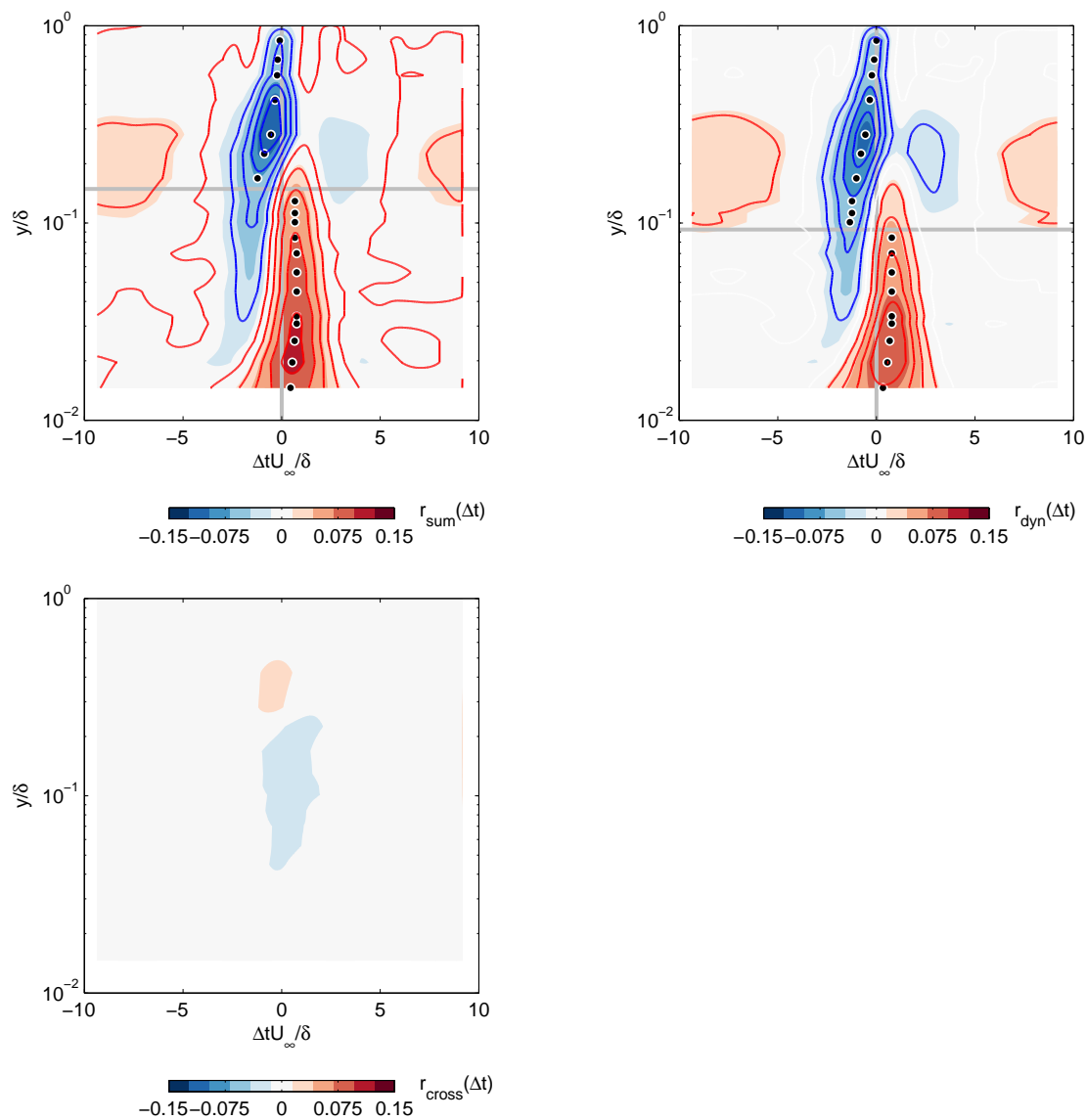


Figure 8.6: Superposition of the isocontour maps of the streamwise cross-correlation function,  $r_{uu}(\Delta t)$ , following equation 8.5. On the top: (Left)  $r(\Delta t)_{PL} + r(\Delta t)_{st}$ , which can be compared with (Right)  $r(\Delta t)_{dyn}$ ; on bottom: the difference between the linear superposition and the actual cross-correlation in the dynamically perturbed case,  $r(\Delta t)_{cross}$

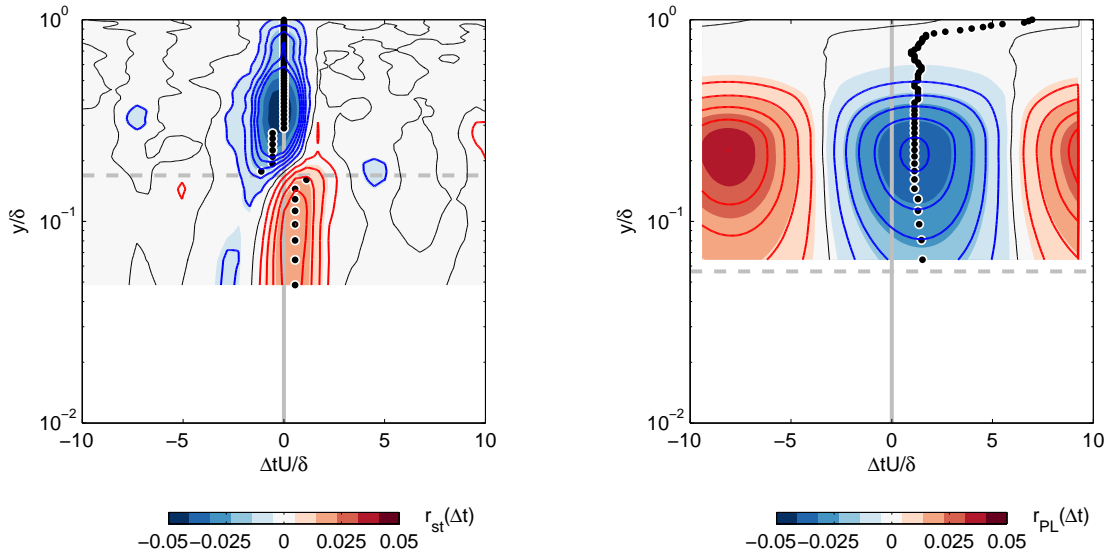


Figure 8.7: The isocontour maps of the streamwise-to-wall-normal cross-correlation function,  $r_{uw}(\Delta t)$ , without normalization, using the hotwire measurements with filter size  $\tau = 3\delta/U$  at streamwise location  $x/\delta \approx 3.4$ . (Left) statically perturbed; (Right) the phaselocked cross-correlation from the dynamically perturbed study. Contour lines are scaled and equispaced between the opposite signed extrema in each graph; color levels are identical between different figures. The dots trace along the ridgeline of local extrema of the cross-correlation functions. The horizontal line indicates the wall-normal location of the discontinuity along the ridge-line, representing a phase shift of  $\pi$ .

magnitude of approximately 10–15% of the mean magnitude of the dynamic map itself.

The decomposition of the cross-correlation can also be conducted on the envelope of small scale wall-normal fluctuations, as shown in figures 8.7 and 8.8. The relative strength of the wall-normal cross terms with respect to the dynamically perturbed total cross-correlation is approximately the same as in the case of the streamwise cross terms. However, the streamwise cross terms seem to be significant primarily in the vicinity of the zero-lag point of the cross-correlation, whereas the wall-normal cross terms tend to be significant also in the lobes of the dynamic perturbation (at normalized time lags near  $\pm 10\Delta tU/\delta$ ), meaning that the nonlinear effects of the artificial scale extend over larger spatial and temporal scales than the rather localized effect in the streamwise direction.

The location of the zero-crossing point in the correlation coefficient analysis is equivalent to the location of the phase-jump observed in the isocontour maps of the cross-correlation function, as reported in the previous chapter. Examining the streamwise phase-jump locations in table 8.1, there appear to be two inconsistent trends between the hotwire and PIV measurements. For the hotwire measurements, the wall-normal location of the phase-jump can be ranked as  $D < U < S$  for the dynamic (D), unperturbed (U), and statically perturbed (S) flows. However, the PIV measurements indicate a ranking of  $U < D < S$ , in both the temporal and spatial cases. In other words, the location in the dynamic case is always nearer to the wall than the static case, but the hotwire measurements

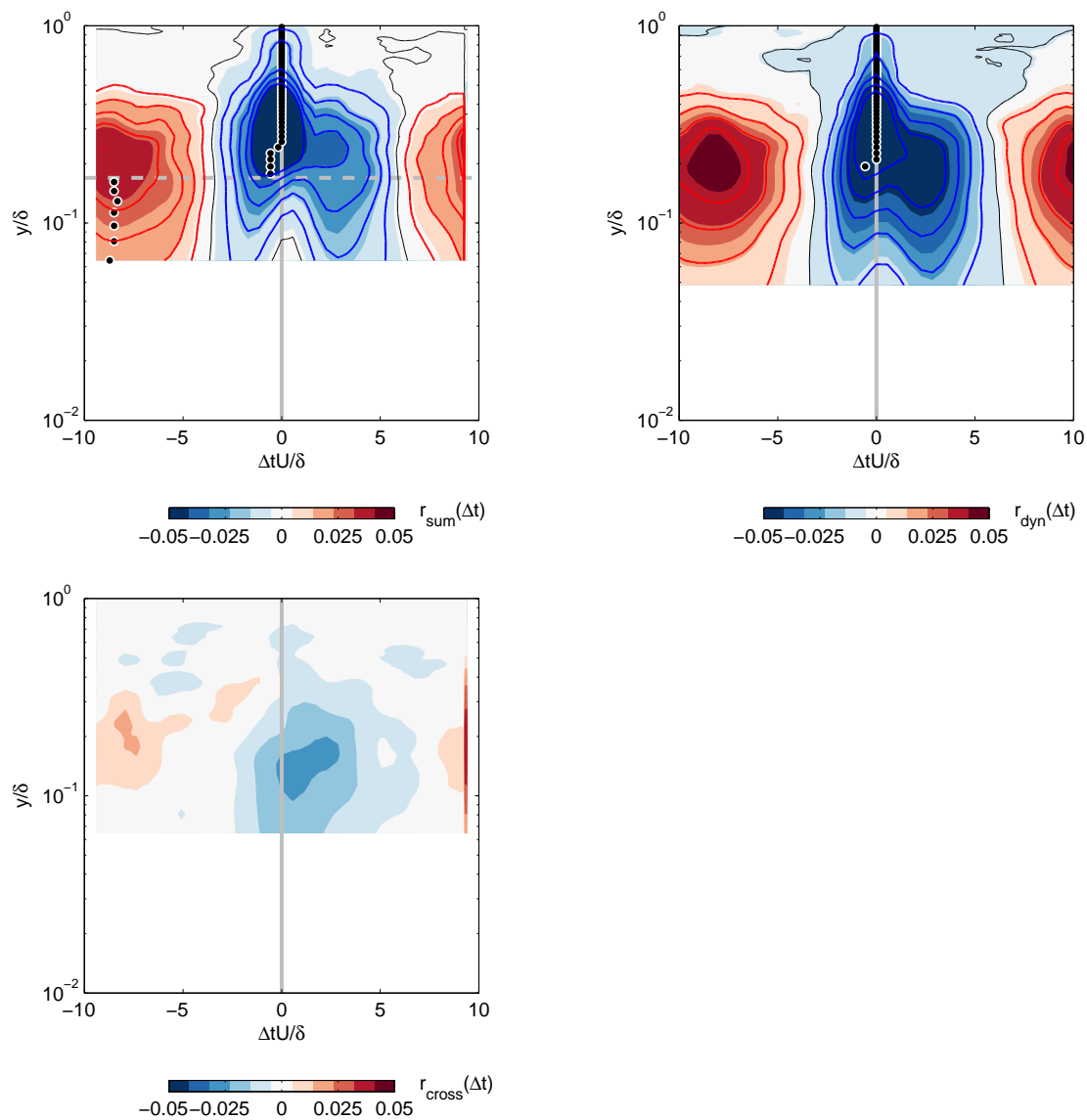


Figure 8.8: Superposition of the isocontour maps of the streamwise-to-wall-normal cross-correlation function,  $r_{uv}(\Delta t)$ , following equation 8.5. On the top: (Left)  $r(\Delta t)_{PL} + r(\Delta t)_{st}$ , which can be compared with (Right)  $r(\Delta t)_{dyn}$ ; on bottom: the difference between the linear superposition and the actual cross-correlation in the dynamically perturbed case,  $r(\Delta t)_{cross}$

	Temporal $\tau = 3\delta/U$			Spatial $\rho = 0.5\delta$	
	Hotwire	PIV		PIV	
	$u_L \star u_S$	$u_L \star u_S$	$u_L \star v_S$	$u_L \star u_S$	$u_L \star v_S$
Unperturbed	$0.12 \pm 0.02$	$0.16 \pm 0.02$	$0.08 \pm 0.02$	$0.14 \pm 0.02$	$0.18 \pm 0.02$
Static	$0.20 \pm 0.06$	$0.25 \pm 0.02$	$0.17 \pm 0.02$	$0.23 \pm 0.02$	$0.17 \pm 0.02$
Dynamic	$0.09 \pm 0.02$	$0.19 \pm 0.02$	$0.19 \pm 0.02$	$0.20 \pm 0.02$	$0.15 \pm 0.02$

Table 8.1: Phase-jump locations

suggest it is even closer than in the unperturbed flow. Recalling that the spatial PIV can fully resolve wavelengths from  $[0.03 \delta, 2.14 \delta]$ , the temporal PIV can resolve wavelengths from  $[2.29 \delta, 1170 \delta]$ , and the temporal hotwire signals can resolve wavelengths from  $[0.04 \delta, 6.0 \times 10^4 \delta]$ , it appears that the PIV always excludes a complementary portion of the spectrum for the dynamically actuated case, either the objectively large or small scales. In other words, if the artificial scale is  $18\delta$ , then it can be sensed by the temporal PIV, to the exclusion of all of the unperturbed small scales; at the same time, that same artificial large scale cannot be sensed spatially (due to the subfundamental sampling phenomenon, discussed above), while the small scales can. This means that the full interaction of the artificial scale with the ‘natural’ small scales of the unperturbed flow cannot be fully resolved with the PIV measurements.

The implication of this filter effect can then be understood in the context of the ‘small’ scales detected by the phase-locking procedure (shown above in figures 8.1 and 8.2). The ‘small’ scales under phase-locking represent scales that are small with respect to the phase-locked scale. But in the current experiments, the artificial scale is so large ( $18\delta$ ) that the ‘small’ scales will necessarily include what would otherwise be considered ‘large’ scales in the unperturbed flow. This fact helps to explain some of the success in the linear superposition of cross-correlation functions, since the phase-locked cross-correlation will implicitly carry some fraction of the nonlinear (‘cross’ term) content. But this fact can also explain the phase-jump discrepancy.

Recalling the relationship between phase and the relative physical inclination of structures in the flow, described in detail in section 7.5 above, the location of the phase-jump is an indicator of the perceived physical inclination of large-scale motions with respect to the envelope of small-scale fluctuations. Therefore, a phase-jump nearer to the wall can be interpreted to indicate a steeper gradient in the phase with respect to wall normal location; in other words, the phase increases more quickly to reach the  $\pi/2$  point, and thus the phase-lead by the small-scale envelope is greater at a given wall normal location compared to a flow with a phase-jump farther from the wall. With this in mind, we can employ a logic table to explain the phase-jump observations in table 8.1. If we assume that the natural small scales of the flow lead the artificial large scale which in turn leads the natural large scales, then we would expect the hotwire measurements to show  $D < U$  (in the phase-jump location) while the temporal PIV measurements would show  $U < D$ . In fact, of all the

possible permutations of the phase-lag relationships between the different scales, this assumed phase relationship is the only one consistent with both temporal observations (from hotwire and PIV). The assumption involved is that the phase change with wall-normal location is monotonic, such that larger phase leads indicate a more shallowly inclined structure with a phase-jump location nearer to the wall, as noted above.

Now, turning to the streamwise-to-wall-normal cross-correlation function,  $r_{uv}(\Delta t)$ , the observed order is  $U < D \lesssim S$ , which means that the artificial wall-normal scale must lag the unperturbed ‘small’-scale wall-normal signal, or in other words, that the natural wall-normal large scale leads the artificial wall-normal scale (which is consistent with the overall lack of phase change observed in the artificial wall-normal scale phase-locked maps).

Restating the two inferences: in the streamwise direction, the artificial large scale leads the natural large scales but lags the natural small scales; in the wall-normal direction, the PIV evidence suggests that the artificial (wall-normal) large scale lags the natural large scales, which in turn lag the natural small scales (where the small-scale observations in the wall-normal direction come from the spatial cross-correlations reported earlier). The streamwise inferences will be incorporated into a physical picture of the phase interaction between scales, in section 8.6; the wall-normal inferences must await validation due to the filtering effects of the PIV.

#### 8.4.2 Taylor’s Hypothesis

For the unperturbed flow in section 7.4.2, Taylor’s frozen turbulence hypothesis was examined by comparing the correlation coefficients obtained from the spatial and temporal analyses, by reconstructing the correlation coefficient from the cross-correlation phase lags. No definite conclusions could be reached for the unperturbed flow, due to the multiple effects of a possible failure of Taylor’s hypothesis and the subfundamental sampling problem. However, the contrast between the unperturbed and perturbed flows should in principle allow for separating these effects, assuming that the subfundamental sampling problem is consistent across the different flow regimes.

For the unperturbed case, in figure 7.6, the temporal correlation coefficient appeared to be greater, in absolute value, than the spatial coefficient, for all wall-normal locations. This could be explained partially by a convective velocity exceeding the local mean velocity, but also by a decrease in the spatial phase magnitude due to subfundamental sampling. Examining the same correlation coefficients for the perturbed flows, in figure 8.9, shows that they tend to share, in common with the unperturbed flow, a large discrepancy in the wake region, which could be explained by either of the causes cited. However, nearer to the wall, the spatially derived correlation coefficient in both regimes shows a prominent positive bulge, which matches a similar bulge in the temporal correlation coefficient for the static case, but diverges significantly in the dynamic case. (This bulge is present also in figure 8.3, although the reconstruction process from the phase ridgelines tends

to exaggerate the effect.) The reasonable agreement in the statically perturbed flow provides no evidence for any difference in the application of Taylor's hypothesis between it and the unperturbed flow. The significant difference in the dynamically forced case, however, indicates that the actual convection velocity is slower than the local mean (assuming a constant effect of subfundamental sampling) which is entirely consistent with the measured wave speed of the synthetic large scale. This suggests that the synthetic large scale not only violates Taylor's hypothesis itself, but also exerts a strong influence on the overall flow field. Alternatively, the large size of the synthetic large scale may significantly worsen the effect of subfundamental sampling, thereby explaining the discrepancy between spatial and temporal measurements. Therefore, as in the unperturbed flow, there is some indication of the violation of Taylor's hypothesis, consistent with previous measurements, but the inferences are not unambiguous.

## 8.5 Cospectral Density

In order to fully describe the phase relationships between large- and small-scale motions, these phase observations in each flow regime (which have been derived from the cumulative effect of all of the relevant scales) can be decomposed on a scale-by-scale basis, using the cospectral density function, as performed for the unperturbed flow in section 7.5. The cospectral density highlights the relationship between the range of large scales in the large-scale signal,  $u_L$  and comparable scales generated in the small-scale signal as a result of the envelope process. Carrying out the same procedure used previously on the perturbed flow reveals significant changes to the phase-relationship between different scales.

The cospectral density maps in the perturbed flows, figure 8.10, show an increase in the energy density in the region between the internal layers, spread across a wide range of frequencies. In the case of the statically perturbed flow, the location of the peak energy density is relatively unmoved from the ridgeline observed in the unperturbed flow, below the second internal layer, but near the mean edge of the first internal layer, the ridgeline shifts to reflect a broader distribution of relevant large-scale motions. This change indicates that in the statically perturbed flow, there are additional large-scale motions that are strongly correlated with the envelope of small-scale motions. The question is whether this change in the cospectral density is driven by changes in the envelope of small scales or the large-scale signal? To answer this question, we note first that a broad range of high cospectral intensity is also apparent near the wall in all of the flow regimes, indicating that very near the wall, all of the large-scale motions are synchronized with the smaller scales; as the large-scale structures grow away from the wall, only a small range of those scales appear to retain their strong correlation with the envelope of smaller scales.

One possible explanation of this behavior is the failure of Taylor's hypothesis near the wall; if

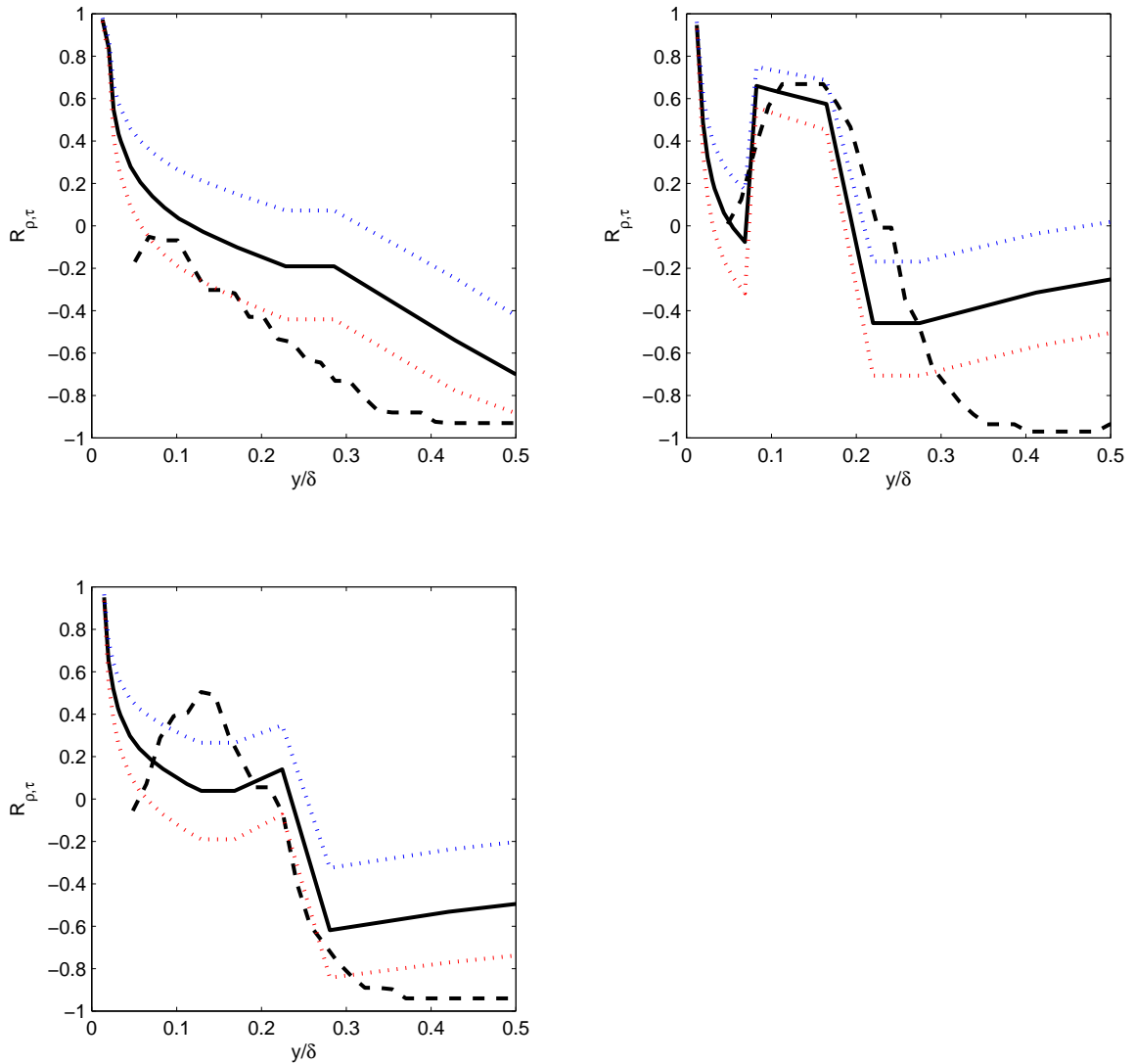


Figure 8.9: The correlation coefficients of  $u_L \star u_S$ , reconstructed from the cross-correlation ridgelines, where the temporal phases were converted to spatial phases using Taylor's hypothesis (black solid line). The conversion was also performed with a convective velocity 15% higher than the mean (red dotted line) and 15% lower than the mean (blue dotted line). The actual spatial measurements are shown in the black dashed line. Therefore, if the blue line is a better fit to the actual spatial measurements, it signifies that the relevant convective velocity is lower than the mean velocity in the flow. The measurements both employed a filter size  $\tau = 0.5\delta/U$  and  $\rho = 0.5\delta$ . Clockwise from top left: unperturbed, static, dynamic

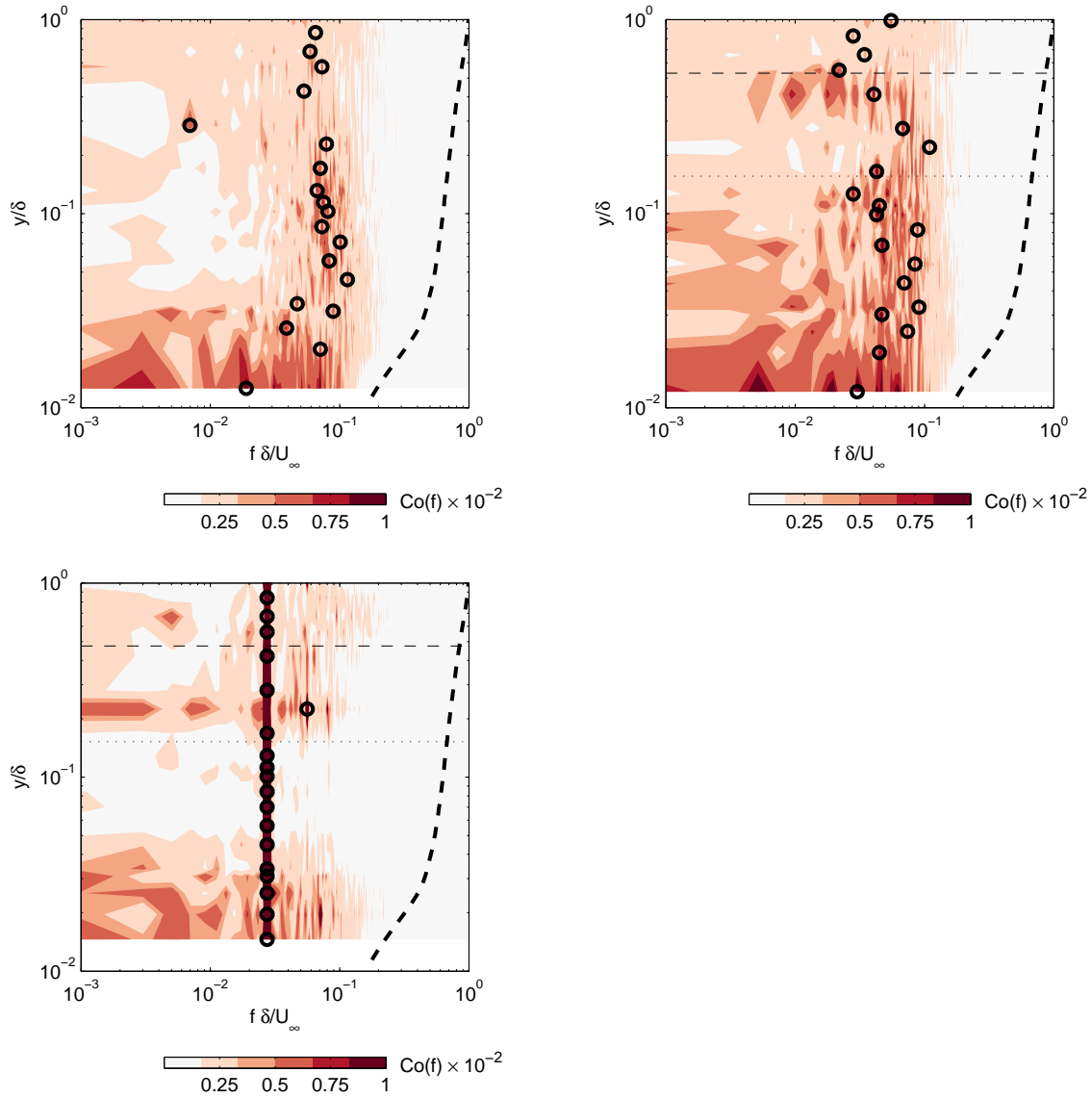


Figure 8.10: The cospectral density for the cross-correlation of  $u_L$  and  $u_S$  defined by temporal means from the hotwire measurements. The peaks from the amplitude at each wall-normal location are denoted by circles. The filter size of  $\tau = 1\delta/U$  is marked by a dashed line, which varies as a function of convective velocity. Clockwise from top left: the unperturbed flow, statically perturbed, and dynamically perturbed

the convective velocity of large scales were higher than the mean velocity in that region, then the filter cutoff would necessarily include more ‘large’ scales in the envelope of small scales than should be included, and those ‘large’ scales would, in turn, correlate with even larger scales, if there were a cascade of scale interactions. As the convective velocity slows to the local mean farther from the wall, fewer large scales would be inappropriately included in the small-scale envelope, thus narrowing the range of scale correlated directly with the envelope. Therefore, in the statically perturbed flow, when the near-wall velocity fluctuations are displaced away from the wall, again the small-scale envelope will tend to include larger scales from near the wall which are still small with respect to the large scales at the displaced wall-normal location. And again, the inclusion of large scales in the small-scale envelope would appear to reveal a wide range of scale interactions which stretch from very large-scale motions, all the way down to large-scale motions on the order of  $10 \delta$ , where the nominal ridgeline persists in the unperturbed flow far from the wall.

Another possible explanation is that the envelope procedure itself behaves differently near the wall, where the higher levels of turbulence intensity tend to contribute a greater range of scale sizes in the envelope, which can correlate with large-scale motions; farther from the wall, the range of small-scale motions is limited in the unperturbed flow, but the perturbed flow retains the diversity of small scales due to the displacement of scales away from the wall. Both perspectives emphasize the profound importance of the envelope in producing the perceived correlation between large- and small-scale motions.

In the dynamically perturbed flow, shown in the bottom row of figure 8.10, the ridgeline shifts completely to the location of the dynamic forcing (the synthetic large-scale motion), indicating that the synthetic large scale has a strong organizing effect on the envelope of small-scale motions in the flow. And, as with the static regime, there appears to be a wide band of high cospectral intensity in the region between the two internal layers, but this time the band is much narrower in wall-normal extent and is shifted closer to the second internal layer, slightly above the location of the critical layer, identified in section 5.3.2.

By tracing along the ridgeline in the cospectral density, the phase corresponding to each peak frequency can be retrieved, as in section 7.5, where coherent averaging of the individual windows was employed to preserve phase information. The phase content for the unperturbed flow is reproduced here for comparison in figure 8.11 and for the perturbed flows in figure 8.12. In addition to tracing along the ridgeline, the average phase across all frequencies can be calculated, weighting each frequency’s contribution by the relative magnitude of its cospectral density. The positive and negative phase contributions to the average can also be separated, where positive phase differences refer to the small-scale envelope leading the large-scale motion by a phase difference between  $[0, \pi]$ , and negative phase difference indicates the small-scale envelope is leading by more than half a period (i.e.,  $[\pi, 2\pi]$ ).

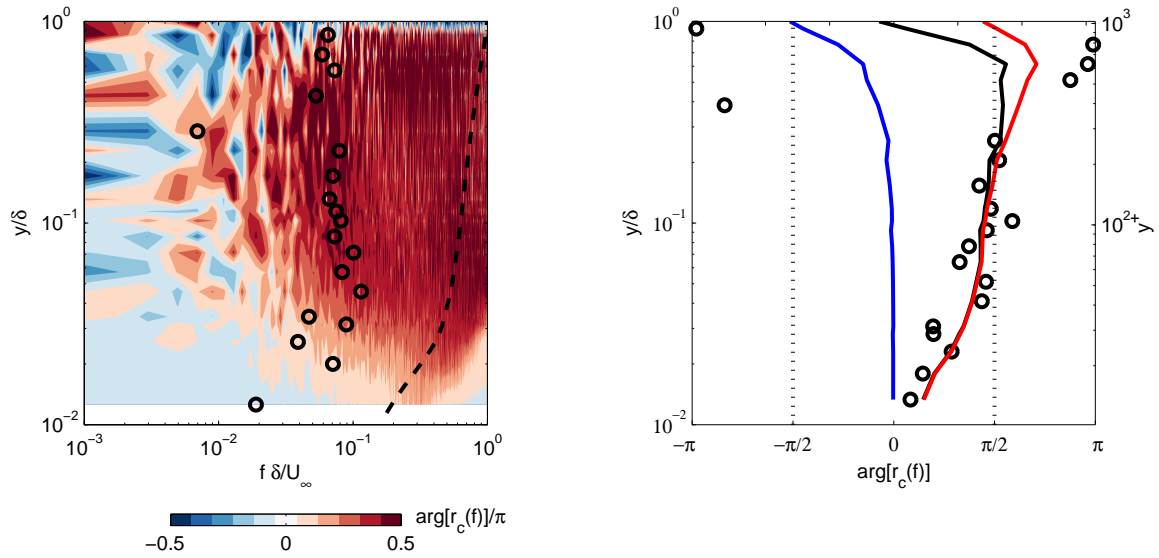


Figure 8.11: (Left) The map of cospectral phase  $,arg[r_c(f\delta/U_\infty)]$ , for the cross-correlation of  $u_L$  and  $u_S$  defined by temporal means from the hotwire measurements. The peaks from the cospectral density amplitude at each wall-normal location are denoted by circles. The filter size of  $\tau = 1\delta/U$  is marked by a dashed line, which varies as a function of convective velocity. (Right) The magnitude of the phase,  $arg[r_c(f\delta/U_\infty)]$ , following the ridgeline of the peak magnitudes, in circles. The mean phase, averaged across all large scale frequencies, and weighted by the power in each frequency, is shown in the solid black line. The red and blue lines are the weighted contributions to the mean phase from positive and negative phase components, respectively. Both maps are displayed for the unperturbed flow for reference.

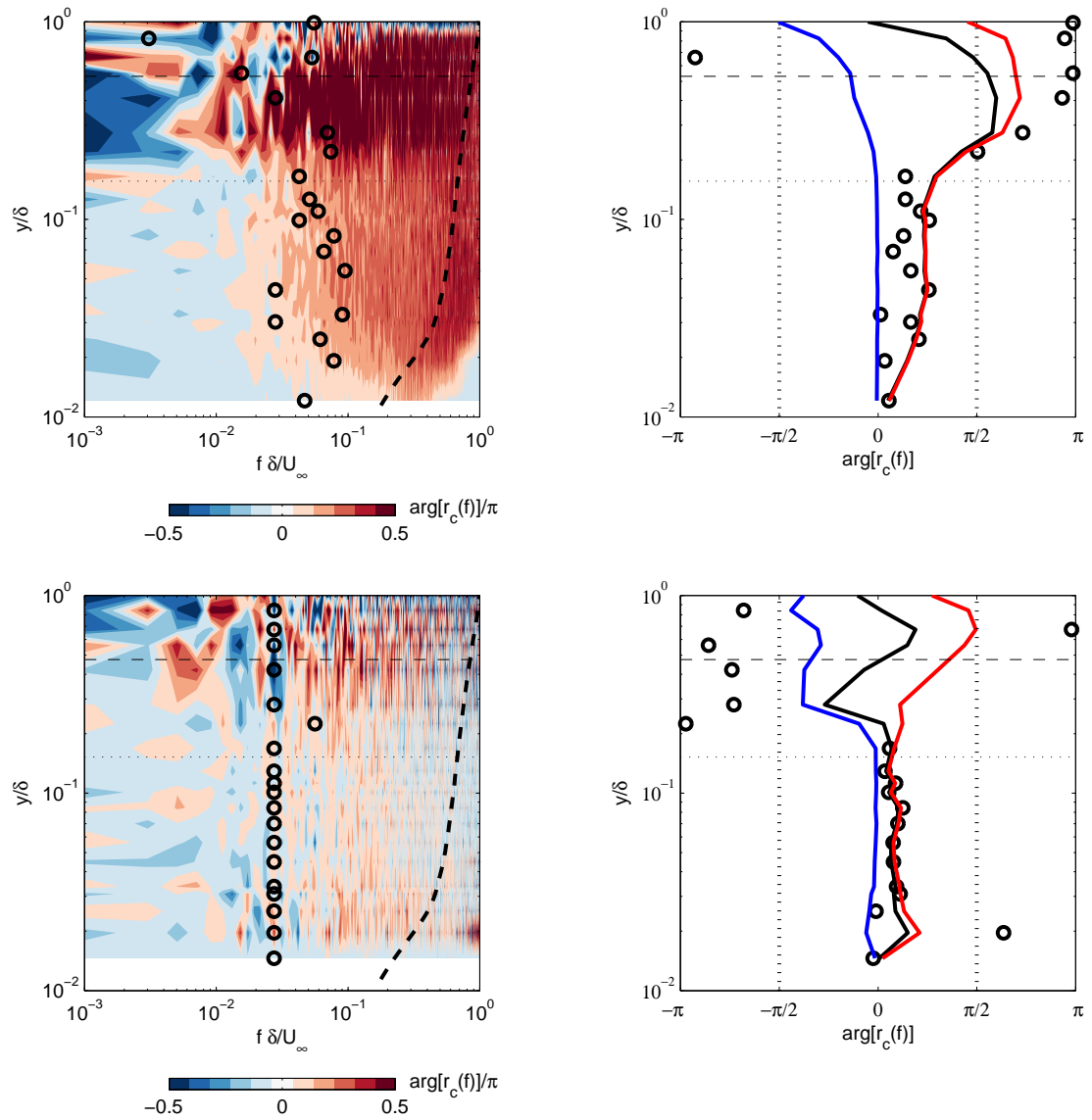


Figure 8.12: The phase maps and profiles for the perturbed flows, following the labeling in figure 8.11. Top row is the statically perturbed flow; bottom is dynamically perturbed.

For the unperturbed flow, the phase increases from 0 at the wall to approximately  $\pi$  at the mean edge of the boundary layer, with an extensive residence in the vicinity of  $\pi/2$  as reported earlier. Importantly, nearly all of the phase trends at different frequencies follow this pattern, and there is very little negative phase contribution except in the intermittent edge of the boundary layer, where we expect more significant phase differences due to intermittent bulges. In the statically perturbed flow, the phase traced along the ridgeline is significantly different: the rate of growth in phase with wall-normal location is slowed significantly beneath the second internal layer, and there is almost no residence about  $\pi/2$ ; beyond the second internal layer the phase changes abruptly, increasing rapidly to  $\pi$ . As with the unperturbed flow, nearly all of the phase lag, at all frequencies, is positive.

The dynamically perturbed flow shows even more significant departures from the phase trend observed in the unperturbed flow. The phase lead of small scales is suppressed even more within the second internal layer, while the behavior between the internal layers shows a change in sign, which is reflected also in the mean phase profiles. The sign change suggests that the small-scale envelope actually begins to lead by more than half a period, thereby aligning with the next sequential lobe of the synthetic large scale (hence resulting in the sign change). This enhanced leading away from the wall is an effect of the shape of the synthetic large scale, which tends to tilt backward (in the upstream direction) between the two internal layers, due to the change in the velocity gradient there, discussed in section 6.3. Near the wall, the lead by the small scales is suppressed even more than in the static case, due to the very shallow inclination of the synthetic large scale, which narrows the phase gap with its corresponding small scales.

In order to isolate the effect of the dynamic forcing, the frequency of the forcing can be excluded from the phase-averaging, as shown in figure 8.13. Without including the frequency of the synthetic large scale, the negative portion of the mean phase profile is no longer present. That negative portion, in which the small-scale envelope tends to lead the large scales by more than half a period, is a result of the curvature of the large-scale modes in the upstream direction far from the wall. The fact that this effect is largely removed by removing the forcing frequency indicates that the curvature of the large-scale motions toward the upstream direction, which was previously speculated to be mostly a consequence of the stress bore, is actually inextricably connected with the dynamic perturbation itself. So although there is some curvature due to the stress more in even the static case, the effect of the curvature is much more pronounced in the dynamic perturbation. These effects will be illustrated in section 8.6.

## 8.6 The Physical Manifestation of the Phase Relationship

Incorporating the inferences about the additive relationship between the perturbed and unperturbed flows, the locations of the zero-crossing in the correlation coefficient (or equivalently the phase-jumps

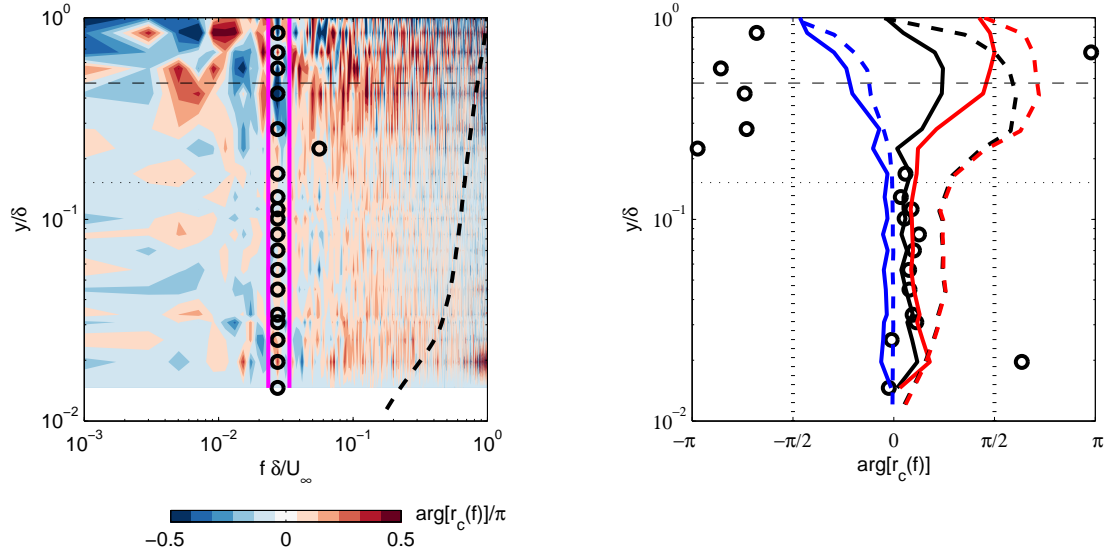


Figure 8.13: The magnitude of the phase,  $\arg[r_c(f\delta/U_\infty)]$ , for the dynamic case, as plotted in figure 8.11, however the weighted averaging was performed on a spectrum with a region between normalized frequencies 0.02–0.03 cutout (demarcated by magenta lines), thereby ignoring the dominant contribution from the artificial scale and showing the phase observed when averaged over the remaining non-forced frequencies. The dashed lines are from the statically perturbed flow (with the same cutout).

in the cross-correlations), and the overall phase profiles averaged from the cospectra, a physical picture of the phase relationships between the different scale motions in the turbulent boundary layer can be constructed, shown in figure 8.14. The relationship between the scale in the unperturbed case, shown in the top figure, matches that described in Chung and McKeon [2010]. For the statically perturbed case, the near wall phase lead becomes slightly less prominent, while the effect of the stress bore in the region between the internal layers tends results in a bending of the large-scale modes in the upstream direction, which shifts the zero-crossing (phase-jump) farther away from the wall. The newly curved large-scale modes are illustrated in red.

In the dynamically perturbed flow, using phaselocking to isolate the effect of the synthetic large scale, the near-wall phase lead is again suppressed due to the shallow inclination of the synthetic large scale paralleling that of the natural small scale. This also enhances the bending effect of the stress bore (discussed in section 6.3) on the phase lag, allowing the small-scale envelope to lead by more than half a period farther from the wall. In the sketch, the small-scale envelope is represented by the corresponding large scale from the statically perturbed case (since they are relatively small compared to the artificial large scale). The artificial large scale is now illustrated in red, showing both a greater bending effect in the upstream direction, as well as an inclination to the wall which is more shallow than that of the unperturbed large scale; these two features combine to yield a phase-jump location nearer to the wall than in the unperturbed flow. By adding linearly the effect

of the synthetic large scale to the statically perturbed flow, the cumulative effect of the dynamic roughness can be reconstructed to reasonable accuracy, as shown in the preceding sections.

The upstream bending of the large scales, associated with the stress bore, occurs in roughly the region between the two internal layers. Therefore, the bending is consistent with the increased shear stress in the stress bore, shown in section 3.1.3, and can be thought of as related to an increased mean prograde vorticity, as explained in section 4.3. In this way, the structural observation of the relative phase between the large- and small-scale motions in the perturbed boundary layer can be related directly to the stress bore and mean vortex core distribution.

## 8.7 Skewness Decomposition

Although the cross-correlation and cospectral approaches provide a rich source of information about the relationship between large- and small-scale motions and appear to be better suited than the correlation coefficient for robust analysis, nevertheless, the correlation coefficient possesses a remarkable similarity to the streamwise velocity skewness which merits further attention. Mathis et al. [2009a] first noted the similarity between the correlation coefficient describing the scale interaction and the streamwise skewness; subsequently Mathis et al. [2011] showed how the two quantities are intimately related through a decomposition of the streamwise skewness into large- and small-scale contributions. The connection between these quantities ultimately helps to explain the variation in the zero-crossing locations of the two functions, where the zero-crossing has been shown in the preceding sections to be important to the physical interpretation of the structure of the boundary layer.

The streamwise skewness, denoted  $S_u$ , when plotted against wall-normal location, typically exhibits a zero-crossing near the wall, as well as an apparent region of tangency (possibly containing one or two additional zero-crossings) in the logarithmic region. Between the near-wall crossing and the tangent region, the skewness is nominally negative and convex, although many measurements at higher Reynolds numbers report this region as marginally positive (Fernholz and Finley [1996] and Örlü [2009]). In any case, the Reynolds number dependence is significant to all of these features. Mathis et al. [2011] divided the instantaneous velocity signal into large ( $u_L$ ) and small ( $u_R$ ) scale signals and then expanded the definition of the third-moment of the velocity fluctuation, yielding equation 8.6

$$\overline{u^2}^{3/2} S_u = \overline{u^3} = \overline{(u_L)^3} + 3\overline{(u_L)^2(u_R)} + 3\overline{(u_L)(u_R)^2} + \overline{(u_R)^3} \quad (8.6)$$

where the over-bars denote time-averages with the means of each component subtracted prior to averaging. Examining the contributions of the four terms indicates that the only negative contribution is from the small-scale skewness,  $\overline{(u_R)^3}$ .

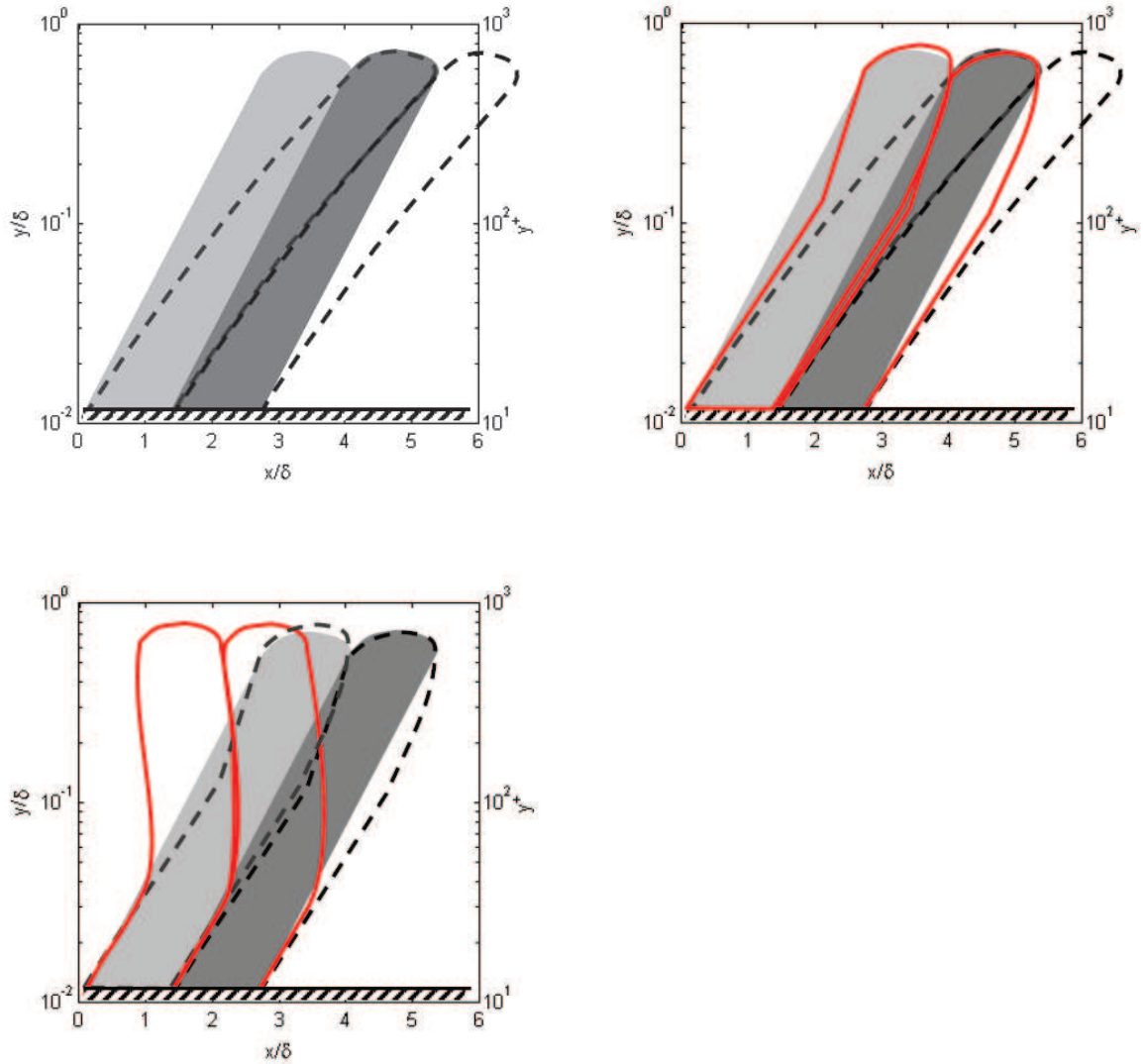


Figure 8.14: Illustrations of the relative orientation of the large-scale motions and corresponding envelopes of small-scale fluctuations, in the streamwise direction. (Top, left) Unperturbed, compare Chung and McKeon [2010]. (Top, right) Static perturbation, where the large-scale inclination (in red) is reversed in the region between the two internal layers, which was speculated to be an effect of the roughness perturbation. (Bottom) Dynamic perturbation in isolation (i.e., phase-locked), where the small-scale envelope is that of the large scales from the static perturbation, and the artificial large scale is in red. Note that the cross-over point tends to shift up in the case of the static perturbation and shifts down in a dynamic case where the artificial, highly inclined large structure dominate. Note also that the artificial scale is more inclined than the natural large scale but less than the natural small scales.

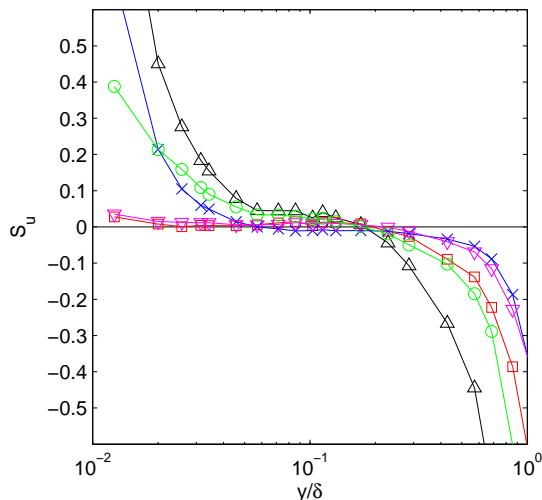


Figure 8.15: The decomposed skewness,  $S_u$ , at  $x/\delta \approx 3.4$  with: black  $\triangle$   $S_u$ ; red  $\square$   $\overline{u_L^3}$ ; purple  $\nabla$   $\overline{u_L^2 u_R}$ ; green  $\circ$   $\overline{u_L u_R^2}$ ; blue  $\times$   $\overline{u_R^3}$ . The first and second internal layers in the perturbed flows are marked with dashed and dotted lines, respectively. The filter size is  $\tau = 2.5\delta/U$ , to match that of Mathis et al. [2011].

Mathis et al. [2011] reported that terms  $\overline{(u_R)^3}$  and  $3\overline{(u_L)(u_R)^2}$  produced the dominant contributions to the skewness. However, they did not emphasize the filter-cutoff dependence of this conclusion: although the overall skewness,  $S_u$ , or correlation coefficient,  $R$ , is insensitive to the choice of filter-cutoff, obviously the distribution of the skewness amongst the different large and small scale components will depend quite strongly on cutoff size. Mathis et al. [2011] employed a filter cutoff of  $\lambda_x^+ = 7000$  or  $\lambda/\delta = 2.5$ . But, if a smaller filter cutoff is employed ( $\lambda/\delta = 1$ ), then the terms  $\overline{(u_L)^3}$  and  $\overline{(u_L)^2(u_R)}$  are no longer insignificant, because more of the large scale motions (greater than  $1\delta$ ) are being included with the  $u_L$  terms, as opposed to being grouped into the  $u_R$  signal. The question of the dependence on filter cutoff becomes even more important in the case of a perturbed flow in which large-scale motions are synthesized. Figure 8.16 shows the skewness for the three flow conditions at a single streamwise location, employing the same cutoff used in Mathis et al. [2011] for consistency, but again caution should be exercised in interpreting the meaning of each of the four terms in the decomposition, until a more careful study of the filter cutoff effect can be performed.

The static perturbation tends to increase the magnitude of the skewness across the boundary layer, while extending the convex region further from the wall. The dynamic perturbation increases the magnitude of the skewness only farther from the wall, thereby increasing the region of negative skew. In order to identify the sources of these effects, figure 8.17 shows the decomposition of the skewness in the perturbed flows. The magnitude increase of the statically perturbed flow can be

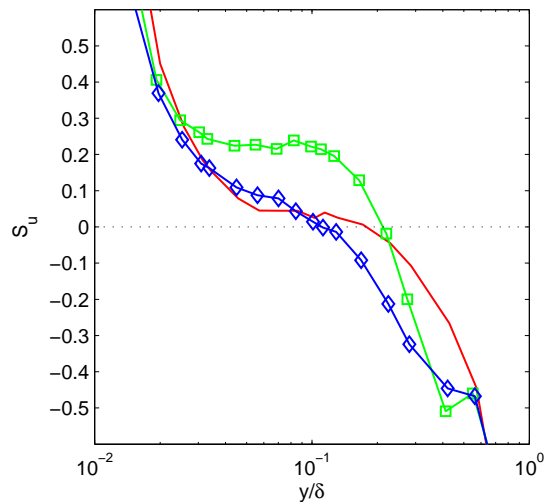


Figure 8.16: The skewness,  $S_u$ , at  $x/\delta \approx 3.4$  with: red unperturbed; green  $\square$  statically perturbed; blue  $\diamond$  dynamically perturbed. The filter size is  $\tau = 2.5\delta/U$ , to match that of Mathis et al. [2011].

attributed to increases in the  $\overline{u_L u_R^2}$  and  $\overline{u_R^3}$  terms, which are both expected from the increase in turbulence intensity observed within the stress bore. In the dynamic case, the negative skewness is associated with an increase in the magnitude of the  $\overline{u_L^3}$  term, which is expected due to the artificial large scales produced in the dynamically actuated flow.

The changes in the components of skewness can also be expressed in the context of shifts in the location of the zero-crossing. The static impulse tended to exaggerate the near-wall positive skew observed previously in the uniform roughness studies (Bandyopadhyay and Watson [1988] and Keirsbulck et al. [2002]), which is a consequence of the increase in small-scale fluctuations from the roughness. The results in the observed zero-crossing shift to a location farther from the wall. The dynamic impulse, however, tended to increase the region of negative skewness, shifting the zero-crossing closer to the wall.

As Reynolds number increases, the near-wall zero-crossing of skewness tends to move nearer to the wall (in outer units), monotonically, increasing the region of negative skewness, as seen in the results of Örlü [2009]. Thus the dynamic actuation tends to produce a skewness profile which shares this attribute of higher Reynolds number flows, despite the smaller momentum thickness. However, the presence of a near-wall zero-crossing may be obscured by both Reynolds number and spatial resolution effects, and therefore the observation that the dynamically perturbed flow appears similar to higher Reynolds number flows must remain tentative. Nevertheless, the connection between the phase information derived from correlation techniques and the streamwise skewness offers a potential avenue for generalizing the phase observations considered in the current study to a much broader set of more general experiments.

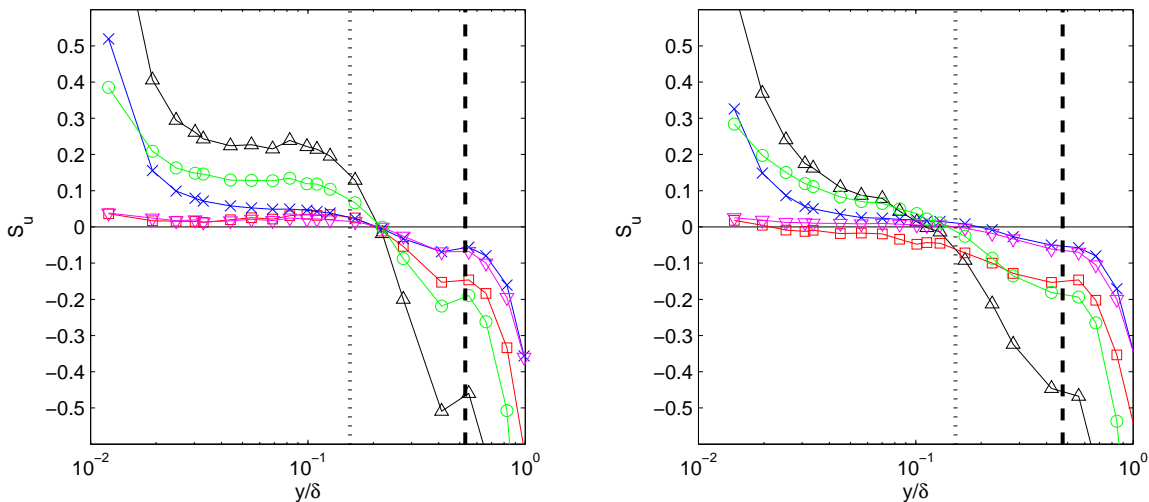


Figure 8.17: The decomposed skewness,  $S_u$ , at  $x/\delta \approx 3.4$  with symbols following figure 8.15, for the statically perturbed flow (left) and dynamically perturbed flow (right)

## 8.8 Demodulation

The naive version of the demodulation procedure employed on the unperturbed flow in section 7.6 can be applied to both perturbed regimes, in order to track the ratio of the peak frequency in the spectrum of the modulating signal to the frequency of the chosen carrier, shown in figure 8.18. As in the demodulation for the unperturbed flow, the marginal indication of a modulating relationship appeared only for a range of very large scale motions, with no obvious indication of smaller-scale involvement. The statically perturbed case appears almost identical to the unperturbed flow; the dynamic case shows that the range of large scale is limited in the region of the internal layers. The proper interpretation of these trends must wait for a more robust demodulation approach.

## 8.9 Summary

The relationship between large-scale and small-scale motions in the perturbed turbulent boundary layer was investigated using the correlation and cospectral techniques previously applied to the unperturbed boundary layer, as well as phase-locked analysis for the dynamically forced flow.

Phase-locked velocity maps of the streamwise and wall-normal fluctuating velocity components and Reynolds stresses allowed for identification of well-defined mode shapes in the envelopes of fluctuating quantities, much like the large-scale fluctuations were isolated previously. These mode shapes were then employed to consider the extent to which the phase relationships between large and small scales in the dynamically perturbed flow could be treated as a linear superposition of those

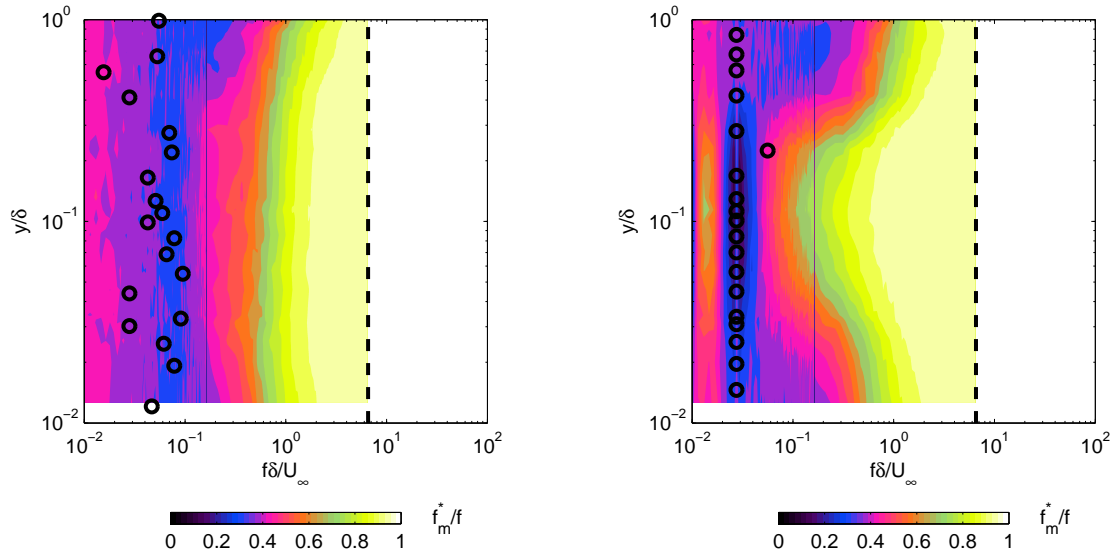


Figure 8.18: The ratio of the peak frequency of the information signal  $m(t)$  denoted  $f_m^*$  to the corresponding frequency of the instantaneous velocity signal spectrum,  $f$ , is shown as a contour map, over the range of the instantaneous velocity signal frequencies and wall-normal locations, normalized in outer units. The dashed black lines mark the spectral limits set by the product detector; the circles are the ridgeline of the dominant interacting scales from figure 8.10. (Left) static (Right) dynamic

relationships in the statically perturbed flow and the synthetic large scales, treated in isolation. By employing the cross-correlation isocontour maps, it was shown that this linear superposition could capture a significant amount of phase relationship in the dynamically perturbed case, which is likely a consequence of the very long wavelength of the synthetic large scale.

The correlation coefficient and the closely related streamwise skewness were also employed to compare the perturbed flows; in particular, the decomposition of the streamwise skewness proposed by Mathis et al. [2011] was used to explore how the balance of contributions from large- and small-scale motions tended to modify the shape and zero-crossings of the correlation and skewness functions. The correlation coefficient was also reconstructed from the cross-correlation function in order to test the validity of Taylor's hypothesis, revealing tentative support for the observation that the synthetic large scale tends to convect slower than the local mean velocity in the flow, across most of the boundary layer, beyond the location of the critical layer.

Finally, the cospectral density maps and accompanying phase maps were used to compare the relative phase lag profile (over the boundary layer thickness) between large- and small-scale motions, as a function of the scale size. The suppression of the lead of small scales over large scales in the static flow was observed to be consistent with the picture of the second internal layer as a newly 'born' boundary layer, indicated also in the phase-locked velocity maps of section 8.2; the more extreme trend in the dynamically perturbed case was consistent with the shallower inclination of

the synthetic large scales, which therefore tend to align more closely with the inclination of natural small-scale motions in the flow field. Moreover, the separability of the dynamic and static effects in the cross-correlation maps must be seen as a consequence of the phase-locked small-scale envelope capturing a significant amount of large-scale content in order to explain the phase trends from the cospectrum. This conclusion magnifies the overall message of the cospectral density maps, which is the profound importance of the use of an envelope procedure on the results of all of the correlation analyses considered.

## Chapter 9

# Conclusions

### 9.1 Summary of Results

The investigation of the perturbed boundary layer considered both a static roughness perturbation and a dynamically actuated roughness perturbation, and the relationship between these perturbed flows and the unperturbed zero-pressure gradient boundary layer. The static perturbation distorted the boundary layer layer in a mean sense, producing a stress bore and temporarily disrupting the near-wall processes associated with the equilibrium boundary layer. The stress bore provided an important means by which to consider the relaxation of the boundary layer back towards equilibrium. A new scaling of the streamwise velocity gradient was proposed and was used in conjunction with statistical and spectral maps of the developing flow field downstream of the perturbation to better understand the structural effects of a roughness perturbation on the boundary layer. This characterization of the static perturbation was essential to interpreting the dynamic perturbation which was subsequently considered. The dynamic perturbation involved actuating the roughness patch temporally in order to target large-scale motions in the boundary layer. The extent to which the dynamic wave aspect of the dynamic perturbation could be considered a linear addition to the underlying roughness perturbation was a constant theme of this experiment, and was explored by spectral and statistical means, and later in the context of large- to small-scale phase relationships in the flow field. The large-scale motion produced in the boundary layer by the dynamic forcing was shown to manifest as a coherent and persistent very long wavelength motion which could be isolated and studied by phase-locked measurements. A resolvent-based technique was used to predict the shape of the synthetic large-scale motion from its experimentally determined parameters, and the predictions were interpreted in the context of the stress bore associated with the roughness actuation. The relationship of the synthetic large-scale motion to smaller scales in the flow was then explored using a collection of correlation based techniques. In particular, the cospectral density between large scales and the envelope of small-scale motions was used to explore both the unperturbed and perturbed boundary layers, and indicated the importance of the envelope technique to previ-

ous observations of an amplitude modulation relationship between scales in the boundary layer. A phase interpretation was developed to provide physical intuition to the relationships between large and small scales, and it was shown that the very large scale synthetic motion generated in the flow could be considered, to a significant extent, a linear superposition on the nonequilibrium base flow, due to the significant difference in its wavelength.

## 9.2 Implications for Flow Control

A fundamental challenge for the control of turbulent flows is identical to the challenge in understanding turbulence: the extreme range of temporal and spatial scales that needs to be resolved to provide a complete picture of the turbulent motions. The range of scales places physical constraints on both sensors and actuators needed for the control of turbulence, some of which are described in Arthur et al. [2006]. And although Cattafesta and Sheplak [2011] report that there has been quite a bit of progress in the design and manufacture of sensors and actuators, a central problem remains. Gad-el Hak [1994] estimated the number and size of actuators needed to engage all relevant motions in the turbulent boundary layer on a typical commercial airliner, and concluded that the entire surface of the aircraft would need to be covered with actuators on the order of  $25 \mu\text{m}$  separated by  $250\text{--}2500 \mu\text{m}$ , making the control problem both a technical and economic nonstarter for any contemporary development timeframe. However, the assumption used in the estimate of Gad-el Hak [1994] is that all of the relevant scales must be actuated and sensed; in reality, the resolvent analysis and dynamic experiments of the current study indicate that certain large-scale perturbations can produce disproportionate effects on a properly receptive boundary layer. Furthermore, these large-scale motions influence smaller scales through a physically intuitive phase relationship. By targeting a turbulent boundary layer with a large-scale forcing, the effect of the forcing can potentially be predicted to reasonable accuracy by the resolvent method with only limited information about the mean flow itself, and not the detailed fluctuating flow conditions. And these large-scale predictions can then be used to understand the corresponding effect of the forcing on the phase of the small-scale motions with respect to those large scales. In this way, the current study supports a new conceptual approach to controlling the details of the turbulent boundary layer by easily achieved large-scale modifications.

## 9.3 Future Work

One of the key challenges of the current study is the interaction between the dynamic wavelike forcing and the impulsive roughness perturbation. A great deal of analysis was performed to establish the contexts in which these two quantities can be treated as essentially independent, and those in

which the nonlinearity must be considered. Ultimately, the roughness effect via the stress bore was found to be intertwined with many of the observations, even in those cases where a linear approximation yielded decent results (e.g., the cross-correlation phase maps). Thus, an important step in developing the techniques established in this study is implementation on a variety of different platforms for forcing the flow, including those which avoid the creation of a strong stress bore in the flow. At the same time, however, the presence of the stress bore raises its own important questions which deserve future experimental attention, not least of which is the dynamic measurement of the skin friction downstream of significant surface forcing, as well as the development of a stress bore in the case of three-dimensional roughness.

The correlation techniques employed in understanding the phase relationship between large- and small-scale motions also merit further inquiry. In particular, the cospectral density highlighted the importance of the enveloping procedure in the detection of the perceived amplitude modulation in the boundary layer; the details by which the envelope generates this perception are not yet well understood. And direct means of demodulating instantaneous velocity signals, perhaps utilizing probabilistic techniques, can also be used to further specify the nature of the phase relationship between large- and small-scale motions.

# Bibliography

- R.J. Adrian, K.T. Christensen, and Z.-C. Liu. Analysis and interpretation of instantaneous turbulent velocity fields. *Experiments in Fluids*, 29:275–290, 2000a.
- R.J. Adrian, C.D. Meinhart, and C.D. Tomkins. Vortex organization in the outer region of the turbulent boundary layer. *Journal of Fluid Mechanics*, 422:1–54, 2000b.
- J. Andreopoulos. The response of a turbulent boundary layer to a double step change in a wall heat flux. *ASME Journal of Heat Transfer*, 105:841–845, 1983.
- J. Andreopoulos and D.H. Wood. The response of a turbulent boundary layer to a short length of surface roughness. *Journal of Fluid Mechanics*, 118:143–164, 1982.
- R.A. Antonia and R.E. Luxton. The response of a turbulent boundary layer to a step change in surface roughness Part 1. Smooth to rough. *Journal of Fluid Mechanics*, 48(4):721–761, 1971a.
- R.A. Antonia and R.E. Luxton. The response of a turbulent boundary layer to an upstanding step change in surface roughness. *Journal of Basic Engineering*, 93:22–34, 1971b.
- R.A. Antonia and R.E. Luxton. The response of a turbulent boundary layer to a step change in surface roughness Part 2. Rough-to-smooth. *Journal of Fluid Mechanics*, 53(4):737–757, 1972.
- G.G. Arthur, B.J. McKeon, S.S. Dearing, J.F. Morrison, and Z. Cui. Manufacture of micro-sensors and actuators for flow control. *Microelectronic Engineering*, 83:1205–1208, 2006.
- B.J. Balakumar and R.J. Adrian. Large- and very-large-scale motions in channel and boundary-layer flows. *Philosophical Transactions of the Royal Society A*, 365:665–681, 2007.
- P.R. Bandyopadhyay. Why do large and small scales couple in a turbulent boundary layer? In *APS Division of Fluid Dynamics Meeting Baltimore*, 2011. APS Division of Fluid Dynamics Baltimore 2011.
- P.R. Bandyopadhyay and A.K.M.F. Hussain. The coupling between scales in shear flows. *Physics of Fluids*, 27(9):2221–2228, 1984.

- P.R. Bandyopadhyay and R.D. Watson. Structure of rough-wall turbulent boundary layers. *Physics of Fluids*, 31(7), 1988.
- R.F. Blackwelder and L.S.G. Kovasznay. Time scales and correlations in a turbulent boundary layer. *Physics of Fluids*, 15(1545), 1972.
- J.P. Boyd. *Chebyshev and Fourier Spectral Methods*. Dover Publications, 2000.
- G.J. Brereton, W.C. Reynolds, and R. Jayaraman. Response of a turbulent boundary layer to sinusoidal free-stream unsteadiness. *Journal of Fluid Mechanics*, 221:131–159, 1990.
- P.J.H. Builtjes. Determination of the eulerian longitudinal integral length scale in a turbulent boundary layer. *Applied Science Research*, 31, 1975.
- L.N. III Cattafesta and M. Sheplak. Actuators for active flow control. *Annual Review of Fluid Mechanics*, 43:247–272, 2011.
- D. Chung and B.J. McKeon. Large-eddy simulation of large-scale structures in long channel flow. *Journal of Fluid Mechanics*, 661:341–364, 2010.
- F.H. Clauser. The turbulent boundary layer. *Advances in Applied Mechanics*, 4:1–51, 1956.
- G. Danabasoglu and S. Biringen. A Chebyshev matrix method for spatial modes of the Orr-Sommerfeld equation. Technical Report CR 4247, NASA, 1989.
- D.B. DeGraaff and J.K. Eaton. Reynolds-number scaling of the flat-plate turbulent boundary layer. *Journal of Fluid Mechanics*, 422:319–346, 2000.
- D.J.C. Dennis and T.B. Nickels. On the limitations of Taylor’s hypothesis in constructing long structures in a turbulent boundary layer. *Journal of Fluid Mechanics*, 614:197–206, 2008.
- P.G. Drazin and W.H. Reid. *Hydrodynamic Stability*. Cambridge University Press, 2 edition, 2004.
- L.P. Erm and P.N. Joubert. Low-Reynolds-number turbulent boundary layers. *Journal of Fluid Mechanics*, 230:1–44, 1991.
- R.E. Falco. Coherent motions in the outer region of turbulent boundary layers. *Physics of Fluids*, 20:124–132, 1977.
- H.H. Fernholz and P.J. Finley. The incompressible zero-pressure-gradient turbulent boundary layer: an assessment of the data. *Progress in Aerospace Science*, 32:245–311, 1996.
- K.A. Flack. Examination of a critical roughness height for outer layer similarity. *Physics of Fluids*, 19, 2007.

- P. Freymuth. Frequency response and electronic testing for constant-temperature hot-wire anemometers. *Journal of Physics E: Scientific Instruments*, 10:705, 1977.
- M. Gad-el Hak. Interactive control of turbulent boundary layers: a futuristic view. *AIAA Journal*, 32(9):1753–1765, 1994.
- M. Gaster. On the effect of boundary-layer growth on flow stability. *Journal of Fluid Mechanics*, 66(3):465–480, 1974.
- C.E. Grosch and H. Salwen. The continuous spectrum of the Orr-Sommerfeld equation. Part 1. The spectrum and the eigenfunctions. *Journal of Fluid Mechanics*, 87:33–54, 1978.
- M. Guala, S.E. Himmelfarb, and R.J. Adrian. Large-scale and very-large-scale motions in turbulent pipe flow. *Journal of Fluid Mechanics*, 554:521–542, 2006.
- M. Guala, M. Metzger, and B.J. McKeon. Interactions across the turbulent boundary layer at high Reynolds number. *Journal of Fluid Mechanics*, 666:573–604, 2011.
- L.H.O. Hellström and A.J. Smits. Visualizing the very-large-scale motions in turbulent pipe flow. *Physics of Fluids*, 23, 2011.
- I.H. Herron. The Orr-Sommerfeld equation on infinite intervals. *SIAM Review*, 29(4):597–620, 1987.
- J.O. Hinze. *Turbulence*. McGraw-Hill College, 2 edition, 1975.
- A.K.M.F. Hussain. Coherent structures and turbulence. *Journal of Fluid Mechanics*, 173:303–356, 1986.
- A.K.M.F. Hussain and W.C. Reynolds. The mechanics of an organized wave in turbulent shear flow. *Journal of Fluid Mechanics*, 41:241–258, 1970.
- A.K.M.F. Hussain and W.C. Reynolds. The mechanics of an organized wave in turbulent shear flow. Part 2: Experimental results. *Journal of Fluid Mechanics*, 54:241–261, 1972.
- N. Hutchins and I. Marusic. Large-scale influences in near-wall turbulence. *Philosophical Transactions of the Royal Society*, 365:647–664, 2007.
- N. Hutchins, J.P. Monty, B. Ganapathisubramani, H.C.H. Ng, and I. Marusic. Three-dimensional conditional structure of a high-Reynolds-number turbulent boundary layer. *Journal of Fluid Mechanics*, 673:255–285, 2011.
- I. Jacobi and B.J. McKeon. New perspectives on the impulsive roughness-perturbation of a turbulent boundary layer. *Journal of Fluid Mechanics*, 2011a.

- I. Jacobi and B.J. McKeon. Dynamic roughness-perturbation of a turbulent boundary layer. *Journal of Fluid Mechanics*, 2011b.
- J. Jeong and F. Hussain. On the identification of a vortex. *Journal of Fluid Mechanics*, 285:69–94, 1995.
- Javier Jiménez. Turbulent flows over rough walls. *Annual Review of Fluid Mechanics*, 36:173–196, 2004.
- Javier Jiménez and Alfredo Pinelli. The autonomous cycle of near-wall turbulence. *Journal of Fluid Mechanics*, 389:335–359, 1999.
- R. Jordinson. The flat plate boundary layer. Part 1: Numerical integration of the Orr-Sommerfeld equation. *Journal of Fluid Mechanics*, 43:801–811, 1970.
- T. Kato. *Perturbation Theory for Linear Operators*. Springer-Verlag, 1966.
- L. Keirsbulck, L. Labraga, A. Mazouz, and C. Tournier. Surface roughness effects on turbulent boundary layer structures. *Journal of Fluids Engineering*, 124:127–135, 2002.
- K.C. Kim and R.J. Adrian. Very large-scale motion in the outer layer. *Physics of Fluids*, 11(2):417–422, 1999.
- L.S.G. Kovaszny, V. Kibens, and R.F. Blackwelder. Large-scale motion in the intermittent region of a turbulent boundary layer. *Journal of Fluid Mechanics*, 41(2):283–325, 1970.
- P.-Å. Krogstad and R.A. Antonia. Structure of turbulent boundary layers on smooth and rough walls. *Journal of Fluid Mechanics*, 277:1–21, 1994.
- P. Å. Krogstad, J.H. Kaspersen, and S. Rimestad. Convection velocities in a turbulent boundary layer. *Physics of Fluids*, 10(4), 1998.
- P. Å. Krogstad, H.I. Andersson, O.M. Bakken, and A. Ashrafian. An experimental and numerical study of channel flow with rough walls. *Journal of Fluid Mechanics*, 530:327–352, 2005.
- J. Lehew, M. Guala, and B.J. McKeon. A study of the three-dimensional spectral energy distribution in a zero pressure gradient turbulent boundary layer. *Experiments in Fluids*, 2011.
- S. Leonardi, P. Orlandi, R.J. Smalley, L. Djenidi, and R.A. Antonia. Direct numerical simulations of turbulent channel flow with transverse square bars on one wall. *Journal of Fluid Mechanics*, 491:229–238, 2003.
- P.M. Ligrani and R.J. Moffat. Structure of transitionally rough and fully rough turbulent boundary layers. *Journal of Fluid Mechanics*, 162:69–98, 1986.

- C.C. Lin. *The Theory of Hydrodynamic Stability*. Cambridge University Press, 1955.
- P.J. Loughlin and B. Tracer. On the amplitude- and frequency- modulation decomposition of signals. *The Journal of the Acoustical Society of America*, 100(3):1594–1601, 1996.
- R. G. Lyons. *Understanding Digital Signal Processing*. Prentice Hall, third edition, 2011.
- I. Marusic, R. Mathis, and N. Hutchins. Predictive model for wall-bounded turbulent flow. *Science*, 329(5988):193–196, 2010a.
- I. Marusic, B.J. McKeon, P.A. Monkewitz, H.M. Nagib, A.J. Smits, and K.R. Sreenivasan. Wall-bounded turbulent flows at high Reynolds numbers: Recent advances and key issues. *Physics of Fluids*, 22, 2010b.
- S.A. Maslowe. Critical layers in shear flows. *Annual Review of Fluid Mechanics*, 18:405–432, 1986.
- R. Mathis, N. Hutchins, and I. Marusic. Large-scale amplitude modulation of the small-scale structures in turbulent boundary layers. *Journal of Fluid Mechanics*, 628:311–337, 2009a.
- R. Mathis, J.P. Monty, N. Hutchins, and I. Marusic. Comparison of large-scale amplitude modulation in turbulent boundary layers, pipes, and channel flows. *Physics of Fluids*, 21, 2009b.
- R. Mathis, I. Marusic, N. Hutchins, and K.R. Sreenivasan. The relationship between the velocity skewness and the amplitude modulation of the small scale by the large scale in turbulent boundary layers. *Physics of Fluids*, 23, 2011.
- B.J. McKeon and A.S. Sharma. A critical layer model for turbulent pipe flow. *Journal of Fluid Mechanics*, 658:336–382, 2010.
- P. Meer and I. Weiss. Smoothed differentiation filters for images. *Journal of Visual Communications and Image Representation*, 3(1):58–72, 1992.
- M.M. Metzger and J.C. Klewicki. A comparative study of near-wall turbulence in high and low Reynolds number boundary layers. *Physics of Fluids*, 13(692), 2001.
- J.P. Monty, J.A. Stewart, R.C. Williams, and M.S. Chong. Large-scale features in turbulent pipe and channel flows. *Journal of Fluid Mechanics*, 589:146–156, 2007.
- J.P. Monty, N. Hutchins, H.C.H. Ng, I. Marusic, and M.S. Chong. A comparison of turbulent pipe, channel and boundary layer flows. *Journal of Fluid Mechanics*, 632:431–442, 2009.
- J.F. Morrison. Boundary layers under strong distortion: An experimentalist’s view. In *Prediction of Turbulent Flows*. Cambridge University Press, 2010.

- J.F. Morrison, B.J. McKeon, W. Jiang, and A.J. Smits. Scaling of the streamwise velocity component in turbulent pipe flow. *Journal of Fluid Mechanics*, 508:99–131, 2004.
- V.K. Natrajan, Y. Wu, and K.T. Christensen. Spatial signatures of retrograde spanwise vortices in wall turbulence. *Journal of Fluid Mechanics*, 574:155–167, 2007.
- R. Örlü. *Experimental studies in jet flows and zero pressure-gradient turbulent boundary layers*. PhD thesis, Royal Institute of Technology, 2009.
- S.A. Orszag. Accurate solution of the Orr-Sommerfeld stability equation. *Journal of Fluid Mechanics*, 50:689–703, 1971.
- M.R. Osborne. Numerical methods for hydrodynamic stability problems. *SIAM Journal of Applied Mathematics*, 15(3), 1967.
- B. Pan, H. Xie, G. Zhiqing, and T. Hua. Full-field strain measurement using a two-dimensional Savitzky-Golay digital differentiator in digital image correlation. *Optical Engineering*, 46(3), 2007.
- S-H. Park, I. Lee, and H.J. Sung. Effect of local forcing on a turbulent boundary layer. *Experiments in Fluids*, 31:384–393, 2001.
- M.H. Patel. On turbulent boundary layers in oscillatory flow. *Proceedings of the Royal Society of London. Series A: Mathematical and Physical Sciences*, 353(1672):121–144, 1977.
- B.R. Pearson, R. Elavarasan, and R.A. Antonia. Effect of a short roughness strip on a turbulent boundary layer. *Applied Scientific Research*, 59(1), 1997.
- A.E. Perry, W.H. Schofield, and P.N. Joubert. Rough wall turbulent boundary layers. *Journal of Fluid Mechanics*, 37(2):383–413, 1969.
- S.C. Reddy, P.J. Schmid, and D.S. Henningson. Pseudospectra of the Orr-Sommerfeld operator. *SIAM Journal on Applied Mathematics*, 53:15–47, 1993.
- W.C. Reynolds and A.K.M.F. Hussain. The mechanics of an organized wave in turbulent shear flow. Part 3: Theoretical models and comparisons with experiments. *Journal of Fluid Mechanics*, 54: 263–288, 1972.
- Stephen K. Robinson. Coherent motions in the turbulent boundary layer. *Annual Review of Fluid Mechanics*, 23:601–639, 1991.
- J.L. Rodgers and W.A. Nicewander. Thirteen ways to look at the correlation coefficient. *The American Statistician*, 42(1):59–66, 1988.
- H. Salwen and C.E. Grosch. The continuous spectrum of the Orr-Sommerfeld equation. Part 2: Eigenfunction expansions. *Journal of Fluid Mechanics*, 104:445–465, 1981.

- A.M. Savill. Recent developments in rapid-distortion theory. *Annual Review of Fluid Mechanics*, 19:531–571, 1987.
- P. Schlatter and R. Örlü. Quantifying the interaction between large and small scales in wall-bounded turbulent flows: A note of caution. *Physics of Fluids*, 22, 2010.
- H. Schlichting. Zur entstehung der turbulenz bei der plattenströmung. *Nachrichten von der Gesellschaft der Wissenschaften*, 38, 1933.
- H. Schlichting. Amplitude distribution and energy balance of small disturbances in plate flow. Technical Report 1265, NACA, 1950.
- H. Schlichting. *Boundary-Layer Theory*. McGraw-Hill, sixth edition, 1968.
- P.J. Schmid and D.S. Henningson. *Stability and Transition in Shear Flows*. Springer-Verlag, 2001.
- W. Schoppa and F. Hussain. Coherent structure generation in near-wall turbulence. *Journal of Fluid Mechanics*, 453:57–108, 2002.
- G.B. Schubauer and H.K. Skramstad. Laminar-boundary-layer oscillations and transition on a flat plate. Technical Report 9595, NACA, April 1943.
- G.B. Schubauer and H.K. Skramstad. Laminar boundary-layer oscillations and stability of laminar flow. *Journal of the Aeronautical Sciences*, 14(2):69–78, 1947.
- M.P. Schultz and K.A. Flack. Outer layer similarity in fully rough turbulent boundary layers. *Experiments in Fluids*, 38:328–340, 2005.
- M.P. Schultz and K.A. Flack. The rough-wall turbulent boundary layer from the hydraulically smooth to the fully rough regime. *Journal of Fluid Mechanics*, 580:381–405, 2007.
- A.J. Smits and D.H. Wood. The response of turbulent boundary layers to sudden perturbations. *Annual Review of Fluid Mechanics*, 17:321–358, 1985.
- A.J. Smits, S.T.B. Young, and P. Bradshaw. The effect of short regions of high curvature on turbulent boundary layers. *Journal of Fluid Mechanics*, 94:209–242, 1979.
- D.B. Spalding. A single formula for the law of the wall. *Journal of Applied Mechanics*, 28:455, 1961.
- P.S. Stewart, S.L. Waters, J. Billingham, and O.E. Jensen. Spatially localised growth within global instabilities of flexible channel flows. In *Seventh IUTAM Symposium on Laminar-Turbulent Transition*, 2009.
- N.R. Strader II. Effects of subharmonic frequencies on DFT coefficients. *Proceedings of the IEEE*, 68(2), February 1980.

- H. Tennekes and J.L. Lumley. *A First Course in Turbulence*. The MIT Press, 1972.
- T. Theodorsen. *Proceedings of the Second Midwestern Conference on Fluid Mechanics*, 17–19 March 1952.
- W. Tollmien. Über die entstehung der turbulenz. *Nachrichten von der Gessellschaft der Wissenschaften*, 1929.
- C.D. Tomkins and R.J. Adrian. Spanwise structure and scale growth in turbulent boundary layers. *Journal of Fluid Mechanics*, 490:37–74, 2003.
- A.A. Townsend. Equilibrium layers and wall turbulence. *Journal of Fluid Mechanics*, 11:97–120, 1961.
- A.A. Townsend. *The Structure of Turbulent Shear Flow*. Cambridge University Press, Cambridge, UK, 1976.
- L.N. Trefethen and M. Embree. *Spectra and Pseudospectra: The Behavior of Nonnormal Matrices and Operators*. Princeton University Press, 2005.
- R.E. Turner and M. Sahani. Demodulation as probabilistic inference. *IEEE Transactions on Audio, Speech, and Language Processing*, 20(10), 2011.
- R.J. Volino, M.P. Schultz, and K.A. Flack. Turbulence structure in a boundary layer with two-dimensional roughness. *Journal of Fluid Mechanics*, 635:75–101, 2009a.
- R.J. Volino, M.P. Schultz, and K.A. Flack. Turbulence structure in a boundary layer with two-dimensional roughness. *Journal of Fluid Mechanics*, 635:75–101, 2009b.
- J.A.C. Weideman and S.C. Reddy. A MATLAB differentiation matrix suite. *ACM Transactions on Mathematical Software*, 26(4):465–519, 2000.
- J. Westerweel. Fundamentals of digital particle image velocimetry. *Measurement Science and Technology*, 8:1379–1392, 1997.
- Y. Wu and K.T. Christensen. Reynolds-stress enhancement associated with a short fetch of roughness in wall turbulence. *AIAA Journal*, 44(12), 2006.
- Y. Wu and K.T. Christensen. Outer-layer similarity in the presence of a practical rough-wall topography. *Physics of Fluids*, 19, 2007.
- J. Zhou, R.J. Adrian, S. Balachandar, and T.M. Kendall. Mechanisms for generating coherent packets of hairpin vortices in channel flow. *Journal of Fluid Mechanics*, 387:353–396, 1999.